



IoT-Based Comfort Control and Fault Diagnostics System for Energy-Efficient Homes

April 2024



DISCLAIMER

This work was prepared as an account of work sponsored by an agency of the United States Government. Neither the United States Government nor any agency thereof, nor any of their employees, nor any of their contractors, subcontractors or their employees, makes any warranty, express or implied, or assumes any legal liability or responsibility for the accuracy, completeness, or any third party's use or the results of such use of any information, apparatus, product, or process disclosed, or represents that its use would not infringe privately owned rights. Reference herein to any specific commercial product, process, or service by trade name, trademark, manufacturer, or otherwise, does not necessarily constitute or imply its endorsement, recommendation, or favoring by the United States Government or any agency thereof or its contractors or subcontractors. The views and opinions of authors expressed herein do not necessarily state or reflect those of the United States Government or any agency thereof, its contractors or subcontractors.

EERE Award Number DE-EE0008694

Award Recipient: Texas A&M University

Available electronically at Office of Scientific and Technical Information website (www.osti.gov) Available for a processing fee to U.S. Department of Energy and its contractors, in paper, from: U.S. Department of Energy Office of Scientific and Technical Information P.O. Box 62 Oak Ridge, TN 37831-0062 OSTI www.osti.gov Phone: 865.576.8401 Fax: 865.576.5728 Email: reports@osti.gov Available for sale to the public, in paper, from: U.S. Department of Commerce National Technical Information Service 5301 Shawnee Road Alexandria, VA 22312 NTIS www.ntis.gov Phone: 800.553.6847 or 703.605.6000 Fax: 703.605.6900 Email: orders@ntis.gov



IoT-Based Comfort Control and Fault Diagnostics System for Energy-Efficient Homes

Prepared for:

U.S. Department of Energy Building America Program
Office of Energy Efficiency and Renewable Energy

Prepared by:

Zheng O'Neill (*Principal Investigator*), Tao Yang
Texas A&M University, College Station, TX, 77843

Jin Wen, Richard Kimball
Drexel University, Philadelphia, PA 19104

Hai Xiao, Ningxuan Wen
Clemson University, Clemson, SC 29634

Danny Taasevigen
Pacific Northwest National Laboratory, Richland, WA 99352
April 2024

Suggested Citation

O'Neill, Zheng, Tao Yang, Jin Wen, Richard Kimball, Hai Xiao, Ningxuan Wen and Danny Taasevigen. 2024. IoT-Based Comfort Control and Fault Diagnostics System for Energy-Efficient Homes. College Station, TX. DOE/GO-102024-6120. www.nrel.gov/docs/fy24osti/85920.pdf

ACKNOWLEDGMENT

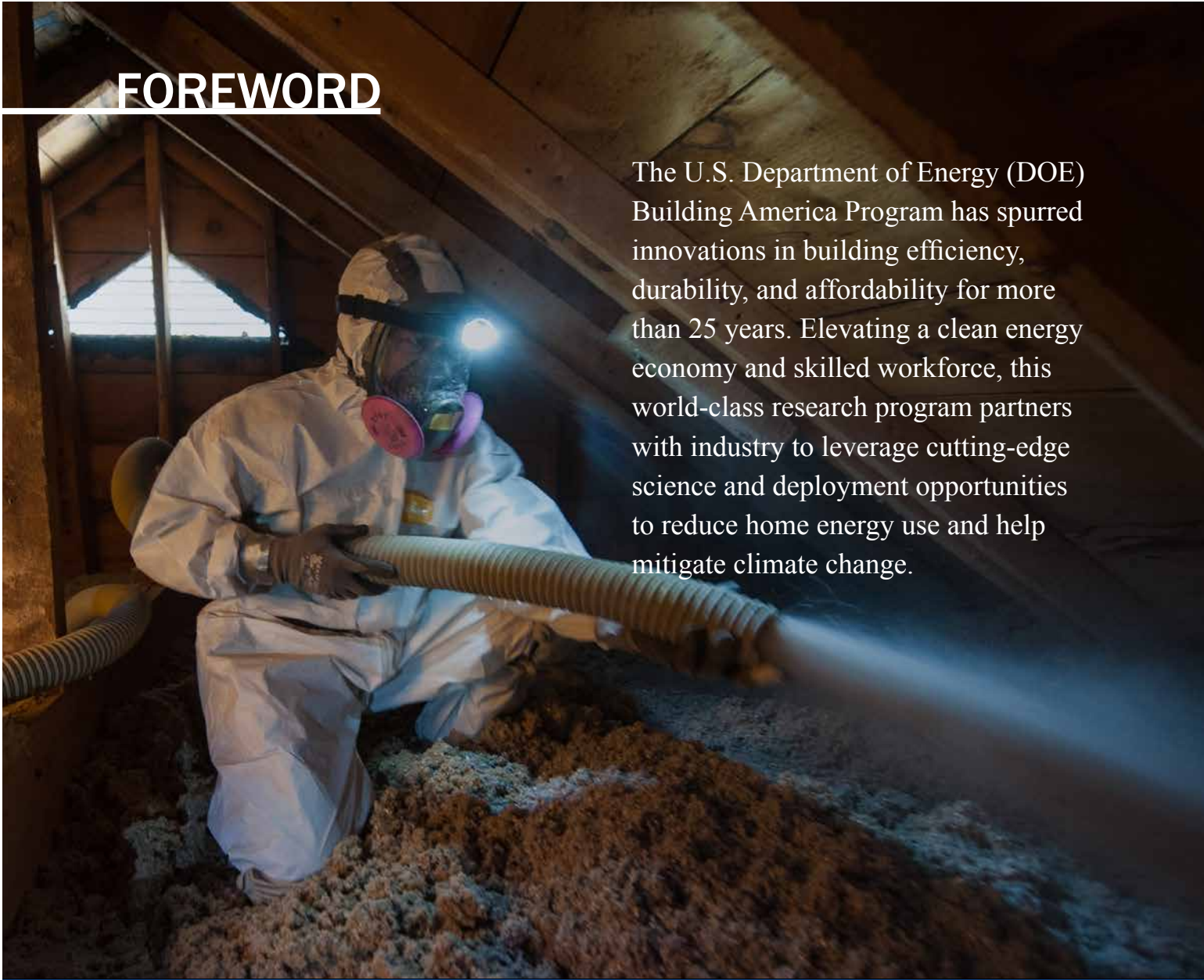
This material is based upon work supported by the Department of Energy's Office of Energy Efficiency and Renewable Energy (EERE) under the Building Technologies Office under Award Number EE0008694.

The work presented in this EERE Building America report does not represent performance of any product relative to regulated minimum efficiency requirements.

The laboratory and/or field sites used for this work are not certified rating test facilities. The conditions and methods under which products were characterized for this work differ from standard rating conditions, as described.

Because the methods and conditions differ, the reported results are not comparable to rated product performance and should only be used to estimate performance under the measured conditions.

FOREWORD



The U.S. Department of Energy (DOE) Building America Program has spurred innovations in building efficiency, durability, and affordability for more than 25 years. Elevating a clean energy economy and skilled workforce, this world-class research program partners with industry to leverage cutting-edge science and deployment opportunities to reduce home energy use and help mitigate climate change.

In cooperation with the Building America Program, Texas A&M University is one of many [Building America teams](#) working to drive innovations that address the challenges identified in the program's [Research-to-Market Plan](#).

This report, *IoT-Based Comfort Control and Fault Diagnostics System for Energy-Efficient Homes*, explores a cost-effective and straightforward smart home system that delivers an occupant-comfort-oriented thermal environment adaptive to faulty conditions.

As the technical monitor of the Building America research, the National Renewable Energy Laboratory encourages feedback and dialogue on the research findings in this report as well as others. Send any comments and questions to building.america@ee.doe.gov.

ACKNOWLEDGMENTS

The work presented in this report was funded by the U.S. Department of Energy (DOE) Office of Energy Efficiency and Renewable Energy Building Technologies Office.

The research was conducted by teams from Texas A&M University, Drexel University, Clemson University, and the Pacific Northwest National Laboratory, with guidance and support from Eric Werling, Building America Program Manager, and Lucas Phillips, Research Engineer from National Renewable Energy Laboratory.

The authors thank the following people for their contributions to this project:

- Dr. William Stuart Dols and Dr. Lisa Ng from the National Institute of Standards and Technology for their technical supports on the CONTAM and EnergyPlus® co-simulation.
- Dr. Vance Payne from the National Institute of Standards and Technology for his technical and data support on the vapor compression cycle fault detection and diagnosis.
- Dr. David Yuill from the University of Nebraska-Lincoln for providing datasets on the vapor compression cycle fault detection and diagnosis.
- Mr. Andrew Costinett and Mr. Dan James from the Pacific Northwest National Laboratory for their assistance in lab testing.
- Mr. Blake Smith-Cortez from Texas A&M University for his technical support on the thermostat application programming interface setup in the lab testing.
- Dr. Zhihong Pang from Texas A&M University/Louisiana State University for his technical support on the economic analysis.

Photo Credits

Cover, from top to bottom: Photos from iStock 182149008, 178447161, 184944590, 467972591;

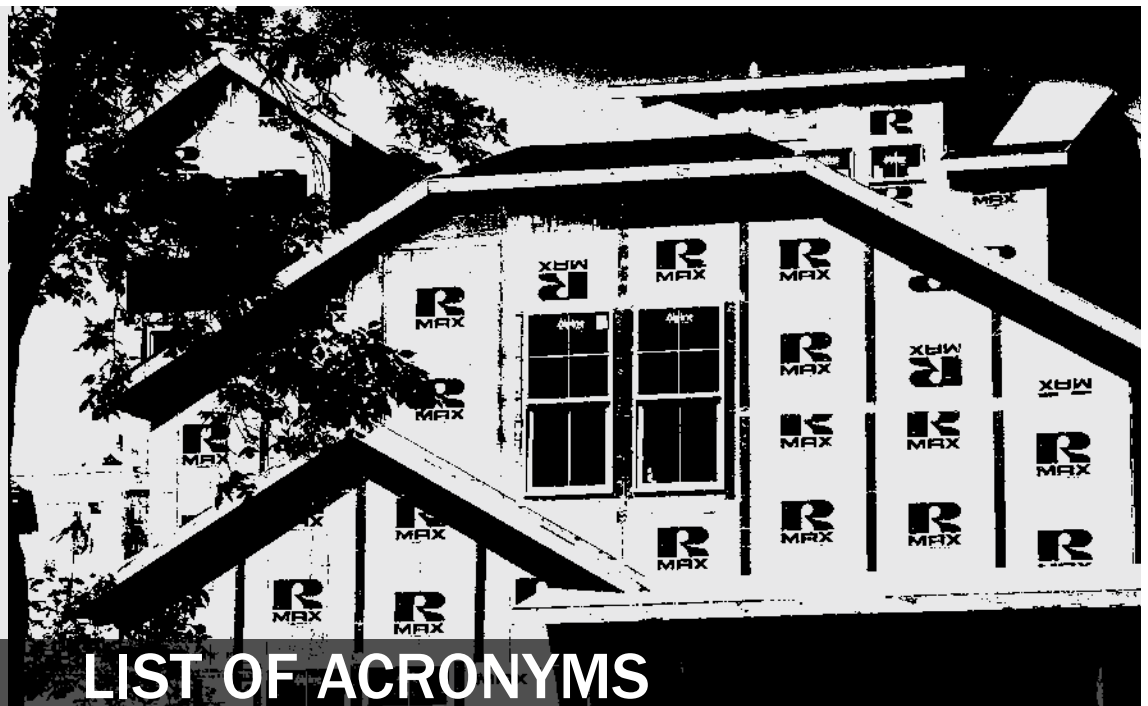
Page ii and iii: Photo from iStock 182149008;

Page v: Photo by Dennis Schroeder, NREL 28764;

Page vi: Photo from iStock 183245764;

Page vii: Photo from iStock 496703961;

Page viii: Photo from iStock 148484827



LIST OF ACRONYMS

AC	air conditioning	MARS	multiadaptive regression splines
AdaBoost	adaptive boosting	MCU	microcontroller unit
ADC	analog-to-digital converter	MPC	model predictive control
AFDD	automated fault detection and diagnosis	NF	no fault
API	application programming interface	NG	non-condensable gas
AWS	Amazon Web Services	NIST	National Institute of Standards and Technology
CDF	cumulative density function	OC	refrigerant overcharge
CF	condenser fouling	PDF	probability distribution function
CNN	convolutional neural network	PNNL	Pacific Northwest National Laboratory
COP	coefficient of performance	PWM	pulse-width modulation
CV	compressor valve leakage	RBC	rule-based control
DOE	U.S. Department of Energy	RMT	robust multivariate temporal
DPC	data predictive control	SVM	support vector machines
EF	evaporator fouling	SVR	support vector regression
FDD	fault detection and diagnosis	TDNN	time delay deep neural network
GLM	generalized linear models	THSP	Temperature-Humidity Sensing Platform
GPIO	general-purpose input/output	UART	universal asynchronous receiver-transmitter
HVAC	heating, ventilating, and air conditioning	UC	refrigerant undercharge
IIC	inter-integrated circuit	VCC	vapor compression cycle
IoT	Internet of Things	WARM	weighted association rule mining
kSVM	kernel support vector machines		
LCCA	life cycle cost analysis		
LL	liquid-line restriction		
LoRa	long range (a wireless audio frequency technology)		



EXECUTIVE SUMMARY

The buildings sector comprises the largest portion of energy consumption worldwide, even surpassing the industrial and transportation sectors.

In the United States, buildings consume around 28% of total energy (with residences accounting for 16% and commercial buildings consuming 12%) (EIA 2022d) and are responsible for 35% of carbon emissions (EIA 2022d). Among them, almost half is consumed by heating, ventilating, and air conditioning (HVAC) (L. Wang and Hong 2013).

Furthermore, 108.9 million out of 123.5 million housing units had installed air conditioning (AC) equipment as of 2020 (EIA 2020a).

This number was 94 million of 113.6 million in 2009 (EIA 2009), and 82.9 million of 100.4 million in 2001 (EIA 2001). Therefore, reducing building HVAC energy consumption, especially in the residential sector, has a significant potential to contribute to the 2030 U.S. greenhouse gas pollution reduction target (The White House 2021). The goal for energy-efficient buildings set by the U.S. Department of Energy (DOE) is to reduce the direct energy intensity of residential and commercial buildings by at least 35% by 2030 while reducing direct fossil fuel consumption by more than one-third. Particularly, the goal of residential buildings is to achieve 50% energy savings through the identification of deep retrofit packages relative to typical homes in 2010 (BTO 2016).

The primary objective of living environment conditioning for residents is to satisfy their well-being and working efficiency requirements, which has become increasingly crucial, particularly due to the widespread adoption of remote work since 2020 (Mehta 2021). However, as an HVAC system degrades over time, it may not always be able to maintain the required thermal environment, especially during heat waves (Zuo et al. 2015). This concern is further amplified by the impacts of climate change, which accelerates the frequency of extreme weather events (Simon Brown 2020).

This project studies an Internet of Things (IoT)-based comfort control and fault diagnostics system (referred as iComfort in this report) for energy-efficient homes. The system delivers an occupant-comfort-oriented thermal environment adaptive to fault scenarios and achieves HVAC energy savings in a cost-effective and straightforward way. This smart iComfort home system consists of the following key features.

- 1. Cost-effectiveness and scalability of the entire hardware and software system:** The system includes low-cost temperature, humidity, and airflow sensors, and a Raspberry Pi-based local hub that interfaces with the cloud and IoT-enabled devices. The cost is low, not only for sensors, but also the costs associated with sensor installation, system setup and commissioning, data communication and storage, and data analytics (e.g., the development of automated fault detection and diagnosis (AFDD), as well as control strategies that are both computationally efficient and practical to implement).
- 2. Energy performance and user satisfaction:** The system delivers user satisfaction and energy savings. This includes a) ease of use, b) optimal occupant thermal comfort, and c) accurate system feedback (e.g., low false alarm of AFDD strategies).
- 3. Favorable demonstrated prototype performance:** The prototype tested at the Pacific Northwest National Laboratory (PNNL) Lab Homes demonstrates the accuracy of fault detections and diagnoses and shows thermal comfort improvement and energy savings through adaptive and optimal HVAC operations.

The following tasks were accomplished to fulfill the project objectives.

IoT-Based Cost-Effective Distributed Sensor System

The low-cost IoT-based distributed sensor system is integrated with wireless sensors, the local hub, and the cloud system. The wireless sensor modules are capable of measuring temperature and relative humidity with a high resolution of 0.1°C and 0.1%, respectively. The development of the local hub targets communicating with the wireless sensors, collecting the sensor data, and uploading the distributed measurement results to the cloud. The cloud service is completed by Amazon Web Services (AWS); the local hub can simultaneously collect data from multiple wireless sensors and send the data to AWS. In addition, the data handling functions are developed inside AWS, which enables the sensor data to be time-stamped, stored, processed, downloaded, and displayed in real time.

The produced sensing platform is powered by a cell battery and communicates with the hub via the LoRa protocol.¹ The sensing functions (e.g., temperature and humidity) are performed by an

¹ Short for “long range,” LoRa is a wireless audio frequency technology.

SHT31 temperature and humidity sensor, which is connected to the processing and communication module through the soldering pads. The Temperature-Humidity Sensing Platform (THSP) can send readings to a hub within 100 meters in an open space. In the indoor test, the signal can penetrate at least three walls. The wireless temperature sensors successfully measured temperatures and passed data to the hub. Long-term testing shows that the system continuously worked for 60 days without human intervention. During the test period, the system overcame at least two power outages and several network disconnections and successfully restored its normal functions. It collected more than 340,000 records in total from four sensors. The database retained about 44,000 records from each sensor for monitoring and analysis.

Virtual Testbed and Fault Models

The virtual testbed used in this project was adapted from the DOE prototype residential building model created by PNNL (DOE 2021), which was developed using survey data, standards, reports, papers, and expert knowledge. The prototype model consists of two floors with a total area of 223 m² (2,400 ft²) and has a slab-on-grade foundation. The HVAC system in the virtual building is a dual-setpoint controlled central air heat pump system, with the default control being a schedule-based fixed setpoint control.

To facilitate the simulation of operational faults in residential HVAC systems, an expandable fault library was created for this project on top of the virtual testbed. This library includes a fault taxonomy that defines each fault and its systematic structure, as well as fault modeling elements such as fault attributes (direction types, bounds, and prevalence) and the corresponding objects and parameters in EnergyPlus. A fault modeling approach was also developed, which includes fault mapping, fault occurrence distribution development, multiple fault combination, and fault sampling. The process of fault injection involves simultaneously modifying the values of all relevant parameters of interest in the EnergyPlus IDF files. This modification is carried out based on the developed fault library and fault modeling approaches. In situations when direct modeling of faults such as heat exchanger fouling or refrigerant charge issues is not feasible in EnergyPlus, the corresponding fault symptoms, such as efficiency and capacity degradation, are instead represented.

In this project, fault modeling was implemented using EnergyPlus to generate 3,000 faulty models, representing 3,000 fault scenarios with a variety of faults. These models can be used to simulate operational faults in residential HVAC systems and conduct a fault-relative investigation, including understanding the impact of faults, guiding and testing AFDD strategies, and assisting with adaptive control.

Learning-Based Models

We developed a framework for learning-based HVAC energy consumption forecasting models, zone temperature forecasting models, and occupant thermal comfort forecasting models. The framework is first examined using a virtual testbed and then applied for the PNNL lab test homes to develop forecasting models. The virtual testbed was utilized to obtain the simulated data that closely resembled the types of data typically available from a real building. These simulated data were then used for training and evaluating forecasting models. Historic and current sensor data from the PNNL lab test homes were used to train and evaluate the developed models.

A multiadaptive regression spline (MARS)-based whole-building energy forecasting model and kernel support vector machine (kSVM)-based occupant thermal comfort vote forecasting model were first developed and tested using the data from the virtual testbed with a 1-hour ahead forecasting horizon. The developed models were used as a preliminary study for the developed framework. A systematic multistep feature selection process was explored to select features used for the models, from virtual measurements. The evaluation results show that both developed forecasting models performed accurately across the virtual testing period according to desired performance of <15% normalized root mean square error.

The developed framework was then used to train two MARS-based models, one for HVAC energy consumption forecasting, and the other one for zone temperature forecasting, using historical data from the PNNL lab test homes with a 1-hour ahead forecasting horizon. The developed systematic multistep feature selection process was adopted to select features for the models. K-fold cross validation was used to train and test the model on all data and reduce model generalization error. The evaluation results show that both developed forecasting models perform accurately across the entire testing period (8 weeks total) according to desired performance of <15% normalized mean absolute error.

Due to a lack of real occupants in the PNNL lab test homes zone, temperature—rather than occupant thermal comfort—was modeled. To examine the performance of the developed thermal comfort forecasting modeling approach, we used virtual testing. Operation data for normal operation and scenarios that would cause occupants to be uncomfortable were generated for training and testing of the developed models. A kSVM-based model was developed and tested using the data from the virtual testbed with 1-hour ahead horizon. The developed systematic multistep feature selection process was again used to select features for the model. It was found that the correlations between features and the target feature, (i.e., occupant thermal comfort), were not strong. Expert knowledge was then explored to finalize the feature selection. A kSVM-based model was trained and used to forecast occupant

thermal comfort for each of the three occupants presented in the virtual testbed. Models developed using the kSVM method are able to successfully predict occupant thermal comfort accurately for the entire testing period (1 week) with more than 90% accuracy.

Computationally Efficient AFDD

Building HVAC systems seldomly perform as designed. Therefore, it is important to keep it maintained and repair the failed equipment in time, or to implement fault-adaptive control (i.e., implementing corresponding control strategies to offset the impact caused by system faults) to proactively respond to these malfunctions. To achieve this goal, detection and diagnosis of existing faults are required.

To address duct leakage, a robust multivariate temporal (RMT)-based variate selection method has been implemented to identify relevant variates for use in a forecasting model. This method ranks variates based on the co-occurrence of key temporal features/events to select variates that have high impact on forecasting of a target variable. Localized multivariate temporal features, which are robust against noise, are extracted by considering multiple scales, temporal characteristics of the time series, and external domain knowledge such as feature-to-feature relationships from a multivariate time series. Using data from the virtual testbed, the fault relevant variates for the target variate are ranked using RMT-based variate selection. Sensitivity tests show that the model performs best when using the attic zone temperature and the top 15% of ranked variates.

Following this, a convolutional neural network (CNN)-based model is trained on a fault-free set and used to forecast the target variate during the faulty period. A data selection framework to create artificial test data based on user's input is also developed to evaluate the strategy. The evaluation results show that the developed strategy is able to successfully identify the fault impact when using the attic mean zone temperature as the target variate. This demonstrates the solidity of the attic mean zone temperature serving for the duct leakage detection. During the initial and final periods of duct leakages, the fault can be accurately identified and flagged with a 100% detection rate.

To address installation and operation faults in vapor compression cycle (VCC) systems, three existing AFDD methods for residential VCC systems were investigated: statistical rule-based chart, sensitivity ratio method, and simple rule-based method. A qualitative comparison was conducted, considering features required, fault-free reference models, potential faults diagnosed, and pros and cons of each method, as well as their performance regarding diagnosis accuracy rate. The statistical rule-based chart is well-developed as it considers probabilities in three uncertainty sources (measurement noise uncertainty, steady-state uncertainty, and fault-free model uncertainty). However, the specific adjustment for coefficients in the probabilities equations is challenging to ensure the acceptable accuracy. The simple rule-based method can obtain a high FDD accuracy while requiring minimal

efforts, as it only necessitates simplified normal thresholds for each fault feature. However, it should be noted that these thresholds are sensitive to specific fault types.

A quantitative comparison analysis was carried out using the NIST experiment data for four metrics: accuracy, false alarm, misdiagnosis, and missed detection. The statistical rule-based chart performs better for no fault (NF) and liquid line restriction (LL) cases with the accuracy of near 100%, while the simple rule-based method performs better for condenser fouling (CF), refrigerant undercharge (UC), and refrigerant overcharge (OC) cases with the accuracy of near 60%, 100%, and 100%, respectively. The sensitivity ratio method does not outperform in any case. The comparison results show that no single method could achieve consistent detection accuracy for different types of faults, which highlights the challenges of using individual FDD methods to achieve acceptable accuracy.

Therefore, we adopt a hybrid FDD approach that integrates the statistical rule-based chart and simple rule-based method in this project. Our approach emphasizes the weight of diagnosed results from the method with high diagnosis accuracy for a given fault. The hybrid FDD approach was tested with a field test dataset, achieving an overall diagnosis accuracy of 83.02% when counting only fault cases and 90.18% when counting all cases, including fault-free ones. The two-class confusion matrix for detection showed that all metrics were higher than 90%, with a detection accuracy of 96.4%.

Model-Based Adaptive Control Framework With Extracted Rules

To deal with the discomfort condition caused by system degradation faults and severe heat waves, precooling is a control cost-effective strategy that pre-cools the building preceding in a given period to enhance the cooling effect by only utilizing the thermal mass of building envelopes and home furniture. To leverage the benefits of optimized control strategies from model predictive control (MPC) and at the same time ensure their practical application in ordinary households, an MPC-informed rule extraction is employed. This technique conducts the MPC offline in one hub, and then extracts several rules from its operation results (a larger-scale simulation is usually required to ensure adaptability in multiple locations). Consequently, these rules can be applied easily in ordinary houses. The process is called rule extraction. The goal of rule extraction is to select a minimum set of inputs, feed them to the rule-based controls, and maintain the same or close levels of thermal comfort and energy consumption with the MPC simultaneously.

We conducted an advanced control strategy MPC for the precooling control in the residential building with only thermal mass in consideration under extreme weather events (e.g., heat waves), and then to extract operation rules with a classification and regression tree to take advantage of the MPC results and make them easier to be applied in homes. It should be noted that the “extreme weather” in this project is a relative concept and defined on the basis of HVAC system operation. The concept

of extreme weather encompasses different scenarios: it can be a combination of normal weather conditions with a faulty HVAC system, abnormal weather conditions with a normal HVAC system, or abnormal weather conditions with an abnormal HVAC system. By providing this additional definition, we aim to clarify the various situations encompassed by the term “extreme weather”.

This framework is implemented in the prototype building and generates several control rules in the form of a decision tree. Simulation results demonstrate that thermal comfort can be improved with MPC-informed rules generated by the simulation results: During the same run period of testing and training, unmet hours decrease from 10 C-hr to 5.1 C-hr from July 14 to August 2, and from 0.6 C-hr to 0 from August 13 to 22; when applied to a different period, the MPC-informed rule control generated from one period can mitigate the unmet hours from 9.2 C-hr to 5.2 C-hr, with a more than 60% decrease rate. Furthermore, the online computation time for MPC-informed rule-based control (RBC) is significantly faster than the original MPC. On average, MPC consumes 870 minutes for a 10-day running period, while MPC-informed RBC finishes in 0.2 minutes on average with the same computer configuration, which is 4,350 times faster. The comparison of time consumption indicates that MPC-informed rules impose a lower computational burden compared to MPC that involves an optimization process. This characteristic allows these near-optimal rules to be easily implemented in regular homes where HVAC controllers have limited computational capabilities. Thus, the simulation results suggest that the developed approach is not only effective in enhancing thermal comfort but also efficient in terms of computational load.

Lab Testing

The technology developed in this project utilizes low-cost sensors developed by the research team, which are installed throughout a residential dwelling. A demonstration of these technologies in a field testing setting was conducted at the PNNL Lab Homes. The demonstration effort entailed a dedicated testing period of seven weeks, from August 10 to September 25, 2022, aimed at evaluating the overall performance of the stability of iComfort sensors and cloud server in a established lab testing bed, as well as the effectiveness and efficiency of developed FDD methods and comfort-oriented algorithms.

First, the majority of sensors operated consistently throughout the experiment, reliably transmitting stream measurements to the cloud every minute. The 16 iComfort sensors collected and pushed 1,413,072 sets of temperature and humidity data (and airflow data from four of them). The cloud database’s application programming interface (API) served more than 5,198,000 query requests from the detection and control algorithms. The cloud database was working at 100% availability and completely error-free during the experiment.

Secondly, for the FDD strategy demonstration, the accuracy of FDD for the heat pump system can achieve 90.18%, counting all cases (including fault-free ones), with zero false alarm. The detection accuracy is 96.4%. Both of metrics met the program's required threshold of 80%.

Furthermore, for the energy saving from the temperature setpoint control, 14% energy saving was obtained by occupancy-based setback strategies, or 10% was achieved by data predictive control. Both of them demonstrate $\geq 10\%$ energy saving, which is one of the program goals. In terms of thermal comfort improvement, unmet hours could be decreased from 2.05°-hr (Lab Home B—baseline case) to 0.22°-hr (Lab Home A—test case), which will help improve residents' thermal comfort under the malfunction of HVAC systems or in heat wave events.

Economic Analysis

The purpose of this simple economic analysis is to provide a description of the value that the developed product offers, as well as to examine current and future market opportunities, barriers, and relevant standards. This analysis evaluates the markets for sensors, automated fault diagnostic systems, and smart home energy management systems, and provides detailed technical and economic analysis.

Table of Contents

1.	Introduction.....	1
1.1	Scope of This Project.....	2
1.2	IoT-Based Sensor Networks and Cloud Systems	3
1.3	Learning-Based Models.....	3
1.4	Fault Modeling for Residential Buildings	4
1.5	Automatic Fault Detection and Diagnosis for Residential HVAC Systems	5
1.6	Model-Based Adaptive Control-Informed Extracted Rules	7
2.	IoT-Based Cost-Effective Distributed Sensor System.....	9
2.1	Fundamental Framework: Sensor Module, Local Hub, and Cloud Data Center.....	9
2.2	Low-Cost Wireless Sensor Platform: Temperature/Humidity Sensors	16
2.3	Low-Cost Wireless Sensor Platform: Airflow Sensors	22
2.4	Summary.....	24
3.	Virtual Testbed and Fault Modeling.....	26
3.1	Baseline Building Model: DOE Prototype Residential Building	26
3.2	Fault Library	28
3.3	Fault Modeling Methodology Based on Residential Fault Library	34
3.4	Generation of Residential Building Fault Models	39
3.5	Summary.....	41
4.	Learning-Based Models	43
4.1	Overall Modeling Framework	43
4.2	Pilot Study of Developing Forecasting Models for Virtual Testbed	49
4.3	Forecasting Models for the PNNL Lab Test	53
4.4	Summary.....	58
5.	Computationally Efficient Automatic Fault Detection and Diagnosis	60
5.1	FDD Process	60
5.2	Duct Leakage Fault Detection Strategy	61
5.3	Vapor Compression Cycle System	70
5.4	Summary.....	83
6.	Model-Based Adaptive Control Framework With Extracted Rules	85

6.1	MPC Framework Methodology.....	85
6.2	MPC Application and Rule Extraction.....	94
6.3	Summary.....	102
7.	Lab Testing.....	103
7.1	Lab Testing Setup and Implementation.....	103
7.2	Analysis of Results.....	109
7.3	Summary.....	118
8.	Economic Analysis.....	119
8.1	Introduction.....	119
8.2	Market Opportunity.....	119
8.3	Life Cycle Cost Analysis.....	127
9.	Conclusions.....	134
10.	Publications.....	138
11.	References.....	138
	Appendix A: IoT-Based Sensor Network.....	150
	Appendix B: Basics for Residential Building Systems.....	154
	Appendix C: Fault Modeling for Residential HVAC Systems.....	160
	Appendix D: Fault Detection and Diagnosis for Residential HVAC Systems.....	174
	Appendix E: Lab Testing.....	186
	Appendix F: Market Analysis.....	201
	Appendix G: Economic Analysis.....	213
	Appendix H: Literature Review.....	219

List of Figures

Figure 1. Schematics of the smart home energy management system developed in this project ...	3
Figure 2. System overview	9
Figure 3. Functional block diagram of the sensor wireless communication platform.....	10
Figure 4. Sensor module design.....	11
Figure 5. Block diagram of the local hub data workflow	12
Figure 6. Block diagram and picture of the USB LoRa Gateway	12
Figure 7. Cloud-based system architecture and the associated AWS solutions	13
Figure 8. Sensor data system test.....	15
Figure 9. Front and back views of a THSP unit.....	16
Figure 10. Components of the temperature and humidity sensing platform.....	17
Figure 11. Workflow of the temperature and humidity sensing module	18
Figure 12. Floorplan and system installation.....	20
Figure 13. Temperature and humidity charts: 30 days of readings.....	20
Figure 14. Revised THSP unit	21
Figure 15. Comparison of the original THSP units and revised units	21
Figure 16. The original GM8901 anemometer system	22
Figure 17. THSP unit housed within the airflow sensor handle	23
Figure 18. Converted wind speed readings of different the input signal frequency	24
Figure 19. Geometry of prototype residential building with slab-on-grade foundation	27
Figure 20. Occupant schedule.....	28
Figure 21. Lighting schedule	28
Figure 22. Miscellaneous devices schedule	28
Figure 23. Taxonomy of residential HVAC fault library	29
Figure 24. Vapor compression cycle for air conditioner system and heat pump system (numbers are corresponding specific faults).....	31
Figure 25. Heating system with a furnace installed (numbers are corresponding specific faults).....	31
Figure 26. Histogram of charge fault ratio collected using measurements from previous studies.....	33
Figure 27. Research methodology outline of EnergyPlus-based faulty model generation.....	34
Figure 28. Example of fault mapping data structure for fault model generation.....	36
Figure 29. Inverse transform sampling with Latin hypercube sampling (Yanfei Li 2018)	38
Figure 30. The procedure of fault parameter sampling.....	39
Figure 31. Examples of fault pdf curves (the x-axis is the fault bias, and the y-axis is the fault occurrence probability).....	40
Figure 32. Visual example of expected error reduction algorithm	44
Figure 33. The complete active learning algorithm for building energy forecasting	45
Figure 34. Systematic multistep feature selection process	47
Figure 35. A visualization of cross validation	48
Figure 36. Functional mock-up interface co-simulation environment integrated in EnergyPlus and MATLAB.....	50

Figure 37. Artificial neural network predicted energy vs. actual	50
Figure 38. Occupant 3 Thermal Comfort @t+1: kSVM predicted vs actual.....	53
Figure 39. MARS HVAC energy forecasting model evaluated on real 2022 PNNL Lab Home A sensor data.....	56
Figure 40. MARS zone temperature forecasting model evaluated on Real 2022 PNNL Lab Home A sensor data.....	58
Figure 41. Airflow network diagram for the virtual testbed.....	62
Figure 42. CNN forecasted attic mean zone temperature for fault free dataset.....	68
Figure 43. Framework for creating artificial test set.....	68
Figure 44. Fault impact on the mean attic zone temperature for Scenario 1-1 (50% leakage).....	69
Figure 45. Forecasting results and absolute difference error for Scenario 1-1 (50% leakage).....	69
Figure 46. Schematic diagram of VCC and monitored variables	72
Figure 47. Numbers and severity levels of fault cases from NIST datasets (percentages on the bars indicate severity levels).....	76
Figure 48. Accuracy performance of different-order multivariable polynomial regression models for all features	77
Figure 49. Comparison of measured and predicted temperatures, taking discharge temperate as an example	78
Figure 50. Results of evaluation metrics (i.e., false alarm, missed detection, misdiagnosis, and accuracy) for four AFDD methods (i.e., SRBC, SRBC with adjusted k and s , SRM, SRBM)	79
Figure 51. Misdiagnosis distribution among four FDD approaches (i.e., SRBC, SRBC with adjusted k and s , SRM, SRBM)	81
Figure 52. Hybrid FDD flowchart for VCC systems.....	82
Figure 53. The workflow of MPC and rule extraction.....	85
Figure 54. Schematic diagram of decision tree.....	86
Figure 55. Open-loop test and closed-loop test	88
Figure 56. Model predictive control framework for residential HVAC systems	89
Figure 57. Co-simulation of EnergyPlus and optimization algorithms (in Python) via functional mock-up unit	90
Figure 58. Performance of model training.....	95
Figure 59. Time-series temperature with the change of weighting factor beta for the smooth item	96
Figure 60. Decision tree and its prediction accuracy for the best fitting weight factor alpha estimation.....	96
Figure 61. Temperature distribution of MPC	97
Figure 62. Unmet hours of model predictive control.....	97
Figure 63. Accuracy of rule extraction in the open-loop test	98
Figure 64. Effect of different depths in the decision tree	98
Figure 65. Classification and regression tree for precooling with depth of 4.....	100
Figure 66. Unmet hours of model predictive control with training data	100

Figure 67. Unmet hours and energy consumption with training data.....	101
Figure 68. Framework of lab testing for FDD and controls	103
Figure 69. Exterior photos of the PNNL Lab Homes.....	104
Figure 70. Layout of the PNNL Lab Homes	104
Figure 71. Heat pump indoor and outdoor units for the PNNL Lab Homes	105
Figure 72. Summary of data flow for the IOT-based comfort control	105
Figure 73. Temperature, humidity and airflow data from the living room area	109
Figure 74. Temperature distribution in the heat pump system	111
Figure 75. Heat pump feature temperature	111
Figure 76. Accuracy performance of different-order multivariable polynomial regression models for all features with field test dataset	111
Figure 77. Scatter comparison of measured and predicted discharge temperature.....	112
Figure 78. Series comparison of measured and predicted discharge temperature.....	112
Figure 79. Diagnosis matrix for the FDD-VCC.....	113
Figure 80. Temperature plot for evaporator inlet air temperature ($T_{\text{eai}}-T_e$) and suction line superheat (T_{sh}).....	113
Figure 81. Energy consumption in Lab Home A and Lab Home B under occupancy adaption scenario 1	114
Figure 82. Unmet hours comparison between Lab Home A and Lab Home B	115
Figure 83. Unmet hours comparison of Lab Home A and B during the whole testing period	115
Figure 84. Online DPC testing timeline	116
Figure 85. Drexel University online DPC testing period—thermostat setpoint and power	117
Figure 86. U.S. smart thermostat market size trend (Pnewswire)	120
Figure 87. Structure of developed smart home energy management system	126
Figure 88. Interface demo for indoor climate monitoring in this home energy management systems.....	127
Figure 89. Structure of the cost-effectiveness analysis (Pang 2022)	128
Figure 90. Geographical distribution of 41 selected cities in the US	129
Figure 91. Number of selected cities in each climate zone.....	129
Figure 92. Energy saving and cost saving	131
Figure 93. Year-based net saving.....	131
Figure 94. Discount payback period	132
Figure 95. Discount payback periods for different sensor prices	133
Figure 96. Smart Home Energy Management coupled with FDD for VCC systems and MPC/rule- based adaptive control.....	134
Figure 97. Example data in the sensor information table	150
Figure 98. Example data in the sensor data table.....	150
Figure 99. Sample data from the cloud database	151
Figure 100. Sensor measurements received by the hub	151
Figure 101. The airflow reading on the hub display.....	151

Figure 102. Temperature and humidity charts of 30 days' readings for living room, kitchen, and study room	152
Figure 103. Processing and communication module	153
Figure 104. Components and interfaces in the processing and communication module.....	153
Figure 105. Three types of residential building foundations	154
Figure 106. Energy flow mechanism of residential heating/cooling systems	155
Figure 107. Air loop in the EnergyPlus model of the prototype residential building.....	157
Figure 108. Heat pump module in the EnergyPlus model of the prototype residential building	157
Figure 109. Water loop in the EnergyPlus model of the prototype residential building	158
Figure 110. Heating and cooling energy consumption	159
Figure 111. An example of fault-by-lacking PDF curve	161
Figure 112. An example of fault-by-excess PDF curve.....	162
Figure 113. An example of fault-by-deviating PDF curve	162
Figure 114. An example of fault-by-uniform PDF curve	163
Figure 115. Monthly fault effect on the heating and cooling energy consumption.....	168
Figure 116. Monthly fault effect on the overall HVAC energy consumption.....	168
Figure 117. Monthly effect on the energy consumption for each fault	169
Figure 118. Performance comparison between individual and coupled faults during the month of July (residential building in Houston).....	170
Figure 119. Fault sampling distribution of cooling coil COP values in 3,000 fault models	171
Figure 120. Probability distribution of HVAC energy consumption from 3000 fault simulations	171
Figure 121. Confusion matrix for fault detection	175
Figure 122. Forecasting results and absolute difference error for Scenario 1-1 (50% leakage). 176	
Figure 123. Forecasting results and absolute difference error for Scenario 1-1 (10% leakage). 176	
Figure 124. Forecasting results and absolute difference error for Scenario 2 (N2-2)	177
Figure 125. Forecasting results and absolute difference error for Scenario 3	177
Figure 126. Comparison of temperature-entropy in normal (black line) and faulty (red line) condition of a VCC system.....	179
Figure 127. Sensitivity ratio method.....	182
Figure 128. Comparison of measured and predicted discharge temperature.....	183
Figure 129. Comparison of measured and predicted superheating temperature.....	184
Figure 130. Comparison of measured and predicted evaporator temperature	184
Figure 131. Comparison of measured and predicted evaporator exit refrigerant vapor temperature	184
Figure 132. Accuracy rate results from statistical rule-based chart method with different combinations of k and s values	185
Figure 133. Two simulated occupancy schedules that are used to test and characterize the performance of the IOT-based comfort control	189

Figure 134. Simulated appliance load schedule that is implemented using an electric resistance space heater.....	189
Figure 135. Installation map of iComfort sensors.....	191
Figure 136. Condenser fouling implemented using paper.....	195
Figure 137. Photo of evaporator fouling simulation.....	195
Figure 138. Refrigerant overcharge and undercharge simulation.....	196
Figure 139. Typical occupant load simulation for the PNNL Lab Homes including heat gains from lighting, occupants, and appliances.....	197
Figure 140. Indoor temperature comparison from iComfort and Ecobee.....	198
Figure 141. Heat pump feature temperature.....	199
Figure 142. Comparison of forecast and real outdoor dry-bulb temperature.....	199
Figure 143. Interface demo for indoor climate monitoring in this home energy management system.....	212
Figure 144. Monthly electricity price for 41 selected cities.....	214
Figure 145. Annual electricity price on average for residential buildings in 41 selected U.S. cities (2022).....	215

List of Tables

Table 1. LoRa Module Features.....	10
Table 2. Sensor Module Performance Features and Specifications.....	11
Table 3. LoRa Gateway Specifications.....	13
Table 4. Structure of the Sensor Information Table.....	14
Table 5. Structure of the Sensor Data Table.....	14
Table 6. Specification of Temperature and Humidity Sensor.....	17
Table 7. Compatible Cell Batteries.....	19
Table 8. Specification of GM8901 Air Velocity Measurement.....	22
Table 9. Building Information of Prototype Residential Building.....	27
Table 10. Definitions of Terms in Fault Library.....	30
Table 11. Historical HVAC Energy Forecasting Model Candidate Feature Set.....	47
Table 12. kSVM Model Performance at Forecasting Occupant Thermal Comfort at 1-Hour Ahead.....	53
Table 13. Forecasting Model Candidate Feature Pool for PNNL Lab Home Testing.....	54
Table 14. MARS HVAC Energy Forecasting Model Selected Features for PNNL Lab Home...	55
Table 15. MARS HVAC Energy Forecasting Model Performance on Historical Data.....	56
Table 16. MARS Zone Temperature Forecasting Model Selected Features for the PNNL Lab Home.....	57
Table 17. MARS Zone Temperature Forecasting Model Performance on Historical Data.....	58
Table 18. Airflow Network Duct Sizes.....	63
Table 19. Summary of Candidate Variates.....	65
Table 20. Fault Scenario Descriptions.....	66

Table 21. Variate Ranking Using RMT for Fault Free Scenario	67
Table 22. Fault Classifier Results for Scenario 1-1 (50% leakage) Over a 3-Day Period.....	70
Table 23. Commonly Studied Faults in VCC Systems.....	72
Table 24. Parameters/Sensors and Features Used in VCC FDD	74
Table 25. Comparison of Three Existing Rule-Based FDD Methods for the VCC System.....	75
Table 26. Statistics Results of Measured and Predicted Temperatures, Taking Discharge Temperate as an Example	78
Table 27. FDD Results of the Developed Hybrid Approach	83
Table 28. Features of the Classification and Regression Tree.....	98
Table 29. Performance Comparison of MPC-Informed RBC	101
Table 30. Testing Design for Adaptive Control to Occupancy.....	107
Table 31. Testing Design for Adaptive Control to HVAC Faults.....	108
Table 32. Confusion Matrix for Fault Detection	114
Table 33. Drexel University Online DPC Testing Period—Percentage Power Saved	117
Table 34. Specification of Commercial Thermostats in the Market.....	124
Table 35. Unit Cost of the Hardware and Software for iComfort Smart Home Control System	128
Table 36. LCCA plan.....	130
Table 37. Energy source used in residential HVAC systems	156
Table 38. Distribution and medium used in residential HVAC systems	156
Table 39. Fault Factors and Levels for Residential HVAC Modeling	164
Table 40. Orthogonal Design of Experiment Table $L_{64}(4^{12})$	165
Table 41. Fault Library for Residential HVAC Systems.....	172
Table 42. Rule-Based Chart of Seven Features for VCC FDD	180
Table 43. Simple Rule-Based Method.....	183
Table 44. Selected Optimum Set of k and s for Different Faults.....	185
Table 45. Timeline for the Lab Testing.....	186
Table 46. Sensor Overview in Lab Homes.....	190
Table 47. Installed Sensors for HVAC FDD Testing.....	191
Table 48. Required Sensors for the Active Learning Based Performance Model.....	192
Table 49. Metrics and Targets for Sensing During Testing.....	193
Table 50. Details of Fault Scenarios	196
Table 51. Data Completion Status in the Experiment Period.....	200
Table 52. Selected Patents for Smart Home Energy Management Systems.....	205
Table 53. Specification of Commercial Sensors in the Market	207
Table 54. Current AFDD Technologies for Residential HVAC Systems	209
Table 55. Example of Data Processing for Missing Electricity Price.....	213
Table 56. Input Data for the Computation of Material Costs	218
Table 57. Literature Review of Fault Modeling	219
Table 58. Comparison of Different FDD Methods for the VCC System	221
Table 59. Literature Review of Rule Extraction Research	222

1. Introduction

The buildings sector comprises the largest portion of energy consumption worldwide, even surpassing the industrial and transportation sectors. In the United States, buildings consume around 28% of total energy (with residences accounting for 16% and commercial buildings consuming 12%) (EIA 2022d) and are responsible for 35% of carbon emissions (EIA 2022d). Among them, almost half is consumed by heating, ventilating, and air conditioning (HVAC) (L. Wang and Hong 2013). Furthermore, 108.9 million out of 123.5 million housing units had installed air conditioning (AC) equipment as of 2020 (EIA 2020a). This number was 94 million of 113.6 million in 2009 (EIA 2009) and 82.9 million of 100.4 million in 2001 (EIA 2001). Therefore, reducing building HVAC energy consumption, especially in the residential sector, has a significant potential to contribute to the 2030 U.S. greenhouse gas pollution reduction target (The White House 2021). The goal for energy-efficient buildings set by DOE is to reduce the direct energy intensity of residential and commercial buildings by at least 35% by 2030 while reducing direct fossil fuel consumption by more than one-third. Particularly, the goal of residential buildings is to achieve 50% energy savings through the identification of deep retrofit packages (BTO 2016).

One way of reducing HVAC energy consumption is by improving the energy efficiency of building HVAC operations. Extensive technical research has already been conducted on building design and optimal control to solve the problem of low efficiency. However, less attention has been paid to operational faults even though most buildings have varying degrees and types of operational problems during the whole life of the building, which creates a gap between real operation and ideal design conditions. According to a Downey and Proctor survey, 65% of residential buildings in the United States suffer from various faults (Downey and Proctor 2002), which result from improper installation, component degradation, inefficient control strategies, etc. In addition to causing energy waste in HVAC systems, these faults typically result in inadequate thermal comfort (Au-Yong et al. 2014).

Moreover, occupancy behaviors are not well incorporated with HVAC controls in residential homes in an effective way. For example, a building's HVAC system typically operates when the space is not occupied during the day. Therefore, there are significant energy saving opportunities from connecting the temperature setpoint with the occupancy status in a house—i.e., relax a zone's temperature setpoint when it is not occupied. Internet of Things (IoT)-enabled devices can also lead to improved energy saving and occupant comfort.

Some researchers have made efforts to address these problems. However, despite the wide adoption of building automation systems in commercial buildings, there is a dearth of integrated control systems for residential building HVAC systems to proactively and adaptively consider residential building and HVAC system characteristics, as well as the health status (e.g., whether there are faults). Current residential buildings are typically equipped with very limited numbers of thermostats and no other indoor environment monitoring capabilities. Energy saving control strategies are limited to prescheduled setpoints. Although the IoT technologies empower the

occupants with easy-to-use and remote setpoint reset capabilities (can be done over their smartphones), occupants frequently struggle to determine the appropriate setpoint to achieve their comfort and energy savings objectives. Building HVAC degradation and malfunction can only be diagnosed through expensive and manual energy auditing and service processes and hence are rarely detected in the field. Moreover, such fault status is disconnected with the house comfort control system (i.e., the control system is not adaptively responding to the HVAC system health status). Recent developments of smart home technologies, IoT technologies, and low-cost sensing technologies present a great opportunity to develop an IoT-based comfort control system that can provide integrated control and automated fault diagnostics to achieve better occupant satisfaction and energy efficiency in residential homes.

To achieve HVAC energy savings in the residential sector while maintaining thermal comfort priorities for occupants in real-time, this project aims to address the following gaps:

- 1) Lack of low-cost and distributed **sensor systems** for comfort and energy measurements, as well as for system performance monitoring.
- 2) Lack of cost-effective and computationally efficient and accurate learning-based **models** for system monitoring, optimization, and AFDD.
- 3) Lack of an advanced control **framework** that integrates adaptive controls with AFDD, IoT-enabled devices, and human-in-the-loop machine learning for residential homes.

1.1 Scope of This Project

Our cost-effective and straightforward smart home system (illustrated in Figure 1) delivers a comfort-oriented thermal environment that improves occupant satisfaction and saves HVAC energy compared to the baseline control framework.

- 1) **Cost-effectiveness and scalability of the entire developed system:** The system includes low-cost temperature, humidity, and airflow sensors, and a Raspberry Pi-based local hub that interfaces with the cloud and IoT-enabled devices. The cost is lower, not only for sensors, but also the costs associated with sensor installation, system setup and commissioning, data communication and storage, and data analytics (e.g., computationally efficient and implementable AFDD and control strategies).
- 2) **Energy performance and user satisfaction:** The system delivers user satisfaction and energy savings. This includes a) ease of use, b) optimal occupant thermal comfort, and c) accurate system feedback (e.g., low false alarm of the developed AFDD strategies).
- 3) **Favorable demonstrated prototype performance:** The prototype tested at the PNNL Lab Homes demonstrates the accuracy of faults detections/diagnoses of faults and shows energy savings and thermal comfort improvement through optimized HVAC operations.

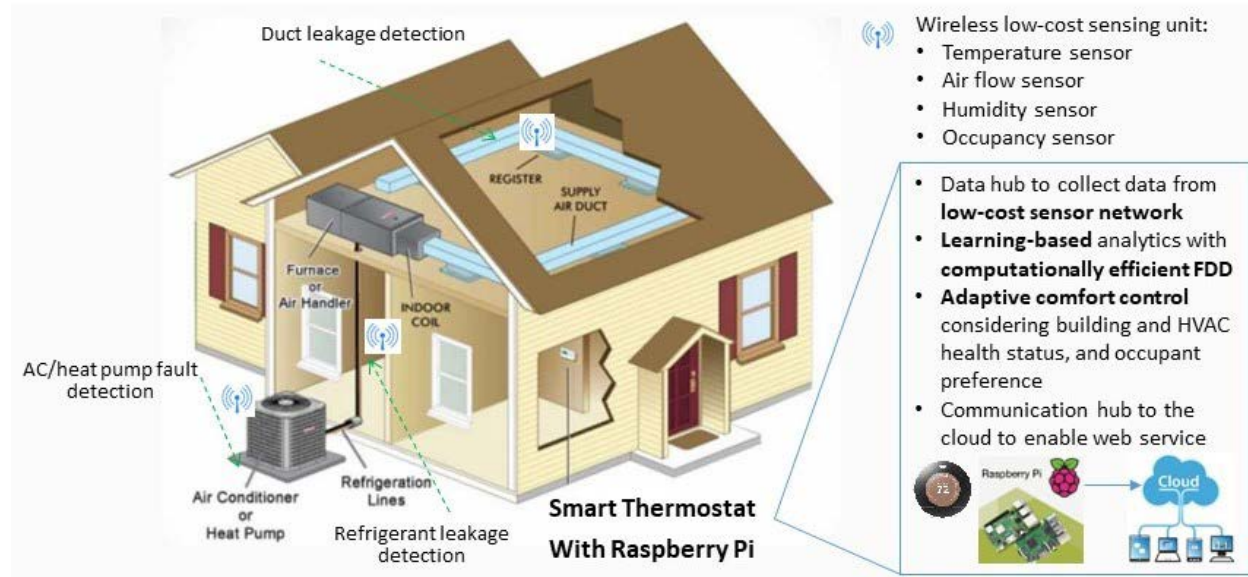


Figure 1. Schematics of the smart home energy management system developed in this project

Before proceeding to each section, the corresponding literature reviews are presented in the following subsections.

1.2 IoT-Based Sensor Networks and Cloud Systems

In most modern residential buildings, the thermostat controls the HVAC system to blow warm or cool air based on a simple comparison of nearby air temperature (e.g., utilizing the built-in temperature sensor of the thermostat) to the setpoint.

Yet, this kind of simple control system may not achieve a desirable thermal comfort level for every room due to various factors such as the location of vents and thermostat, the insulation design, the sealing quality of the windows and doors, etc. To build a smarter control strategy so that the HVAC system can be operated efficiently while maintaining an acceptable comfort level, it is necessary to know the temperature and humidity distribution, airflow, and human occupancy status in the building.

In such cases, wireless sensing networks are often used to gather the required distributed environment data for advanced control algorithms. A typical wireless sensing network consists of a gateway device and multiple wireless sensors. The wireless sensors can be distributed installed in the measuring area, and the gateway device forwards the sensor readings to any data consumer (usually a database). In addition, the wireless sensing networks can be connected to a cloud platform for reliable data storage and easier access for remote applications.

1.3 Learning-Based Models

A high-fidelity building operation model (e.g., energy forecasting model) is critical for advanced building control and energy abnormality detection. Data-driven modeling approaches, especially those that use machine learning and artificial intelligence methods, have demonstrated improved

cost-effectiveness and ease of application in the field, when compared with traditional physics-based methods.

However, the quality of a data-driven model is heavily dependent on the quality of data that the model is trained from. In the application of data-driven forecasting modeling, training data typically comes from building operation data, such as the building automation system data. Yet, data from building operations often have data bias problems, which means that the data sample is collected in such a way that some members of the intended data population are less likely to be included than others. As a result, the data sample obtained is not representative of the data population intended to be analyzed. For example, the zone temperature setpoint, a feature that strongly affects building energy, is often unchanged from collected normal building operation data. The utilization of data-driven energy forecasting models based on such data introduces a potential bias. It means that the limited range of setpoints used during the training data generation process constrains the model's capacity to accurately predict scenarios that fall outside of this narrow range. Consequently, the trained model may exhibit suboptimal performance when confronted with conditions that deviate from the limited setpoint range. This increases the likelihood of significant forecasting errors when applied to model predictive control (MPC) for zone temperature control.

Active learning is a solution to the data bias problem and is used to generate information-rich training data to develop high-fidelity forecasting models (L. Zhang 2018, previous work completed by the team). L. Zhang (2018) demonstrated that data-driven models trained by data generated through active learning strategies outperform models trained on normal operation data. By using active learning to generate training data, the resulting models are less biased and can better predict building energy consumption, resulting in more effective energy management and control strategies.

1.4 Fault Modeling for Residential Buildings

Fault-related research includes studying the impact of faults (Cheung and Braun 2013b, 2013a), fault detection and diagnosis (FDD) (Cheung and Braun 2015; Chintala et al. 2021; Bailey and Kreider 2003), fault-tolerant control (Homod 2014; Salsbury and Diamond 2001; Shahnazari 2018), etc. Fault emulation—transforming fault-free systems to faulty systems by partially modifying parameter values—acts as an elementary approach to conducting all these studies. The two ways to emulate faults are real tests and simulation. Even if real data can be obtained without any computation errors, it is costly to implement real testing (Bellanco et al. 2021). Research on various combinations of faults occurring at the same time is limited and cannot be carried out thousands of times in lab tests. Other disadvantages of lab tests include large time consumption, the difficulty of decoupling single variables, adverse impacts on thermal comfort, and irreversible damage to the system. On the contrary, except for the weakness in completely capturing uncertainties in the real world, the advantage of simulation is to get rid of the real experiment limitation by implementing a wider range of values and expanding results without

affecting the actual system and occupants' thermal comfort. Therefore, fault modeling has become a popular method of investigating HVAC faults in recent years.

Two modeling approaches, forward modeling and inverse modeling, are also applied to fault modeling. The forward modeling method, i.e., physical modeling, is defined based on physical principles; hence it is more flexible and adaptable to different situations. Inverse modeling, i.e., empirical modeling, is the performance curve of data training instead of first-principles physics. It is simpler compared to the forward one, but has restrictions on transferring from one case to another. A comprehensive review of fault modeling practices covering building types, modeling approaches, and fault descriptions can be found in Table 57 of Appendix H, which includes the previous work of the team (Yanfei Li and O'Neill 2019).

1.5 Automatic Fault Detection and Diagnosis for Residential HVAC Systems

HVAC systems seldom perform as designed. Therefore, it is important to keep it maintained and repair failed equipment, or to implement fault-adaptive control to proactively respond to these malfunctions. To achieve this goal, detection and diagnosis of existing faults are required.

FDD for HVAC systems has been studied in the last three decades (Bellanco et al. 2021; Zhao et al. 2019). Those applicable methods can be classified into three categories: quantitative analysis, qualitative analysis, and historical data analysis, which is commonly accepted by multiple researchers (Venkatasubramanian, Rengaswamy, and Kavuri 2003; Venkatasubramanian, Rengaswamy, Kavuri, et al. 2003; Venkatasubramanian, Rengaswamy, Yin, et al. 2003; Katipamula and Brambley 2005a, 2005b; Mirnaghi and Haghghat 2020; Singh et al. 2022; Alzghoul et al. 2014).

Historical data analysis, also known as data-driven methods in some studies, has been increasingly prevalent in the past decade, largely due to the rapid development of communication and computation technology (Hosseini and Nik-Bakht 2021). This kind of approach can be easier to achieve higher detection and diagnosis accuracy (Mirnaghi and Haghghat 2020) and find the hidden patterns from the abundance of data that qualitative analysis (e.g., rule-based/knowledge-based approach) cannot complete (Zhao et al. 2019). According to the statistics of Zhao et al. (2019), 79% of existing FDD research focuses on the historical data-driven method in the field of HVAC systems.

Compared to the historical data analysis (i.e., data-driven methods) and quantitative analysis (i.e., model-based methods), knowledge-based reference, categorized in qualitative model-based approach, also has its unique advantages, such as much simpler application, less computation load, less data required, easily interpretability, higher generality and transferability, etc. These features make this method more practical to be applied in ordinary homes where computation source for HVAC control is considerably limited.

Air-sources vapor compression cycle (VCC) systems are widely used in most residential buildings in the United States, including rooftop units, heat pumps, etc. (Hu and Yuill 2021).

However, at the same time, more than 65% of residential VCC systems suffer from various faults (Shi and O'Brien 2019), which typically arise from improper installation, equipment degradation, sensor offset, or control logic problems (Yanfei Li and O'Neill 2018; previous work completed by the team). Soft faults, such as heat exchanger fouling, or a slow leakage through ductwork, are more difficult to detect and diagnose, compared to hard failures (Breuker and Braun 1998a). Although some of these faults do not occur in high severity frequently, they could lead to premature failure of the HVAC components, dissatisfied thermal comfort, or unnecessary energy cost. Therefore, FDD research that is applied to the air-source VCC system is attractive.

Knowledge-based reference is usually represented by multiple rules, which is also the reason researchers usually call it the rule-based approach. These rules can be as simple as a normal threshold, or as complicated as patterns for recognition through measured values of multiple selected features (Nelson and Culp 2022). The first research concentrating on rule-based FDD for an air-cooled VCC system was conducted in 1989 by Yoshimura et al. (Yoshimura and Ito 1989), who integrated a diagnosis approach in the air-cooled packaged air conditioner. The features they selected include air-side temperature (evaporator and condenser), refrigerant-side temperature (subcooling and superheating), high-pressure coefficient (condensing measured/rated), and low-pressure evaporating coefficient (evaporating measured/rated).

Evaporator malfunction, undercharge, and expansion valve clog are diagnosed with the threshold for each feature by a fuzzy variable, which is based on one of two membership functions. Rossi and Braun (Rossi 1995; Rossi and Braun 1997) proposed a remarkably classic approach, the statistical rule-based FDD method, for their air-cooled vapor compression cycle system. They targeted five faults (undercharge, condenser fouling, evaporator fouling, liquid line restriction, and compressor valve leakage). Nine temperature measurements and one humidity measurement were selected as the features for the fault-free reference model and fault classification. These features and faults categories as well as FDD workflow are widely used in the following VCC-related FDD research (Breuker 1997; Breuker and Braun 1998b; Braun 2003; M. Kim et al. 2008; Payne 2020; Heo et al. 2012).

Chen and Braun (B. Chen 2000; B. Chen and Braun 2000, 2001) created two simpler approaches, the sensitivity ratio method and simple rule-based method, which look at the measured values instead of residuals for each feature. This means that they do not require fault-free models. Compared to the generic set of directional changes in statistical rule-based chart, these two need additional adjustment for the normal threshold of each feature according to the specific measurement. To enrich the evaluation metrics for various FDD methods, Yuill et al. constructed a comprehensive evaluation method for the performance of FDD tools applied to unitary air conditioners and evaluated three FDD protocols with the simulation of multiple VCC systems (Yuill et al. 2014; Yuill and Braun 2013).

Table 58 in Appendix H collects the literature review of existing FDD studies related to the air-source VCC systems, in terms of features, reference models, faults detected, and specific FDD methods (features, reference models, and fault detected will be explained and discussed in detail

in the later sections). The criterion for the selection and evaluation of FDD methods largely relies on the system characteristics and available sensor data. Thus, it is challenging for researchers and practitioners to apply existing FDD methods for residential VCC systems in an effective way.

1.6 Model-Based Adaptive Control-Informed Extracted Rules

Building mechanical systems will degrade gradually and develop capacity downfall as time passes. This contributes to the difficulty of meeting the required thermal environment, especially amid a heat wave (Zuo et al. 2015). Overheating is harmful to human health and productivity, and can lead to heat-related illnesses, like heat stroke, heat cramps, or even fainting (Howe and Boden 2007). This concern is further amplified by climate change, which accelerates the frequency of extreme weather events (Simon Brown 2020).

To deal with severe heat wave conditions, several coordinated responses can be adopted, including the following steps.

- 1) Replace HVAC systems with new ones with a higher capacity
- 2) Retrofit the house (e.g., add building envelope insulation or replace the windows)
- 3) Purchase thermal storage (e.g., an ice tank) to supplement the cooling ability of the original HVAC system when the heat waves come.

All these measures require additional initial investments, which are usually not feasible for ordinary families. An alternative method to the above steps is precooling, which is a control strategy that pre-cools the building preceding a given period to enhance the cooling effect by only utilizing the thermal mass of building envelopes and home furniture, rather than extra equipment/devices. As long as the programmable thermostat or remote thermostat is installed in the house, precooling can be applied to alleviate the effect of a heat wave to some extent. This is what is required as a flexible supplementary measure for air conditioning amid the heat wave period.

The most commonly adopted precooling control method is rule-based control (RBC). This control strategy is predefined by expert knowledge in the “if-then” form with two or three fixed setpoints. For example, Turner et al. (2015) designed three precooling windows with deep ($22.2^{\circ}\text{C}/72^{\circ}\text{F}$) and shallow ($23.3^{\circ}\text{C}/74^{\circ}\text{F}$) precooling temperatures and concluded that the best precooling strategy is using a medium (5 hour) precooling time window with a shallow precooling setpoint temperature. RBC is straightforward to understand and includes valuable human experiences. However, those “optimum rules” are selected from the limited candidates due to time and brainpower limitations of humans. In addition, precooling implementation is related to taking account of future information when generating next-step action signals by control strategies. Manual adaption cannot ensure the optimum operation, because the manual process is constrained by limited measurement of environmental boundary conditions (Piscitelli et al. 2019).

Consequently, automatic optimization methods are employed to compensate for the limitation of manually determined rules. The precooling control strategy is implemented in the future time dimension, so MPC can be applied to tackle this problem because it considers the time series forward and backward simultaneously and features a delay-response system (Joe 2022). In this case, MPC can consider the future weather uncertainty as well as the thermal response dynamics of buildings.

MPC also has its shortcoming, since it involves a high computation burden compared to the simpler RBC. This is why it is seldomly implemented commercially in the real world. Therefore, an alternative way is to conduct the MPC offline in one hub, probably on a large scale, and then extract several rules from its operation results (May-Ostendorp 2012). Consequently, these rules can be applied easily in ordinary houses. The process is called rule extraction (Yu and Pavlak 2022). The goal of rule extraction is to select a minimum set of inputs, feed them to the RBCs and maintain the same or close levels of thermal comfort and energy consumption with the MPC simultaneously. Compared to the beforementioned expert knowledge involved rules, MPC-informed rules are closer to the optimum and more automatic by deriving the merits of MPC operation. At the same time, rule extraction avoids online execution of computationally expensive optimization, thus alleviating computation load in building HVAC controllers with no cloud computation incorporated.

To date, several studies have investigated the benefits of rule extraction in the building control sector. The first application of this rule extraction approach was conducted by Wei and Hsu (2009) who developed simplified control rules for the water resources management (M. Robillart et al. 2017). Then in 2011, Coffey (2011a) implemented it in the HVAC field by developing control look-up tables with precalculation of optimal setpoints over a grid of possible conditions from offline MPC results. After that, multiple researchers devoted themselves to exploring. For example, May-Ostendorp et al. (2011) initially proposed using logistic regression to mimic the performance of the optimizer results, which is applied in the window operation. More recently, Bursill et al. (2020) developed several MPC-informed rules in the decision tree to adjust the airflow by modulating the variable air volume damper. They concluded that only the classification and regression tree and boosting rules were able to maintain reasonable performance during closed-loop testing (see also: May-Ostendorp, Henze, Rajagopalan, and Corbin 2013).

Table 59 in Appendix H summarizes the work related to the rule extraction for HVAC systems, in terms of rule extraction methods, systems, control variable, data source, testing approach, etc. The MPC-informed RBC strategy is promising, as it integrates the virtues of manual expert knowledge and automatic computer optimization mutually.

2. IoT-Based Cost-Effective Distributed Sensor System

2.1 Fundamental Framework: Sensor Module, Local Hub, and Cloud Data Center

This subsection describes the fundamental framework of the low-cost IoT-based wireless sensor, local hub, and cloud system for distributed measurement of temperature, humidity, and airflow.

2.1.1 Overview of the Fundamental Framework

The fundamental framework is designed to implement a low-cost, IoT-based, wireless distributed sensor system for home temperature, humidity, and airflow data gathering and a cloud data center to manage these data. As shown in Figure 2, the system consists of three main parts: sensor modules, the local hub, and the cloud data center. Multiple small, low-cost wireless sensor modules can be distributed in different places in a building to collect data individually. A multifunctional local hub with networking (wired or wireless) capability is used to manage all the sensors, gather data from sensors, preprocess data, and submit them to the cloud. The cloud service is developed to collect, store, and analyze data submitted from hubs and to provide a user interface through a web site.

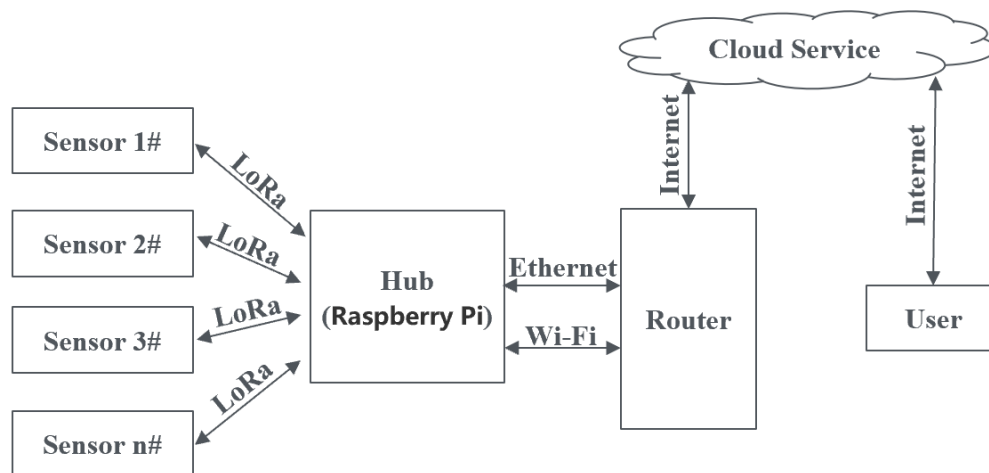


Figure 2. System overview

2.1.2 Sensor Module Design

2.1.2.1 LoRa Wireless Communication Module

Figure 3 shows the block diagram of the wireless communication platform for sensors. The platform chooses the STM32L412 microcontroller unit (MCU) to support the sensor operations. The STM32L412xx devices are **ultra-low-power microcontrollers** based on the high-performance Arm Cortex-M4 32-bit RISC core operating at a frequency of up to 80 MHz. The Cortex-M4 core features a floating-point unit single precision, which supports all Arm single-precision data-processing instructions and data types. It also implements a full set of digital signal processing instructions and a memory protection unit, which enhances the application

security. The MCU is programmable using the provided serial wire debug interface, which is accessible through the soldering pads.

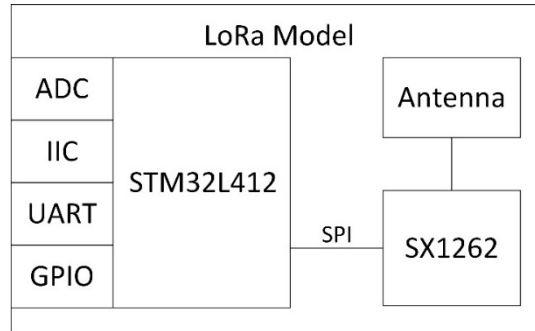


Figure 3. Functional block diagram of the sensor wireless communication platform

Note: ADC stands for analog-to-digital converter; IIC stands for inter-integrated circuit; UART stands for universal asynchronous receiver-transmitter; GPIO stands for general-purpose input/output; and SPI stands for serial peripheral interface.

The data collection and communication function are performed by a Long Range (LoRa) Module, with its features summarized in Table 1. LoRa is a proprietary low-power wide-area network modulation technique. It is based on spread spectrum modulation techniques derived from chirp spread spectrum technology. This LoRa module is packaged by Surface Mount Technology to make it compact and easy to use. The external interfaces of the LoRa Model include an analog-to-digital converter (ADC), inter-integrated circuit (IIC), universal asynchronous receiver-transmitter (UART), general-purpose input/output (GPIO) and pulse-width modulation (PWM). The LoRa transceiver adopts SX1262, which is connected to the STM32L412 microcontroller by the serial peripheral interface (SPI) bus.

SX1262 sub-GHz radio transceivers are ideal for long-range wireless applications. The device is designed for long battery life with just 4.2 mA of active receive current consumption. The SX1262 can transmit up to +22 dBm with highly efficient integrated power amplifiers. Its high sensitivity is down to -148 dBm, with programmable bit rates up to 62.5 kbps.

Table 1. LoRa Module Features

Features	Parameters
Power Supply	1.71V to 3.6V
Frequency Band	915MHz
Size	L=30mm, W=22mm, H=2mm
Interface	ADC, IIC, UART, GPIO, PWM

2.1.2.2 Sensor Module

Temperature and relative humidity are measured by the individual sensor module SHT31 manufactured by Sensirion. It builds on a new CMOSens sensor chip, with the functionality of enhanced signal processing, two distinctive and user-selectable IIC addresses, and up to 1 MHz communication speed.

Figure 4 shows the block diagram of the sensor module. For the temperature and humidity measurement, the LoRa module gets the data from the temperature/humidity sensor through the IIC interface. The airflow measurement is performed by a rotary anemometer. The airflow data is then read as a frequency signal from the rotary anemometer and transmitted to the LoRa Module via GPIO. The entire sensor module is powered by a CR2032 battery. The battery life is designed for one year with normal operations.

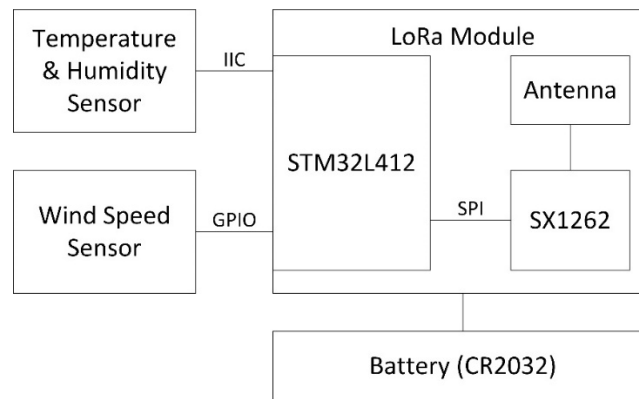


Figure 4. Sensor module design

Table 2 summarizes the performance features and specifications of the developed sensor module.

Table 2. Sensor Module Performance Features and Specifications

Features	Parameter
Power Supply	CR2032(3V)
Frequency Band	915MHz
Temperature Accuracy Tolerance	$\pm 0.1^{\circ}\text{C}$
Humidity Accuracy Tolerance	$\pm 2\%$
Wind Speed Accuracy Tolerance	$\pm 3\%$
Size	L=43mm, W=23mm, H=8mm

2.1.3 Local Hub Design

2.1.3.1 Local Hub on Raspberry pi

The local hub system is built on a Raspberry pi, which is a low-cost single-board computer with built-in Internet connectivity and multiple universal hardware interfaces. The main function of

the hub is to collect sensor readings through the Universal Serial Bus (USB) LoRa Gateway device, submit data to the cloud data center, and store/manage the information for each sensor. In addition, data conversion and preprocessing can be performed to the collected or stored data once the data arrives at the hub. Supplemental information (e.g., timestamp and sensor ID) is also attached to the sensor data during this step. The workflow of the sensor data handling is shown in Figure 5. All the data are converted into JSON format and submitted to the cloud application programming interface (API).

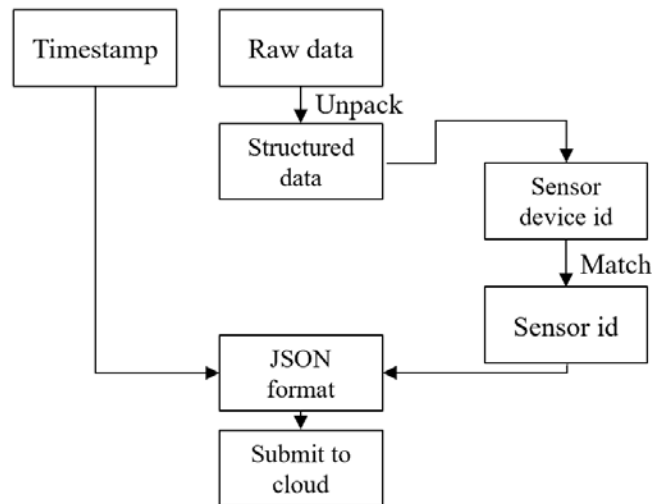


Figure 5. Block diagram of the local hub data workflow

2.1.3.2 LoRa Receiver of the Local Hub

The local hub communicates with the distributed sensors via a LoRa Gateway, which is responsible for communicating with the sensor acquisition terminal and forwarding the sensor data to the local hub. The LoRa Gateway is also developed to have a debug capability and provides power through a USB interface. Figure 6 shows the block diagram and a picture of the developed USB-based LoRa Gateway. Table 3 lists the performance characteristics and specifications of the USB LoRa Gateway.

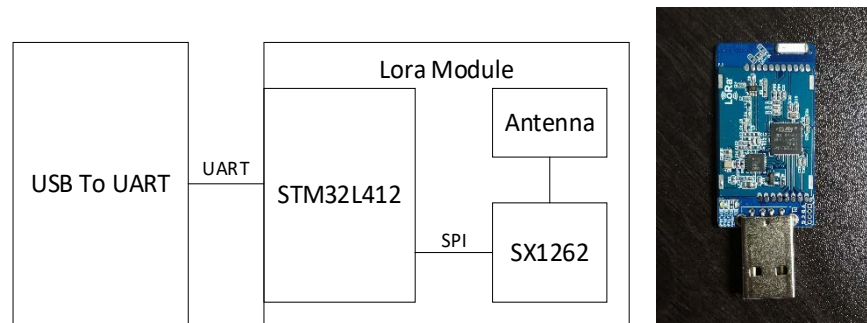


Figure 6. Block diagram and picture of the USB LoRa Gateway

Table 3. LoRa Gateway Specifications

Features	Parameter
Power Supply	USB(5V)
Frequency Band	915MHz
Size	L=60mm (including USB connector), W=23mm, H=3.5mm

2.1.4 Cloud Data Center Development

2.1.4.1 Cloud Data Center Architecture

The cloud-based sensor interface, data management, and control system are shown in Figure 7, where the readings from the wireless sensors are collected by the local hub (Raspberry pi) and sent to the cloud. The sensor data are tagged, indexed, preprocessed, and stored in the database in the cloud. The user can request data from the cloud database for specific applications.

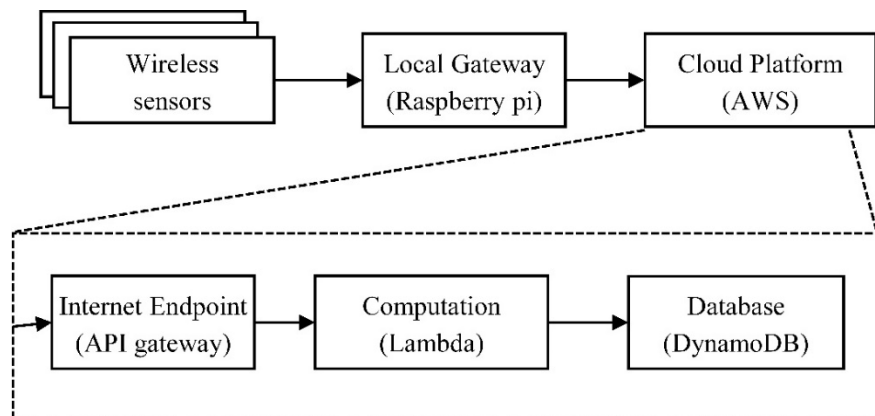


Figure 7. Cloud-based system architecture and the associated AWS solutions

The cloud service for this project is developed using the Amazon Web Service (AWS, a cloud service provided by Amazon) cloud platform where the API Gateway (internet), Lambda (computation), and DynamoDB (database) services are chosen to build the system. The API Gateway provides a standard internet endpoint for data submission and querying. The Lambda functions are scalable, and the stateless computation services are invoked for every incoming submission. The DynamoDB is a key-value database used for storing sensor information and sensor readings.

2.1.4.2 Cloud Databases

The database is organized into two tables: one of them stores all the sensor information in the specific measurement/monitoring system, and the other one stores the data records submitted from all the sensors. As shown in Table 4, the sensor information table stores all the important information of all the sensors. This allows the user to manage the entire sensor suite and register/delete sensors from the suite. The information table is scalable and can be easily

maintained/updated as necessary. A data table, as shown in Table 5, stores all the data records submitted. Individual records are accessible through the combination of sensor ID and record ID. The example data corresponding to the information table and the sensor data table is presented in Figure 96 and Figure 97 of Appendix A.

Table 4. Structure of the Sensor Information Table

Columns	Description
sensor-id	A sensor-specific identification number
sensor-name	A readable name of the sensor
sensor-type	A description of the sensor device type
record-id-start	The starting record ID in the data table for this sensor
record-id-latest	The latest record ID in the data table for this sensor
record-latest	A copy of the latest reading for fast access
report-interval	The interval between two reports in seconds
unit	Unit description of the sensor data

Table 5. Structure of the Sensor Data Table

Columns	Description
sensor-id	A sensor-specific identification number (same as in the sensor information table)
record-id	A numerical record ID, automatically increased by order of submission
timestamp	The time recorded when the sensor is requested to submit its readings
value	The value of the sensor reading

2.1.4.3 Data Security and Access Control

An access-key-based authentication and authorization system is implemented to prevent unauthorized access to the cloud database. Several access keys (strings with 64 random characters) are generated and stored in an additional table. Each key is associated with one of the two permissions: read-only or read-and-write. The interfaces of the cloud database require an access key with proper permission. The access keys are securely delivered to participants of the project and coded into the hub to enable their access to the database.

2.1.4.4 Web Dashboard for Data Visualization

A web dashboard is developed to display the real-time data arriving at the cloud. The web page is written in HTML and JavaScript, while the Chart.js library is used to draw charts on the page. After the webpage is successfully loaded, the script on the page communicates with the cloud

data center and fetches the latest record ID in the database. Then, the webpage attempts to fetch new data with a more recent record ID from the database and adds it to the chart. An individual chart is designated for each sensor.

2.1.5 Test Case and Result

Tests were performed on the cloud-based sensor data system in order to prove the system's functionality in data collection, submission, retrieval, and visualization. Two wireless sensors are included in the test. Each of them is powered by a CR2032 3V lithium coin cell battery. A Raspberry pi 4B (8 GB version) is set up as the hub with a wired internet connection. The LoRa receiver is connected to the hub's USB 2.0 port (with an extension cable for a better demonstration layout on the table). A tablet is used in the test to show the web dashboard page. And a hairdryer is used to manipulate the temperature and humidity around sensors.

Readings that are newly submitted to the cloud are plotted on the dashboard in two charts, with one for each sensor.

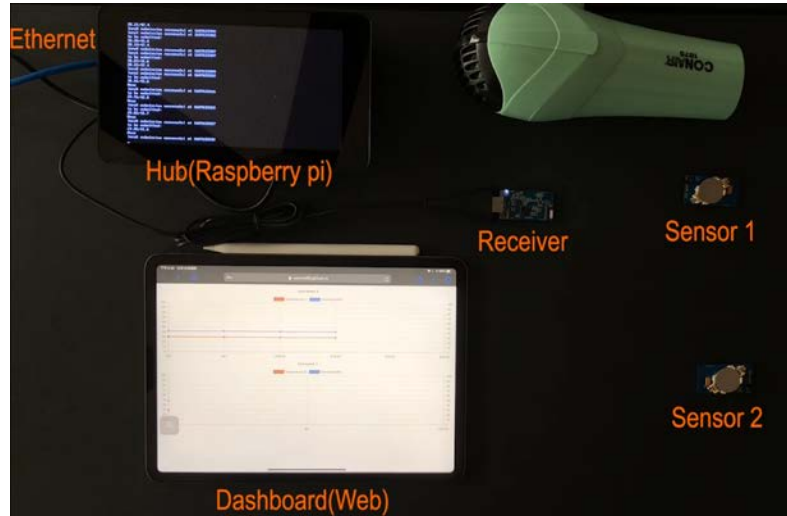


Figure 8. Sensor data system test

Figure 8 is a screenshot of the test/demonstration video that was recorded and submitted to the U.S. Department of Energy (DOE). Temperature and humidity are plotted against the timestamp on the dashboard when the reading is captured from the sensor. Colored lines are used to represent each type of reading: orange for temperature and blue for humidity. During the test, each sensor is heated and cooled by the hairdryer. The reading during the heating and cooling process shows an expected trend of temperature and humidity changing, which confirms the functions of this cloud-based data system. The snapshot of the data table stored in the cloud during the demonstration is displayed in Figure 98 in Appendix A. The table shows the reading index, the record ID, the time stamp, and the measurement results collected from the sensors. The results clearly show that the sensor has a resolution of 0.01°C for temperature and 0.1% for relative humidity. The reading is fast, with about 4 seconds for each reading.

2.2 Low-Cost Wireless Sensor Platform: Temperature/Humidity Sensors

Sections 2.2 and 2.3 focus on a detailed description of the development, testing, and evaluation of wireless sensors networked with a Gateway hub. This subsection, Section 2.2, will start with the temperature and humidity sensors.

2.2.1 Temperature-Humidity Sensing Platform

To measure indoor temperature and humidity distribution, the low-cost, energy-efficient, wireless Temperature-Humidity Sensing Platform (THSP) is designed, fabricated, and validated. The THSP is powered by a cell battery and communicates with the hub via the LoRa protocol. The THSP has a modular design, consisting of **three modules (illustrated in Figure 4): the temperature and humidity sensing module, the processing and communication unit that includes a low-power microcontroller and a long-range LoRa transceiver, and the antenna module**. Figure 9 shows the front and back images of a THSP. In addition, the board is installed with an indicator LED and a cell battery socket.

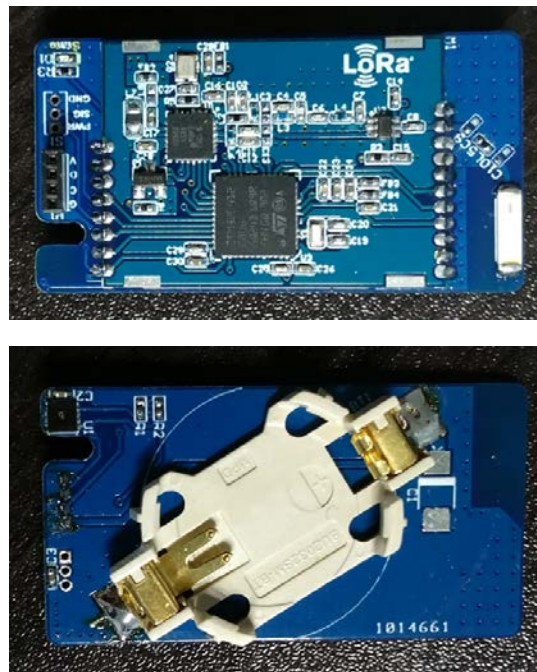


Figure 9. Front and back views of a THSP unit

The specification of the temperature and humidity sensing feature is shown in Table 6.

Table 6. Specification of Temperature and Humidity Sensor

Feature	Value
Temperature Accuracy	$\pm 0.3^{\circ}\text{C}$
Temperature Resolution	0.015°C
Temperature Range	$-40 \sim 125^{\circ}\text{C}$
Humidity Accuracy	$\pm 2\%RH$
Humidity Resolution	$0.01\%RH$
Humidity Range	$0 \sim 100\%RH$

Processing and communication for the sensor platform is explained in Section 2.1. Specific details for the THSP are described in Appendix A.2.

2.2.2 The Temperature and Humidity Sensing Module

The sensing functions (e.g., temperature and humidity) are performed by an SHT31 temperature and humidity sensor, which is connected to the processing and communication module through the soldering pads. The diagram in Figure 10 shows the connection between the processing and communication module and the temperature and humidity sensing module. The SHT31 digital temperature and humidity sensor are placed at the corner of the board to minimize interference by other onboard components. The sensor communicates with the processing and communication module by IIC interface and starts a measurement following the MCU's demand. The measurement result is sent back to the MCU in two 16-bit unsigned integers, which can be converted to physical scales based on the conversation rate.

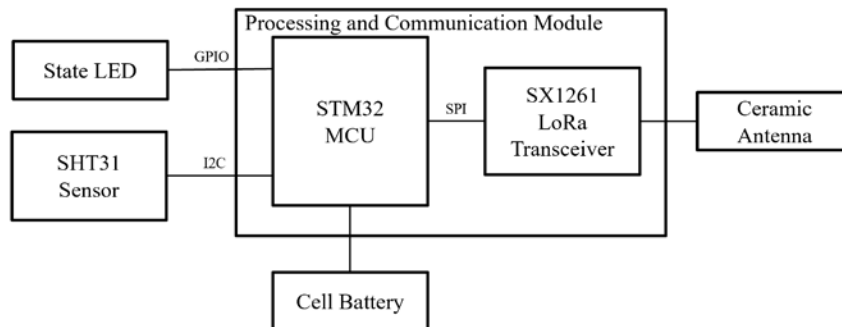


Figure 10. Components of the temperature and humidity sensing platform

An indicator LED is installed on the board and connected to one of the GPIO ports of the Core Module. The LED blinks once when a data frame is sent out by LoRa.

2.2.3 Sensing and Data Transmission

The MCU on the LoRa Core Module is programmed to acquire and process the temperature and humidity monitoring data from the sensor. After the THSP is powered on or reset, the MCU

initializes the watchdog timer, clock, interfaces, and the chip's power control. After initialization, the MCU enters its main loop. At the beginning of each loop, the MCU wakes up from standby mode and clears the watchdog timer that has awakened it. Then the MCU initiates the temperature and humidity sensor for a new measurement. After that, the MCU uses the built-in analog-to-digital converter module to measure the voltage of the battery. Once the two measurements are completed, the MCU starts to build the sending buffer, including the temperature, humidity, and voltage measurements, the unique ID (hardware ID) of the LoRa chip, and a checksum calculated using all other data in the buffer. After the buffer is successfully built, the buffer is converted to ASCII and ready for transmission. At the end of the buffer, a pair of CR(r) and LF(\n) control characters are added as the frame separator. The MCU turns on the LoRa transceiver and checks the channel. If the channel is clear, the MCU sends the buffer by LoRa to the hub. Otherwise, the MCU waits until the channel is clear. Finally, the MCU sets the watchdog timer, enters the low-power-consumption standby mode, and waits for the next command. The flow chart of this process is shown in Figure 11.

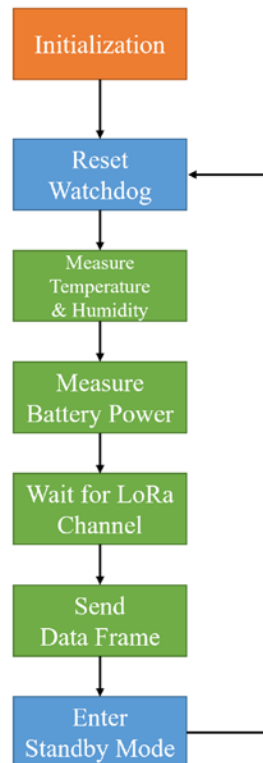


Figure 11. Workflow of the temperature and humidity sensing module

2.2.4 Battery Life

The THSP is designed to perform unattended temperature and humidity monitoring, which means the battery life is an important criterion for the module. Two primary factors contribute to battery life: battery capacity and power consumption.

The THSP is powered by a 3V cell battery installed in the battery socket. According to the size of the module, three candidates are picked for the cell battery model that could fit the board:

CR2032, CR2450, and CR2477. The size, weight, and capacity of these three batteries are listed in Table 7.

Table 7. Compatible Cell Batteries

Battery	CR2032	CR2450	CR2477
Diameter	20mm	24mm	24.5mm
Thickness	3.2mm	5.0mm	7.7mm
Weight	2.9g	6.3g	10.5g
Capacity	225mAh	620mAh	1000mAh

The power consumption of the module varies in different operation statuses. In standby mode, the MCU consumes about $0.7\mu\text{A}$ current since most of the components are in sleep mode. The time of sleep is dependent on the desired rate of reporting. During measurement, the MCU and the sensor together consume about 5mA current. During LoRa transmission, the unit's power consumption depends on the spreading factor of LoRa. The spreading factor determines the tradeoff between the bit rate and transmission range. A higher spreading factor can bring a larger transmission range and a lower bit rate, which means the data will take longer to send from the sensor. The unit consumes 17mA current with factor 5, or 20mA with factor 8.

When the sensor unit uses a 20-second report interval and spreading factor 8, the estimated average current consumption is about $51\mu\text{A}$. Theoretically, a CR2477 battery can power the sensing unit for at most 1.2 years under this current usage.

2.2.5 Transmission Test

The THSP unit was tested with the hub for transmission range and signal penetration. The THSP could send readings to a hub for at least 100 meters in open space. In the indoor test, the signal can penetrate at least three walls, which is enough to cover a typical apartment unit. The screenshot of user interface for sensor measurements received by the hub is presented in Figure 99 in Appendix A.

2.2.6 Field Test of the Temperature and Humidity Sensor Network

The system was tested in a local apartment unit for 60 days. The system included a hub and four sensors. It was tested to monitor the temperature and humidity in four rooms. All the data were uploaded into the cloud-based database, and the dashboard was used to visualize and analyze the data. The floor plan of the apartment unit and the installation of the system are shown in Figure 12.



Figure 12. Floorplan and system installation

The system continuously worked for 60 days without human intervention. During the test period, the system overcame at least two power outages and several network disconnections and successfully restored its normal functions.

During the 60-day test period, the system collected more than 340,000 records in total from the four sensors. The database retained about 44,000 records from each sensor for monitoring and analysis. The remaining were stored as JSON files in archive storage, about 36 MB in total. Figure 13 shows the 30-day bedroom data stored in the database in line charts. Plot examples for other rooms are shown in Figure 101 in Appendix A.

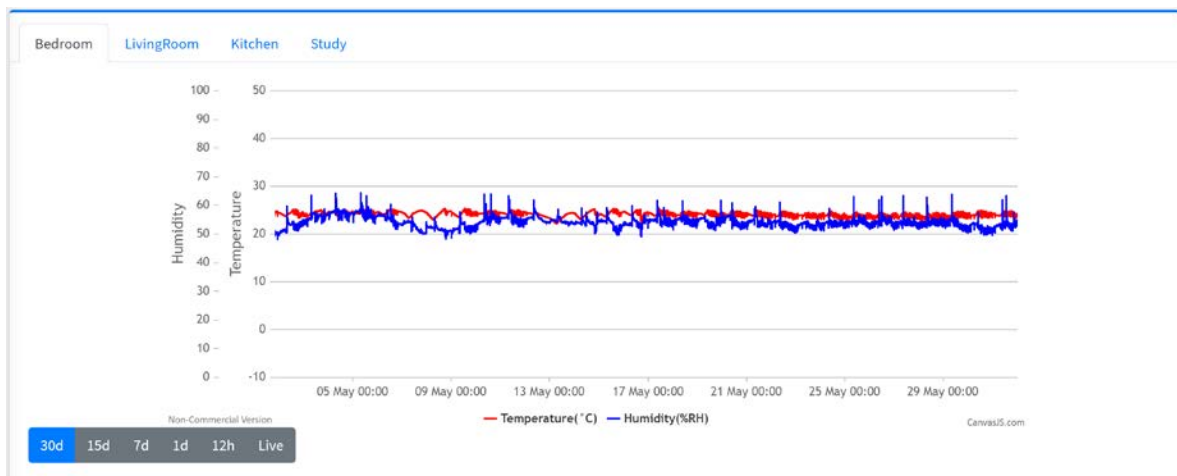


Figure 13. Temperature and humidity charts: 30 days of readings

2.2.7 Improvement in the Temperature and Humidity Sensor Network

Following the test in a local apartment, the THSP system continuously collected temperature and humidity data from multiple locations over a month. To solve the issue of weak signal strength of the THSP system in a larger building with thicker walls, the design of THSP was upgraded.

The onboard antenna chip was replaced by a Linx ANT-915-uSP410 antenna chip, which featured a longer transmission range and better signal penetration. In addition, the onboard antenna was upgraded to include a socket to host an external antenna if needed. An external antenna could be used to extend the transmission range when needed. A digital communication and control port was also reserved on the improved design to interface the airflow sensor. The battery used in the THSP units was changed to CR2477 (doubled volume with a slightly increased size) to support the upgraded hardware and the extended airflow sensor. Figure 14 shows the revised THSP unit with new features. The revised THSP design is slightly larger than the prior version, as shown in Figure 15.



Figure 14. Revised THSP unit



Figure 15. Comparison of the original THSP units and revised units

2.3 Low-Cost Wireless Sensor Platform: Airflow Sensors

With the revised THSP unit, an off-the-shelf airflow sensor has been integrated into the wireless sensor system. The Benetech GM8901 hand-held anemometer was chosen to test the design and prototype. The original anemometer contains an anemometer (airflow sensor) and a hand-held device for interpreting the anemometer's signal, as shown in Figure 16. The specification of the air velocity measurement feature is shown in Table 8.

To integrate the airflow sensor into the wireless sensor system, the anemometer was disconnected from the hand-held device. The circuits, cable, and connector were removed from the handle. The three wires (power, ground, and signal) within the airflow sensor are connected to the communication and control port on the THSP. The signal output from the anemometer is processed by the microprocessor on the THSP unit, and the converted reading of air velocity is transmitted along with the temperature and humidity reading. The THSP unit connected with the airflow sensor can be housed within the handle of the airflow sensor, as shown in Figure 17 (a). Holes were drilled on the handle to allow the THSP to measure temperature and humidity from inside. Figure 17 (b) shows the fully integrated unit that can measure temperature, humidity, and air velocity simultaneously.



Figure 16. The original GM8901 anemometer system

Table 8. Specification of GM8901 Air Velocity Measurement

Feature	Value
Range	0–45 m/s
Minimum resolution	0.01 m/s
Threshold	0.3 m/s
Accuracy	$\pm 3\% \pm 0.1 \text{ dgts}$



Figure 17. THSP unit housed within the airflow sensor handle

To integrate the airflow sensor into the wireless sensor system, the anemometer was disconnected from the hand-held device. The circuits, cable, and connector were removed from the handle. The three wires (power, ground, and signal) within the airflow sensor are connected to the communication and control port on the THSP. The signal output from the anemometer is processed by the microprocessor on the THSP unit, and the converted reading of air velocity is transmitted along with the temperature and humidity reading. The THSP unit connected with the airflow sensor can be housed within the handle of the airflow sensor, as shown in Figure 17 (a). Holes were drilled on the handle to allow the THSP to measure temperature and humidity from inside. Figure 17 (b) shows the fully integrated unit that can measure temperature, humidity, and air velocity simultaneously.

The anemometer measures air velocity from the rotation of fan blades. Each time a fan blade passed the optical sensor installed on the lower beam, a pulse signal was output. The frequency of the pulse signals is linearly related to the wind speed. However, the relationship between the frequency and the air velocity reading was programmed in the hand-held device. To retrieve the formula of air velocity, the hand-held device was connected to a functional signal generator. The generated pulse signals of different frequencies were input into the hand-held device, and the reading shown on the screen was recorded. By plotting the recorded air velocity value against the input frequency, the linear function with R^2 of 0.997 can be retrieved, as shown in Figure 18. This conversion factor was then programmed into the THSP microprocessor and used to convert the anemometer reading into airflow speed.

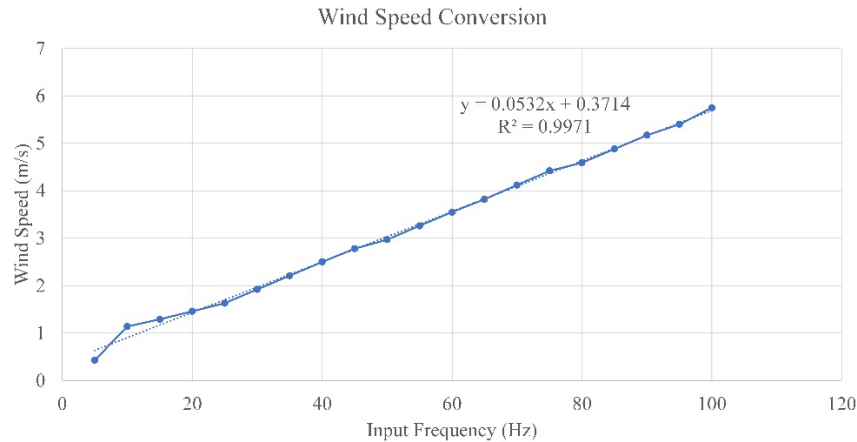


Figure 18. Converted wind speed readings of different the input signal frequency

The THSP-integrated airflow sensor was tested together with the hub. The sensor could measure the air velocity in addition to temperature and humidity, and all three readings were successfully transmitted to the hub. A screenshot for the airflow reading on the hub display is shown in Figure 100 in Appendix A.

2.4 Summary

The low-cost IoT-based distributed sensor system is integrated with wireless sensors, the local hub, and the cloud system. The developed prototype wireless sensor modules can measure temperature and relative humidity with a resolution of 0.1°C and 0.1% , respectively, which exceed the requirements of 1°C in temperature and 5% in relative humidity. The development of the local hub targets communicating with the wireless sensors, collecting the sensor data, and uploading the distributed measurement results to the cloud. The cloud service is completed by AWS. It is demonstrated that the local hub can simultaneously collect data from multiple wireless sensors and send the data to AWS. In addition, the data handling functions are developed inside the AWS, allowing the sensor data to be time-stamped, stored, processed, downloaded, and displayed in real-time.

The produced THSP is powered by a cell battery and communicates with the hub via the LoRa protocol. The sensing functions (e.g., temperature and humidity) are performed by an SHT31 temperature and humidity sensor, which is connected to the processing and communication module through the soldering pads. The THSP can send readings to a hub within at least 100 meters in an open space. In the indoor test, the signal can penetrate at least three walls.

The system was tested in a local apartment unit for 60 days. The testing system included a hub and four sensors. It was tested to monitor the temperature and humidity in four rooms. All the data were uploaded into the cloud-based database. The wireless temperature sensors successfully measured temperatures and passed data to the hub.

The system continuously worked for 60 days without human intervention. During the test period, the system overcame at least two power outages and several network disconnections and successfully restored its normal functions. They collected more than 340,000 records in total from the four sensors. The database retained about 44,000 records from each sensor for monitoring and analysis.

3. Virtual Testbed and Fault Modeling

This section introduces a workflow for fault modeling of residential HVAC that includes fault library development and modeling method construction. Prior to that, we introduce the virtual testbed, DOE residential prototype building models.

Discussion on this topic is organized as follows. Basic background for the residential building is described in Appendix B.1. A description of prototype residential buildings with heat pumps is presented in Section 3.1. The residential fault library is developed in Section 3.2. In Section 3.3, we describe how these faults can be modeled in a whole-building energy simulation using the fault library. This model is essential as it is one of the cornerstones for this project. Furthermore, Section 3.4 presents the fault modeling results and analyzes the fault impact at the same time. Finally, a summary of this section is highlighted in Section 3.5.

3.1 Baseline Building Model: DOE Prototype Residential Building

The baseline virtual building is developed from the DOE residential prototype building models, which were built by the Pacific Northwest National Laboratory (PNNL) from survey data, and data from standards, reports, papers, and expert knowledge (DOE).

3.1.1 Building Information

As shown in Table 9, this building, located in Houston, has two floors with a total area of 223 m² (2,400 ft²), with a slab-on-grade foundation. Its zones consist of a conditioned zone that includes rooms on two floors, and an unconditioned attic zone. The conditioned zone houses three occupants and all the electric appliances, while the HVAC system components are primarily housed in the attic zone. The HVAC system is a dual-setpoint controlled central air heat pump system. The default control of the HVAC system is a schedule-based fixed setpoint control. The key parameters of the building and the HVAC system are shown in Table 9, while the geometry of the prototype residential building is illustrated in Figure 19. Connection of the air loop and water loop in the EnergyPlus model of this prototype residential building can be found in Appendix B.2.

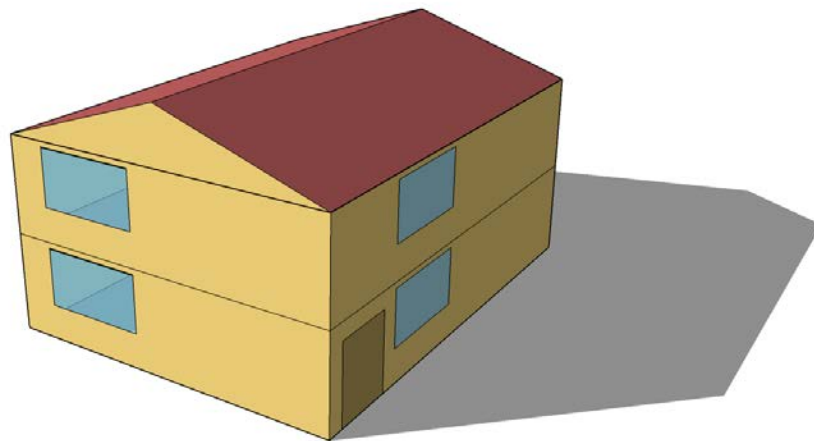
3.1.2 Schedules

Figure 20 plots a typical occupancy schedule of residents for the prototype residential building. The plot shows the occupancy fraction as it changes across each day. When the fraction is at 1, all three occupants are present in the building. At 0.33, only one occupant is present. Opposite to the work schedule, most of the people go to work during the day, so the occupant rate is low, while at the night, it rises up to 1. The weekdays and the weekend are assumed to have the same schedule.

Similarly, Figure 21 and Figure 22 illustrate the operation schedules of lighting and electric devices. The lighting schedules remain the same between weekdays and weekends, whereas the schedules for electric devices vary. The refrigerator is not sensitive to the time series, because it operates all day in ordinary life.

Table 9. Building Information of Prototype Residential Building

Parameter	Value
Number of floors	2
Floor area	223 m ² (2400 ft ²)
Window-wall ratio	14.20%
Foundation	Slab on grade
People	3
Equipment	Lighting, refrigerator, clothes washer, clothes dryer, dishwasher, cooking range, miscellaneous electrical appliances, etc.
HVAC system	Heat pump
Fan	On/Off
Setpoint	Cooling 23.9°C (75 °F); Heating 22.2°C (72 °F)

**Figure 19. Geometry of prototype residential building with slab-on-grade foundation**

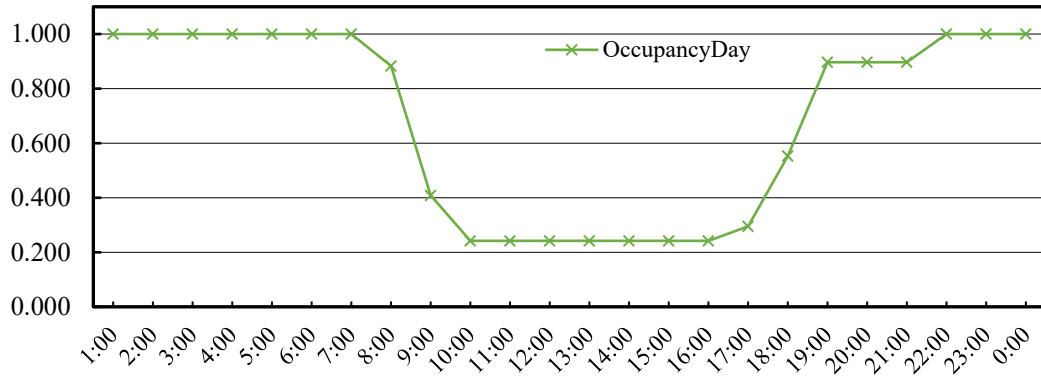


Figure 20. Occupant schedule

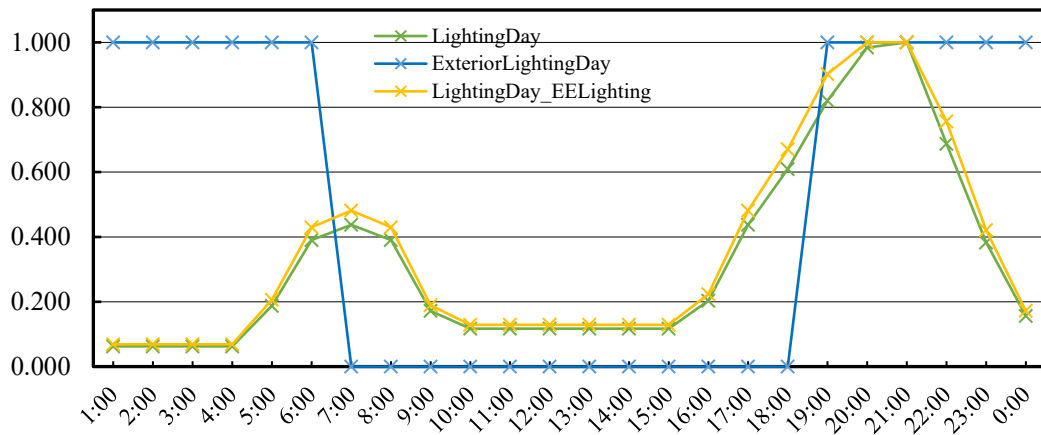


Figure 21. Lighting schedule

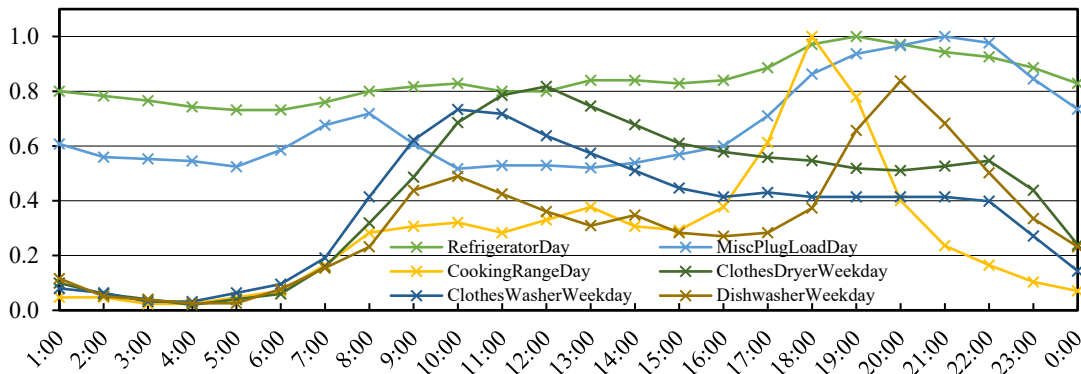


Figure 22. Miscellaneous devices schedule

An example of the monthly energy consumption of heating and cooling in this prototype residential building in Houston weather conditions is shown in Appendix B.3.

3.2 Fault Library

The fault library is the critical basis of fault modeling. It is a package containing fault taxonomy (which defines a structure of potential faults) and fault modeling elements (which describes modeling-related characteristics of potential faults, including fault directions, fault bounds, and

fault prevalence). Further, it serves as the cornerstone to map fault symptoms for the real systems, with the input parameters in the whole building simulation program (e.g., EnergyPlus).

To develop a fault library that is reusable and expandable to any residential building, several papers and reports on residential HVAC faults were reviewed first. These publications are not limited to the topic of fault modeling but also include fault impact analysis, fault detection and diagnosis, robust operation test, etc.

3.2.1 Fault Taxonomy: Definition and Structure

A fault is defined as an abnormal operation of the HVAC system, which results in a deviation from normal building performance and results in higher energy consumption than fault-free conditions and/or worse thermal comfort, with thermostat setpoints unmet (Cheung and Braun 2015). A fault's effects include the loss of efficiency and capacity of the system.

A fault taxonomy should serve as a road map to locate the fault and then link it with the corresponding information in the fault library (Y. Chen et al. 2020). To achieve that, a hierarchy of residential HVAC systems is developed in Figure 23. This taxonomy consists of three levels – fault system, fault component, and fault name. From the bottom up: a fault name (i.e., a fault) denotes a single malfunction at one location; a faulty component is a separate physical part of one complete machine, operating with certain faults; a fault system is a complete system comprising multiple components, among which some are in fault conditions. For example, a fault system of a heat pump comprises condenser, evaporator, refrigerant, etc., which all belong to the fault components. For the fault component of refrigerant, the specific fault is likely undercharge, overcharge, or non-condensable gas. Complete definitions and examples of terms to structure the fault library are listed in Table 10.

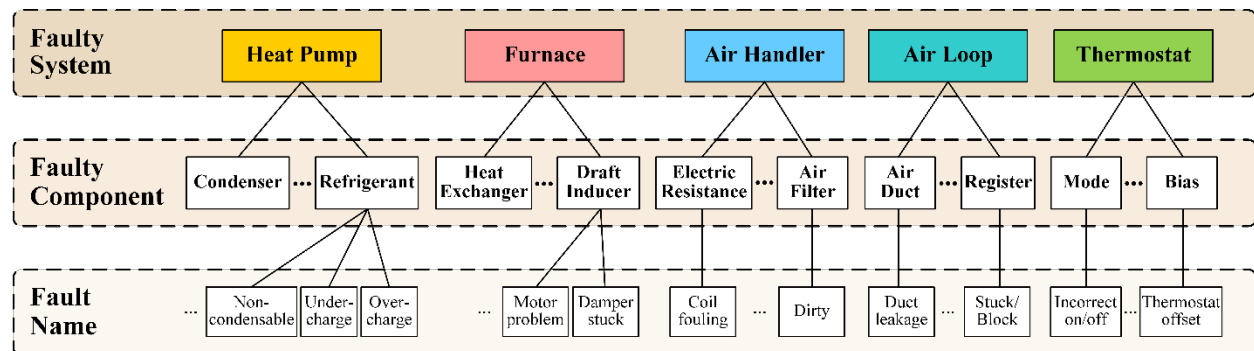


Figure 23. Taxonomy of residential HVAC fault library

Table 10. Definitions of Terms in Fault Library

Term	Definition	Category	Example
Fault	A single malfunction at one location	Event (reality and simulation)	Condenser fouling, Compressor degradation
Fault Model	Fault in the simulation	Event (simulation)	Condenser fouling, Compressor degradation
Fault Mode	Multiple faults that can occur simultaneously	Event (set of faults) (reality and simulation)	Fault Mode 01: consists of condenser fouling, liquid line restriction, etc.
Fault Component	A separate physical part of one complete machine, operating with certain faults	Equipment (reality and simulation)	Condenser, compressor, expansion valve
Fault System	A complete system comprising multiple components, among which some are fault components	Equipment (set of components) (reality and simulation)	Heat pump system, furnace system, AC system, building envelope
Fault Symptom	A single biased operating parameter, contributed by fault mode; it could represent one fault system or one fault component	Value (reality and simulation)	COP (for one system - heat pump) motor efficiency (for one component - blower)
EnergyPlus-based Fault Models	A whole building level, including all faults that span different systems, or physical elements	Event (set of fault modes) (simulation)	
Faulty Parameter in IDF	It maps to fault symptom in the IDF file (EnergyPlus input file)	Value (simulation)	

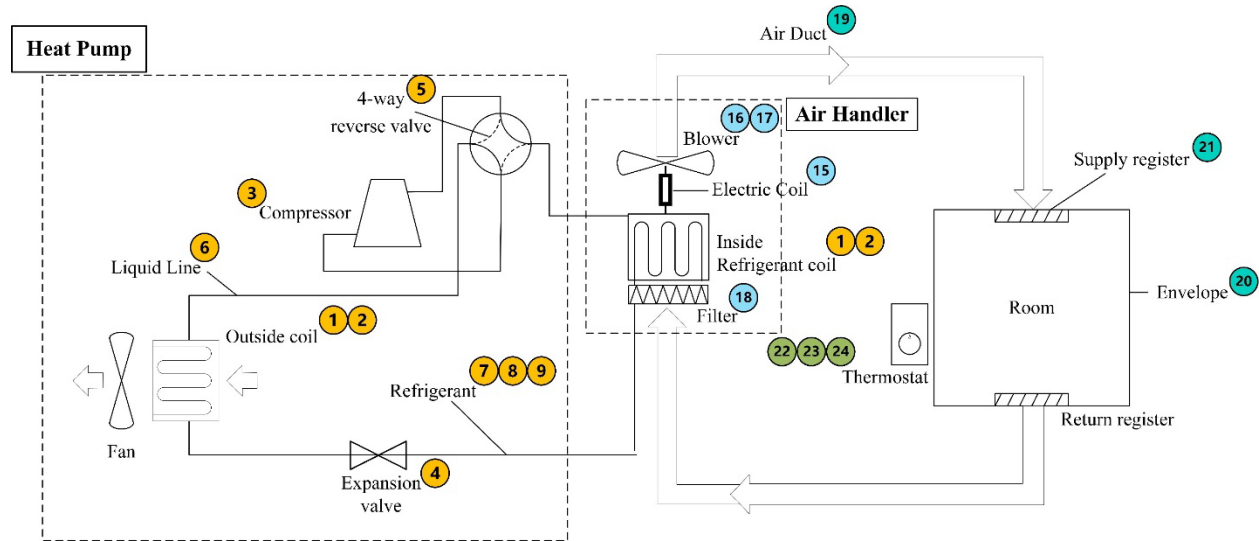


Figure 24. Vapor compression cycle for air conditioner system and heat pump system (numbers are corresponding specific faults)

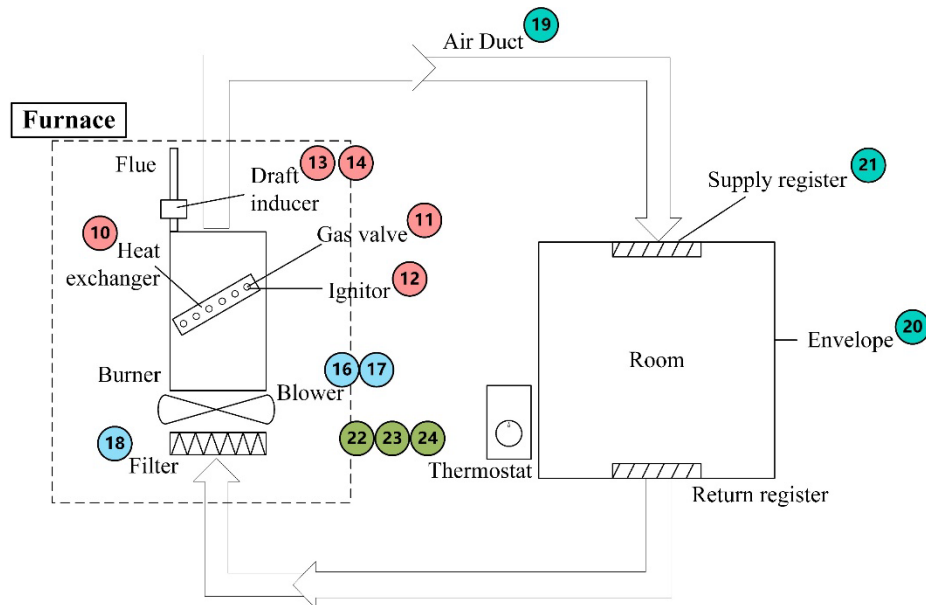


Figure 25. Heating system with a furnace installed (numbers are corresponding specific faults)

Twenty-four faults in five categories (heat pump, furnace, air handler, air loop, and thermostat) are curated in this project. Their locations are sketched separately in Figure 24 (a vapor-compression cycle system) and Figure 25 (a furnace system). The numbers in the circle represent the location of potential HVAC faults in the system. The yellow and red circles represent the heat pump and furnace, respectively, while the blue circle displays the air handling system. The cyan circles are related to the faults in the air distribution system, and the green circles mark the sensor faults. Descriptions of all potential faults are summarized in Appendix C. Among the described faults, condenser fouling, evaporator fouling, compressor degradation, refrigerant

undercharge, dirty air filter, air duct leakage, and thermostat error are most common in residential HVAC systems (Rogers et al. 2019a).

In the fault library, multiple faults may contribute to the same fault symptom simultaneously. A typical example is that the cooling capacity may be decreased due to faults from condenser fouling, liquid line restriction, non-condensable gas in the refrigerant, etc. In other cases, one fault in the fault library may have fault symptoms associated with one or more parameters. For example, liquid line restriction may impact the cooling coefficient of performance (COP) and cooling capacity at the same time.

3.2.2 Fault Elements

Fault modeling elements for the residential HVAC system include fault directions, fault bounds, fault prevalence, and fault objects and parameters in the simulation tool.

3.2.2.1 Fault Directions

Considering the characteristics of HVAC components, fault directions can be categorized into four types:

- **Fault-by-lacking:** The faulty value is lower than the normal one. Condenser fouling is a typical example, which may result in the degradation of the cooling capacity and COP of a cooling system.
- **Fault-by-excess:** The faulty value is higher than the normal one. One typical example is the fan pressure rise caused by a dirty air filter.
- **Fault-by-deviating:** The faulty value can either increase or decrease from the normal one. For example, thermostat offsets can lead to a lower or higher measured temperature than the fault-free conditions.
- **Fault-by-uniform:** The faulty value distributes randomly in a limited range. The infiltration rate is a typical example.

3.2.2.2 Fault Bounds and Fault Prevalence

Fault bounds define the limited range of values for each fault parameter. For most of the faults, the amplitude of the strongest effect is not uniform or random. Instead, it depends on the system configuration and the surrounding environment. Fault prevalence, which is usually represented by occurrence probability, indicates how often one fault appears at the desired level of fault severity. This is necessary when investigating the impact of a combination of multiple faults. The consideration of fault prevalence helps improve the calculation accuracy because faults have diverse existing probabilities in real life and are not likely to always appear at the same time.

To make the inserted faults have meaningful effects in the models, it is critical to estimate the lower bound and upper bound for each fault and their fault prevalence. For the fault bounds, we investigated a literature review to collect all existing fault ranges for the residential HVAC systems, which is shown in Figure 26. Based on the characteristics of HVAC faults, the four

types of models we analyze include (a) fault-by-lacking, (b) fault-by-excess, (c) fault-by-deviating, and (d) fault-by-uniform (Yanfei Li and O'Neill 2019).

Fault prevalence lacks sufficient research. For commercial buildings, Winkler et al. (2020) collected fault data of the indoor airflow rate and refrigerant charge from previously published research and created the corresponding fault histograms. Figure 26 is an example of the charge fault using frequency for each fault level (Winkler et al. 2020). For residential buildings, two research teams from the University of Nebraska–Lincoln (University of Nebraska–Lincoln) and the University of Central Florida (Florida), sponsored by DOE, are working on the prevalence and severity of HVAC faults in residential systems, but are still in progress. Therefore, this project estimates the residential fault prevalence with assumed distribution models proposed by Li et al. (Yanfei Li and O'Neill 2016), including Weibull function (for fault-by-lacking and fault-by-excess) (Bourguignon et al. 2014), Gaussian distribution (for fault-by-deviating), and uniform distribution (for fault-by-deviating).

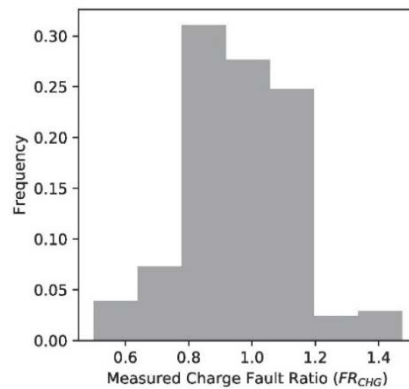


Figure 26. Histogram of charge fault ratio collected using measurements from previous studies (Winkler et al. 2020)

Calculations and examples of prevalence distribution for four types of faults are shown in Appendix C.1.

3.2.2.3 Fault Objects and Parameters in EnergyPlus

When the fault library is implemented, each fault should be mapped with a parameter in the simulation tool. Once the relationship is developed, the fault values can be easily modified in the simulation according to the predefined fault performance. Ideally, it is good to emulate all faults physically in the simulation. However, for EnergyPlus, its models of heating/cooling plant systems are developed to represent the symptoms of the faults in the behavior. For example, heat exchanger fouling, compressor degradation, or refrigerant charge issues all result in the same faulty symptom in the plant, i.e., degradation of efficiency and capacity. So, we emphasize the fault symptoms and the corresponding parameters in the EnergyPlus application, rather than the specific physical process.

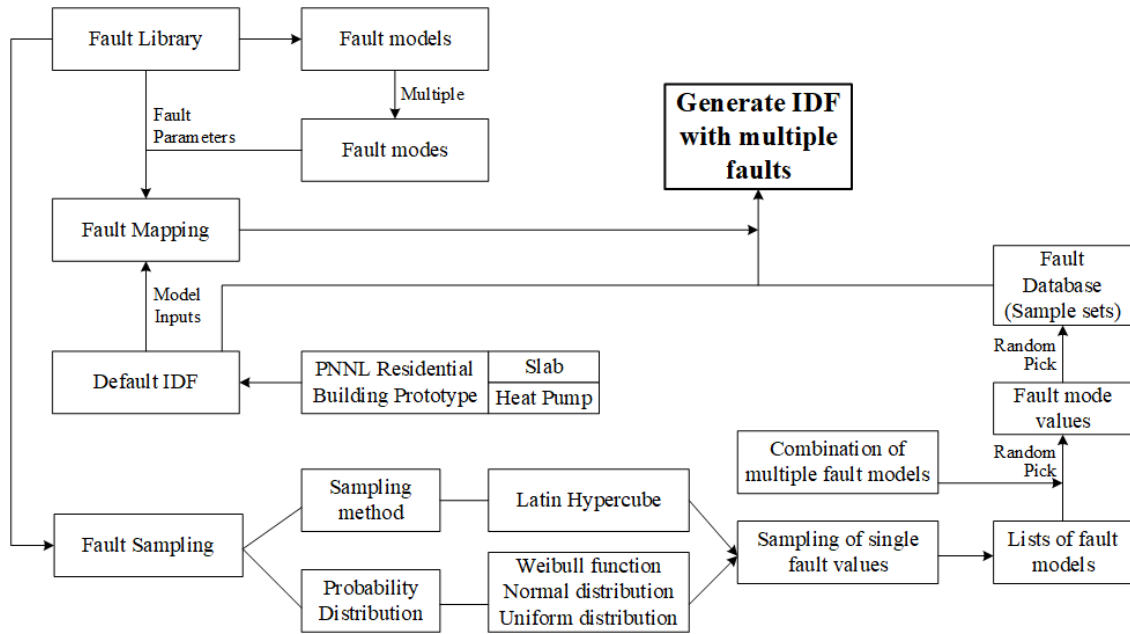


Figure 27. Research methodology outline of EnergyPlus-based faulty model generation

3.3 Fault Modeling Methodology Based on Residential Fault Library

Fault model construction is a fundamental step in conducting further studies, like fault impact analysis, FDD, fault-adaptive control, etc. The workflow for constructing the EnergyPlus-based fault model is illustrated in Figure 27, which is adapted from Li et al.'s work for commercial buildings (Yanfei Li and O'Neill 2019). The fault simulation is conducted with considerations of multiple faults and faults prevalence. The fundamental elements for fault model construction are as follows:

- 1) **Fault mapping:** Corresponding faults from physical modeling to associated parameters in EnergyPlus one by one.
- 2) **Fault bound:** Upper and lower limits for each fault severity (described in Section 3.2).
- 3) **Fault prevalence distribution:** Probabilities for a given severity of one single fault (described in Section 3.2).
- 4) **Fault sampling approach:** Generating samples of abundant fault modes.

3.3.1 Fault Mapping

A mapping between input parameters of EnergyPlus and the faults in the developed fault library was created and can be accessed in Appendix C.3. Figure 28 shows the data structure (adapted from (Yanfei Li and O'Neill 2019)) that gives a guide to model multiple faults simultaneously using the whole-building energy simulation (e.g., EnergyPlus), regarding various fault elements, described in Section 3.2. The definition of each column (Yanfei Li and O'Neill 2019) is presented as below:

- 1) Mode ID: the ID for each fault mode.

- 2) Case ID: the ID for each fault input parameters case.
- 3) Fault mode name: the name for each fault mode.
- 4) Fault mode IDF module: the IDF object name in EnergyPlus corresponding to the fault mode.
- 5) Fault mode IDF parameter: the input parameter to be revised in the IDF of EnergyPlus.
- 6) Fault mode unit: the unit of IDF input parameter.
- 7) Fault mode IDF component: the IDF component name within the given object.
- 8) Fault mode nominal: the nominal value (fault-free) for the input.
- 9) Mode lower: the lower bound for each IDF input parameter with a given fault mode.
- 10) Mode upper: the upper bound for each IDF parameter with a given fault mode.
- 11) Mode type: the fault occurrence distribution type (i.e., lacking, excessing, nominal, or uniform).
- 12) Notes: the note for each fault.
- 13) Fault model 1 name: the name of the fault model 1 that belongs to the given fault mode.
- 14) Fault model 1 lower bias: the lower bias relative to the nominal value for the fault model.
- 15) Fault model 1 upper bias: the upper bias relative to the nominal value for the fault model.
- 16) Fault model 1 type: the fault model distribution type (i.e., lacking, excessing, nominal, or uniform).
- 17) Fault model 1 note: the extra note for the fault model.
- 18) Repeat (13)–(17) with new models that belong to the same given fault mode.

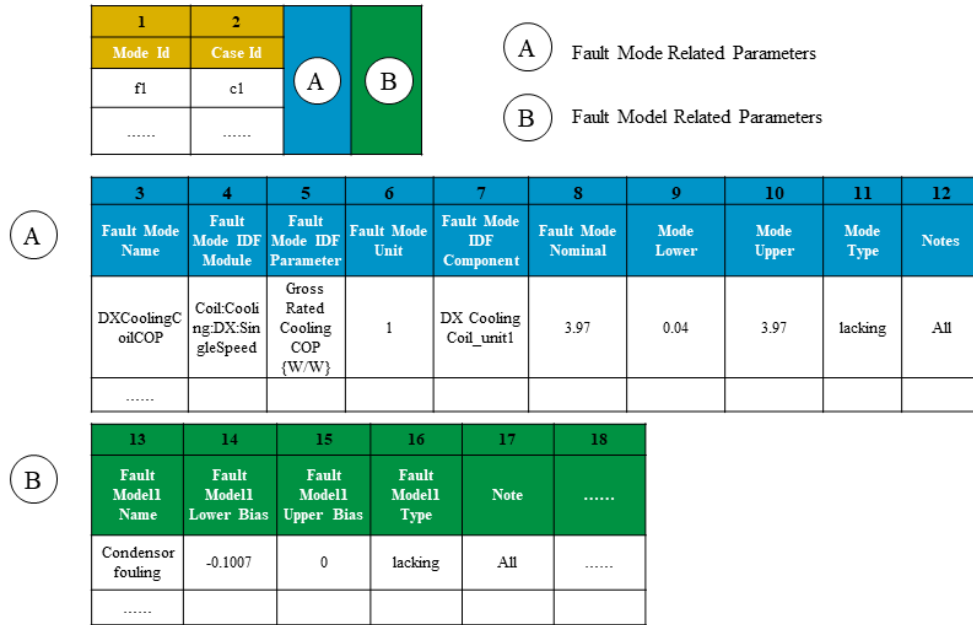


Figure 28. Example of fault mapping data structure for fault model generation

3.3.2 Fault Modeling Implementation

EnergyPlus, an advanced whole-building energy consumption simulation, is used as the studied simulation tool in this project. There are four ways to model HVAC faults in EnergyPlus (R. Zhang and Hong 2017):

- 1) **Change parameters directly:** This is the easiest way to implement fault injection in the HVAC system and can be finished within the idf text file by changing input parameters or performance curves. Faulty values should be carefully determined if this approach is adopted.
- 2) **Use an energy management system in EnergyPlus:** This approach is designed for customized supervisory control routines for some preselected sets of parameters. It is more flexible than the direct parameter change, because it overrides specific aspects of EnergyPlus modeling.
- 3) **Utilize built-in fault objects in EnergyPlus:** This approach gives the users full access to all parameters in the source code of EnergyPlus. Developers implement generic physical logic in the source codes. Users do not need to describe this calculation logic like an energy management system.
- 4) **Modify the source code of EnergyPlus:** This approach can be used if the above three methods fail to satisfy the users' requirements. It requires the user to have a full understanding of EnergyPlus source code and to devote significant programming efforts.

In this project, considering the distribution of residential HVAC faults, direct parameter adjustment and native fault objectives were considered to construct faulty energy models with EnergyPlus. These two methods are sufficient to inject faults into the baseline EnergyPlus

model. Moreover, as we need to investigate the distribution of faults and their effect on energy consumption, an external computing language, Python, is used to adjust fault-related parameter values and generate thousands of faulty EnergyPlus models.

3.3.3 Fault Sampling

For a given EnergyPlus fault model, multiple faults are included with a predefined fault occurrence probability. As illustrated in Figure 27, various predefined probability distributions are first used to do sampling for single fault values. The process involves inverse transform sampling technique with the Latin hypercube sampling. Latin hypercube sampling is a statistical sampling technique widely employed in the experimental design and numerical analysis. It proves especially beneficial when investigating parameter spaces with multiple dimensions, as it guarantees a representative and uniformly distributed sample. The fundamental concept of Latin hypercube sampling involves dividing the parameter space into equally sized intervals, or “bins,” and randomly selecting one point within each bin. The Latin hypercube component ensures an even distribution of samples throughout the entire parameter space by enforcing that each bin contains only one sample per dimension.

The sampling procedures are outlined in detail as follows:

- 1) Calculate the cumulative density function (CDF) corresponding to the probability density distribution ($F(x)$), calculated by Equation (1).
- 2) Invert the CDF to get the inverse function (Equation (2)).
- 3) Employ Latin hypercube sampling for the variable y , ranging from 0 to 1 (Equation (3)).
- 4) Substitute the sampled values into the CDF to obtain X , representing the samples that adhere to the desired probability density function (PDF), calculated by Equation (4).

$$F(x) = \int_{-\infty}^x f(t)dt \quad (1)$$

$$X = F^{-1}(y) \quad (2)$$

$$y = LHS \text{ in } [0,1] \quad (3)$$

$$f(x) = \frac{dF(x)}{dx} \quad (4)$$

In Figure 29, the inverse transform sampling for fault sampling is depicted. The X-axis represents the desired sampled parameters (indicated by the blue points) that adhere to the desired probability density function (PDF). The Y-axis corresponds to the Latin hypercube sampling (represented by the red points) derived from the inverse function. The black line illustrates the CDF.

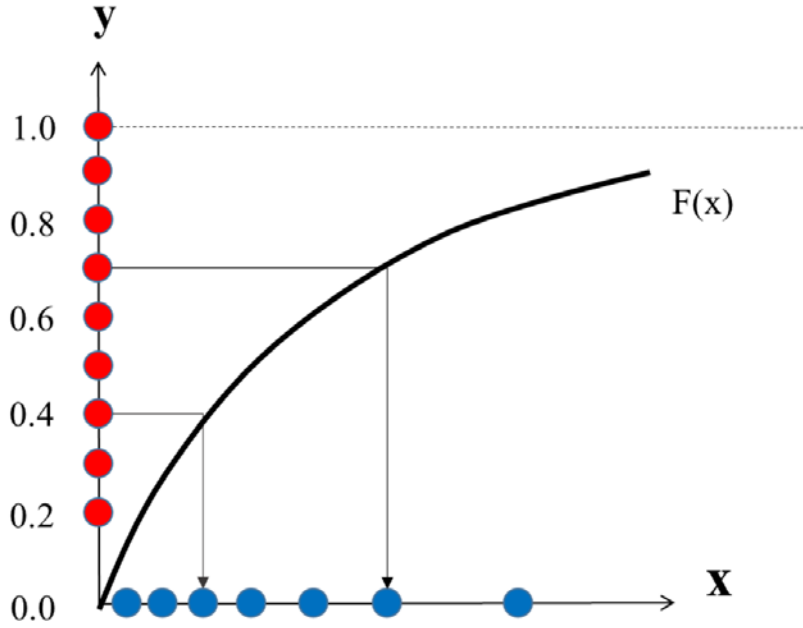


Figure 29. Inverse transform sampling with Latin hypercube sampling (Yanfei Li 2018)

Following the single fault sampling, the next step involves randomly combining multiple fault models to obtain fault model values, and the sampled value for each of all faults are picked in each combination (“no fault” is allowed because zero error is included in the sampling process). Fault model values then served as the fault database to be picked up randomly and injected into the baseline EnergyPlus model. The following Equation (5) (Li and O'Neill 2019) is used to inject multiple faults into the baseline model.

$$X_f = X_o + X_o \sum_{i=0}^n [a_{lo} + f_i(a_{hi} - a_{lo})]_i \quad (5)$$

where,

X_f is the fault parameter from a fault mode.

X_o is the fault parameter in the nominal condition (fault-free).

i is the index for each fault model.

f_i is the fault occurrence probability of an individual fault with the range of [0, 1].

a_{hi} is the maximum bias percentage (upper bound) of a directly affected parameter under a faulty condition.

a_{lo} is the minimum bias percentage (lower bound) of a directly affected parameter under a faulty condition.

n is the total number of faults impacting the fault parameter X .

By using the probability distribution and the multiple faults impact formula, the EnergyPlus fault model samples (i.e., 3,000 EnergyPlus IDF models with faults) can be generated using Python scripts. Figure 30 illustrates the sampling procedure.

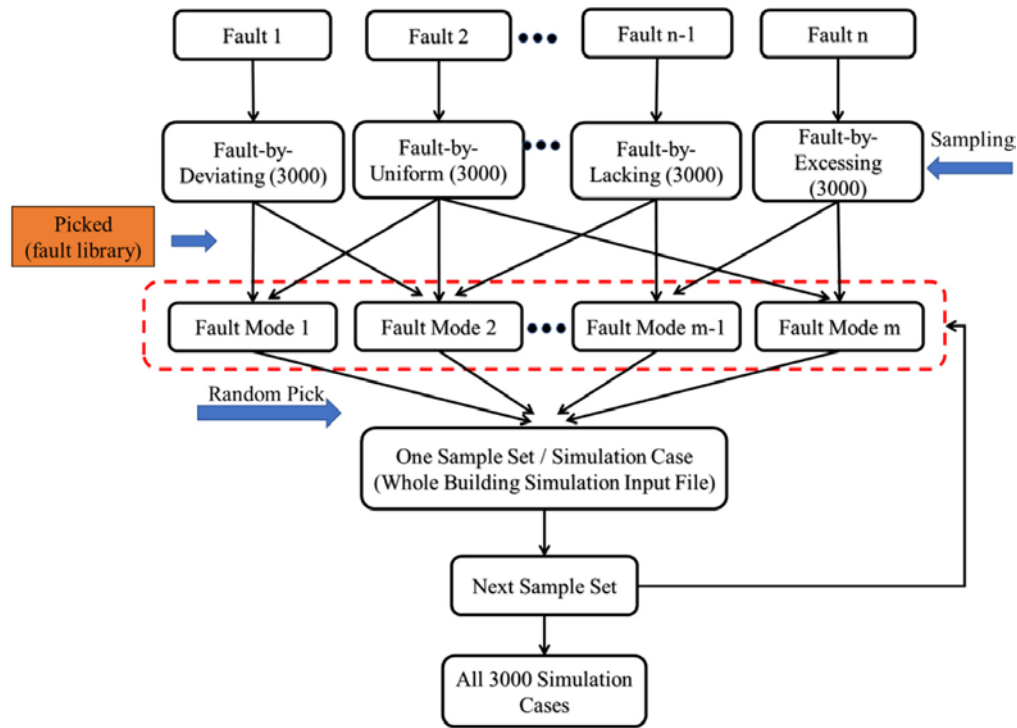


Figure 30. The procedure of fault parameter sampling

(Yanfei Li and O'Neill 2019)

3.4 Generation of Residential Building Fault Models

Generated fault data based on the fault library can be applied in a variety of ways to facilitate research as follows.

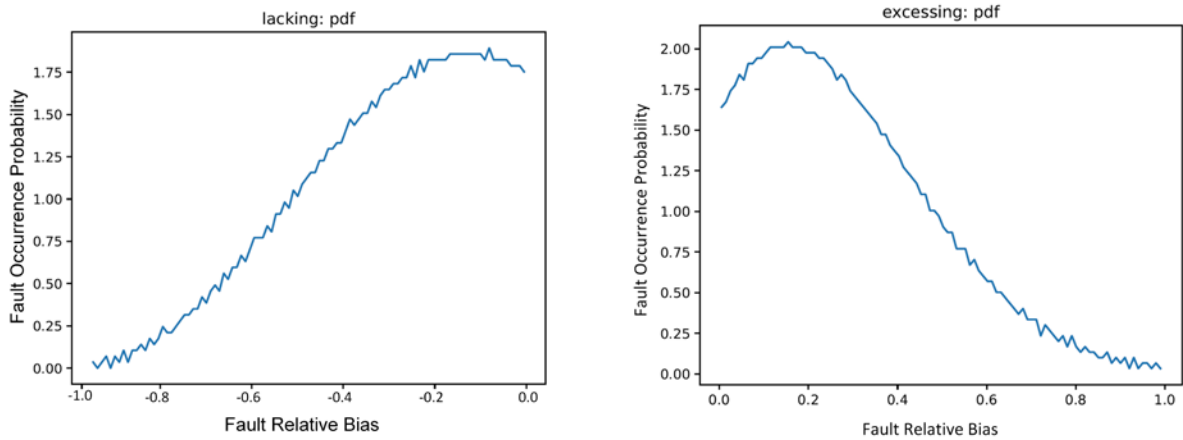
- 1) **Understanding faults impact:** This facilitates a comprehensive understanding of fault impact by quantifying the response on energy consumption and thermal comfort with diverse perspectives of input values (M. Kim et al. 2006; Lu et al. 2021). Energy consumption (periods, seasons, peaks, etc.) and thermal comfort (PMV-PPD, unmet hours, etc.) are the two main metrics of interest (Rahman et al. 2022).
- 2) **Guiding and testing FDD:** Constructing faulty cases to develop various performance patterns and features, which can provide a comprehensive guide and virtual data for FDD strategy generation (Cheung and Braun 2015; Zhao et al. 2014). The rule-based approach and data-driven approach are two ways to generate detection and diagnosis algorithms, with labeled fault data generated on the fault library (Mirnaghi and Haghghat 2020).
- 3) **Supporting commissioning and retrofit:** Modeling operational faults can improve the accuracy of existing building model calibration, which serves as a baseline for retrofit or

commissioning, thus increasing the analysis accuracy of different measures (Shih 2014; Lyu et al. 2021).

- 4) **Assisting adaptive control:** Virtual testbed with faults injected can support testing fault correction measures or flexible control decisions to maximize the conditioning ability of HVAC systems within degraded conditions (Gunay 2016; Xu et al. 2021). System capacity (e.g., oversizing and degradation) is a typical fault that can be conveniently injected and studied in EnergyPlus (Cetin et al. 2019).

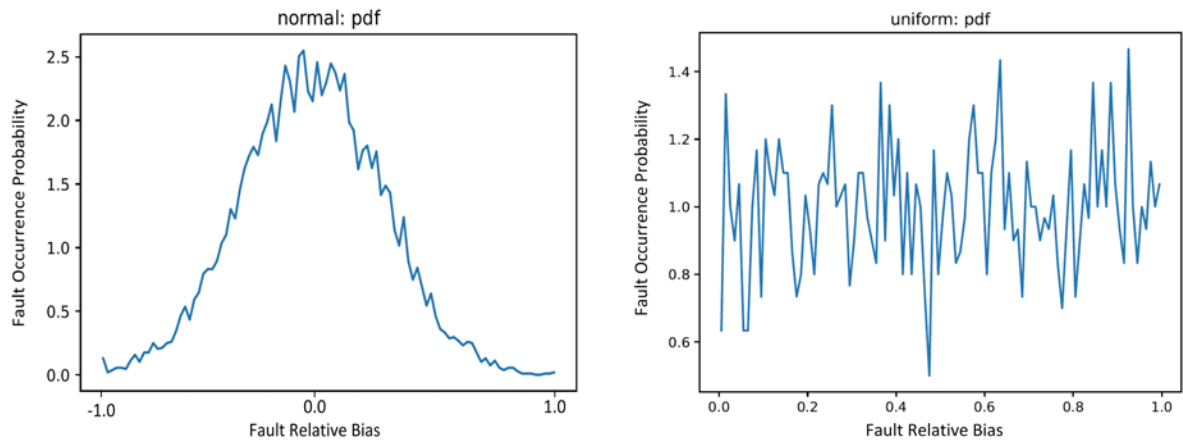
In this section, the fault models for residential buildings are generated using the workflow described in Section 3.3, based on the fault-free DOE residential building prototype (DOE), and a simple fault impact analysis is presented.

3.4.1 Faulty EnergyPlus Model Generation



(a) An example of the fault-by-lacking pdf curve

(b) An example of the fault-by-excess pdf curve



(c) An example of the fault-by-deviating pdf curve

(d) An example of the fault-by-uniform pdf curve

Figure 31. Examples of fault pdf curves (the x-axis is the fault bias, and the y-axis is the fault occurrence probability)

According to the explanation in Section 3.3.2, fault emulation in EnergyPlus is achieved by direct parameter value change and built-in fault objects. For the residential building in this section, there are a total of 12 fault modes injected into EnergyPlus, based on 19 faults (5 faults for the furnace are not included, because this virtual testbed is with a pure heat pump for heating and cooling). According to the workflow illustrated in Figure 27, each fault model is sampled with the consideration of its fault bound and fault prevalence. Three thousand cases are generated in total. Figure 31 shows distribution examples for each type of fault from the sampling results. Figure 31(a) shows a fault-by-lacking pdf curve, where a smaller negative bias occurs more frequently while a larger one is for less often. This curve is the result of capacity-degradation-like faults. Its occurrence distribution follows the Weibull model (Bourguignon, Silva, and Cordeiro 2014). Similarly, Figure 31(b) is a fault-by-excess pdf curve, where faults occur less frequently for a larger positive bias while more often for a smaller bias. This curve is the result of pressure-rise-like faults. Figure 31(c) is a fault-by-deviating pdf curve, resulting from thermostat-offset-like faults and obeying Gaussian distribution. Figure 31(d) shows a fault-by-uniform pdf curve, with infiltration rate as a typical example, following the uniform distribution.

Fault impact analysis based on the generated fault models can be found in Appendix C.3.

3.5 Summary

Section 3 presents an expandable fault library of residential HVAC systems along with the generation of faults using EnergyPlus based on the developed library. It can assist in simulating operational faults in residential HVAC systems and conduct a fault-relative investigation, including fault impact, fault detection and diagnosis, fault-adaptive control, etc. The fault library consists of 1) fault taxonomy, which defines each fault in the residential building and its systematic structure and 2) fault modeling, which includes fault attributes (direction types, bounds, prevalence), as well as the corresponding objects and parameters in EnergyPlus. Based on this fault library, a fault modeling approach for residential HVAC is developed. A basic modeling approach consists of fault mapping, fault occurrence distribution development, multiple fault combination, and fault sampling.

Fault modeling of residential HVAC systems is beneficial for understanding faults impact, guiding and testing the FDD, and assisting adaptive control. Three thousand fault models of residential HVAC systems are generated in this project, by following the developed fault modeling methodology. These fault models will support the research of FDD and fault-adaptive control in the following sections. A fault impact analysis is also conducted in the scenarios of single fault, double faults, and multiple faults.

This section also contributes generally to the HVAC fault research community by constructing a residential fault library. This innovative library encompasses all possible faults in residential HVAC systems that have not been previously addressed in a comprehensive way in the existing literature. It provides extensive information about the locations, fault taxonomy, and fault

attributes of each fault. Furthermore, it outlines the application of this fault library in simulations using EnergyPlus. Although this fault library was demonstrated in the EnergyPlus simulation environment, it can be easily integrated with other whole-building simulation programs.

4. Learning-Based Models

In this section, the developed learning-based forecasting models are discussed. First, Section 4.1 introduces the overall modeling framework used for developing the learning-based forecasting models. Section 4.2 covers a comprehensive discussion on the utilization of such framework as a virtual testbed for the development of forecasting models, and evaluation of the developed models. Finally, Section 4.3 concludes the section with a discussion on the development and evaluation of the forecasting models used for the PNNL lab test home.

4.1 Overall Modeling Framework

Several learning-based forecasting models were developed for this study, which include a whole-building energy forecasting model, an HVAC energy forecasting model, a zone temperature forecasting model, and a thermal comfort forecasting model. All of these forecasting models shared the same framework as created by the project team (L. Zhang and Wen 2019, 2021):

- 1) Weather block analysis
- 2) Systematic multistep feature selection
- 3) Active learning
- 4) Cross validation model training
- 5) Model testing

This framework starts with the available normal operation data either from the virtual testbed of the DOE prototype building in EnergyPlus or historical data from the PNNL lab test home. The data selection and measurement process mainly considers how easily the data can be obtained from real buildings in practices. Using this dataset, a weather block analysis is first performed to determine the impact of weather disturbances on the forecasting models. After the weather block analysis, a systematic multistep feature selection is performed to determine the smallest set of features that provide the best fit for the model. Following is an active learning process, which is a machine learning-driven process to improve the richness of the data, which means their generation under a wide range of conditions, encompassing various settings and not limited to just one or two thermostat setpoints. Using the enhanced data, a K-fold cross validation model training process occurs to train the forecasting models. The trained models are then evaluated on different testing data to assess their performance. More detailed discussions of all parts of the framework can be found in the following subsections.

4.1.1 Active Learning Algorithm and Weather Block Analysis

Active learning within machine learning-based modeling is similar to the strategy of excitation and experiment design in the fields, in terms of system identification and parameter estimation (Zhang and Wen 2018; Zhang 2018). Active learning works well with machine learning-based models. Compared with traditional excitation methods in a system identification process, much less domain knowledge is needed by active learning algorithms, since it is guided by data itself

and is generally plug-and-play with minimum engineering efforts. Among the various active learning algorithms, the expected error reduction method (Zhang and Wen 2018) places a significant emphasis on model generalization or extendibility. The idea is to enhance the model's ability to perform accurately not just on the training data, but also on unseen or future data. This trait is of paramount importance in dynamic fields like constructing energy forecasting models. The expected error reduction strategy aims to identify an unlabeled dataset that, when included, minimizes the discrepancy between a model trained solely with labeled data and a model trained with both the labeled data and the newly incorporated unlabeled data point. An example of this algorithm can be seen in Figure 32. Step (a) shows three unlabeled data points that can be selected, and step (b) shows that the red point is selected because that results in the least difference in the newly trained model. The process is repeated in steps (c) and (d).

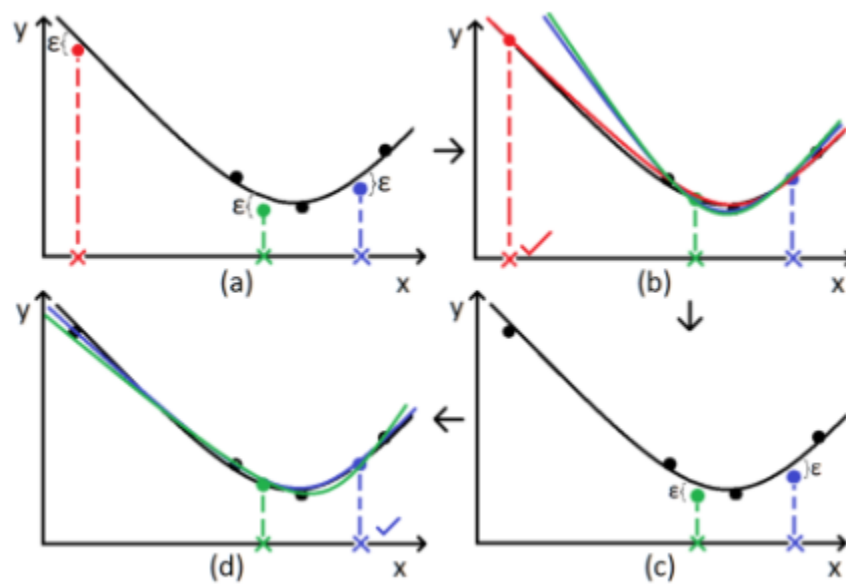


Figure 32. Visual example of expected error reduction algorithm

The main purpose of an active learning algorithm is to provide information-rich training data for a data-driven model. Hence, it is developed with a data-driven modeling structure. A straightforward data-driven modeling algorithm, multivariate adaptive regression spline (MARS), is used as the default modeling algorithm in this study. MARS was selected because it outperforms other commonly reported modeling algorithms such as regression tree, artificial neural network, and polynomial regression in our previous studies (Zhang and Wen 2019, 2018; Zhang et al. 2016).

Figure 33 illustrates the process of applying an active learning algorithm using the expected error reduction method (L. Zhang 2018). The process starts with a collected normal building operation dataset L , which is generated under very limited setpoints (being fixed, not dynamic variation over time step) during a building's normal operation. This dataset goes through a preliminary feature selection process to reduce the numerous possible features within building operation to a manageable selection. Data is considered "labeled" in this dataset: for each set of model inputs

(e.g., the setpoints and weather conditions), there is a corresponding model output (building energy consumption for this study). Hence, a data-driven model h_0 (in our study, a MARS model) is developed based on this normal operation dataset (L). This step can be done offline before the active learning process. More details about the process can be found in Zhang and Wen (2019).

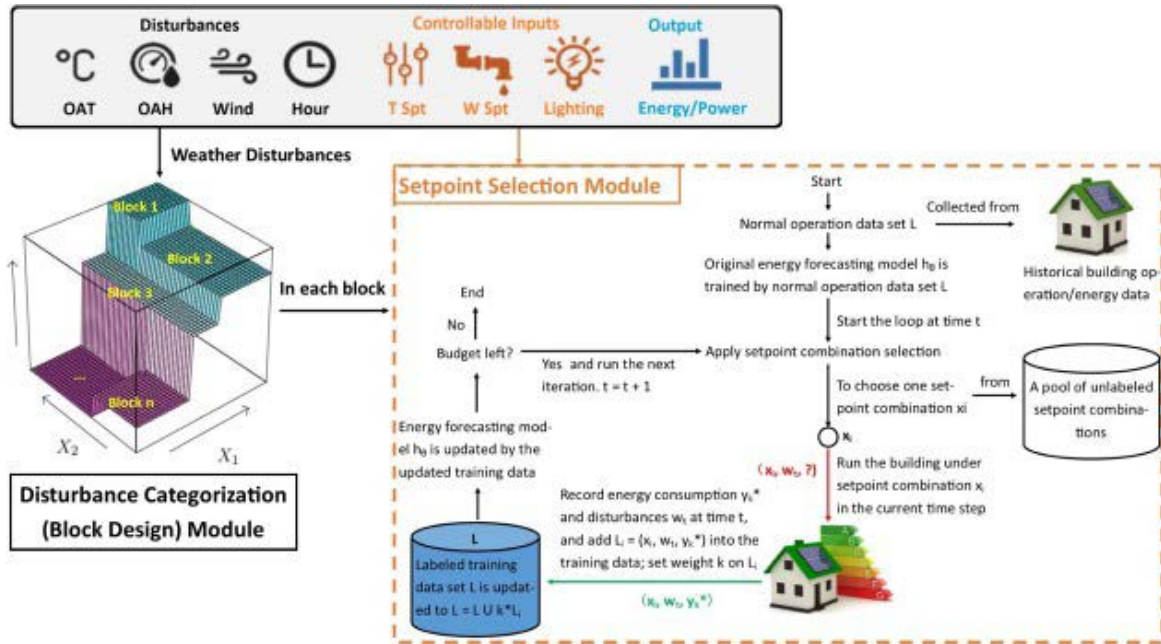


Figure 33. The complete active learning algorithm for building energy forecasting

The weather disturbances categorization process is performed by using a classification algorithm to examine the collected normal operation dataset. Given the inability to actively perturb weather conditions during the learning process, they are classified as disturbances. The categorization of weather disturbances involves grouping them into distinct blocks or categories. Within each block, the effect of weather disturbances on the model output, specifically the overall building energy consumption, is expected to exhibit lower variability compared to the variations observed between different blocks. Put simply, each block represents a specific type of weather condition (e.g., outdoor air temperature $>30^{\circ}\text{C}$) where energy consumption displays reduced variability in response to weather disturbances. In this process, key weather features (input variables) and their specific values to differentiate blocks are identified.

A classification model is built with weather disturbances as inputs, and future (1-hour ahead) building energy consumption as outputs. In this study, the decision tree method is used as the classification algorithm for weather disturbances categorization.

To sum up, the developed algorithm considers the two key factors of active learning for building energy forecasting: it efficiently generates informative training data in a short time, and it passively considers weather disturbances at the same time.

The developed active learning algorithm is used in the virtual testbed models but not the lab test home models because there was no time available during the lab testing period to utilize the algorithm and also collect historical data that are considered rich enough to develop forecasting models.

4.1.2 Systematic Multistep Feature Selection

To develop a machine learning-based model, inputs (i.e., features) are needed. For building system modeling, features are typically selected from building measurements. The virtual testbed and the historical lab test home data include many measurements. For the virtual testbed data, only those virtual measurements that could be obtained in a real residential building are considered in this study. For both virtual and historical data, irrelevant or redundant variates are first examined based on a previously developed feature selection process.

An example of candidate features used for the lab test home historical forecasting models are presented in Table 11. The candidate features are selected from measurements that 1) could be obtained in a real residential building, and 2) could have a relevance with the HVAC energy consumption.

All features in the candidate feature set are provided at times t (current time), $t-1$ (previous time step), $t-2$ (two time steps earlier), and time $t-3$ (three time steps earlier). The reason to include these time lag features is because features could be correlated to environmental features from previous timesteps. For this study, a time step of 1-hour was used based on the building thermal capacitance.

Table 11. Historical HVAC Energy Forecasting Model Candidate Feature Set

Feature Acronym	Feature Name	Feature Acronym	Feature Name
ZTCSP	Zone Thermostat Cooling Setpoint Temperature [°F]	TC_Therm	Thermostat Temperature [°F]
TC_Kit	Kitchen Temperature [°F]	Solar	Solar Radiation Rate per Area [W/m ²]
TC_Din	Dining Room Temperature [°F]	Solar_Outside	Outside Solar Radiation Rate per Area [W/m ²]
TC_Liv	Living Room Temperature [°F]	OA	Outside Air Temperature [°F]
TC_WBed	West Bedroom Temperature [°F]	OAAT	Outside Air Absolute Humidity [g/m ³]
TC_EBed	East Bedroom Temperature [°F]	Occ	Home Occupancy Value [occupied or not occupied]
TC_MBed	Master Bedroom Temperature [°F]	HVAC	HVAC Energy Consumption [W]

A feature selection process was performed to identify the best set of features from the candidate feature list that were most useful to forecast the target variable. The goal of this feature selection was to reduce data dimensionality.

The process performed was based on that described by Zhang and Wen (2018), which was a systematic multistep feature selection using historic building data (generated from the virtual testbed as described below). Figure 34 shows the steps of the process (Zhang and Wen 2018).

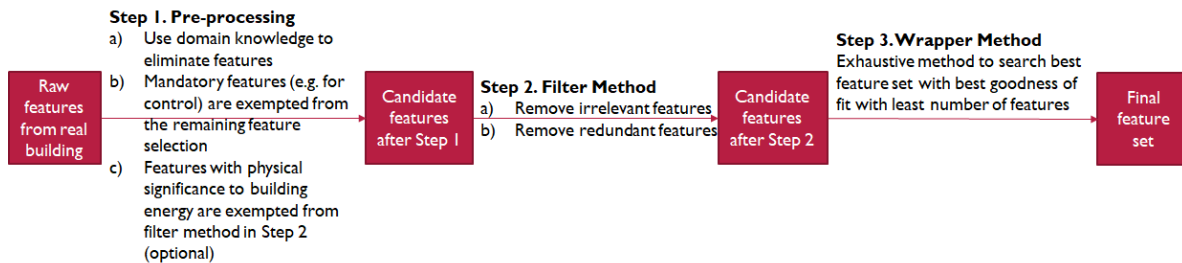


Figure 34. Systematic multistep feature selection process

Step 1 of this process was performed offline and resulted in the candidate feature set shown in Table 11. Step 2 utilized the Pearson correlation coefficients to remove irrelevant (with correlation with target) and redundant (with correlation among features) features while Step 3 used a machine learning-based model structure, which was MARS or kSVM for this study, to determine the final feature set with the best goodness of fit. The features selected from this process were specific to different test cases.

4.1.3 K-Fold Cross Validation Model Training

Cross validation is a technique used in model training to assess how well the model will perform on new data. It involves excluding some subset of the training data during the model training and using it to evaluate the model performance on new data that it has not seen before. It then chooses another subset to exclude and trains the model again with the last subset included. This results in all data being used for both training and testing. This approach offers advantages over a simple train-test split, where a portion of the data is set aside for testing and the remainder is used for training. Such a method can provide a comprehensive understanding of the model's training efficacy and its potential performance on new, unseen data. Therefore, cross-validation provides an idea during training about the nature of the model fit.

For this study a K-fold cross-validation model training and testing process is selected. For this process, the available data are divided into k folds. K-1 folds are used to train the model and the remaining kth fold is used to test the model. This process is repeated for each fold with the hold-out kth fold changing each iteration. However, during each fold, a systematic multistep feature selection (described above) is performed before the model is trained. The result is that for each weather block, a month of data is used for both training and testing at some point during the process, and the features selected for each fold (new features selected for each fold) are determined from the training subset rather than all available data. Figure 35 shows a visualization of the process where $k=10$.

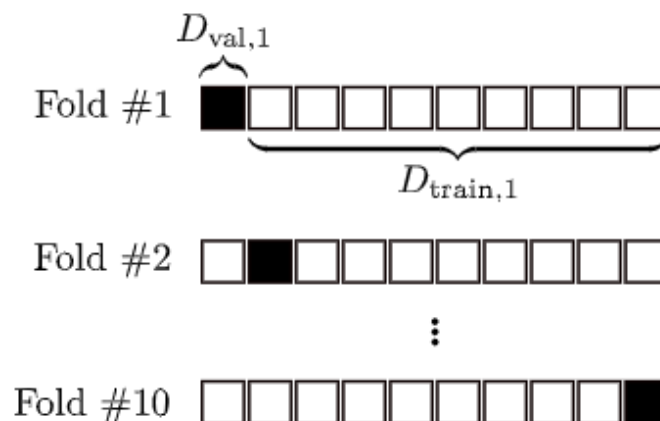


Figure 35. A visualization of cross validation

To determine the optimal value of K , a sensitivity analysis is performed first in the context of K -fold cross-validation. The analysis chosen is a leave-one-out cross-validation. This process performs a K -fold analysis where $k=N$, the number of samples in the training set. This is a computationally expensive analysis that results in the best possible performance if computation cost and time were not considered. Then a range of potential k values are tested to find the k mean (mean performance of all folds). For this study, a potential k range from 2 to 10 are examined, as previous literature suggests that K equals 10 is a frequently used upper limit. The smallest k value, thus having reduced computation time and cost and yielding a performance close to the best, is selected for application in the K -fold cross-validation process. Once the best k value is found, the K -fold cross-validation is performed, and the model performance on the validation data can be assessed. The training subset of the best performing fold is then used to train the final model.

4.2 Pilot Study of Developing Forecasting Models for Virtual Testbed

This section details the development of the HVAC energy forecasting model and the occupant thermal comfort vote forecasting models for the virtual testbed. These models were developed as a preliminary study before the development of the forecasting models for the PNNL lab test home.

The virtual testbed models included the active learning algorithm but did not include the K -fold cross-validation algorithm because the models developed here were used as preliminary models to guide the development of the lab test home models, specifically regarding which model structures and algorithms were beneficial. The preliminary models are a foundation for creating more advanced or specialized models. The intention is to start with simpler models to understand the fundamental dynamics and relationships in the data. These preliminary models can help to identify significant features, potential issues such as biases or class imbalances, and provide a baseline performance that more complex models strive to exceed.

4.2.1 Co-Simulation Environment

In order to apply the developed algorithm to the DOE prototype residential building virtual testbed, a co-simulation environment is needed to integrate the EnergyPlus environment (where the virtual building is simulated) and the MATLAB environment (where the active learning algorithm and feature selection algorithms are programmed). For this purpose, a functional mock-up interface was selected as the co-simulation tool.

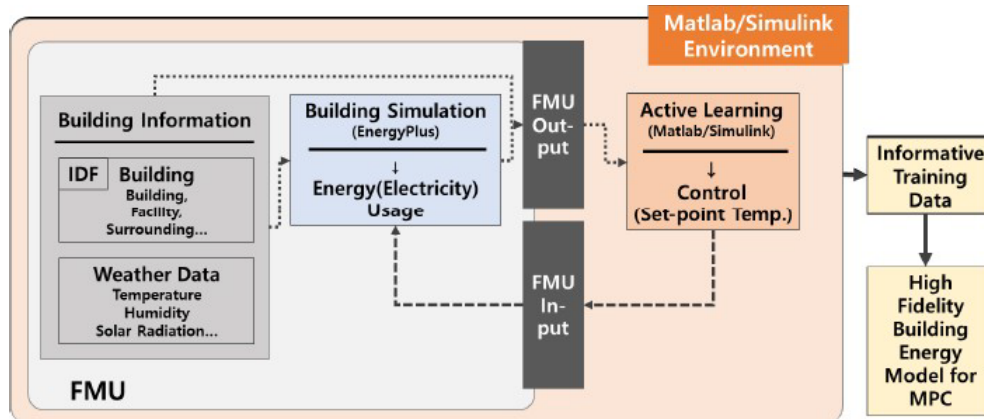


Figure 36. Functional mock-up interface co-simulation environment integrated in EnergyPlus and MATLAB

4.2.2 Preliminary Whole-Building Energy Forecasting Model

In this subsection, the whole-building energy forecasting model for the virtual testbed is discussed. High-fidelity energy and comfort models are crucial for model predictive control framework, a key component of the smart home energy management system. These models enable the optimization of building operation to strike a balance between energy efficiency and occupant comfort.

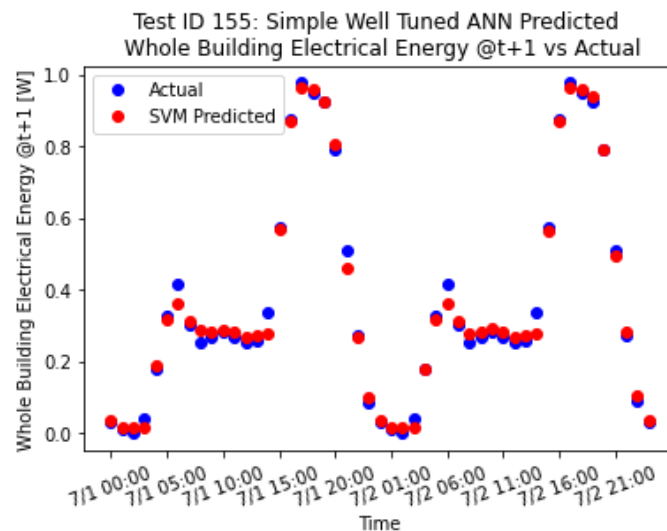


Figure 37. Artificial neural network predicted energy vs. actual

An artificial neural network-based whole-building energy forecasting model was evaluated on two days (chosen due to the similarity and repetition of the energy usage each day) selected from the normal operation dataset. The metric used for model evaluation was normalized root mean square error. The artificial neural network-based whole-building energy forecasting model performed within the desired performance with 3% normalized root mean square error. Figure 37 shows the model forecasting result graphically. This model was not used in the final lab testing and instead acted as a preliminary model to guide the development of an HVAC energy forecasting model for use in the lab testing period.

4.2.3 Preliminary Occupant Thermal Vote Forecasting Model

In this subsection, the virtual occupant thermal vote forecasting model is discussed. A constraint for occupants' thermal comfort needs to be considered when applying MPC for building energy reduction to warrant a building's service for its occupants. Moreover, uncomfortable occupants may engage in behaviors (e.g., adjusting the thermostat setpoint, opening/closing windows and/or doors) that have drastic impact on the building operation. Thus, for this study, a forecasting model was developed for predicting occupant's thermal comfort. However, given that no occupants would be present in the PNNL Lab Homes during the lab testing period, this model was not used other than as a preliminary study.

A kernel support vector machine (kSVM) is used to develop the occupant thermal vote forecasting model. The principle of a kSVM is to use existing labeled data to learn labels for new unlabeled data. kSVMs are typically used for classification problems, often referred to as support vector classification where they are used to classify new data into one of a number of classes, but they can also be used for regression problems, referred to as support vector regression (SVR). kSVMs learn these data labels by learning the patterns that are present in the data (Noble 2006).

Once this pattern is learned, a kSVM will develop a hyperplane in the dataspace that will separate the different data characteristics or classes. This hyperplane is determined through the creation of support vectors, which are vectors made of data points that show the most similar examples between the different classes. The distance between these support vectors is what makes up the decision boundary, at the center of which lies the hyperplane. The resulting hyperplane and decision boundary allows the kSVM to correctly label new data based on its position according to the hyperplane. The optimal hyperplane maximizes the distance between the data classes and has the widest decision boundary, or margin.

A standard SVM uses the above premise but is hard to optimize as data dimensionality grows and if data are non-linear. kSVM addresses these issues by using kernels to transform the data to a higher dimension in which it is easier to separate the data. Examples of potential kernels are Polynomial, Gaussian, Radial Basis Function, etc. Using these kernels can allow for a better optimized SVM that can learn complex non-linear data patterns. The choice of kernel is important because an incorrect transformation of data will result in poor model performance and add unnecessary complexity to the model optimization. For this milestone, a Radial Basis Function kernel was used based on the non-linearity nature of the problem and literature suggestions.

In addition to selecting kernel functions, there are two major parameters that need to be tuned for optimal kSVM model performance. These parameters are the regularization parameter (c) and gamma (γ). The regularization parameter is used during the optimization to determine how much a kSVM misclassifies training examples. A higher value for the regularization parameter will result in a smaller, more complex margin. This will allow for fewer examples to be misclassified but will result in a higher risk of overfitting because the model is adapting the margin to be

specific to this set of training data and will not be able to perform as well when presented with other data to label. Thus, increasing the regularization parameter can result in better performance on the training data but must be increased with care to not reduce model generalization and scalability.

The other parameter, gamma, influences the distance from the potential hyperplane that data for support vectors will be considered. Given that the hyperplane is determined by its support vectors, gamma is critical in determining the location of the hyperplane. Higher values of gamma will result in lower distances from a potential hyperplane considered, while lower values will consider more points that are at a further distance. Thus, high values of gamma can result in better model training performance as the hyperplane will be chosen based on data that are closer together and will avoid including data from other classes. This has the same potential as the regularization parameter to cause model overfitting.

For this milestone period, the values of the regularization parameter and gamma were chosen through a grid search. Literature was reviewed (Rojas-Domínguez et al. 2017) to determine potential value ranges for these parameters, and then models were trained while iterating through these ranges to determine the best values of each parameter to achieve the best model training performance while allowing for the model to retain good generalization and scalability.

A kSVM-based occupant thermal comfort forecasting model was trained for each occupant and was evaluated on a week of data from the enriched occupant comfort dataset. The output of the model is a comfort vote of -1, 0, or 1, corresponding to thermal sensations of cold, comfortable, or hot, respectively. Reported in Table 12 is the accuracy of the kSVM model in forecasting occupant thermal comfort at 1-hour ahead forecasting horizon. Accuracies are reported for each of the three kSVM models representing each occupant. Clearly, all occupant models reached the desired accuracy for forecasting occupant thermal comfort at 1-hour ahead. Figure 38 graphically shows the kSVM forecasting result. A value of 0 signifies a neutral comfort level. A value of -1 indicates a sensation of coolness, whereas a value of 1 represents a feeling of warmth. Blue dots are actual values, while red dots are predicted values. The overlapping of blue and red dots, particularly in the zone indicating neutral comfort, signifies a high level of accuracy in the forecast model's predictions.

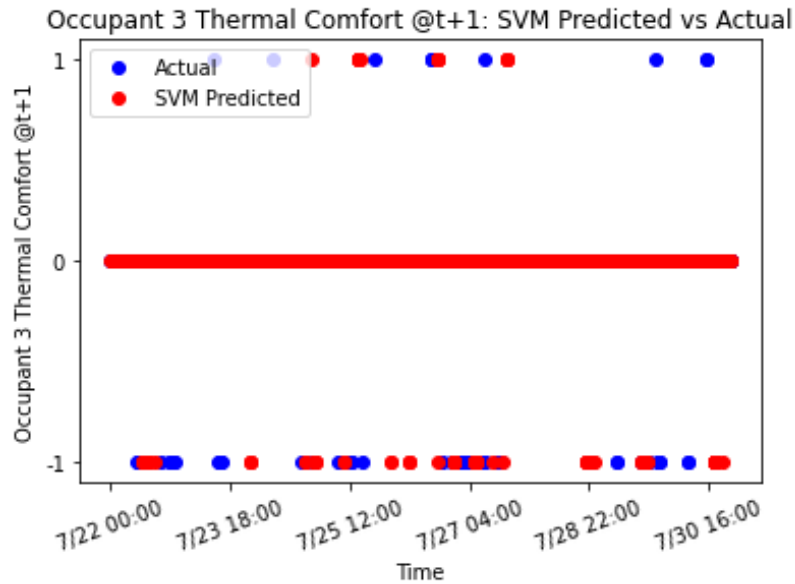


Figure 38. Occupant 3 Thermal Comfort @t+1: kSVM predicted vs actual

Table 12. kSVM Model Performance at Forecasting Occupant Thermal Comfort at 1-Hour Ahead

	Occupant 1	Occupant 2	Occupant 3
Accuracy for the testing week	91%	90%	94%

4.3 Forecasting Models for the PNNL Lab Test

To enable a data-driven MPC, it's crucial to incorporate occupant comfort as a constraint to the optimization process. This ensures that while the control system is optimized to reduce energy consumption, it does not compromise the thermal comfort of the occupants, thereby maintaining a comfortable living environment. However, for the lab testing, there are no real occupants present in the lab test home. Thus, instead of forecasting occupant comfort directly, zone temperature is forecasted. Accurate prediction of zone temperatures can be used in lieu of occupant comfort by establishing a range of comfortable temperatures.

4.3.1 Training and Testing Data

The framework described in Section 4.1 is again applied to develop the two forecasting models (HVAC energy and zone temperature). To evaluate the performance of the models, two testing cases are designed for this study: (1) historical operation data from the PNNL lab test home, and (2) current sensor data from the PNNL lab test home. Both developed models were trained on the same dataset but used different selected features (discussed below).

For this study, historic operation data for the PNNL lab test home from February 2021 to October 2021 were available. For the historic data, 1-hour sampled data from three months (June 2021, July 2021, August 2021) are used here based on a weather block analysis. From this data, seven weeks in July and August (July 5 to August 27) were selected. Some days and weeks were omitted due to errors present in the data. These seven weeks were used for both training and

testing the models. A candidate feature pool, shown in Table 13, was created using only features that are available during the lab testing period from the PNNL lab home database, Clemson iComfort sensors, and local weather data. There is no direct record of occupancy from the PNNL lab home database. The project team created this feature and determined its values based on power meter data (when the power meter had very low readings, it was assumed that the home was unoccupied and that the power used was just to keep the appliances running), since this feature was considered essential for model accuracy and zone temperature comfort range.

Table 13. Forecasting Model Candidate Feature Pool for PNNL Lab Home Testing

Candidate Features for 1-Hour Ahead HVAC Energy Forecasting Model			
ZTCSP at time t, t-1, t-2, t-3, t-4	HVACEE at time t, t-1, t-2, t-3, t-4	T_kitchen at time t, t-1, t-2, t-3, t-4	T_dining at time t, t-1, t-2, t-3, t-4
T_living at time t, t-1, t-2, t-3, t-4	T_Wbed at time t, t-1, t-2, t-3, t-4	T_Ebed at time t, t-1, t-2, t-3, t-4	T_Mbed at time t, t-1, t-2, t-3, t-4
Solar_int at time t, t-1, t-2, t-3, t-4	Solar_ext at time t, t-1, t-2, t-3, t-4	OADB at time t, t-1, t-2, t-3, t-4	OARH at time t, t-1, t-2, t-3, t-4
Occupancy at time t, t-1, t-2, t-3, t-4	-	-	-

4.3.2 Lab Test Home HVAC Energy Forecasting Model

To enable the MPC strategy used during the lab testing period, an HVAC energy forecasting model was developed. MARS was selected as the model structure based on preliminary studies and literature recommendation.

4.3.2.1 Model Training

A feature selection process was first used to identify input features for the models from the candidate feature pool. The selected features for the HVAC energy consumption forecasting model, with a 1-hour ahead prediction horizon, are shown in Table 14.

Table 14. MARS HVAC Energy Forecasting Model Selected Features for PNNL Lab Home

Feature Number	Feature Name
1	Zone Thermostat Cooling Setpoint at time t
2	Occupancy at time t
3	HVAC Electric Energy at time t
4	Outside Solar Radiation at time t-1
5	Outside Air Drybulb Temperature at time t
6	Outside Air Drybulb Temperature at time t-1
7	Thermostat Drybulb Temperature Measurement at time t-1

For the HVAC energy forecasting model, a K-fold cross validation model training was performed. A sensitivity analysis for the value of k resulted in the selection of k=16. Then, from the K-fold cross validation, the eighth fold performed the best. The HVAC energy model trained in the eighth fold was considered the best model and was used going forward.

4.3.2.2 Model Evaluation

The performance of the HVAC energy forecasting model was evaluated using historical data from the lab testing home as well as current sensor data. The performance metric used to evaluate these algorithms is the normalized mean absolute error. This metric quantifies the algorithms' accuracy in predicting HVAC energy consumption by comparing their predictions to the "actual" HVAC energy consumption. For the historical data evaluation, the model is evaluated on each of the seven weeks defined above.

Additionally, during model development, limited data were available from the current lab testing database (populated by the Clemson iComfort sensors). This data was from August 8–12, 2022, and August 15–18, 2022, and utilized the PNNL lab home database and the Clemson iComfort sensors to provide data (for all candidate features described above) to the cloud. These data were pulled from the cloud to evaluate the developed model using the live testing data gathered by the sensors.

The HVAC energy model is evaluated on both historical data from the lab testing home, and current data from the lab testing home. Historical data refers to the data gathered prior to the specialized lab testing conducted for this particular project (before August 2022). Current data denotes the data collected during the execution of this project. Table 15 summarizes the model performance across the seven testing weeks in the historical data.

Table 15. MARS HVAC Energy Forecasting Model Performance on Historical Data

Testing Week	Testing Period	Normalized Mean Absolute Error [%]
1	07/05/2021 – 07/11/2021	9.06
2	07/10/2021 – 07/16/2021	8.31
3	07/26/2021 – 07/31/2021	8.64
4	08/01/2021 – 08/07/2021	12.0
5	08/08/2021 – 08/14/2021	8.91
6	08/15/2021 – 08/21/2021	8.27
7	08/22/2021 – 08/27/2021	7.98

The performance of the model on the current data from the lab testing home (via iComfort sensors) can be seen in Figure 39.

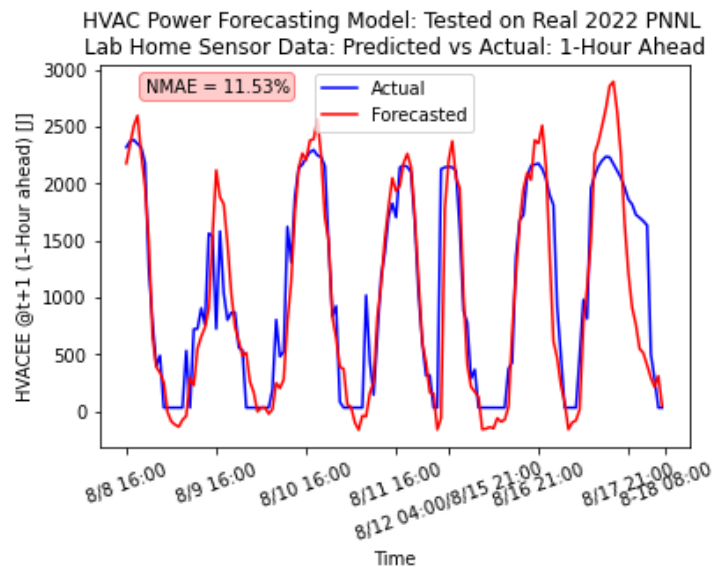


Figure 39. MARS HVAC energy forecasting model evaluated on real 2022 PNNL Lab Home A sensor data. The performance of the model was <15% normalized mean absolute error for all cases and achieves the desired performance (<15%) for this study. The model was used for the lab testing period described in more detail in Section 7.

4.3.3 Lab Test Home Zone Temperature Forecasting Model

4.3.3.1 Model Training

A feature selection process was first used to identify input features for the models from the candidate feature pool. The selected features for the zone temperature forecasting model, with a 1-hour ahead prediction horizon, are shown in Table 16.

Table 16. MARS Zone Temperature Forecasting Model Selected Features for the PNNL Lab Home

Feature Number	Feature Name
1	Zone Thermostat Cooling Setpoint at time t
2	Occupancy at time t
3	Outside Air Drybulb Temperature at time t
4	Thermostat Drybulb Temperature Measurement at time t-1
5	Outside Air Drybulb Temperature at time t-2

For the zone temperature forecasting model, a K-fold cross validation model training was performed. A sensitivity analysis for the value of k resulted in the selection of k=3. Then, from the K-fold cross validation, the third fold performed the best. The zone temperature model trained in the third fold was considered the best model and was used going forward.

4.3.3.2 Model Evaluation

In a similar manner to the HVAC energy forecasting model, the performance evaluation of the zone temperature forecasting model involved the use of historical data from the lab testing home, as well as the utilization of current sensor data. The evaluation metric utilized was still the normalized mean absolute error, which compared the predicted zone temperature generated by the algorithms with the actual zone temperature. For the evaluation of historical data, the model was tested on each of the seven weeks that were defined previously.

The same set of current data from the lab home sensors was employed to evaluate the zone temperature forecasting model. This data, collected from August 8–12, 2022, and August 15–18, 2022, was obtained from the PNNL lab home database and the Clemson iComfort sensors. The data encompassed all the candidate features described earlier and was transferred to the cloud for analysis and evaluation purposes.

The zone temperature model is evaluated on both historical data from the lab testing home, and current data from the lab testing home. Table 17 summarizes the model performance across the seven testing weeks in the historical data.

The performance of the model on the current data from the lab testing home can be seen in Figure 40.

Table 17. MARS Zone Temperature Forecasting Model Performance on Historical Data

Testing Week	Testing Period	Normalized Mean Absolute Error [%]
1	07/05/2021 - 07/11/2021	7.69
2	07/10/2021 - 07/16/2021	7.67
3	07/26/2021 - 07/31/2021	6.30
4	08/01/2021 - 08/07/2021	5.73
5	08/08/2021 - 08/14/2021	4.72
6	08/15/2021 - 08/21/2021	3.98
7	08/22/2021 - 08/27/2021	4.08

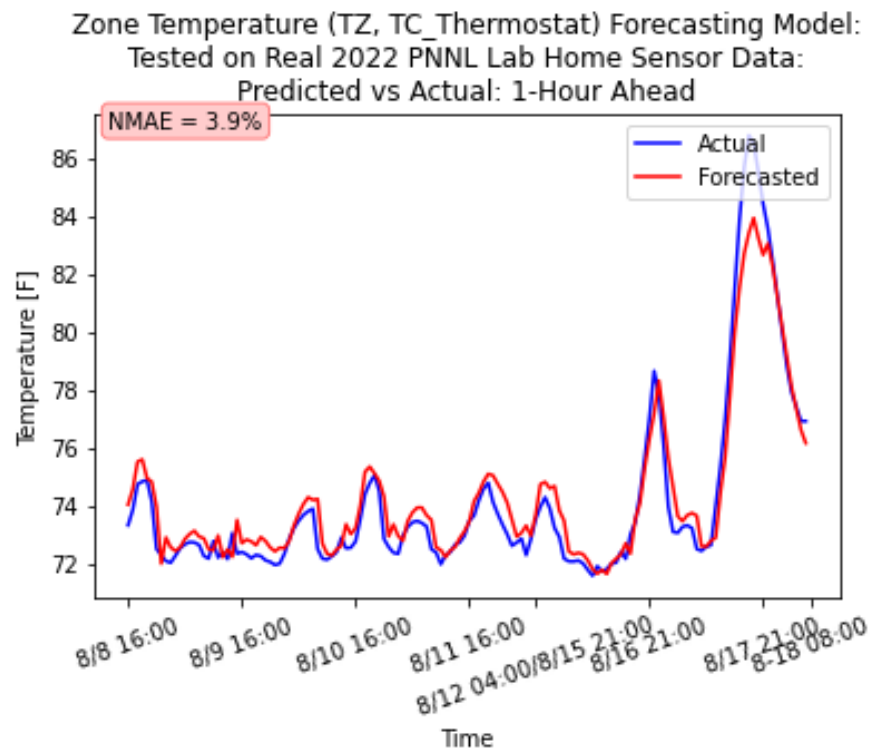


Figure 40. MARS zone temperature forecasting model evaluated on Real 2022 PNNL Lab Home A sensor data

The performance of the model was $<10\%$ normalized mean absolute error for all cases and achieves the desired performance ($<15\%$) for this study. The model was used for the lab testing period.

4.4 Summary

Section 4 provides a detailed description of the development and evaluation of a framework to develop learning-based models that include whole-building energy forecasting model, HVAC

energy consumption forecasting model, zone temperature forecasting model, and occupant thermal comfort forecasting model for a typical residential building. A virtual testbed as well as historic and current sensor data from the PNNL lab test homes were used to train and evaluate the developed models.

For the HVAC energy consumption forecasting model and zone temperature forecasting model, two MARS-based models were developed and tested using the data from the PNNL lab test homes with a 1-hour ahead forecasting horizon. A systematic multistep feature selection process was first explored to select features used for the models, from historic measurements. K-fold cross validation was used to train and test the model on all data and reduce model generalization error. The evaluation results show that both developed forecasting models perform accurately across the entire testing period (eight weeks total) according to desired performance of <15% normalized mean absolute error.

For the occupant thermal comfort forecasting model, operation data for normal operation and scenarios that would cause occupants to be uncomfortable were generated for training and testing of the developed models. kSVM-based models were developed and tested using the data from the virtual testbed with 1-hour ahead horizon. A systematic multistep feature selection process was first explored to select features used for the models from virtual measurements. It was found that the correlations between features and the target feature (i.e., occupant thermal comfort), were not strong (less than 10% Pearson correlation coefficient). Expert knowledge was then explored to finalize the feature selection. A kSVM-based model was trained and used to forecast occupant thermal comfort for each of the three occupants presented in the virtual testbed. Models developed using the kSVM method are able to successfully predict occupant thermal comfort accurately for the entire testing period (1 week) with less than 10% misjudgment.

5. Computationally Efficient Automatic Fault Detection and Diagnosis

Building heating, ventilating, and air conditioning (HVAC) systems seldom perform completely as designed. For example, numerous studies have provided evidence that buildings tend to consume higher energy levels in the operational phase compared to the energy predictions made during the design phase (Taal et al. 2018; de Wilde 2014). This deviation from design expectation may be caused by various factors, including improper equipment installation, equipment degradation, sensor failures, or incorrect control sequences (L. Wang et al. 2013). Therefore, it is important to keep equipment maintained and repair the failed equipment in time, or to implement fault-adaptive control to proactively respond to these malfunctions. To achieve this goal, detection and diagnosis of existing faults are required. These faults often present challenges to the conventional control of residential HVAC systems, making it difficult to meet the occupants' thermal comfort requirements. In this section, two different locations of faults in the residential HVAC system are investigated: duct leakage in Section 5.2 and vapor compression cycle (e.g., heat pump) in Section 5.3. This section also investigates two FDD approaches (data-driven and knowledge-based).

5.1 FDD Process

There has been a growing interest in AFDD technology over the last 20 years. The main concept behind AFDD is to directly check if the value of features is in the normal bound or to compare the feature values between the predictions and actual measurements, which can be used to calculate feature residuals. Residual patterns are the evidence for fault detection and diagnosis. The mapping between residual patterns and specific faults is identified by FDD design methods. Either expert knowledge inference or a data-driven approach could be used to accomplish this task. A common AFDD process is summarized as follows (Rogers, Guo, and Rasmussen 2019a):

- 1) **Feature selection:** The selection of an optimal subset of attributes increases the probability of detecting faults in a system, mitigates the incidence of spurious correlations (between feature residual patterns and identified faults) and false alarms, reduces the risk of model overfitting, and diminishes model complexity (Yan et al. 2018). This subset of selected features should be cost-effective. That means the features required for FDD methods are as few as possible and as easily measured as possible. At the same time, the FDD accuracy should be ensured to be acceptable (e.g., greater than 80%). Compared to data-driven approaches that emphasize feature selection with multiple data mining methods, rule-based approaches mostly determine features of interest manually by experts.
- 2) **Steady-state filter:** This refers to detecting the steady-state period and filtering data accordingly. Filtering out the steady state is the basis for the reference model construction and FDD classification, and is reliable only when the operation state is steady. Standard deviation and slopes in the moving window are usually applied for steady-state detection.

- 3) **Fault-free reference model (optional):** This refers to developing a fault-free model for feature comparison. In this context, a baseline refers to the state in which the building's operation is deemed satisfactory. For example, it could represent the condition immediately after the completion of a commissioning process (Zhelun Chen et al. 2023). A lot of methods can be used in fault-free model development, such as simple polynomial models or more advanced neural networks. The selection of models depends on the data availability, computation limitation, accuracy requirements, system characteristics, etc.
- 4) **FDD classification:** This refers to classifying the system operation as faulty or not, and even identifying the specific faults. Although detection and diagnosis classifiers are typically executed as distinct procedures, there are instances when they are carried out concurrently in a single step (Rogers, Guo, and Rasmussen 2019a).

5.2 Duct Leakage Fault Detection Strategy

This section provides a detailed description of the development and evaluation of a machine learning-based data-driven duct leakage fault detection strategy for typical residential buildings. Since this method utilizes data obtained from the building to determine the fault state of the building, the method is suitable for applications for all types of residential buildings. The virtual testbed, using the DOE prototype single-family detached home described in Section 3, is employed here for generating building operation data. Operation data for fault free and artificially implemented faulty scenarios are generated for training and testing of the machine learning-based model using the TensorFlow package in Python.

Detection of faults in a building mechanical system is key for advanced building control and energy efficiency. Undetected faults can result in an uncomfortable thermal environment or substantial energy losses. Accurate detection of faults can be used to support a model-based optimal control strategy.

Data-rich robust multivariate temporal (RMT) features used in conjunction with machine learning based methods are applied in data-driven fault detection models and have shown promise in detecting faults with high accuracy and reduced false positive rates, while requiring minimum expert knowledge and manual effort in identifying important features from the dataset (Tiwasakar et al. 2021). This study investigates the application of RMT variate selection used for the training of a convolutional neural network (CNN) for duct leakage fault detection. The developed strategy is applied to detect duct leakage faults for a virtual residential building, which is described in Section 3.

In the rest of this subsection, Section 5.2.1 gives a brief recap on the virtual testbed with a focus on the duct airflow network and introduces how operation data that contain duct leakage faults are generated. Following is a discussion on RMT variate selection and CNN in Section 5.2.2. A series of evaluation cases are designed to assess the performance of the strategy according to fault-free and faulty operation conditions in Section 5.2.3. The result of evaluation is discussed in Section 5.2.4.

5.2.1 Virtual Testbed

The developed duct leakage fault detection strategy is trained and tested according to data generated from the DOE prototype residential building virtual testbed as discussed in Section 3. For the generation of the duct leakage data, an airflow network was added to the virtual testbed using an EnergyPlus Airflow Network creation module (Documentation 2019). The Airflow Network was created to simulate a duct system for Living_unit1 (the only conditioned zone) of the residential prototype building. Figure 40 provides a visual representation of the duct system and the nodes created for data generation.

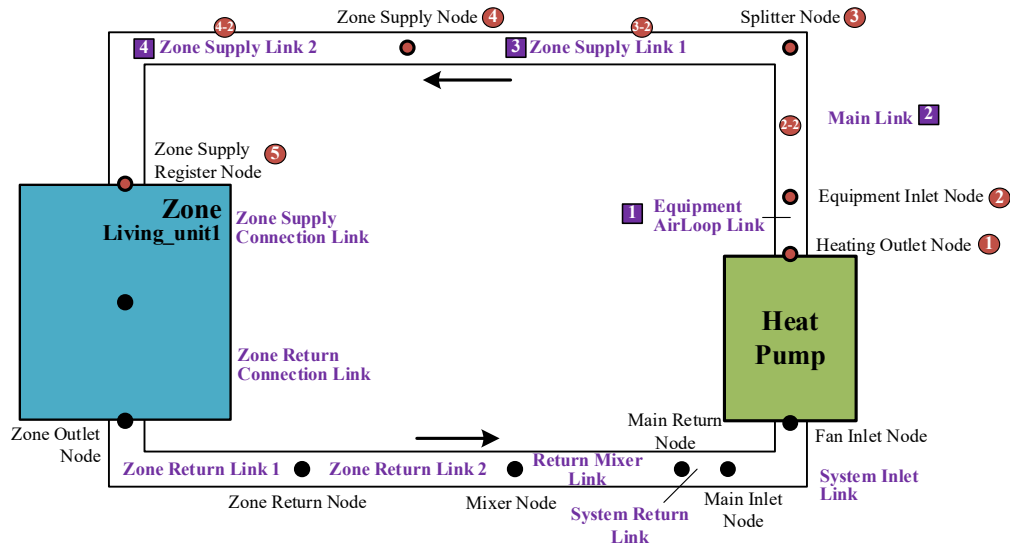


Figure 41. Airflow network diagram for the virtual testbed

Given the prototype building has only one conditioned zone, the duct system is quite simple. There are five nodes implemented to be able to generate data at selected points throughout the attic duct (between the heat pump and the zone). The nodes in the airflow network represent different states and locations of air in the model. Each node in the network can possess specific properties such as air pressure, temperature, or humidity. These nodes are interconnected by links, which represent the potential pathways for air to travel between them. Table 18 discusses the size of the ducts in the attic and the nodes at the endpoints of each duct section.

Table 18. Airflow Network Duct Sizes

Duct	Node 1	Node 2	Length (m)	Hydraulic Diameter (m)	Cross-section area (m ²)
Air supply duct	1 - Heating outlet node	2 - Zone equipment inlet node	0.1	1	0.7854
Main truck	2 - Zone equipment inlet node	3 - Splitter node	2	0.4064	0.1297
Zone supply duct	3 - Splitter node	4 - Zone Supply Node	10	0.4064	0.1297
Zone supply duct	4 - Zone Supply Node	5 - Zone supply register node	10	0.4064	0.1297

The EnergyPlus Leakage Ratio variable for the airflow network was adjusted and used to generate the fault-free data (leakage ratio = 0), as well as the faulty data (leakage ratio varied as discussed below).

5.2.2 RMT and CNN

High data dimensionality results in many problems for the training and usage of machine learning-based models. Considering that there are hundreds or thousands of sensors from a building automation system, often consisting of redundant measurements, the selection of informative and representative variates strongly affects the performance of any data-driven model. The inclusion of irrelevant or redundant variates results in greatly increased computational costs and can result in overfitting of the model or excessive noise in the data. Many models require a variate selection before model training to reduce model complexity and overfitting issues.

The necessity for variate selection is especially true when working with temporal data such as building thermal environment data. Temporal data often include many dependencies between univariate time series along different scales (S. Liu et al. 2018). The temporal relationship between these variates is often critical to determine which variates will be used as key inputs when using time series data for forecasting problems. This applied RMT variate selection is focused on identifying and extracting localized temporal features that are robust against noise and are maximally different from the overall pattern in their local neighborhoods (Tiwaskar et al. 2021). The temporal features are defined as the temporal events, for instance the onset of a rise or drop in amplitude of a variate.

Within the RMT variate selection process, the first step is to create a scale-space consisting of multiple smoothed versions of a given series to obtain what is referred to as the difference-of-Gaussian series. This step eliminates features that are not robust to noise and smoothing. Following this, the extrema features are searched across multiple scales and locations of the given time series. Once these key features are extracted, the algorithm computes the degree of temporal alignment among variates based on how often the features between two variates overlap or co-occur together. For example, highly correlated variates would have a higher feature

overlap. The variates with the highest alignment with the target variable are ranked and selected for training a predictive model.

Deep learning methods have proven effective in time series forecasting through automatic learning of temporal dependencies and handling of temporal structures like trends and seasonality (Szegedy et al. 2015). A CNN is a class of artificial neural network that apply convolution operations along with non-linear activation functions and pooling operations to identify multiscale patterns of different complexities. In contrast to commonly used recurrent models, CNNs learn to search for local patterns and do not look at the entire time series sequence, making them cheaper to train while attaining similar performance as recurrent models (Assaf et al. 2019). CNN is used in this study to be integrated with RMT for fault detection strategy modeling.

5.2.3 Development and Evaluation of Duct Leakage Fault Detection Model

The developed fault detection strategy is based on training a neural network model using historically collected data to forecast the target variate during the faulty period. RMT-based variate selection is used to determine the key input for training the model. Due to the discrepancies in system operation between the historical data and the incoming faulty data, a higher forecasting error (the difference between predicted fault-free values and measured values) during the fault window is expected, which allows for efficiently detecting faults.

In order to perform the RMT variate selection and develop a CNN model, operation data are needed for use as training data. As discussed in Section 4.2.2, the airflow network created in the virtual testbed's EnergyPlus model is used to generate both training data and also testing data to evaluate the performance of the developed RMT-CNN fault detection strategy.

In the following sections, Section 5.2.3.1 discusses the details about the generation of training and testing datasets. Section 5.2.3.2 summarizes the candidate features that the RMT variate selection method identified for each test scenario. Section 5.2.3.3 discusses the different fault scenarios used for testing the CNN. Test data are then used to evaluate the model performance for these three models. The discussion of the results of the test cases created to assess the performance of the algorithm and a discussion on overall performance are provided in Section 5.2.3.4.

5.2.3.1 Design and Generation of Training and Testing Data

This study involves several datasets, which are generated using the virtual testbed. For this study, Typical Meteorological Year weather for Houston, TX (Bush International Airport – USA_TX_Houston-Bush.Intl), is used as the weather file. Based on domain knowledge, it is understood that a residential building's attic temperature is strongly affected by weather conditions, HVAC operation, and duct leakage ratios. The testing and training data are designed to reflect the variation of these driving conditions with various datasets for different leakage ratios.

For all datasets, the virtual testbed was simulated for an entire year at a 1-hour sampling rate. The building was operated under normal conditions with the exception of the faulty scenarios.

During HVAC normal operation, the thermostat controls the indoor temperature to be between 22.22°C and 24.44°C for the summer season, following the default occupancy schedule as described in Section 3.

5.2.3.2 Candidate Features

Table 19 provides a summary of the candidate variates (i.e., potentially available sensor measurements and weather conditions) that the RMT variate selection was performed upon.

Table 19. Summary of Candidate Variates

Candidate Variates		
Site Outdoor Air Drybulb Temperature	Site Outdoor Air Relative Humidity	Site Outdoor Air Humidity Ratio
Site Wind Speed	Site Wind Direction	Site Outdoor Air Barometric Pressure
Living Zone 1 Zone Thermostat Cooling Setpoint Temperature	Living Zone 1 Zone Thermostat Heating Setpoint Temperature	Attic Zone 1 Zone Thermostat Cooling Setpoint Temperature
Attic Zone 1 Zone Thermostat Heating Setpoint Temperature	Living Zone 1 Zone Ventilation Mass Flow Rate	Living Zone 1 Zone Mean Air Humidity Ratio
Attic Zone 1 Zone Mean Air Humidity Ratio	Living Zone 1 Zone Mean Air Temperature	Living Zone 1 Zone People Occupant Count
People Zone 1 People Occupant Count	Living Zone 1 Zone Lights Electric Power	Central System Air System Electric Energy
Central System Air System Gas Energy	Supply Fan Air Mass Flow Rate	Supply Fan Electric Power
System Availability Scheduled Control Status	DHW Loop Plant System Cycle On Off Status	Mains Pressure Pump Electric Energy
IECC ADJ Electric Equipment Electric Power	Electric MELS Electric Equipment Electric Power	Electric Dryer Electric Equipment Electric Power
Clotheswasher Electric Equipment Electric Power	Refrigerator Electric Equipment Electric Power	Electric Range Electric Equipment Electric Power
Dishwasher Electric Equipment Electric Power	Living Zone 1 Zone Electric Equipment Power	

Since the duct system is located in the attic of the residential building, the primary variate that is expected to show the most significant fault impact is the mean attic temperature. The RMT variate selection and the CNN forecasting model is thus used to forecast the mean attic temperature, as described in the following sections.

5.2.3.3 Fault Scenarios

Several fault scenarios are designed and implemented as summarized in Table 20 to generate training and testing data. The scenarios cover both single and multiple leaking locations, as well as a wide range of effective leakage ratio as shown in the following table.

Table 20. Fault Scenario Descriptions

Scenario	Description	Number of Cases	Leaking Nodes	Effective Leakage Ratio
1-1	Different levels of effective leakage ratios	5	N3	10%, 20%, 30%, 40%, 50%
1-2		5	N4	10%, 20%, 30%, 40%, 50%
2	Single leaking locations	9	Fault-free, N1, N2, N2-2, N3, N3-2, N4, N4-2, N5	10%
3	Multiple leakage locations	1	N1+N2+N2-2+N3+N3-2+N4+N4-2+N5	10%

From Table 20, the names of each node can be found to correspond to the numerical identification used in this table: N1 = Heating Outlet Node, N2 = Equipment Inlet Node, N3 = Splitter Node, N4 = Zone Supply Node, and N5 = Zone Supply Register Node.

The fault-free dataset was generated using normal operation conditions. It was used for training and testing of the RMT-CNN fault detection strategy. Each scenario generated its own dataset that is then used for testing the developed RMT-CNN strategy. Following is a brief discussion of each fault scenario.

Scenario 1

Scenario 1 seeks to investigate the impact of different leakage ratios on the attic temperature. The scenario is split into two parts, one part (1-1) in which N3 - the Splitter Node is leaking, and another part (1-2) where N4 - the Zone Supply Node is leaking. For both parts, leakage ratios of 10%, 20%, 30%, 40%, and 50% are implemented.

Scenario 2

Scenario 2 seeks to investigate a fixed leakage ratio for different locations throughout the attic duct. The leakage ratio for all locations is 10%. The locations include all five nodes discussed above as well as midpoint nodes N2-2, N3-2, and N4-2 which reside between nodes N2 and N3, N3 and N4, and N4 and N5, respectively.

Scenario 3

Scenario 3 investigates one test case in which all eight nodes (including the midpoint nodes) are leaking. Each node is injected with a 10% leakage ratio and the attic temperature is measured.

5.2.3.4 Forecasting Model

A CNN model trained using top-X% ranked variates ($X = 10\%$, 15% , 20% , and 50%) is chosen as the forecasting model for the fault detection strategy. The CNN model uses 1 hidden layer with 200 computational units, with linear activation function. The model is trained for 200 epochs with batch size of 1, using “MAE” and “RMSProp” as model loss and optimizer (Tiwasakar et al. 2021). The mean attic zone temperature is selected as the target variate to investigate the duct leakage fault. A sensitivity test is carried out to determine the variate ratio cutoff.

5.2.4 Evaluation

Using data from the virtual testbed, the fault relevant variates for the attic mean zone temperature are obtained using RMT based variate selection. Table 21 shows the top 10 ranked variates selected from the fault-free dataset.

Table 21. Variate Ranking Using RMT for Fault Free Scenario

Rank	Variate Description [Units]
1	Environment: Site Outdoor Air-Dry Bulb Temperature [C]
2	Environment: Site Outdoor Air Relative Humidity [%]
3	LIVING_UNIT1: Zone Ventilation Mass Flow Rate [kg/s]
4	ELECTRIC_DRYER1: Electric Equipment Electric Power [W]
5	LIVING_UNIT1: Zone Mean Air Humidity Ratio [kgWater/kgDryAir]

To show the validity of the CNN forecasting model, the attic mean zone temperature is forecasted at a 1-hour ahead forecasting horizon. This model is trained on 256 days and validated (for hyper-parameter tuning) on a further 74 days of fault free data. The resulting model is tested on the remaining 34 days of fault-free data. To find the appropriate ratio of variates to use in training in the model, different ratios of ranked variates (top 10%, 15%, 20% and 50%) are used to train the model. It is observed that the model suffers from overfitting and decreases performance when using a greater number of variates in training. The model performs best when using the top 15% of ranked variates and hence is chosen as the cutoff percentage. Figure 42 shows cases this forecasting validity.

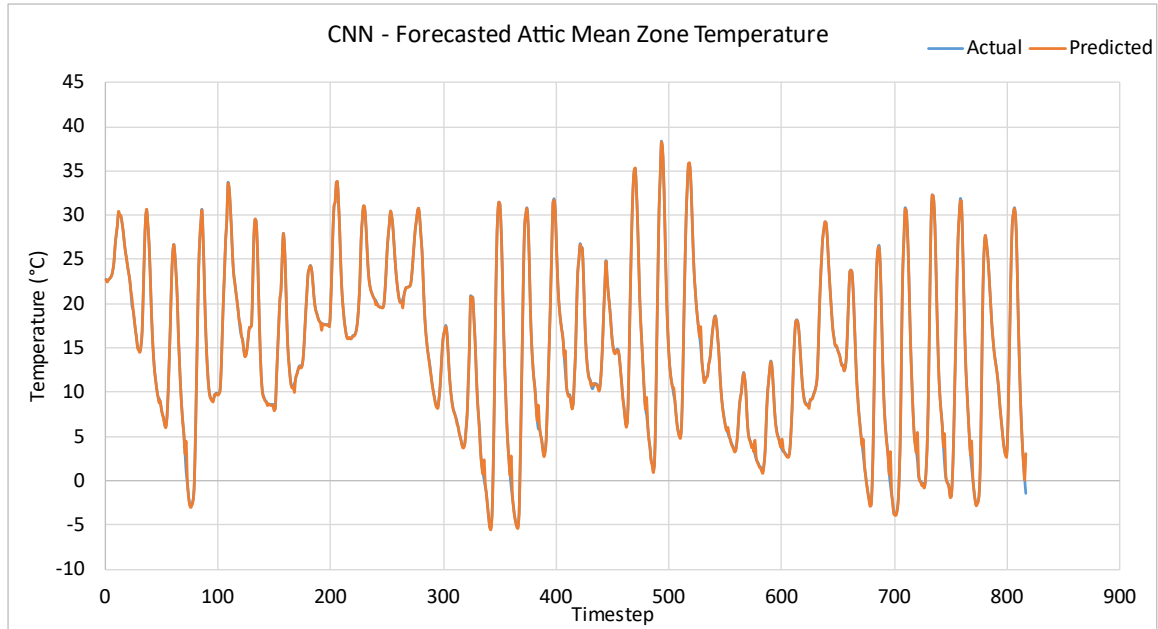


Figure 42. CNN forecasted attic mean zone temperature for fault free dataset

With the validity of the model confirmed, the trained model is then used to forecast the attic mean zone temperature during the faulty period. An artificial test set is created using two months of fault-free data and one month of faulty data, referred as M . Figure 43 illustrates the framework used to create the testing set.

For example: $M = 12$ (Dec.)

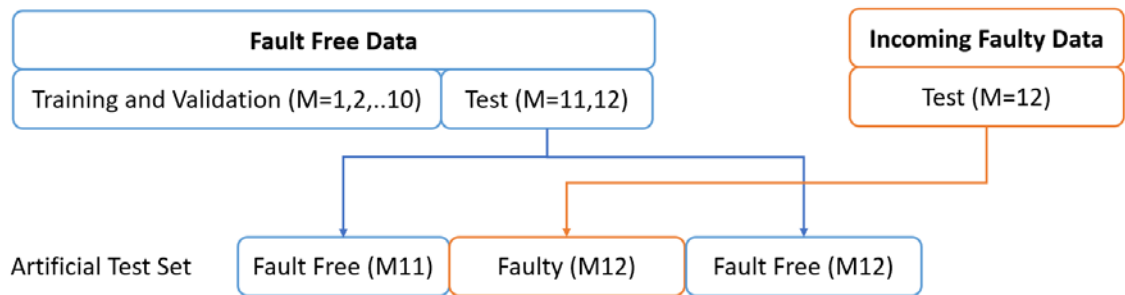


Figure 43. Framework for creating artificial test set

To evaluate the fault detection strategy, the following fault scenarios are tested: Scenario 1-1 (10%, and 50% leakage), Scenario 2 (N2-2) and Scenario 3. Faulty data from December are used for the evaluation.

Figure 44 illustrates the fault impact on the attic mean zone temperature and Figure 45 illustrates forecasting results and the absolute difference error between the actual and predicted values for Scenario 1-1 (50% leakage) fault scenarios. The complete plots are attached in Appendix D: Fault Detection and Diagnosis.

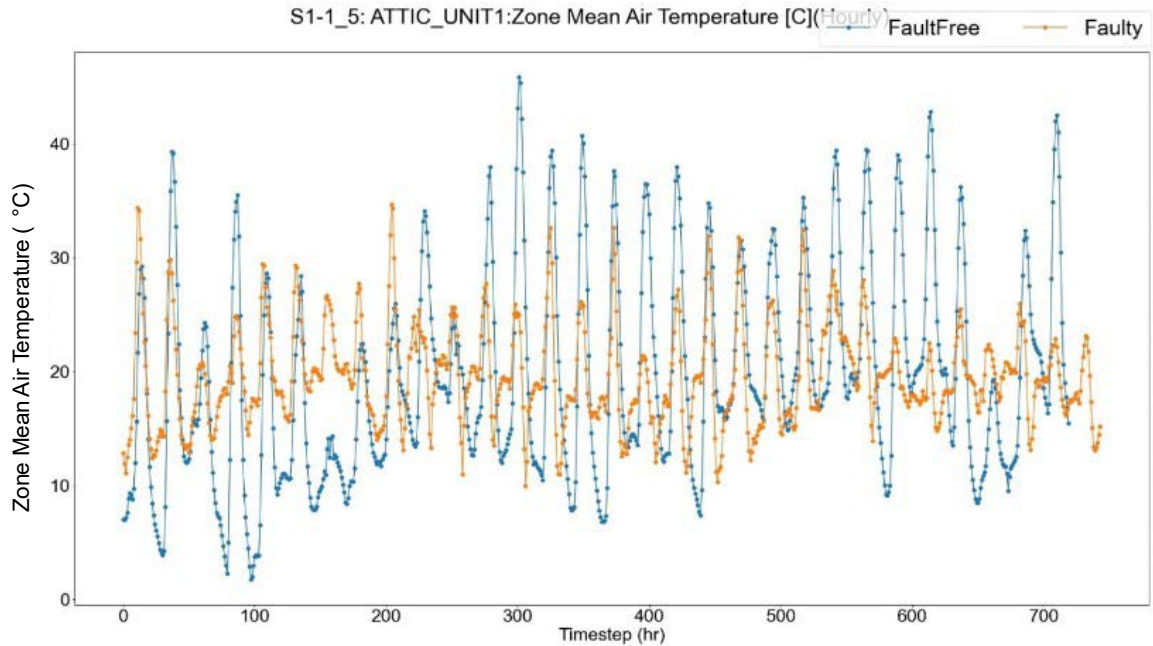


Figure 44. Fault impact on the mean attic zone temperature for Scenario 1-1 (50% leakage)

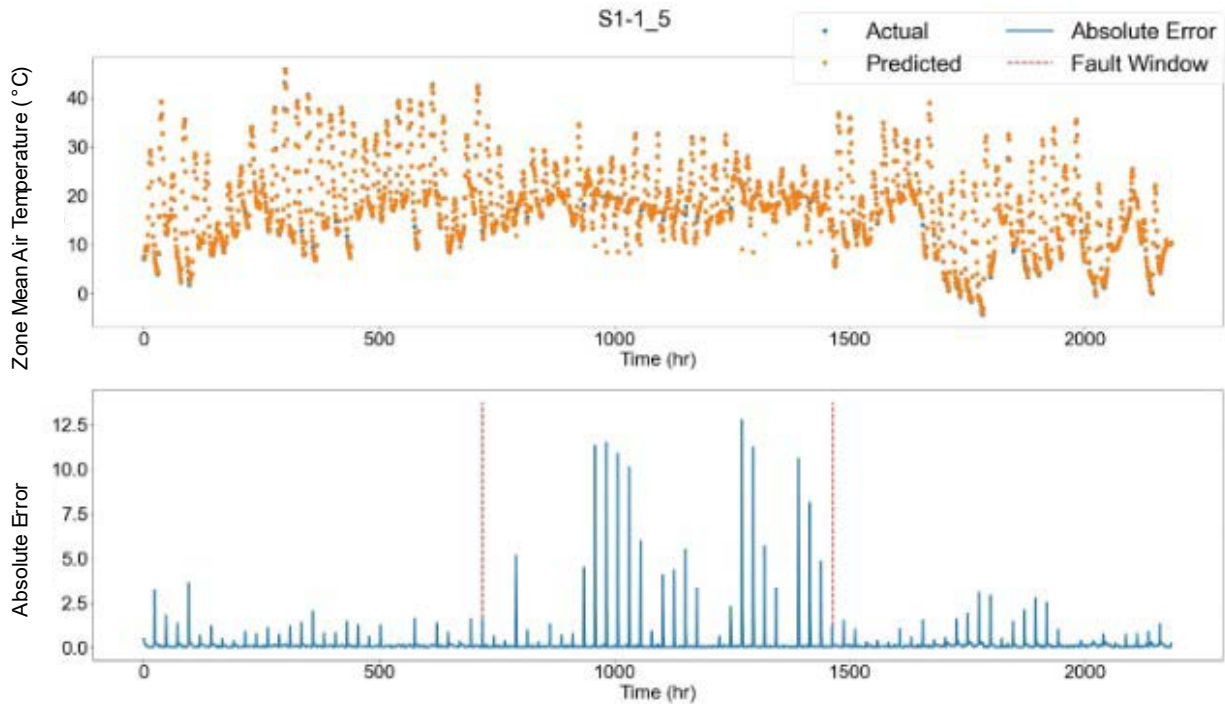


Figure 45. Forecasting results and absolute difference error for Scenario 1-1 (50% leakage)

From the plots above, it can be observed that during the fault window, the mean attic temperature is lower than the fault-free case due to the leakage in the duct. Since less heating is provided to the attic, the mean temperature is observed to be lower when the fault is present. In terms of the forecasting outputs, there is a significant increase in the forecasting error in the fault window

which can be used to flag and detect the fault in the system. Similar patterns are observed in the remaining three scenarios that are tested using this approach.

Various classifier methods can be used to flag the fault, since the CNN error patterns demonstrate significant differences between the fault free and fault periods. A classifier method, i.e., 1D SVM classifier as described in Tiwaskar et al. (2021), is evaluated first here. Results shown in Table 22 demonstrates that the classifier is able to flag the faults' starting and ending time accurately. However, there are cases where fault free periods were considered as a fault continuation period by the classifier.

Table 22. Fault Classifier Results for Scenario 1-1 (50% leakage) Over a 3-Day Period

Actual		Predicted			
		No Fault	Fault Start	Fault Continuation	Fault End
No Fault		14	0	53	0
Fault Start		0	3	0	0
Fault Continuation		18	0	99	0
Fault End		0	0	0	3

5.2.5 Discussion of Overall Performance

The evaluation of the developed fault detection strategy on the limited testing on the artificially simulated faults showed that:

- 1) The baseline model trained using fault-free data can be used to detect faults in the system by observing the increase in forecasting error within the fault window. A larger error is usually seen during the period when the target variate is impacted by the fault.
- 2) For the developed duct leakage model, the mean attic zone temperature serves as a good indicator of fault impact in the system and is thus used as the target variate in the CNN model. Alternatively, when using the temperature at the leakage nodes in the duct system as target variates, the CNN model does not identify the fault impact at each of the leakage nodes. This limited the effectiveness of the fault detection strategy.
- 3) The sensitivity test on the variate cutoff threshold showed that the baseline model trained using the top 15% of ranked variates has the best model performance. Increasing the number of variates used in training led to overall increase in forecasting error since the model suffers from overfitting.

5.3 Vapor Compression Cycle System

The main purpose of the FDD task for residential air-source VCC systems in this project is to investigate existing rule-based methods and perform a comparative analysis using open-source

lab data and figure out one FDD approach for VCC systems that can achieve more than 80% detection accuracy and less than 10% fault alarm.

Table 23 collects the literature review of existing FDD studies related to the air-source VCC systems in terms of features, reference models, faults detected, and specific FDD methods. The criterion for the selection and evaluation of FDD methods largely relies on the system characteristics and available sensor data.

This project focuses on three typical rule-based AFDD methods—statistical rule-based charts, the sensitivity ratio method, and the simple rule-based method. The rest of this FDD research for the VCC system is organized as follows. Common VCC faults and features are described first in Section 5.3.1, followed by a comparative summary of existing rule-based AFDD methods for VCC systems and the typical FDD procedure described in Section 5.3.2 (i.e., steady state filter, fault-free reference model, and FDD classification). Furthermore, these AFDD methods are evaluated and analyzed with open-source lab test data from the National Institute of Standards and Technology (NIST) in Section 5.3.3 and a hybrid FDD approach is developed for VCC systems. The field test for this developed hybrid approach is presented in Section 7.

5.3.1 Common Faults and Features for the VCC System

5.3.1.1 Comment Faults Found in Studies

A fault is “a departure from an acceptable range of an observed variable or a calculated parameter associated with a process” (Shi and O’Brien 2019). It can lead to failures and malfunctions of systems (Shi and O’Brien 2019). In residential buildings, design and installation faults lead to degradation and reduction of system performance which in turn negatively impact thermal comfort and energy usage in buildings. These faults can be identified as improper HVAC sizing, incorrect duct sizing, duct leakage, incorrect refrigerant charge, incorrect airflow rate, etc. (Ejenakevwe and Song 2021). According to regional field studies conducted by utilities and anecdotal reports from industry experts, incorrect refrigerant charge levels and incorrect airflow rates are the most significant and the most researched (Winkler et al. 2020; Ejenakevwe and Song 2021; DOE 2018). This project will only focus on the faults that occur in the VCC components.

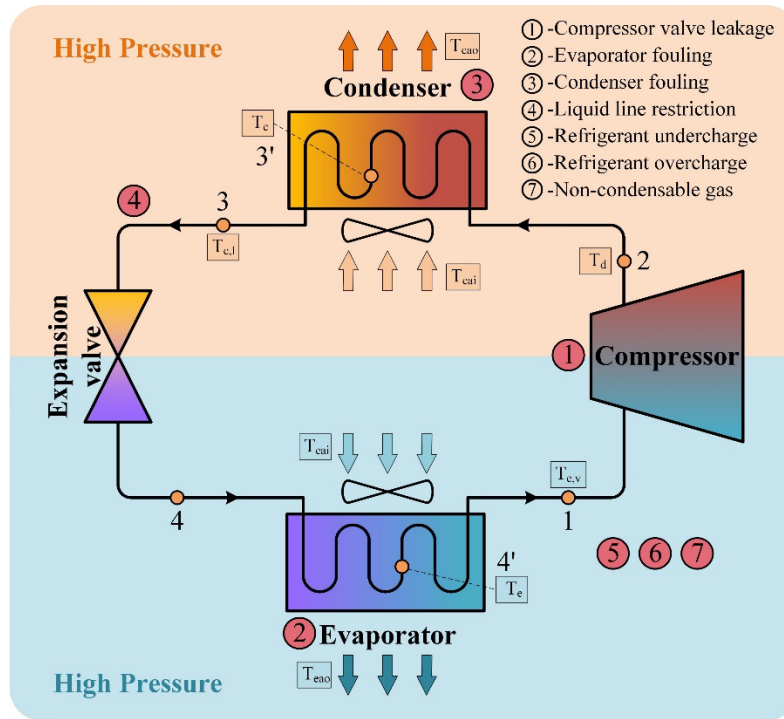


Figure 46. Schematic diagram of VCC and monitored variables

Seven typically studied faults for VCC systems are listed in Table 23. Among them, four faults (i.e., compressor valve leakage, evaporator fouling, condenser fouling, liquid line restriction) are component-specific, while the other three faults exist in the whole system. The existence of the latter ones usually influences the identification of the former ones, as their effects run through the system. From the perspective of the heat transfer medium, two faults (i.e., evaporator fouling and condenser fouling) are at the air side, while the remaining belong to the refrigerant side. The locations of these faults of the analyzed vapor compression cycle are depicted in Figure 46 with corresponding label numbers. T-s diagrams in different fault conditions are illustrated in Appendix D.3.

Table 23. Commonly Studied Faults in VCC Systems

No.	Fault name	Abbreviation	Classification	Medium
1	Compressor valve leakage	CV	Component level	Refrigerant side
2	Evaporator fouling	EF	Component level	Air side
3	Condenser fouling	CF	Component level	Air side
4	Liquid line restriction	LL	Component level	Refrigerant side
5	Refrigerant undercharge	UC	System level	Refrigerant side
6	Refrigerant overcharge	OC	System level	Refrigerant side
7	Presence of non-condensable gas	NG	System level	Refrigerant side

5.3.1.2 *Typical FDD Features Used for VCC Systems*

Features are the variables that represent the operating characteristics of the given VCC system and can be analyzed for fault detection and diagnosis. Some features can be measured directly (e.g., evaporating temperature), while others need to be calculated indirectly (e.g., suction line superheat equals the difference of evaporator exit refrigerant temperature and evaporator two-phase refrigerant temperature, $T_{sh}=T_{ev}-T_e$). In some cases, feature values are utilized directly with some predefined “normal” range, while in other cases, the residual (the difference between predicted values and measured values) of features is essential for applying the diagnosis algorithm. Fault identification sometimes relies on single features or a set of features that are sensitive to one given fault. The selection of sensors and features for analysis is a crucial step in the development of FDD systems. To minimize instrumentation costs, it is recommended to choose a minimum number of direct measurements for domestic vapor compressor systems (Bellanco et al. 2021).

The category of features for the VCC system consists of temperature, pressure, flow rate, mass, etc. Not all features are easily obtained in ordinary residential homes. For example, the total refrigerant mass is a significant feature in diagnosing the status of refrigerant with overcharge or undercharge, but considerable efforts are required to measure refrigerant charge (Rogers, Guo, and Rasmussen 2019a). Thus, it is not practical in common residential buildings. From the perspective of real-life applications, this project only considers the temperature as the feature to be studied.

Table 24 lists commonly used temperature features in the VCC FDD and the sensing parameters corresponding to these features (Rossi and Braun 1997; Breuker and Braun 1998b; M. Kim et al. 2008; Heo et al. 2015; Payne 2020). The locations of the measurement for temperatures are illustrated in Figure 46. These seven “pillars” support the operating characteristics of one VCC system and are able to serve as hints collectively to diagnose multiple faults of VCC systems in different conditions. Correspondingly, ten temperatures in total are usually required in measurement for AFDD of the VCC system. In Table 24, fault-dependent variables represent the measured features that are affected by existing faults, while fault-independent variables, which are not influenced by faults in the steady state, are monitored for being used in the fault-free reference model to generate predicted values of those fault-dependent variables. In the diagnosis stage, fault-independent variables are also fed into these fault-free reference models to estimate an expected value of fault-dependent variables with an assumption of no fault.

Table 24. Parameters/Sensors and Features Used in VCC FDD

	No.	Parameters/Sensors	No.	Features
Fault-dependent	1	Evaporator two-phase refrigerant temperature (T_e)	1	Evaporating temperature (T_e)
	2	Evaporator exit refrigerant vapor temperature (T_{ev})	2	Suction line superheat ($T_{sh}=T_{ev}-T_e$)
	3	Compressor discharge refrigerant temperature (T_d)	3	Compressor outlet temperature (T_d)
	4	Condenser refrigerant saturation temperature (T_c)	4	Condensing temperature (T_c)
	5	Condenser refrigerant liquid temperature (T_{cl})	5	Liquid line subcooling ($T_{sc}=T_c-T_{cl}$)
	6	Evaporator inlet air temperature (T_{eai})*	6	Evaporator air temperature change ($dT_{ea}=T_{eai}-T_{eao}$)
	7	Evaporator outlet air temperature (T_{eao})		
	8	Condenser inlet air temperature (T_{cai})*	7	Condenser air temperature change ($dT_{ca}=T_{cao}-T_{cai}$)
	9	Condenser outlet air temperature (T_{cao})		
Fault-independent	10	Outdoor dry-bulb temperature (T_{od})*	8	Outdoor dry-bulb temperature (T_{od})
	11	Indoor dry-bulb temperature (T_{id})*	9	Indoor dry-bulb temperature (T_{id})
	12	Indoor dew point temperature (T_{idp})	10	Indoor dew point temperature (T_{idp})

*No.6 temperature = No.11 temperature, and No.8 temperature = No.10 temperature

5.3.2 Comparison of Three Existing Rule-Based FDD Classification Methods

Three existing AFDD methods for the residential VCC system are investigated: statistical rule-based chart, sensitivity ratio method, and simple rule-based method. They are described in detail in Appendix D: Fault Detection and Diagnosis.

A comparison of different commonly used rule-based AFDD classification methods for VCC systems is listed in Table 25. It includes features required, fault-free reference model, potential faults diagnosed, pros and cons of each method, and performance regarding diagnosis accuracy rate.

Table 25. Comparison of Three Existing Rule-Based FDD Methods for the VCC System

FDD Methods	Features Required	Fault-Free Reference Model	Faults Diagnosed	Pros and Cons	Performance Regarding Accuracy Rate*
Statistical Rule-Based Chart (Payne 2020; M. Kim et al. 2008; Braun 2003; Rossi 1995; Breuker and Braun 1998b)	$T_e, T_{sh}, T_d, T_c, T_{sc}, dT_{ea}, dT_{ca}$	Yes	NF, UC, OC, LL, CV, CF, EF	<p>Pros:</p> <p>Measurement uncertainties are considered using probabilities</p> <p>Imperfect model and quasi steady state are considered</p> <p>Cons:</p> <p>Amplifier factors (k and s) and threshold determination</p> <p>Inability to diagnose non-condensable gas</p>	EF (63.11%), LL (100%), UC (66.53%), NF (95.47%),
Sensitivity Ratio Method (B. Chen and Braun 2000)	T_e, T_{cl}, T_c, T_{sc}	Yes	NF, UC, OC, LL, CV, CF, EF, NG	<p>Pros:</p> <p>Least number of required sensors</p> <p>No need to have absolute thresholds</p> <p>Cons:</p> <p>Diagnosis accuracy is relatively lower</p>	EF (100%)
Simple Rule-Based Method (B. Chen and Braun 2000)	$T_e, T_{eai}, T_c, T_{cai}, T_{cl}, T_{sc}$	No	NF, UC, OC, LL, CV, CF, EF, NG	<p>Pros:</p> <p>A fault-free reference model is not required</p> <p>Cons:</p> <p>Uncertainty quantification is not considered</p> <p>Threshold determination could be a challenge</p>	EF (91.23%), OC (100.00%), UC (100.00%), NF (69.14%)

* based on NIST VCC lab test data

Note that NF = no fault, UC = refrigerant undercharge, OC = refrigerant overcharge, LL = liquid-line restriction, CF = condenser fouling, EF = evaporator fouling, and NG= Non-condensable gas

The statistical rule-based chart requires more measurements and reference models. It needs three dependent variables (outdoor dry-bulb temperature T_{od} , indoor dry-bulb temperature T_{id} , and indoor dew-point temperature T_{idp}). Therefore, it could be regarded as a combination of data-

driven and knowledge-based, as it needs to train a fault-free reference model with, for example, multivariate polynomial regression (MPR). Classification is conducted on a qualitative approach. On the contrary, the simple rule-based method does not need reference models. It just gives a range for the fault-free condition for each feature.

5.3.3 Evaluation of FDD Methods With Open-Source Experiment Testing Dataset

The following two sections present the comparative analysis of selected rule-based FDD methods for air-source VCC systems. An open-source dataset is used first to test the capability of those three selected FDD methods (i.e., statistical rule-based chart, sensitivity ratio method, and simple rule-based method) with the evaluation metrics of false alarm, missed detection, misdiagnosis, and accuracy, from which the advice for integrated application is derived. Then, an additional dataset collection from lab home field testing is described.

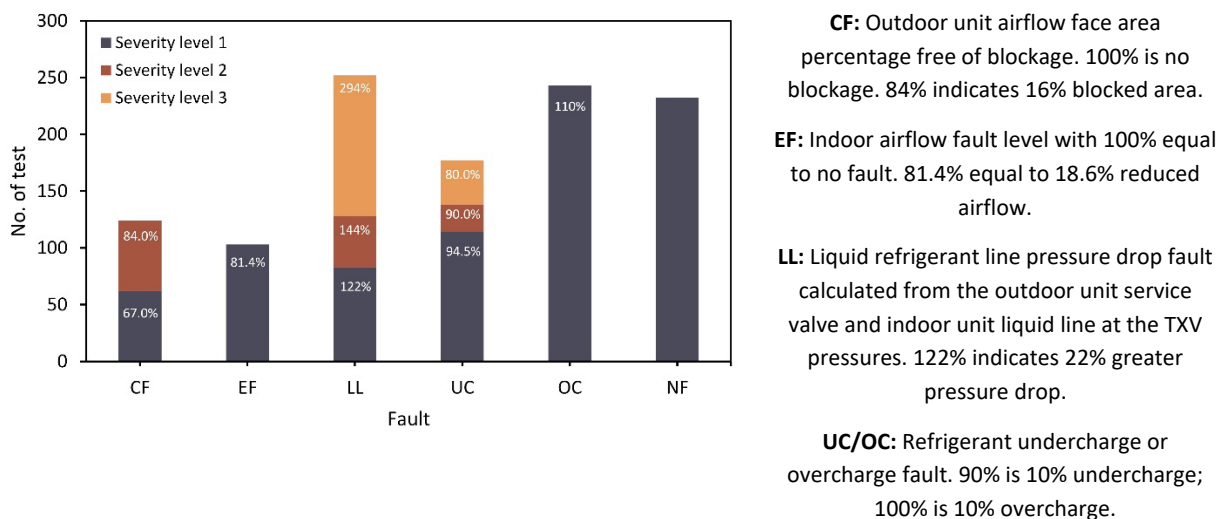


Figure 47. Numbers and severity levels of fault cases from NIST datasets (percentages on the bars indicate severity levels)

5.3.3.1 Open-Source Dataset

The open-source lab test dataset used in this project was obtained by NIST in 2006 (M. Kim et al. 2009; M. Kim et al. 2006). They studied the performance of a unitary split heat pump with a long line set length and a thermostatic expansion valve for residential applications. R410A was circulated as the refrigerant. The nominal power rating was 8.8 kW (11.80 hp).

As plotted in Figure 47, there are five types of faults and one fault-free condition. The faults include condenser fouling, evaporator fouling, liquid line restriction, refrigerant overcharge, and refrigerant undercharge. The compressor/four-way valve leakage fault is not included in this dataset.

5.3.3.2 Steady State Filter and Fault-Free Reference Model

This open-source dataset provided by NIST is all in a steady state, so steady-state filter processing is not required.

The fault-free reference model is essential for the statistical rule-based chart and sensitivity ratio method because they require actual values of selected features to estimate the residuals. Considering the target is temperature, R^2 , rather than $cv(RMSE)$, is used to evaluate the accuracy of developed models. The models exhibit a high degree of accuracy for most of the features, largely due to testing conditions that are easily controlled and fewer uncertainties in the experimental setup, except the subcooling temperature and superheating temperature where the accuracy may be compromised (see Figure 48). However, subcooling and superheating are calculated by T_c/T_{cl} and T_e/T_{ev} , respectively (all four temperature models have a high accuracy), so these two features are indirectly calculated in the FDD classification steps.

After comparing polynomial models with neural networks, NIST researchers (M. Kim et al. 2008) recommended the former as the method for the VCC FDD fault-free reference model because it can provide a reasonable fit uncertainty and obtain a higher accuracy than the artificial neural network model. For the multivariable polynomial regression of the fault-free reference model, outdoor dry-bulb temperature (T_{od}), indoor dry-bulb temperature (T_{id}), and indoor dew point temperature (T_{idp}) are typically selected as the independent variables to predict the features. In addition, as illustrated in Figure 48, the third order does not have a significant benefit over the second order by comparing the performance of different orders of multivariable polynomial regression models. Therefore, the second order multivariable polynomial regression is sufficient when the fault-free values of selected features are estimated when calculating residual values. Table 26 gives an example of evaluation metrics for the model regression of discharge temperature T_d . $cv(RMSE)$ is calculated for the FDD classification steps. Figure 49 plots an example of the comparison of actual temperature and estimated temperature from three orders of multivariable polynomial regression models. It can be seen that these two curves are very close. Other plots are attached in Appendix D: Fault Detection and Diagnosis.

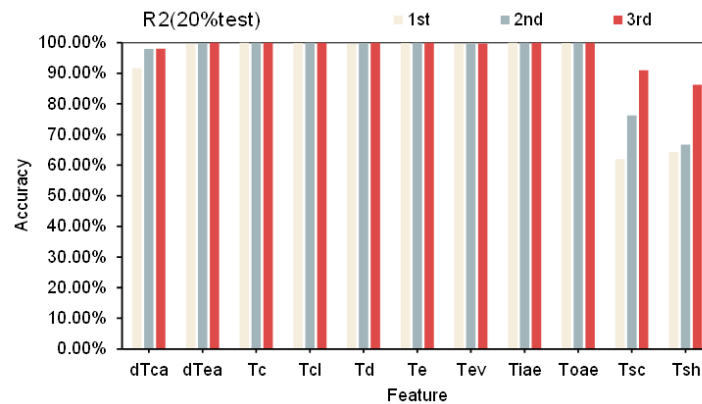


Figure 48. Accuracy performance of different-order multivariable polynomial regression models for all features

Table 26. Statistics Results of Measured and Predicted Temperatures, Taking Discharge Temperature as an Example

Feature	Degree	MSE	CV(RMSE)	R2(20%t)	R2(cv=5)
Td	1st	0.636	0.56%	99.5%	99.0%
	2nd	0.294	0.38%	99.7%	99.3%
	3rd	0.161	0.28%	99.8%	96.6%

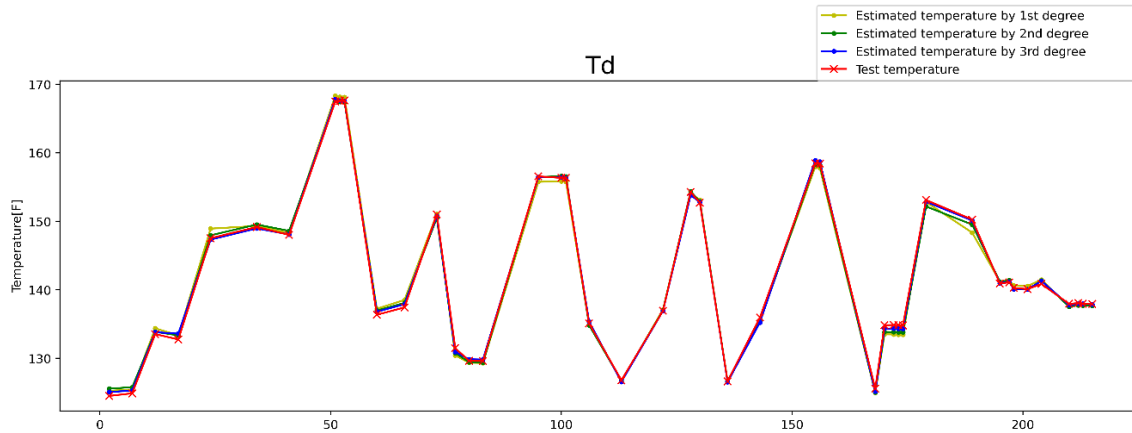


Figure 49. Comparison of measured and predicted temperatures, taking discharge temperature as an example

5.3.3.3 Comparative Analysis

Figure 50 shows a comparative analysis of three FDD methods (i.e., statistical rule-based chart, sensitivity ratio method, simple rule-based method) in terms of false alarm, missed detection, misdiagnosis, and accuracy. The statistical rule-based chart considers probabilities in three uncertainty sources and is sensitive to its threshold standard deviation multiplier s and confidence interval of uncertainties k . The adjustment of these two coefficients, usually conducted by expert with professional experience, influence FDD sensitivity and false alarm in a reverse way. The statistical rule-based chart considers probabilities in three uncertainty sources and is sensitive to its threshold standard deviation multiplier s and confidence interval of uncertainties k . The adjustment of these two coefficients, usually conducted by experts with professional experience, influences FDD sensitivity and false alarm in a reversed way. Therefore, to observe the difference of the statistical rule-based chart with/without adjusting balance amplifier k and s , an additional case called the statistical rule-based chart with adjusted k and s is also included in the comparison (the details for amplifier adjustment are included in Appendix D: Fault Detection and Diagnosis).

False alarm. Figure 50(A) shows the false alarm results of four FDD cases (i.e., statistical rule-based chart, statistical rule-based chart with adjusted k and s , sensitivity ratio method, simple rule-based method). The lower the rate is, the better the FDD approach performs. The statistical

rule-based chart method performs the best with a false alarm rate of 0%. On the other hand, it is relatively easy for the sensitive ratio method to trigger a false alarm of 100%.

Missed detection. Figure 50(B) illustrates the missed detection rate of four FDD approaches for different faults with various severity levels. Lower missed detection indicates better performance of the FDD approach. The statistical rule-based chart method with default k and s values has the highest probability of missing detection, especially for the evaporator fouling and liquid line restriction cases. The sensitivity ratio method performs the best regarding the missed detection rate, as it is most sensitive to the threshold. As a consequence of this, the likelihood of false alarms being reported by the sensitivity ratio method is also increased. On the other hand, if the false alarm of the sensitivity ratio method is mitigated by adjusting the threshold, the missed detection rate will go up. This implies that a high false alarm rate and a low missed detection rate are mutually exclusive. It is important to determine the threshold to balance these two metrics. For practical implementation, ensuring a lower false alarm rate should be prioritized.

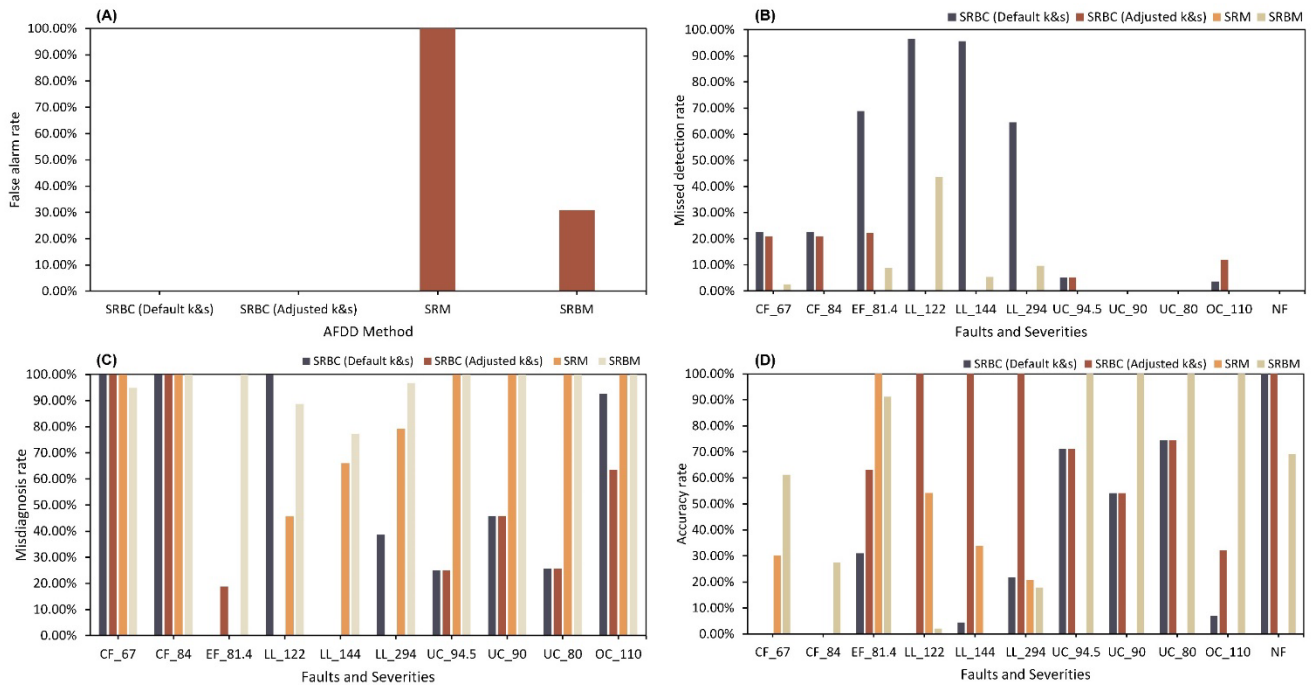


Figure 50. Results of evaluation metrics (i.e., false alarm, missed detection, misdiagnosis, and accuracy) for four AFDD methods (i.e., SRBC, SRBC with adjusted k and s , SRM, SRBM)

SRBC = statistical rule-based chart; SRM = sensitivity ratio method; SRBM = simple rule-based method

Misdiagnosis. Figure 50(C) shows the misdiagnosis rate results of four FDD approaches. A lower rate indicates better performance of the FDD approach. As the diagnosis results of the simple rule-based method are mutually inclusive (i.e., multiple diagnosed faults might be reported), two metric modes are applied. In the simple rule-based method, the misdiagnosis rate is defined as the ratio of the inaccurately diagnosed target faults (i.e., all outcomes in which a

diagnosis identifies anything other than the target fault) and to the total number of appropriate detections. It is obvious that if we only check whether the method diagnoses the target fault, the misdiagnosis rate is much lower compared with the case only considering the exact identification as diagnosis success. In addition, for the statistical rule-based chart with default amplifier k and s values, the misdiagnosis rates are high for the case of condenser fouling, liquid line restriction and overcharge, while it has a lower misdiagnosis rate for evaporator fouling and overcharge cases. The performance of the sensitivity ratio method is satisfactory only when applied to the evaporator case. Figure 51 illustrates the distribution of misdiagnosed results for each fault scenario. In contrast to other methods, the simple rule-based method exhibits the accumulated percentages for each fault scenario, exceeding 100% in certain instances. This results from the fact that the simple rule-based method checks if one fault exists one by one independently, not mutually exclusive. This feature makes it potentially applicable in circumstances where multiple faults occur simultaneously.

Accuracy. Figure 50(D) shows the accuracy of four FDD approaches. The higher the rate, the better the FDD approach performs. The accuracy rate is the key metric for the FDD evaluation, and a rate greater than 80% could be considered satisfactory (Yuill 2014). The sensitivity ratio method performs well only in evaporator fouling cases, while the statistical rule-based chart with default k and s values only do well in no-fault cases. The statistical rule-based chart with adjusted k and s values performs well for liquid line restriction and no-fault cases, while the results are still acceptable for undercharge and evaporator cases. The simple rule-based method performs the best by achieving over 90% accuracy rate for three cases—evaporator fouling, undercharge, and overcharge. For the no fault and condenser fouling with less severity, the simple rule-based method also performs reasonably well.

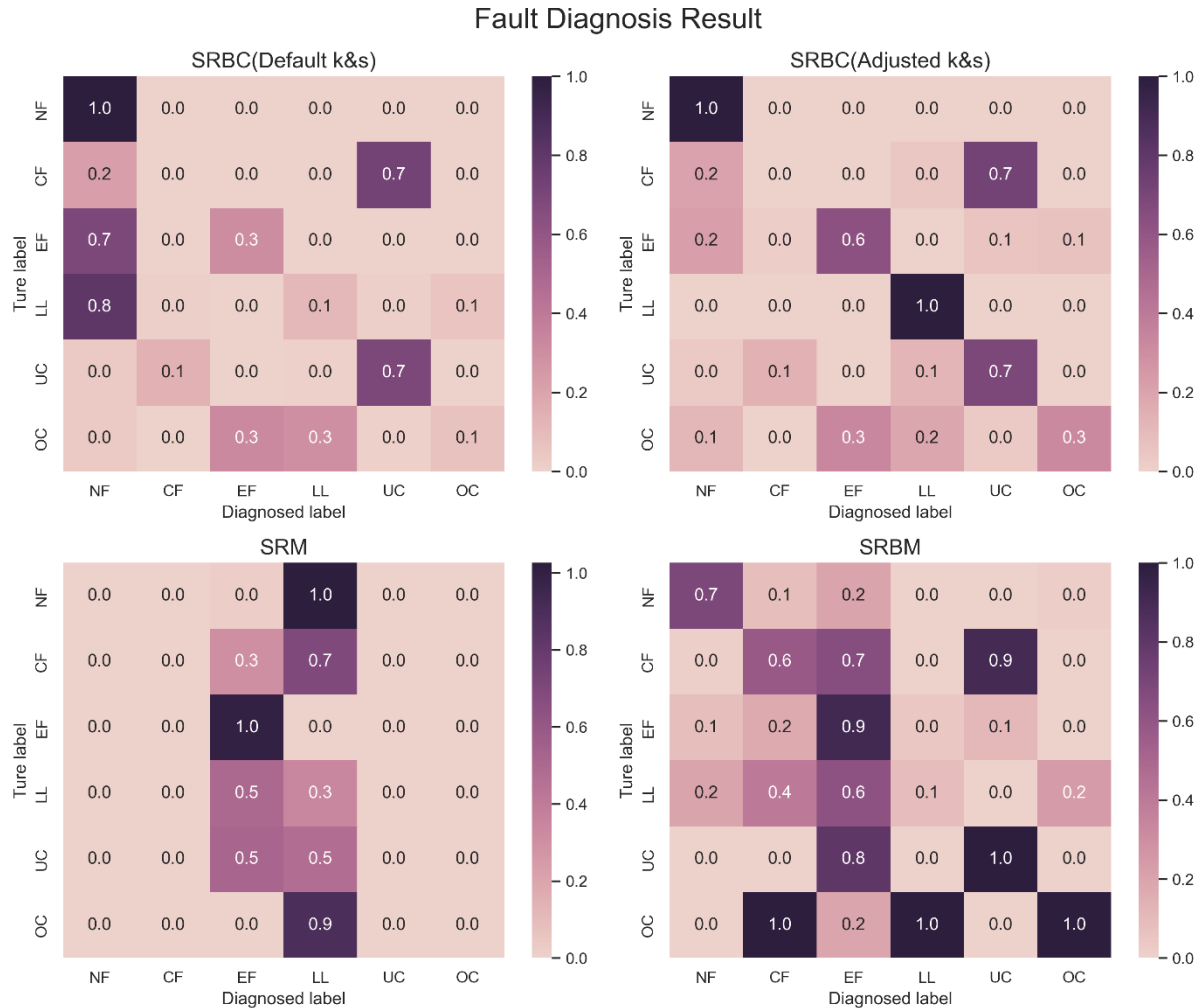


Figure 51. Misdiagnosis distribution among four FDD approaches (i.e., SRBC, SRBC with adjusted k and s , SRM, SRBM)

SRBC = statistical rule-based chart; SRM = sensitivity ratio method; SRBM = simple rule-based method

Figure 50 and Figure 51 demonstrate that no single method could achieve a consistent detection accuracy for different types of faults. For example, the statistical rule-based chart with adjusted k and s values mostly obtained an acceptable accuracy rate (e.g., >80%) for the fault-free case and charge faults, but the results are worse for the fouling faults. Therefore, it is challenging to use individual FDD methods to achieve an acceptable accuracy rate. A hybrid FDD method must be developed and applied.

Table 25 lists the comparison of required features, diagnosed faults, and fault-free reference models of these three existing VCC AFDD methods (i.e., statistical rule-based chart with adjusted k and s , sensitivity ratio method, simple rule-based method) using the NIST raw data. A hybrid approach, which uses both the statistical rule-based chart method and simple rule-based method, could be recommended for better performance.

5.3.3.4 Hybrid FDD Approach for VCC Systems

A suggested FDD flowchart for VCC systems that integrates the statistical rule-based chart and the simple rule-based method is illustrated in Figure 52. This hybrid FDD approach places greater emphasis on the diagnosed results obtained from methods with higher accuracy in diagnosing specific faults. It puts more weight of no fault and liquid line restriction on the statistical rule-based chart, and condenser fouling, evaporator fouling, undercharge, and overcharge on the simple rule-based method.

This hybrid FDD approach places greater emphasis on the diagnosed results obtained from methods with high accuracy in diagnosing specific faults.

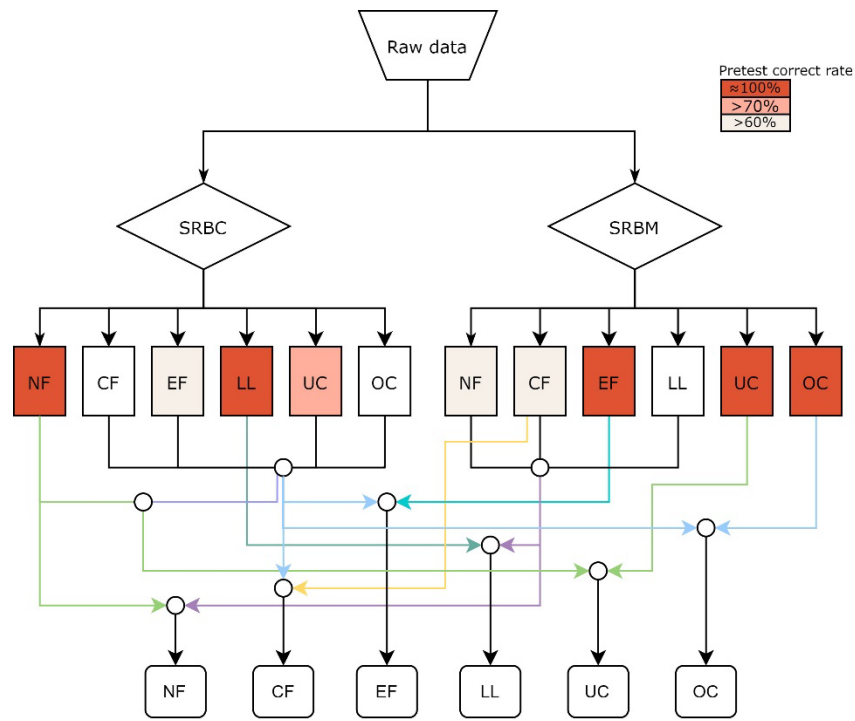


Figure 52. Hybrid FDD flowchart for VCC systems

NF = no fault, CF = condenser fouling, EF = evaporator fouling, LL = liquid line restriction, UC = undercharge, and OC = overcharge

A refrigerant fault in the VCC system can have a widespread impact, potentially affecting the entire system. As a result, it is more likely to be recognized as an air-side fault. This scenario is not anticipated if only a single fault is present. In contrast, an air-side fault specifically affects the air side components, such as the evaporator and condenser. Therefore, for the single fault scenario, additional rules are introduced:

- If a refrigerant fault is diagnosed, air side fault diagnosis is skipped.
- If the refrigerant fault is not filtered, the result for the airside fault is then displayed.

A hybrid approach—which uses both the statistical rule-based chart method developed by NIST and simple rule-based method, which originated from Purdue University—is adopted for this

project. The test results are provided in Table 27. The overall AFDD accuracy is 95.46% for this NIST dataset, and the false alarm rate is 4.53%, which exceeds the project requirement (i.e., the AFDD detection accuracy is demonstrated to be higher than 80% with a false alarm rate that is less than 15%).

Table 27. FDD Results of the Developed Hybrid Approach

Fault Name	No. of Cases	No. of Correctness	Accuracy rate
No fault (NF)	243	232	95.47%
Condenser fouling (CF)	153	114	74.51%
Evaporator fouling (EF)	198	198	100.00%
Liquid line restriction (LL)	285	274	96.14%
Refrigerant undercharge (UC)	210	210	100.00%
Refrigerant overcharge (OC)	254	254	100.00%
	Diagnosis accuracy		95.46%
	False alarm rate (False positive)		4.53%

5.4 Summary

In Section 5.2, we introduced our developed method of fault detection using a CNN forecasting model trained on fault-free normal operation data.

An RMT-based variate selection was implemented to identify the fault relevant variates to be used in the forecasting model. This method ranks variates based on the co-occurrence of key temporal features/events to select variates that have high impact on forecasting of a target variable. Localized multivariate temporal features, which are robust against noise, were extracted by considering multiple scales, temporal characteristics of the time series and external domain knowledge such as feature-to-feature relationships from a multivariate time series. Using data from the virtual testbed, the fault relevant variates for the target variate were ranked using RMT based variate selection. Sensitivity tests show that the model performs best when using the attic zone temperature and the top 15% of ranked variates.

Following this, a CNN-based model was trained on a fault-free set and used to forecast the target variate during the faulty period. A data selection framework to create artificial test data based on user input was also developed to evaluate the strategy. The evaluation results show that the developed strategy is able to successfully identify the fault impact when using the attic mean zone temperature as the target variate. This demonstrates the solidity of the attic mean zone temperature serving for the duct leakage detection. At the beginning and end period of duct leakages, the fault can be flagged accurately at 100%.

Section 5.3.2 investigates three existing AFDD methods for the residential VCC system: statistical rule-based chart, sensitivity ratio method, and simple rule-based method.

A qualitative comparison is conducted first in terms of features required, fault-free reference model, potential faults diagnosed, pros and cons of each method, and performance regarding diagnosis accuracy rate. The statistical rule-based chart is well-developed because it considers probabilities in three uncertainty sources (measurement noise uncertainty, steady-state uncertainty, and fault-free model uncertainty). However, it is sensitive to its threshold standard deviation multiplier s and the confidence interval of uncertainties k . Thus, adjustment for specific cases is difficult to ensure acceptable accuracy. The simple rule-based method can obtain a high FDD accuracy, though with a simplified normal threshold for each feature. These normal thresholds are sensitive to specific fault types.

A quantitative comparison analysis is accomplished with the NIST experiment data regarding four metrics—accuracy, false alarm, misdiagnosis, and missed detection. With respect to diagnosis accuracy, the statistical rule-based chart performs better for no fault and liquid line restriction cases, while the simple rule-based method performs better for condenser fouling, refrigerant undercharge, and refrigerant overcharge cases. The sensitivity ratio method does not outperform in any case. No single method could achieve consistent detection accuracy for different types of faults. This highlights that it is challenging to use individual FDD methods to achieve acceptable accuracy. Therefore, a hybrid FDD approach is recommended according to the accuracy rates for different faults. This places a greater emphasis on the diagnosed results obtained from methods with higher accuracy in diagnosing specific faults.

A hybrid FDD approach that integrates statistical rule-based chart and simple rule-based method was developed and tested with an additional field test dataset. Overall, the diagnosis accuracy is 83.02% if only counting fault cases, and 90.18% when counting all cases, including fault-free ones. A two-class confusion matrix for detection shows all metrics are all higher than 90%, with a detection accuracy of 96.4%.

As for the fault-free reference model for VCC refrigerant side and air side temperatures, second multivariable polynomial regression models are sufficient to obtain a good accuracy with T_{id} , T_{idp} , and T_{od} . Higher-order multivariable polynomial regression models do not yield significant additional benefits.

6. Model-Based Adaptive Control Framework With Extracted Rules

One of this project's objectives is to generate a set of rules by extracting information from MPC results. These rules, called MPC-informed rules, are intended for a precooling control strategy that utilizes only the thermal mass of residential buildings to deal with extreme weather conditions when HVAC capacity is limited under faults. The rest of this section is organized as follows. First, in Section 6.1, the MPC framework is developed, followed by the rule extraction description. The prototype residential building (described in Section 3.1) is used to generate MPC-informed rules in Section 6.2, with benefits of this process quantified.

6.1 MPC Framework Methodology

The methodology section describes the workflow of MPC for precooling and MPC-informed rule extraction methods, following a brief of related models and evaluation methods. A high-level overview of the whole process includes three steps total (Piscitelli et al. 2019):

- 1) Obtaining optimal control schedules
- 2) Extracting rules from the optimal control schedule
- 3) Testing the extracted rules

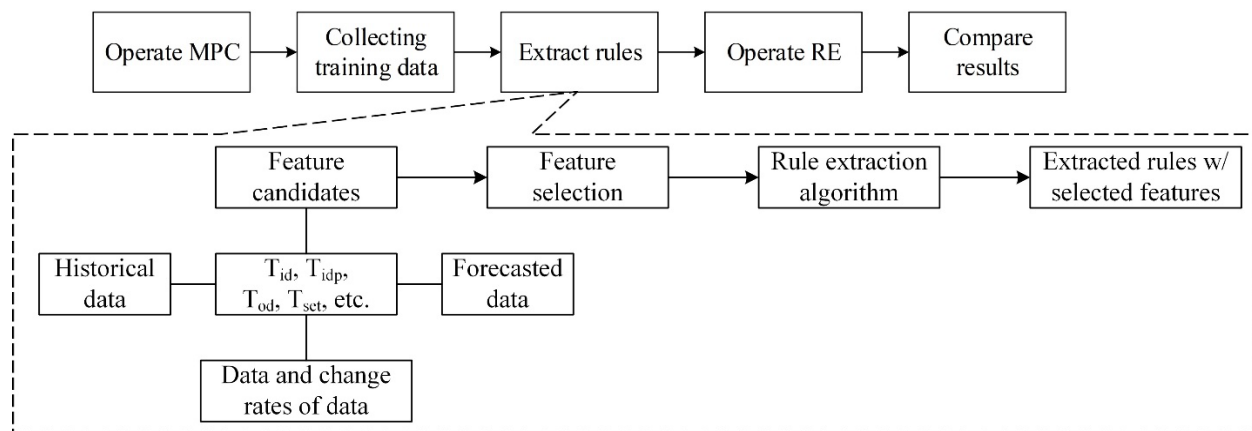


Figure 53. The workflow of MPC and rule extraction

6.1.1 Rule Extraction Algorithm Control Decision

The prediction model is critical in the whole process of the MPC-informed rule extraction workflow. It accepts multiple features as inputs and produces corresponding targets as outputs, serving as references for determining optimal control actions.

6.1.1.1 Classification and Regression Tree Model

The classification and regression tree, usually applied in fault detection and diagnosis (Mirnaghi and Haghghat 2020), is used to estimate weight factors for objective functions and extract control rules from well-predefined setpoint schedules. The classification and regression tree is

formulated as a cascade of binary decisions, as shown in Figure 54 (DEVOPS) and can be easily transformed into an “if-then” control logic form to predict the result variables with the feed of features through a sequence of conditional statements. There are decision nodes, branches, and leaf nodes. Typically, the tree is shown inverted, with the root node at the top and the leaves representing the conclusion at the bottom. Each decision node corresponds to one predictor input variable.

The rules for constructing the classification and regression tree are generated by iteratively dividing the predictor variables. This process begins with the variable that exhibits the strongest relationship with the response variable. The determination of this relationship relies on specific metrics chosen based on the data nature and algorithm employed. For classification tasks, metrics such as Gini impurity or information gain are commonly utilized, while variance reduction is employed for regression tasks (Yu and Pavlak 2022). This procedure is known as learning or expanding the decision tree. For each branch (node) of the tree, a subset of predictor variables is reviewed, and a single predictor is chosen to divide the subset into groups (branches) that similarly classify the response variable. When classification or misclassification rate is the only parameter used to determine where to split the predictor set, this procedure continues until each branch leads to a terminal node containing a single data point, also known as a leaf. Typically, a fully developed tree (one in which each branch terminates in a single value) is too complex and overfit to the data to be usable; therefore, it must be simplified (pruned) in order to be useful (Tanner 2014).

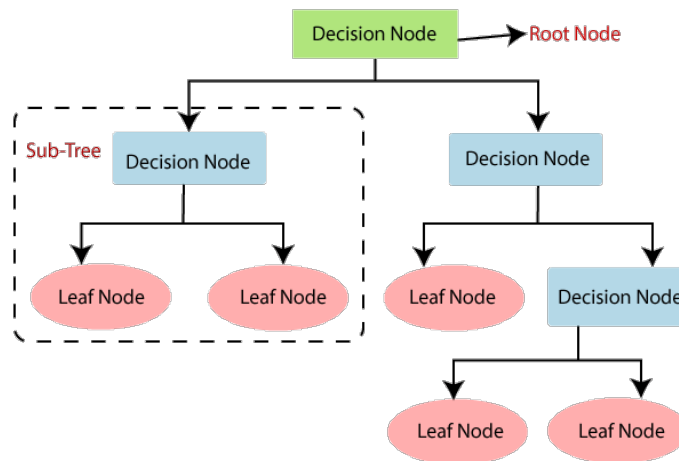


Figure 54. Schematic diagram of decision tree

6.1.1.2 Model Evaluation/Skill Evaluation

As shown in Figure 55, open-loop test and closed-loop test are two evaluation methods for the models applied in this research. The open-loop test is based on static offline data, which has been prepared completely before testing. Cross-validation is widely used approach for the open-loop testing. Explained in Equation (6), the coefficient of the variation of the root mean square error, or $cv(RMSE)$, is used for error evaluation. Another metric is R^2 (see Equation (7)–(8)), used to compare the predicted and the measured targets. R^2 is particularly well-suited for temperature

model because temperature can be expressed using different unit systems, such as Celsius (°C) and Fahrenheit (°F). These diverse unit systems can lead to different metric values when using $cv(RMSE)$.

The measured data are commonly partitioned into training and validation sets, with the former typically consisting of 70% of the data and the latter containing 30%. A model that is appropriately trained should demonstrate equivalent performance on both the training and testing datasets (Afram et al. 2017).

$$cv(RMSE) = \frac{1}{\bar{y}} \sqrt{\frac{\sum_{i=1}^N (y_i - \hat{y})^2}{N}} \quad (6)$$

$$R^2 = 1 - \frac{RSS}{TSS} = 1 - \frac{\sum_{i=1}^N (y_i - \hat{y})^2}{\sum_{i=1}^N (y_i - \bar{y})^2} \quad (7)$$

$$\bar{y} = \frac{1}{N} \sum_{i=1}^N y_i \quad (8)$$

Where,

RSS is sum of squares of residuals.

TSS is total sum of squares.

y_i is i^{th} value of the variable to be predicted.

\hat{y} is predicted value of y_i .

\bar{y} is mean value of a sample.

N is upper limit of summation.

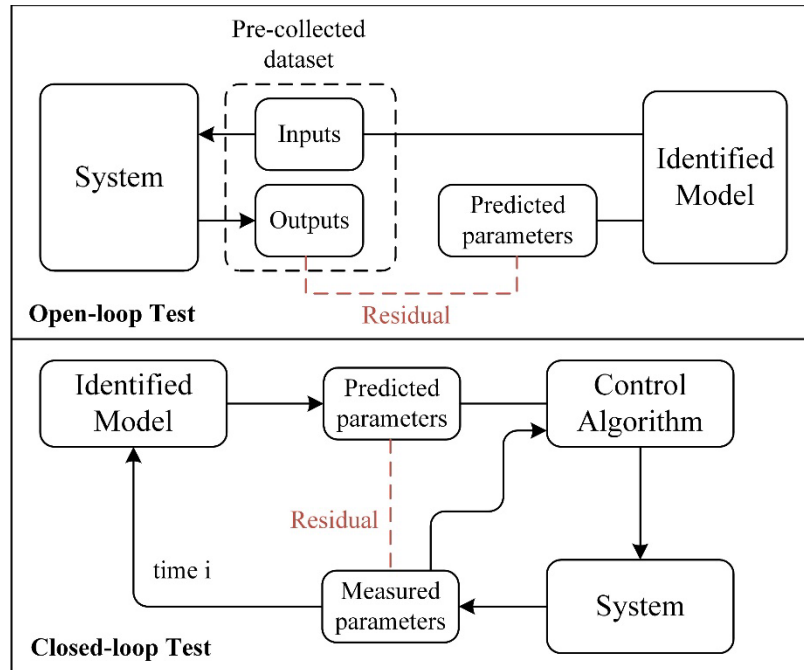


Figure 55. Open-loop test and closed-loop test

The closed-loop test is for an on-line implementation of the model, where it is tested in real time during the system operation, timestep by timestep, which is different from using a precreated dataset without incorporating predictive modeling. By simulating and testing the model in real time, it offers a more realistic representation of the identified system models and decision-making rules. Consequently, this method enables a practical evaluation of the system's performance under real-world conditions. The model's inputs are generated in real time, and its outputs are continuously used as inputs in the next timestep, which forms a closed control loop. This is the closest approximation of embedded performance on a "live" building automation system. Compared to the open-loop test, the closed-loop one depicts testing much closer to the actual operation of real systems with extracted rules (M. Robillard, Schalbart, and Peuportier 2017).

The "closed" nature of this test arises from the fact that actions taken by the rule in the current timestep have an immediate impact on the prediction set employed by the rule in the subsequent iteration. Misclassification errors originating from the rule can rapidly result in deviations in thermal states and, as a consequence, lead to the predictor set deviating from the optimal solution encountered (May-Ostendorp, Henze, Rajagopalan, and Kalz 2013).

6.1.2 MPC for the Precooling Control

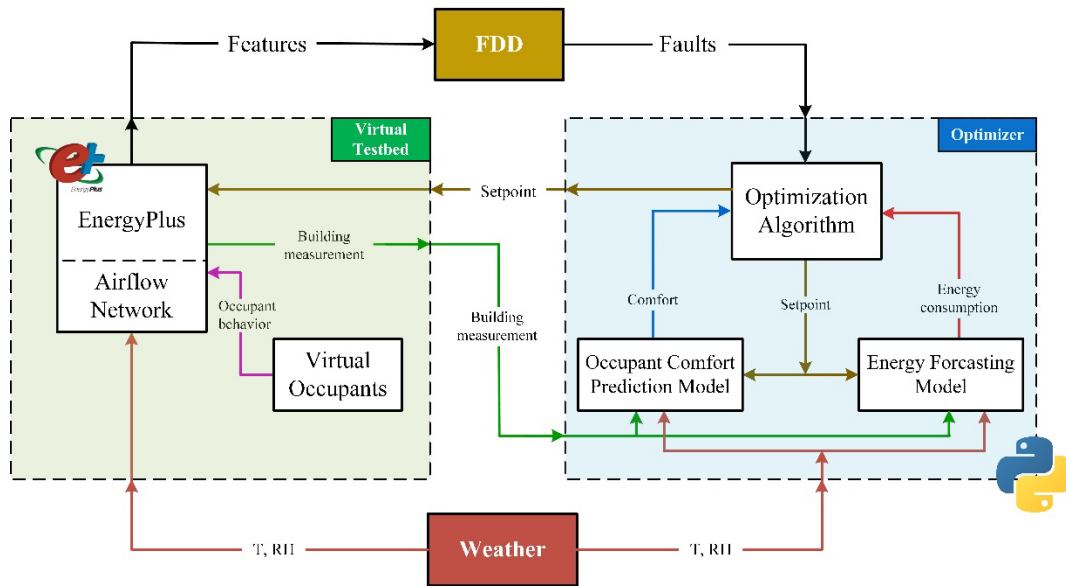


Figure 56. Model predictive control framework for residential HVAC systems

6.1.2.1 Control Platform Development

The control platform combines EnergyPlus (Crawley et al. 2001) and Python (Van Rossum 2007) within a co-simulation environment that allows for a rapid development and deployment of control for the residential HVAC system. EnergyPlus is used as a virtual testbed, simulating a real-time building response at each timestep. Python serves as a co-simulation master program (applied with the PyFMI package (Andersson et al. 2016) in this project). Python initializes and processes data, and generates and sends the control variables to EnergyPlus/virtual testbed. These steps are executed using a functional mock-up unit as a bridge to connect EnergyPlus and Python.

The detailed schematic diagram is illustrated in Figure 57. In each time step, EnergyPlus transmits the time information to the control algorithm in Python, which in turn provides the optimal control parameters to the HVAC controller (C. Wang et al. 2020). EnergyPlus receives and updates new control values through a functional mock-up unit, and then performs the simulation until the next time step. At the same time step, the comfort index is also evaluated and recorded in the Python algorithm, based on the indoor and environmental parameters provided by EnergyPlus. The optimization algorithm solves the control problem in Python and generates optimal control parameters (e.g., cooling and heating setpoint) based on the measured or predicted information and outside temperature. The resulting parameters, like cooling zone temperature and thermostat setpoint, are stored as historical data for the decision of the next control action.

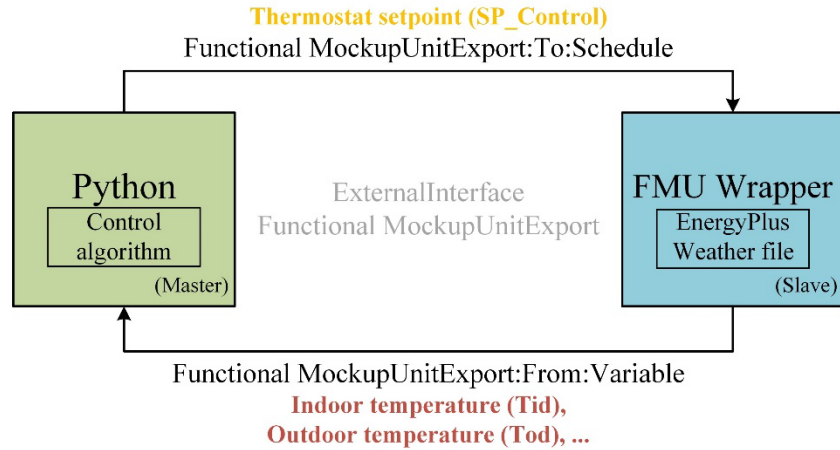


Figure 57. Co-simulation of EnergyPlus and optimization algorithms (in Python) via functional mock-up unit

6.1.2.2 Optimization Formulation

The primary goal of the precooling strategy is to mitigate the discomfort in given periods. This can be assessed by unmet degree hours, a metric that quantifies both the degree and duration when the indoor air temperature deviates from the comfort bound (Zeng et al. 2022). Degree hours was chosen as it provides an indication of the severity of a cooling capacity deficit during a heat wave. Precooling leverages the excess cooling capacity available during off-peak hours to compensate for a cooling capacity shortfall during peak hours. Consequently, degree hours serves as a valuable objective to be incorporated into the optimization formulation.

Energy consumption is another objective considered in the optimization. However, in this study, energy consumption is less important compared to thermal comfort (i.e., unmet degree hours). The capacity of the HVAC system diminishes which causes the HVAC system to struggle for maintaining the required thermal comfort, especially during extreme weather conditions. Occupant well-being has a higher priority during such a scenario (e.g., heat waves).

Therefore, two objectives are considered, unmet hours and HVAC power. The problem formulation of MPC is presented in Equations (9) - (12).

$$J = \sum_{i=1}^{ph=n} (P_i + \alpha(DH_i) + \beta(S_i)) \quad (9)$$

$$DH_i = \begin{cases} T_{sp,i} - T_h, & \text{if } T_{sp,i} > T_h \\ T_l - T_{sp,i}, & \text{if } T_{sp,i} < T_l \end{cases} \quad (10)$$

$$\text{Objective function} = \min(J) \quad (11)$$

$$\begin{aligned} &\text{Subject to} \\ &T_l \leq T_{sp} \leq T_h \end{aligned} \quad (12)$$

J is the objective function, which consists of three items, HVAC Power P , unmet degree hours DH , and smooth item S . The objective function, typically a weighted sum of these three components, is a mathematical expression utilized by the control system to guide its decision-making process and minimize the sum of objective values over the prediction horizon. It serves as a criterion for determining the controller's priorities and directs its control actions accordingly. A smooth item is used to reduce the frequent severe variation of generated setpoint schedule, as the MPC optimization easily generates some oscillations. This project utilizes temperature setpoints in the last two steps (see Equation (13)) to minimize the curvature of the input signal (Cigler et al. 2013). Weight factors α and β are incorporated into the objective function. They are used to balance the importance of those three items. As there is no standard approach to determine the value of weights, multiple trials with the purposes of optimization are inevitable. The final decision, after multiple trials, is based on the outcome that most effectively reduces unmet hours, while simultaneously preventing the indoor temperature setpoint from consistently staying at the lower bound. This means avoiding consuming excessive energy. To enhance the efficiency of adjusting weight factors for the objective function as well as enable more reliable comparisons and aggregations of diverse measures, all objective items (i.e., HVAC power and unmet degree hours) are normalized by their max values. This procedure is necessary since these performance aspects can have vastly different scales. For instance, energy consumption could be quantified in thousands of kilowatt-hours, while unmet degree hours might be measured in less than ten-degree Celsius hours. Directly applying weights to these disparate raw values could create complications in the optimization process, as the scales of the terms could disproportionately affect the solution's influence. A normalization brings all values to a standardized scale, usually ranging between 0 and 1, allowing for more meaningful and an effective comparison and aggregation of different measures in the optimization.

Moreover, i is the timestep, while ph means the prediction horizon. T_{sp} is the setpoint temperature, while the T_l and T_h are the lower bound and higher bound, the constraint for the setpoint temperature.

$$smooth(k) = (T_{sp,k-2} - 2T_{sp,k-1} + T_{sp,k})^2 \quad (13)$$

6.1.2.3 Variant Weight Factors for the Objective Function of MPC

Even though smooth dealing actions are conducted, there are still several unpleasant oscillations in the generated setpoint schedule. The oscillation hinders the optimization process and the extraction of rules, and therefore, is not a desirable occurrence. Certain oscillations can be attributed to improper weighting factors within the objective function for MPC optimization. For example, weight factor β is assigned to the constraints of unmet hours. In an attempt to minimize the unmet hours as much as possible in a single operational period, β might be selected to be a larger value. However, the downside of this approach is that in another operational period, a larger β may easily lead to unnecessary precooling. If it is done too aggressively or at the wrong times, it can waste energy and lead to undesirable temperature swings. Therefore, it becomes crucial to assign different weight factor values tailored to various

operational conditions. By adjusting these weights contextually, the model can balance the competing objectives more effectively and minimize undesired oscillations, leading to a more efficient optimization process and better rule extraction. The weight-generation procedure includes:

- 1) Run multiple simulations with different weight factors. Offline MPC is time-insensitive. Thus, multiple iterations of MPC can be conducted beforehand.
- 2) Find out the best weight factor for each day in the simulated data: the number of unmet hours is the highest priority.
- 3) Train a model for the best weight factor selection with the classification and regression tree.

6.1.2.4 Optimization Approach

To find a series of optimal temperature setpoints, reliable HVAC energy model, and thermal environment prediction models for occupant comfort are essential to be established. In the MPC optimization process, at each time step t , the MPC solves an optimization problem in an iterative, finite horizon by minimizing the objective function to determine the optimal heating/cooling trajectory based on the prediction of indoor zone temperature that satisfies the comfort requirement. In this project, solver “differential evolution” is used for the Global Problem optimization. Differential evolution is a type of evolutionary algorithm, a class of optimization methods inspired by biological evolution. These algorithms operate by creating a population of potential solutions, then iteratively evolving the population over time by applying operations analogous to mutation, crossover, and selection. Derivatives are a common tool in many optimization techniques as they can help to identify the direction of the steepest ascent or descent (i.e., the direction in which the function increases or decreases the most rapidly). However, the model used in this project is indifferentiable artificial neural network model. So these gradient-based methods cannot be used, as they heavily rely on derivative information for convergence. Heuristic methods, like the one employed by differential evolution, don’t require derivatives and can therefore handle such models effectively.

In control systems and optimization processes, establishing appropriate initial conditions is vital as they define the starting point for calculations and simulations. In this specific scenario, the lower bound temperature is used as the initial condition. Consequently, when the optimization process commences, it initiates from this lower bound temperature. The objective of this process is to accomplish precooling, which involves deliberately cooling a system prior to an anticipated temperature rise or increase in load. By utilizing the lower bound temperature as the initial condition, our aim is to guarantee that the system will attain a temperature lower than its current state, effectively achieving the desired precooling effect.

6.1.3 Rule Extraction From MPC Results

The optimal control signal schedule is generated from the MPC process. The objective of the rule extraction is to leverage the time-insensitive nature of offline MPC. This refers to the ability to

perform computationally intensive tasks of the control process ahead of time, in an offline manner. By conducting these calculations in advance when computational resources are more readily available, the resulting control decisions can be stored and quickly accessed when required during actual operation, based on the current system state. This approach significantly reduces the computational demands during system operation, which proves especially advantageous in situations where real-time computation resources are limited. Moreover, it facilitates more extensive and thorough optimization since there is typically ample time for computations during the offline phase. Thus, multiple iterations of MPC can be conducted beforehand.

Another reason is that optimization is difficult to be applied in ordinary residential buildings, where the computation source is very limited for the thermostat. Therefore, those computation loads can be transferred to some computing centers in companies or research institutes before the rules are implemented in real homes.

The basic requirement for the rule extraction algorithm is the ability to mimic the performance of MPC and result in a similar operation and thus lead to similar energy consumption and thermal environment. At the same time, extracted rules should also be simply and logically explanatory so that they can be easier to be applied in the average homes, even for those non-remote thermostats, i.e., traditional programmable thermostats. In this case, the optimal setpoint schedules can be determined quickly at the beginning of one day and reported to the nearby household in one area (Zeng et al. 2022).

Considering those requirements, the classification and regression tree is a suitable algorithm used to extract rules from the predefined operation schedule and to be implemented in common life. Gini impurity metrics are convenient to be used to split over a given predictor variable.

Gini impurity quantifies the level of “impurity” (i.e., mixture of classes) within a node. It provides a measure of how well the classes are separated within that node. The Gini impurity is calculated by determining the probability of misclassifying a randomly chosen element in the dataset if it were randomly assigned a class label based on the class distribution in the dataset. Essentially, Gini impurity serves as a measure of uncertainty or disorder within a specific node of the tree and the aim of the decision tree algorithm is to minimize this uncertainty and achieve the most homogeneous (pure) subsets of data. A higher Gini impurity value, which indicates a more mixed or impure node, suggests a suboptimal split in the decision tree. On the other hand, a lower Gini impurity value that indicates a more pure or homogeneous node, is preferred in decision tree construction.

For binary classification (two classes), the calculation of Gini impurity is as Equation (14):

$$Gini\ Impurity = 1 - Gini\ Index = 1 - \sum_{i=1}^k p_i^2 \quad (14)$$

Where, k is the number of class labels. p_i is the proportion of i^{th} class label.

Feature selection and tree depth are two significant designs for the classification and regression tree algorithm to make sure a higher accuracy of rule extraction.

Different depth determines the historical data storage and control logic implemented in the local thermostat. It also influences the performance of the classification and regression tree. If the depth is too shallow, it will lose the ability to perform well in variant conditions. If the depth is too deep, even though this tree can perform perfectly in the training data, it is very easy to be overfitting, which is difficult to be applied to other conditions. This is because the overfitted tree may have learned specific details and noise from the training data that are not relevant or applicable to new data. Consequently, it may struggle to generalize and make accurate predictions on unseen examples. Therefore, the depth of the tree should be determined carefully.

Proper selections of feature candidates benefit the application of extracted rules in practice where these features can be easily measured. Therefore, the indoor dry-bulb temperature and dewpoint temperature (or relative humidity), and outdoor dry-bulb temperature are selected as the regressors for the classification and regression tree in this study. For the forward-lagged data, only outdoor dry-bulb temperature is included, as it is easily accessible from the public weather reports, which is regarded as the perfect prediction for the MPC in this study.

The process of rule extraction includes the following steps:

- 1) Collecting training dataset: Indoor dry-bulb temperature (T_{id}), indoor dew point temperature (T_{idp}), outdoor dry-bulb temperature (T_{od}) at timestep ($i-8, \dots, i-1, i$), temperature (T_{sp}) at (i), T_{cu} at ($i+1, \dots, i+8$). The resolution of T_{sp} depends on the control time step. T_{cu} is the difference between future outdoor temperature and upper bound of comfort (i.e., 26°C (78.8°F)).
- 2) Training the classification and regression tree and saving it as a callable model: T_{id} , T_{idp} , T_{od} and T_{cu} are the features and T_{sp} is the target. Most of the time, a depth of 3 or 4 is sufficient.
- 3) Testing the trained tree model in a closed loop.
- 4) Comparing the tree-generated schedule and other schedules (e.g., baseline schedule, boundary schedule, MPC schedule, rule-based schedule).

6.2 MPC Application and Rule Extraction

6.2.1.1 Building System Identification

Models of indoor temperature and HVAC power are required for the objective function of MPC. Training data is collected from the EnergyPlus simulation during June and September. The indoor temperature forecast model obtains a good accuracy with an R^2 of 0.98, and Figure 58 shows its samples are closely distributed around the 1:1 line. For the power prediction model (described in Equation (15)), its $cv(\text{RMSE})$ is as low as 6.76%.

$$P_{i+n} = f(P_{his}, T_{his}, T_{sp, i+n-1}, T_{ou, i+n}) \quad (15)$$

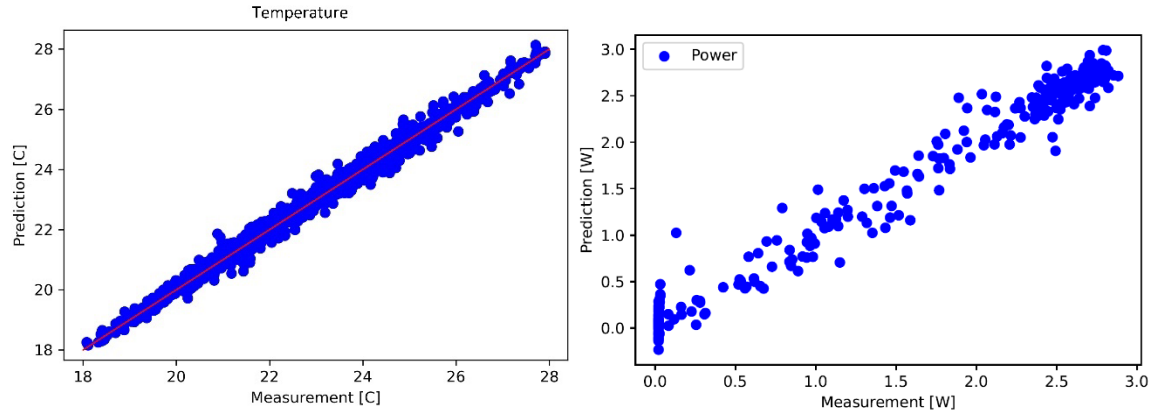


Figure 58. Performance of model training

Weight factors. The MPC optimization for this residential building located in Houston is conducted in the period of Aug. 4–13. The objective formulation is described by Equation (9) - (12). As discussed in Section 6.1, weight factors play an important role in the objective function. Weight factor *beta* for smooth factor is investigated first, with multiple trials of different values (0, 0.01, 0.05, 0.1, 0.5, 1, 5). Finally, 0.01 is chosen because it can avoid frequent significant variations of temperature setpoints. An example extracted from multiple trials is shown in Figure 59.

Weight factor *alpha* is variant day by day, and determined at the beginning of the day. Degree hour T_{dh} is used to estimate the difference between outdoor temperature and upper bound of indoor thermal comfort in one hour. This value could be either positive or negative. A peak degree hour T_{dh_peak} in one day and the sum of absolute values of hourly degree hours T_{dh_abs} are selected from a data pool by the feature selection to serve as the input to forecast the best-fitting weight factor *alpha* for one day. This model is developed with the classification and regression tree. Its tree flow is shown in Figure 60, with a 100% accuracy. It can be easily observed that when the peak degree hour is lower than 9.3 C-hr, 0 is set as the value of *alpha*. For the rest, if the sum of absolute values of hourly degree hours is lower than 187.1 C-hr, 1 goes as *alpha*. For the remaining cases, 5 is more suitable.

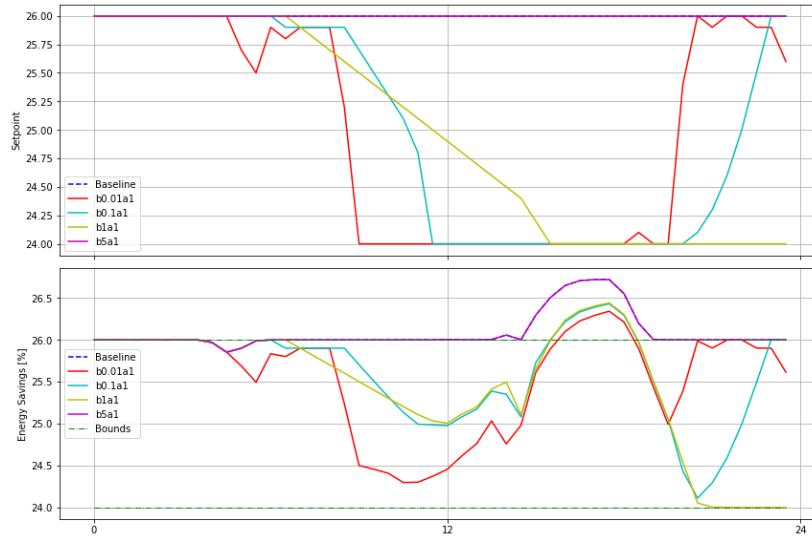


Figure 59. Time-series temperature with the change of weighting factor beta for the smooth item

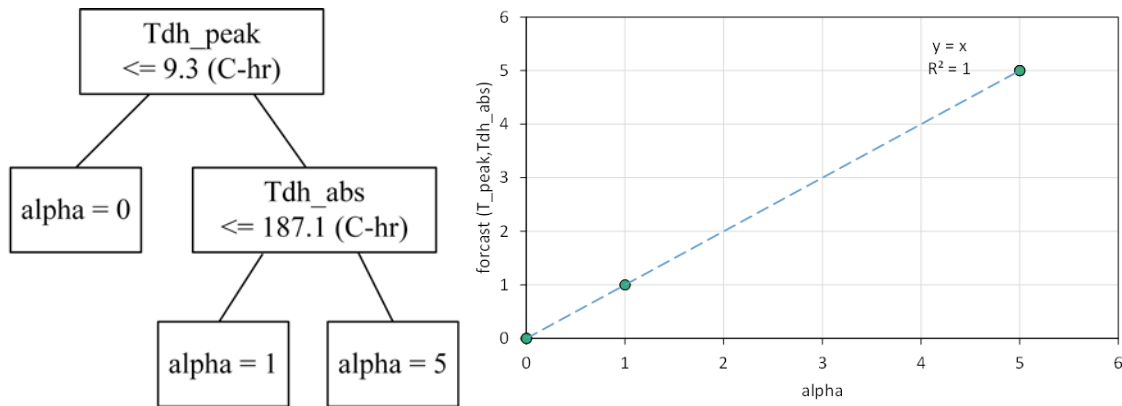


Figure 60. Decision tree and its prediction accuracy for the best fitting weight factor alpha estimation

MPC simulation. After all setup—including model setup, system parameters, objective function, constraints, optimization setting, data inputs, etc.—is properly configured, MPC optimization is conducted in the virtual EnergyPlus testbed. The results of the MPC simulation are shown in Figure 61 and Figure 62, which display that the MPC can generate a setpoint schedule that results in the mitigation of unmet hours from 9.2 C-hr to 3.4 C-hr, when the heat hump capacity reduced by 30% with a fouling condenser unit during hot August days in Houston, TX.

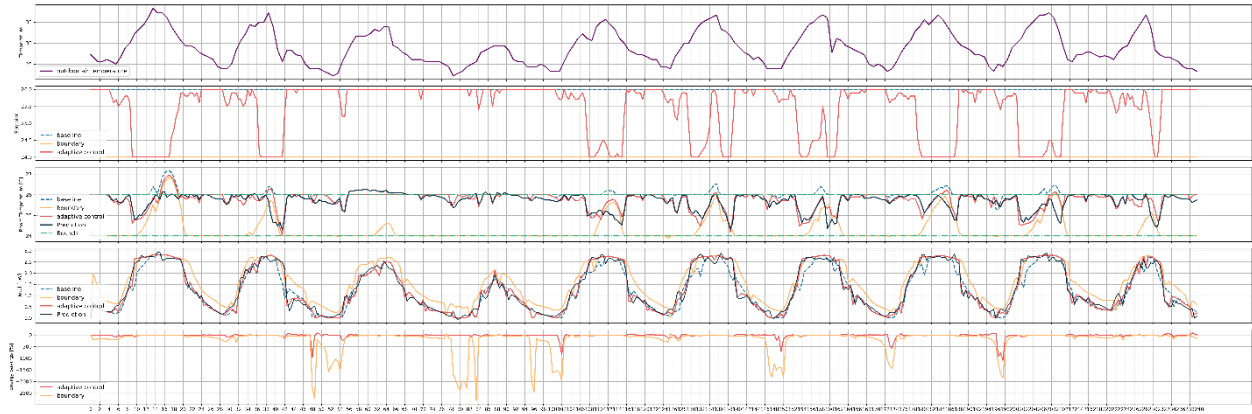


Figure 61. Temperature distribution of MPC

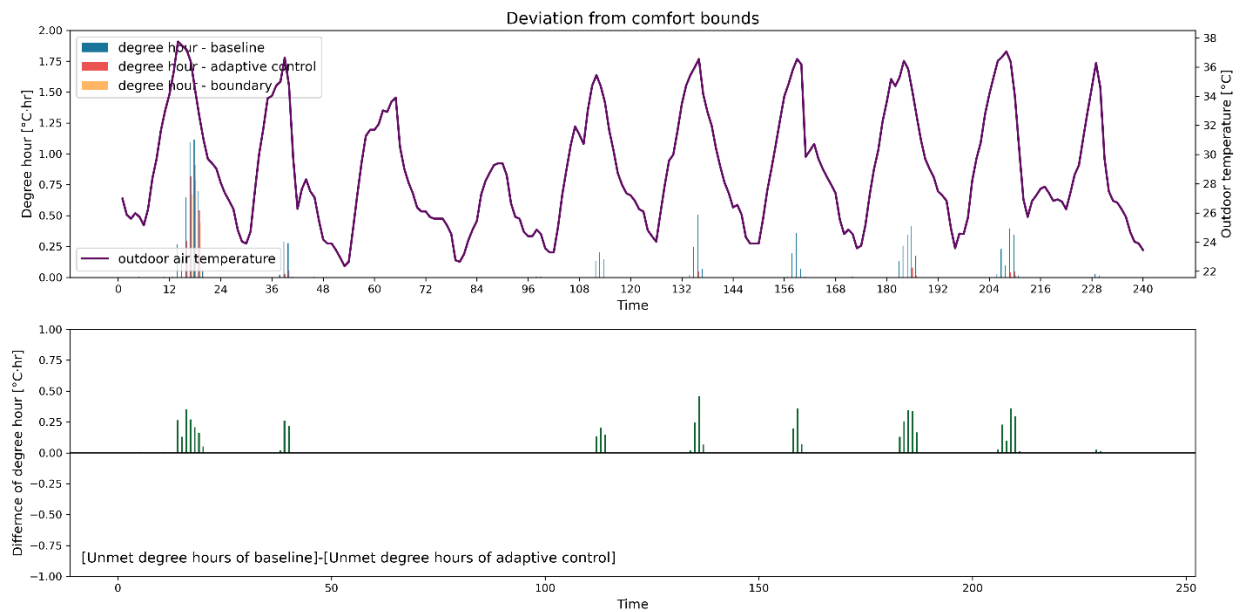


Figure 62. Unmet hours of model predictive control

6.2.2 Rule Extraction

Setpoint discrete. Rule extraction is conducted with the classification and regression tree. Setpoint discrete resolution is 0.2°C (0.36°F). The value with the digit of an odd number is rounded down because the precooling (i.e., a lower temperature) is expected to be designed. For example, 24.7°C (76.46°F) is lowered to 24.6°C (76.28°F), categorized with the original 24.6°C (76.28°F) as the same group.

Table 28. Features of the Classification and Regression Tree

Variable name	Symbol	Unit	Backward lag	Variable name
Indoor dry-bulb temperature	T_{id}	°C (°F)	..., k-4, k-3, k-2, k-1, k	
Indoor dewpoint temperature	T_{idp}	°C (°F)	..., k-4, k-3, k-2, k-1, k	
Outdoor dry-bulb temperature	T_{od}	°C (°F)	..., k-4, k-3, k-2, k-1, k	k+1, k+2, k+3, k+4, ...

6.2.2.1 Classification and Regression Tree Training and its Depths

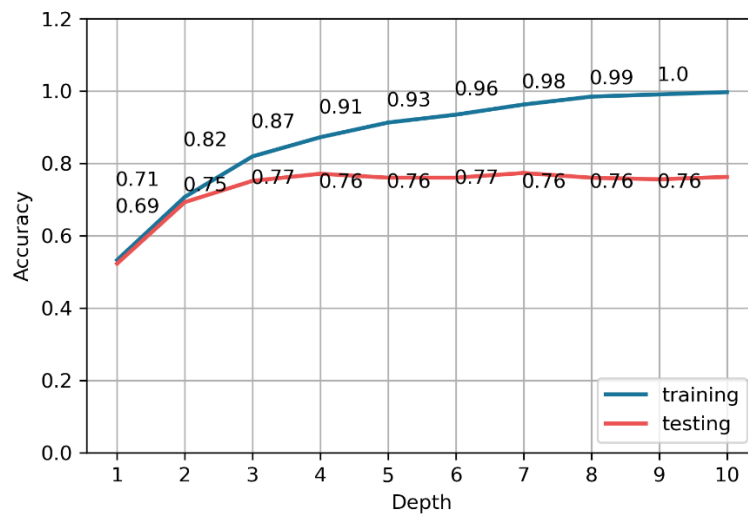


Figure 63. Accuracy of rule extraction in the open-loop test

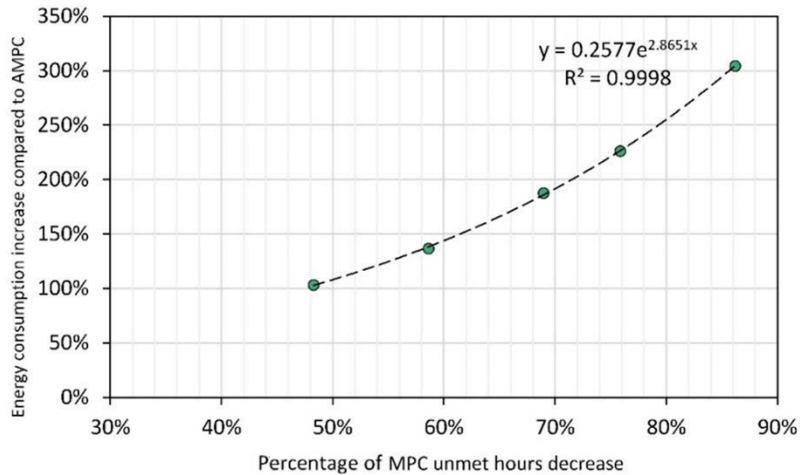


Figure 64. Effect of different depths in the decision tree

T_{id} , T_{idp} , and T_{od} , listed in Table 28 are considered the feature inputs. The future outdoor temperatures are transformed into degree differences to the comfort higher bound. The forecast accuracy of the rules model converges above 75% in the open-loop test (see Figure 63). When it comes to the closed-loop test, the effect of different depths in the MPC-informed rules tree is evaluated with Equation (16)–(18). It is apparent that when thermal comfort improves (as demonstrated by a decrease in unmet hours, represented on the x-axis), it comes at the expense of increased energy consumption (i.e., a higher energy consumption increase compared to MPC, depicted on the y-axis). This tradeoff should be varied regarding specific scenarios. A depth of 4 is chosen for the tree model used in this study.

$$P_{dh} = \frac{R_{dh_rbc}}{R_{dh_MPC}} \quad (16)$$

$$R_{ec} = \frac{ER_{rbc}}{RR_{MPC}} \quad (17)$$

$$Ratio = \frac{P_{dh}}{R_{ec}} \quad (18)$$

R_{dh_mpc} : Unmet hours decreasing rate of MPC, compared to the baseline

R_{dh_rbc} : Unmet hours decreasing rate of MPC-informed rules, compared to the baseline

ER_{mpc} : Energy consumption saving rate of MPC, compared to the baseline

ER_{rbc} : Energy consumption saving rate of MPC-informed rules, compared to the baseline

P_{dh} : Percentage of unmet hours decreasing rate of MPC-informed rules in MPC

R_{ec} : Energy consumption increasing rate of MPC-informed rules compared to MPC

6.2.2.2 Tree and Its Features

A readable decision tree for the precooling setpoint forecast is shown in Figure 65. It can be learned that not all features at all time steps are required to constitute a complete decision tree. Preliminary investigations imply that the indoor temperature at the current time step is the most important parameter to make a decision on the action of the next step, which is followed by the indoor temperature at the last time step and the indoor dewpoint temperature at the i-3 time step. The outdoor temperature is the most frequently used parameter.

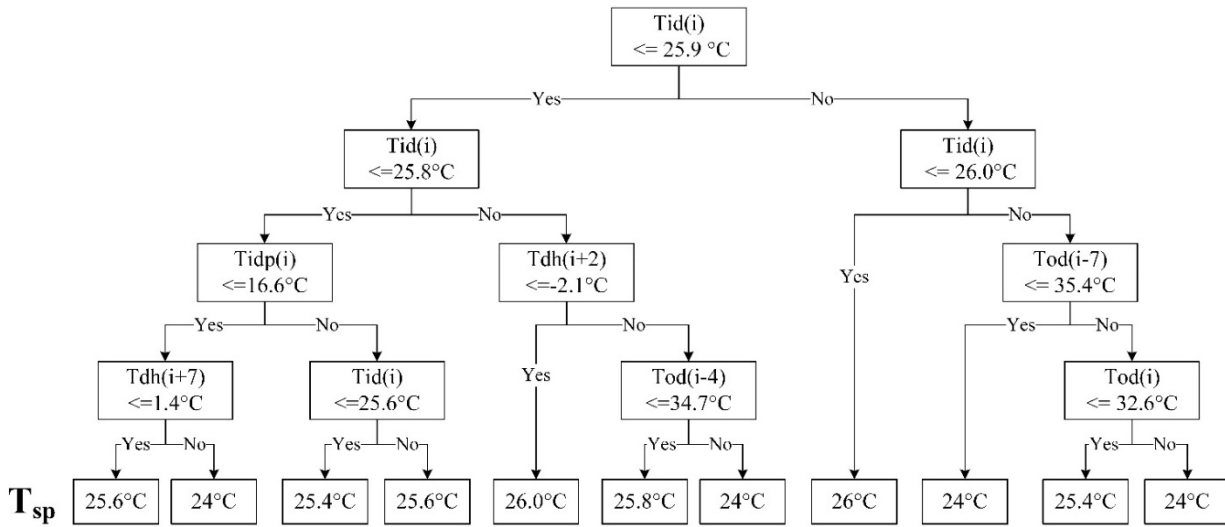


Figure 65. Classification and regression tree for precooling with depth of 4

6.2.2.3 Test Using Training Days and Testing Days

The training period is from Aug. 3–12. Figure 66 and Figure 67 plot the comparison of unmet hours in the training run. They highlight that the MPC-informed rule control generated from one period can mitigate the unmet hours from 9.2 C-hr to 5.2 C-hr for 10 days, with a more than 60% decrease rate, when applied to another period. At the same time, it only consumes more energy of 45 kWh for 10 days, around a 15% increase rate, compared to the baseline.

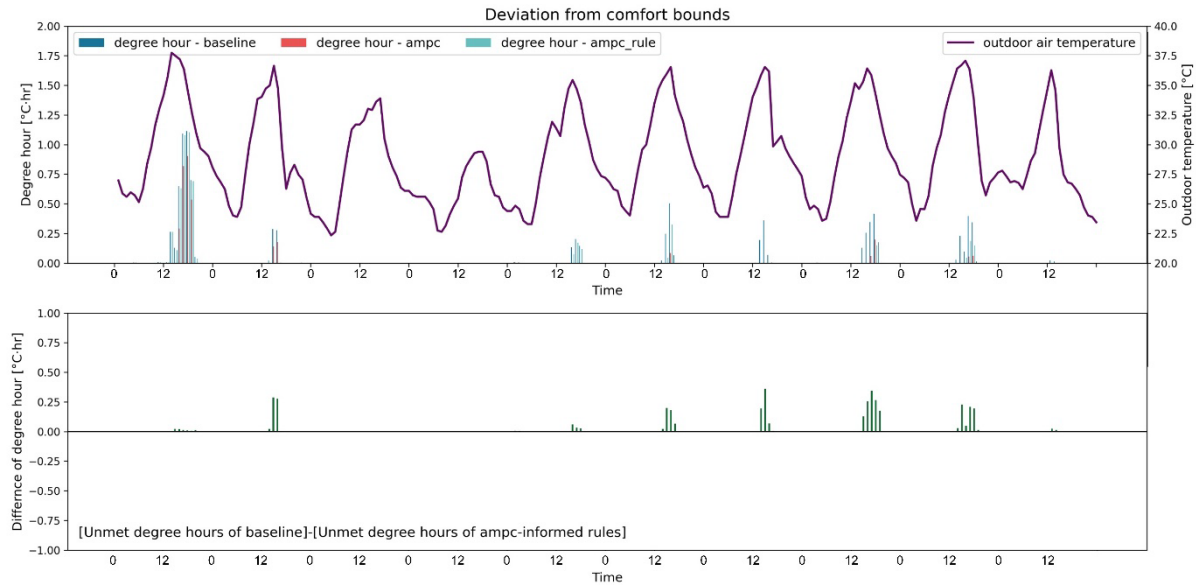


Figure 66. Unmet hours of model predictive control with training data

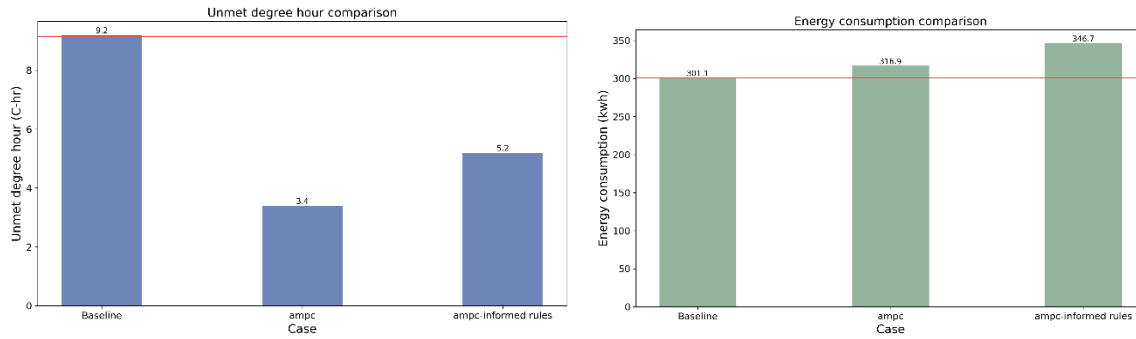


Figure 67. Unmet hours and energy consumption with training data

Apart from the test with training data, it is more important to test with testing data that are from different periods. An additional test is conducted in the run period of July 24–Aug. 2 and Aug. 13–22. The results are listed in Table 29. It can be learned that comfort level is improved to some extent in all periods (unmet hours decrease from 10 C-hr to 5.1 C-hr from July 14–Aug. 2, and from 0.6 C-hr to 0 from Aug. 13–22).

Regarding online computation time, within the same computer configuration, MPC consumes 870 mins for a 10-day running on average, while MPC-informed RBC finishes in 0.2 minutes on average, significantly faster than the original MPC.

Table 29. Performance Comparison of MPC-Informed RBC

		Training Data		Testing Data			
		08/03–08/12		07/14–08/02		08/13–08/22	
		Unmet (C-hr)	Energy (kwh)	Unmet (C-hr)	Energy (kwh)	Unmet (C-hr)	Energy (kwh)
Values	Baseline	9.2	301.07	10	295.2	0.6	196.7
	MPC	3.4	316.93	3.4	310.7	0.5	200.2
	MPC-informed RBC	5.2	346.7	5.1	314	0	237.5
Change rate compared to the baseline	MPC	-63.0%	5.3%	-66.0%	5.3%	-16.7%	1.8%
	MPC-informed RBC	-43.5%	15.2%	-49.0%	6.4%	-100.0%	20.7%
	Pdh	69.0%	N/A	74.2%	N/A	600.0%	N/A
	Rec	N/A	187.7%	N/A	21.3%	N/A	1065.7%
Effectiveness		36.7%		348.7%		56.3%	

6.3 Summary

This section conducts an advanced control strategy MPC for the precooling control in the residential building with only thermal mass in consideration under extreme weather events (e.g., heat waves), and then to extract operation rules with classification and regression tree to take advantage of the MPC results and make them easier to be applied in homes. This framework is implemented in the prototype building and generates several control rules in the form of decision tree. It demonstrates that thermal comfort can be improved (i.e., the decrease in unmet degree hours) with MPC-informed rules generated by the simulation results during another period.

7. Lab Testing

The technology developed in this project utilizes low-cost sensors developed by the research team, which are installed throughout a residential dwelling. A demonstration of these technologies in a field testing setting was conducted at the PNNL Lab Homes. The demonstration effort entailed a dedicated testing period of seven weeks, from Aug. 10 to Sept. 25, 2022. This testing assessed the comprehensive performance of various components: the sensor network capabilities, FDD algorithms, and comfort-oriented algorithms.

The testing framework is shown in Figure 68.

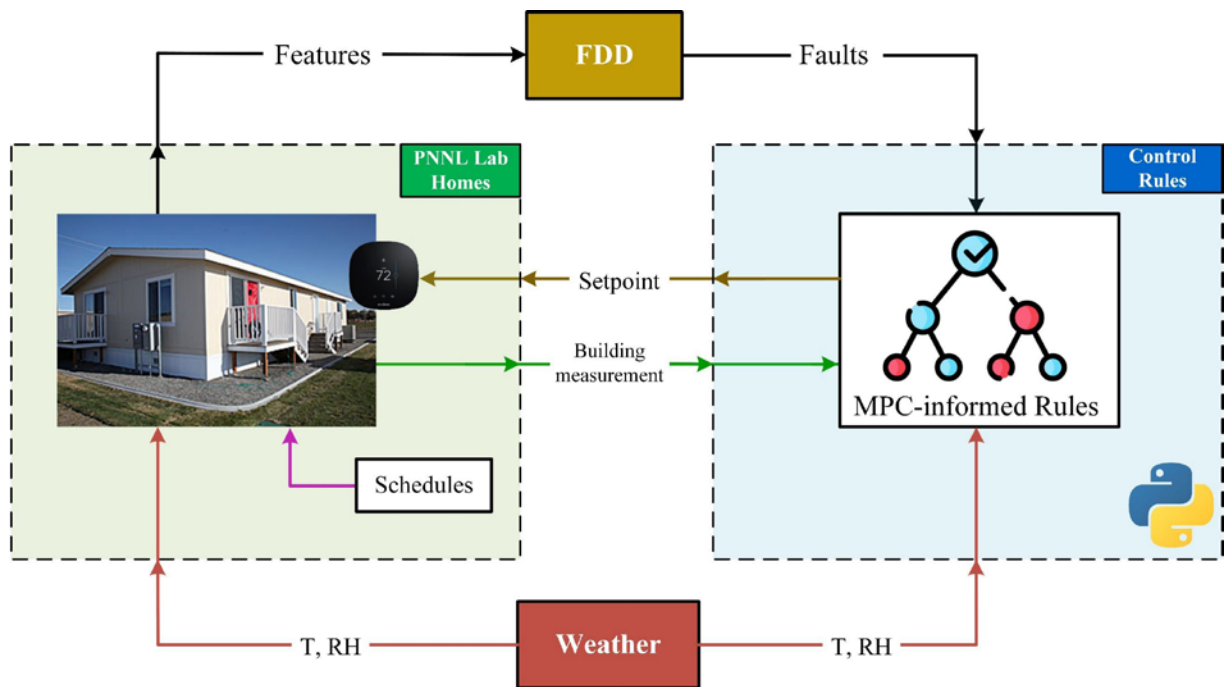


Figure 68. Framework of lab testing for FDD and controls

7.1 Lab Testing Setup and Implementation

7.1.1 Testing Homes

Two identical Lab Homes, located in Richland, WA, were used for the field testing. Among them, Lab Home A serves as the test home, while Lab Home B is the baseline home.

Each of the homes has three bedrooms and two bathrooms. They have one floor with an area of 138.7 m^2 (1493 ft^2). Photographs of the homes are shown in Figure 69. The homes are equipped with double-pane windows (18.4 m^2 (198 ft^2) total of window area), wood siding, and composition asphalt shingle roofing. The interior flooring consists of sheet vinyl in areas with carpet throughout the rest of the home. The home is fitted with R-22 insulation in the floors, R-11 insulation in the walls, and R-22 insulation in the ceiling. The floorplan is displayed in Figure 70. As seen in the floorplan, the home is designed around an open-concept layout for the main gathering space. The home contains standard appliances, including a refrigerator, oven with

range, microwave, dishwasher, clothes dryer, washing machine, and water heater. The house is equipped with LED lighting in all lighting fixtures, and there are exhaust fans located in the kitchen and both bathrooms. There is also an electric vehicle charging station integrated into the homes for research on electric vehicle loads.



Figure 69. Exterior photos of the PNNL Lab Homes

Photos from project team

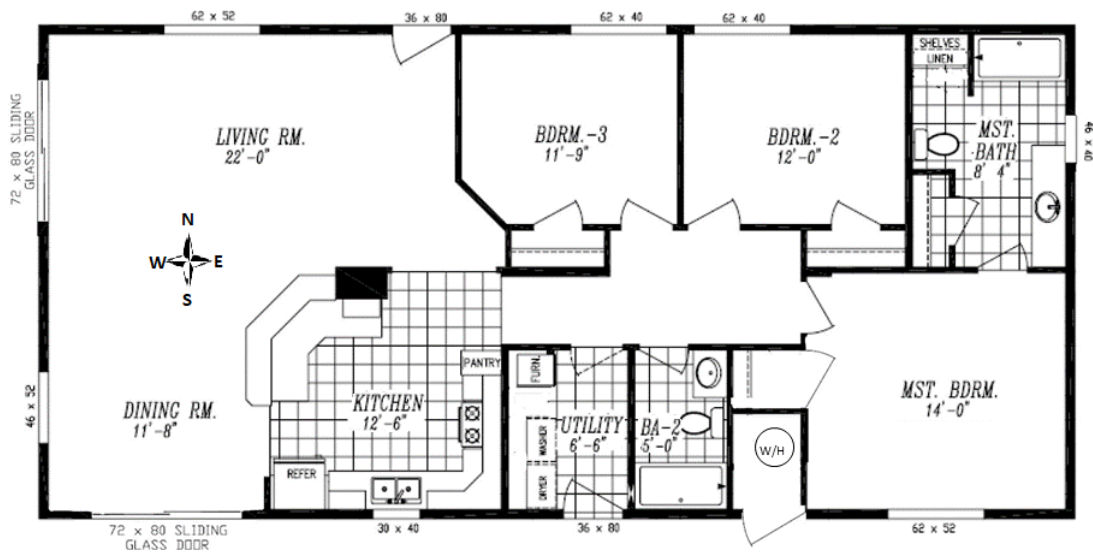


Figure 70. Layout of the PNNL Lab Homes

Image from project team

7.1.2 Heating and Air Conditioning Information

The homes are powered exclusively by electricity. Each home is equipped with an electric heat pump and central air distribution system (see Figure 71). The heat pump has a 13 SEER/7.7 heating seasonal performance factor (HSPF) rating. The house has a dual heating system. In addition to the electric heat pump, there are Cadet electric fan wall heaters. The registers for the central air system are in the floor. As with typical manufactured homes, the floor joists are supported by large steel beams that run under the home. The floor is insulated with a blanket of

insulation that is held in place with a large, watertight tarp between the floor joists and steel beam. The supply ductwork for the heat pump is located between the floor joists and insulation blanket underneath the home.



Figure 71. Heat pump indoor and outdoor units for the PNNL Lab Homes
 Photos from project team

7.1.3 Data Acquisition/Storage and Control Single System

7.1.3.1 Lab Communication

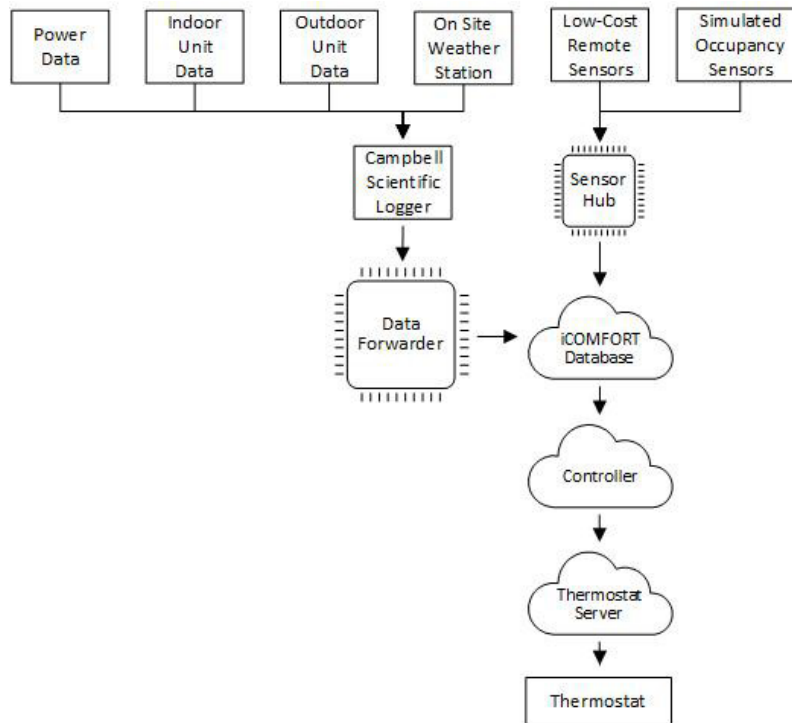


Figure 72. Summary of data flow for the IOT-based comfort control

The IoT-based comfort control requires sensors from multiple sources as well as the capability to implement control commands via the connected thermostat. Figure 72 summarizes the flow of data in the lab testing. Power measurements, FDD sensor measurements (installed on indoor and outdoor units), and weather station measurements are collected through the Campbell Scientific logger system at the PNNL Lab Homes. A data forwarder process running in VOLTTRON then forwards the data to the iComfort cloud database. At the same time, the low-cost sensors communicate with a central hub that also forward data to the database. The control algorithm processes the data and then sends the control signal via API command to the thermostat's server.

7.1.3.2 iComfort Database

To stream and distribute the sensor data to the intelligent control algorithms, the data are uploaded to the cloud-based iComfort database and made accessible through a set of HTTP APIs. The sensor data are formatted by the data producer (the Gateway hub of iComfort sensors and data forwarder from PNNL lab home system) and submitted to the cloud database.

In the database, the sensor records are validated, grouped by the sensor, and sorted by their measuring timestamp. As a data record is put into the database, an incremental index number is assigned to it. By accessing records using successive indexes, the latest records can be streamed to the control algorithms.

The database provides unified APIs for different types of sensors, including iComfort sensors (all variants) and the various existing sensors in PNNL lab home. The APIs use standard HTTP protocol allowing the control algorithms to access easily with standard libraries. To prevent unauthorized access, the APIs are also protected by pre-distributed access control keys. The keys were securely delivered to the participant of this project before the experiment started.

The database was reinitialized to wipe out the old development data at the beginning to prevent unexpected issues. The communication and functionality of the database were tested after reinitialization.

7.1.3.3 Thermostat

The heat pump system is controlled through an ecobee thermostat, which can be operated and adjusted through the cloud to match typical thermostat usage patterns and to implement control strategies. The control decision generated by the comfort control is the thermostat setpoint. The setpoint can be implemented remotely using the ecobee API (Ecobee). The manufacturer's aims are to be backwards compatible with previous versions and have their API be self-documenting and easy to use and understand. Ecobee authorization is based on the OAuth 2.0 protocol and their implementation uses three different methods: authorization code, PIN authorization, and utility authorization (Widén 2015).

7.1.4 Lab Testing Design

Section 7.1.4 outlines the design for the testing of the FDD and control strategies. Further details related to the testing process, such as the testing timeline, occupancy simulation, sensor

installation, weather conditions, fault implementation, and operation schedules can be found in Appendix E.

7.1.4.1 Fault Detection and Diagnosis for the Heat Pump System

Only temperature measurements are used as features for the FDD of the heat pump system. Table 24 lists all sensing parameters and corresponding features required. Some features can be measured directly (e.g., evaporating temperature), while others need to be calculated indirectly (e.g., suction line superheat equals the difference of evaporator exit refrigerant temperature and evaporator two-phase refrigerant temperature, $T_{sh}=T_{ev}-T_e$). Dependent variables are the main features for FDD, while independent variables are monitored to calculate the reference model.

For the cooling mode, evaporator inlet air temperature T_{iai} (No.6) is approximately the same as the indoor dry-bulb temperature T_{ia} (No.11); the condenser inlet air temperature T_{oai} (No.8) is approximately the same as the outdoor dry-bulb temperature T_{oa} (No.10). Therefore, 10 parameters (temperature) in total are required for measurement in the residential HVAC system.

7.1.4.2 MPC-Informed Rule-Based Control

These MPC-informed rules are dedicated to two scenarios: adaptive to the HVAC (e.g., heat pump) faults and adaptive to the occupancy. Table 30 and Table 31 show different configurations for both Lab Homes in two scenarios.

Table 30. Testing Design for Adaptive Control to Occupancy

Lab Home Name	HVAC System Configuration	Setpoint Schedule
Lab Home A	Fault-free	<i>Remote from TAMU: Setback to 28°C (82°F) when unoccupied. Precooling several hours ahead of being occupied</i>
Lab Home B	Fault-free	<i>Scenario 1: Constant of 24°C (76°F) Scenario 2: Setback control 8:00-18:00 28°C (82°F) 18:00-8:00 24°C (76°F)</i>

Table 31. Testing Design for Adaptive Control to HVAC Faults

Lab Home Name	HVAC System Configuration	Setpoint Schedule
Lab Home A	Faulty condition: Refrigerant undercharge/heat exchanger fouling	<i>Remote from TAMU: Setpoints generated from MPC-informed rules (expected 72–76°F (22.2–24.4°C))</i>
Lab Home B	<i>Faulty condition: Refrigerant undercharge/heat exchanger (make sure the same faults and severity levels in the two homes)</i>	Constant of 76°F (24.4°C)

The implemented fault severity for the heat pump systems includes:

- Refrigerant undercharge: 80% and 60% of the original charge
- Refrigerant overcharge: 120% and 140% of the original charge
- Evaporator fouling fault: 85% and 70% of the original airflow
- Condenser fouling fault: 85% and 70% of the original airflow.

7.1.4.3 Active Learning Data-Driven Model and Data Predictive Control

In this project, an online data predictive control (DPC) framework was designed and tested at the PNNL Lab Home. The objective was to evaluate the performance of the developed data-driven forecasting models in a real-time online scenario as well as test the performance of a computationally efficient control strategy that would optimize HVAC system electric energy while constrained by occupant comfort. A comparison was performed between the baseline energy usage (Lab Home B) and the optimized energy usage (Lab Home A).

The DPC framework developed in this project was adapted from L. Zhang (2018). That work sought to minimize the HVAC system electric energy over an hour. A three-hour period forecasting was used to avoid the optimizer being too near-sighted. At each hour, the framework would select a zone thermostat cooling setpoint combination (one setpoint for each hour period) that would result in the lowest energy consumption for the next three hours, while ensuring the zone temperature to be within the desired range.

In Lab Home B (baseline home) the thermostat cooling setpoint was set to 75°F during all occupied periods and set to 78°F during all unoccupied periods. In Lab Home A, which is controlled using the DPC framework, the range of possible setpoints was from 75° to 90°F. The selected setpoints were sent to the installed ecobee Smart Thermostat in Lab Home A through the online framework discussed previously.

There was a constraint for zone temperature so the system did not choose setpoints that would result in an uncomfortable thermal environment should the zone be occupied by real occupants. If a setpoint combination would result in the lowest energy usage but break the comfort constraints at any point in the next three hours (using the forecasts from the zone temperature model), that combination was discarded and the next highest energy usage combination was assessed. This process was repeated until a combination was found that did not break the constraints. The occupant comfort constraint differed depending on whether the lab home was occupied or unoccupied. While there were no physical occupants present during the testing period, the PNNL team implemented an occupancy simulation using heating devices. The schedule simulated the occupants leaving for work during the day and leaving the home unoccupied. During the occupied periods, the occupant comfort range was set from 70° to 78°F. During the unoccupied periods, the range was set from 60° to 90°F.

7.2 Analysis of Results

7.2.1 Demonstration of the Hardware and Cloud Database

During the experiment period, the 16 iComfort sensors collected and pushed 1,413,072 sets of temperature and humidity data (and airflow data from four of them). Also, the cloud database received 2,586,542 records from existing lab home sensors through a data forwarder. About 370 megabytes of data were produced during this period. The cloud database's API served more than 5,198,000 query requests from the detection and control algorithms. The cloud database was working at 100% availability and completely error-free during the experiment. Figure 73 plots the temperature and humidity readings gathered by iComfort sensors in the lab home's living room area, and the airflow sensed from the HVAC supply register nearby.

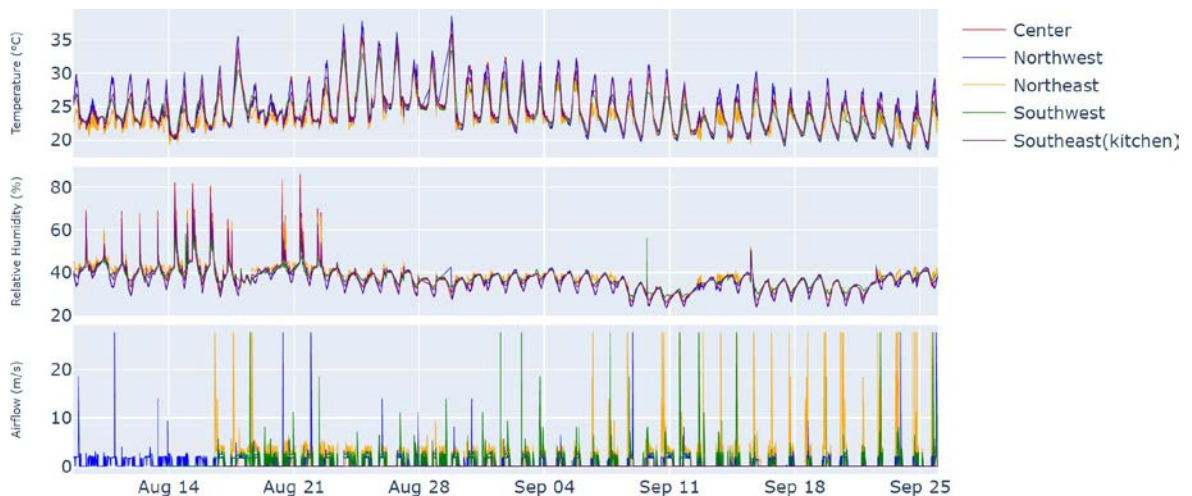


Figure 73. Temperature, humidity and airflow data from the living room area

Most of the sensors operated reliably throughout the experiment, consistently streaming measurements to the cloud at one-minute intervals. However, due to various reasons on the sensor side, part of the data was missing during this period. The data completion status of each day in this period is shown in Table 51 of Appendix E.9.

After analyzing the data, the following issues have been identified:

- 1) PNNL Lab Home A has unstable internet connectivity, causing the data forwarder to occasionally go offline and lose data. Most of the lost data were recovered from PNNL's local database and manually loaded later. Since the iComfort Gateway hub cached data when it failed to push them to the cloud, there was no data loss from the iComfort sensing system due to this issue.
- 2) Five of the iComfort sensors had dead batteries at the beginning of the experiment and were not operating during the first week. After changing the batteries, three of them restored functionality and worked stably for the rest of the experiment time.
- 3) The remaining two iComfort sensors had some hardware issues during assembly. From telemetry data, those sensors drained the battery much faster than others and tended to overdrain the battery. These two sensors provide unstable data streams, as shown in the table. After testing, a soldering defect was found on the two sensors' power supply part and they were fixed by resoldering the board.

7.2.2 Fault Detection and Diagnosis for the Heat Pump System

7.2.2.1 *Steady State Filter and Fault-Free Reference Model*

Figure 73 plots an example of temperature measurement for the heat pump system. All the heat pump-related temperatures correspond to the designed point in Figure 45. Figure 74 shows the steady-state analysis of the features that are used for the rule-based FDD. The value of features is calculated from Figure 73 with equations in Table 24.

Similar to the experiment dataset case, Figure 75 shows the accuracy performance of different-order multivariable polynomial regression models for all features with the field test dataset. Compared to experiment dataset, the models' accuracy levels are lower on average. This is mainly a result of more uncertainties when the test is conducted in the field. The features whose models have a lower accuracy are all estimated indirectly. For example, condenser air temperature change (dT_{ca}) is the difference between condenser inlet air temperature (T_{cai}) and condenser outlet air temperature (T_{cao}). Similarly, features estimated indirectly can be calculated following the directly measured features. These directly measured features are typically associated with models of higher accuracy. Figure 76 and Figure 77, taking discharge temperature as an example, show a comparison of measured and predicted temperature in the scatter and series style, respectively. Those both show a close distribution between predicted values by the fault-free model and the real measured ones.

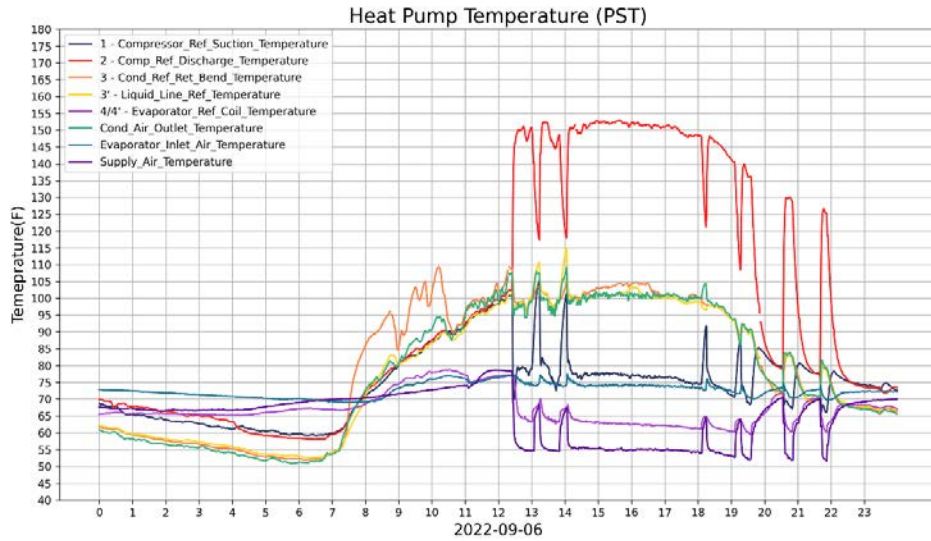


Figure 74. Temperature distribution in the heat pump system

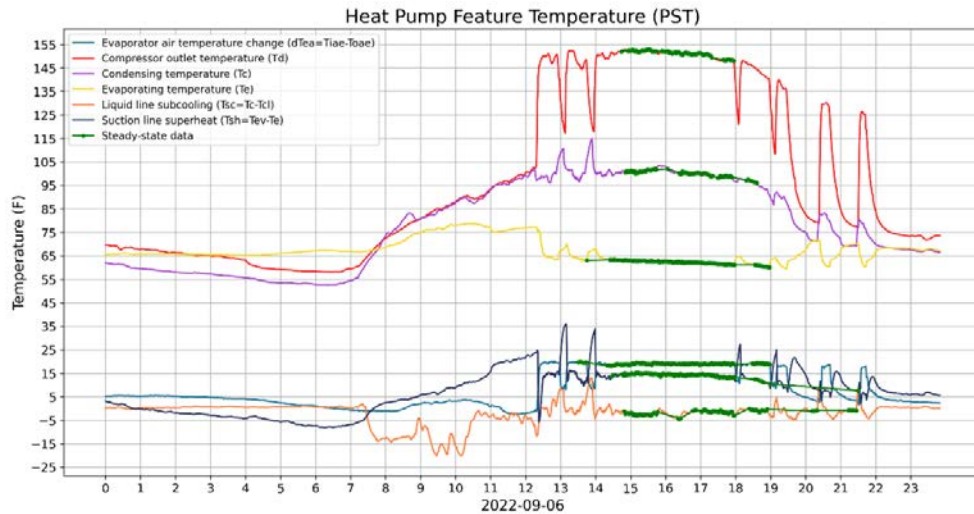


Figure 75. Heat pump feature temperature

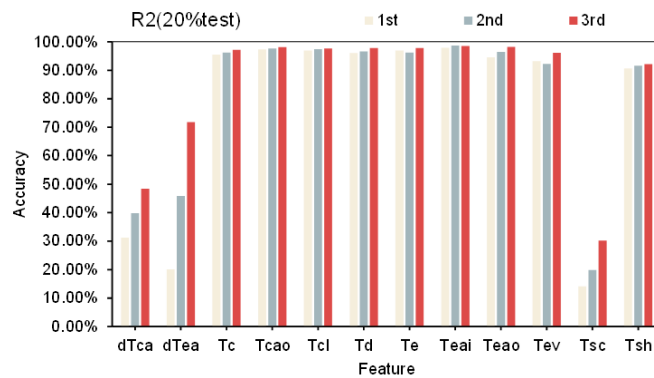


Figure 76. Accuracy performance of different-order multivariable polynomial regression models for all features with field test dataset

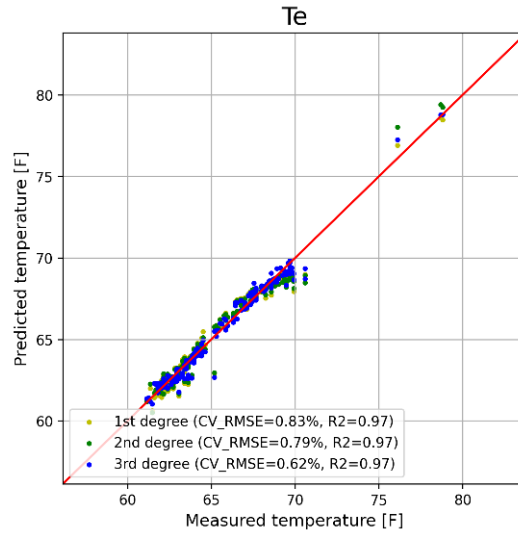


Figure 77. Scatter comparison of measured and predicted discharge temperature

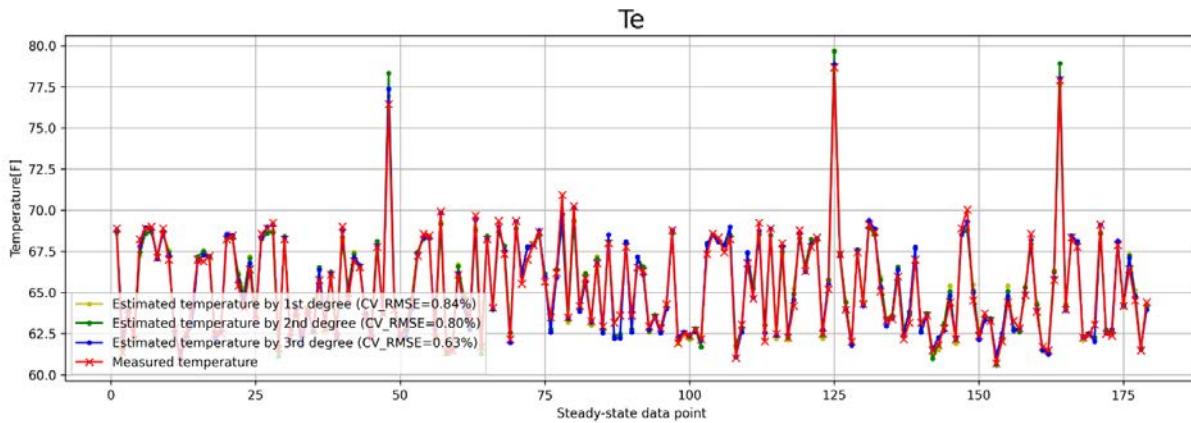


Figure 78. Series comparison of measured and predicted discharge temperature

7.2.2.2 Comparative Analysis and Hybrid FDD Approach Demonstration

The FDD method that is conducted is a hybrid rule-based approach, which is described in Section 4. Because the objective is to diagnose a single fault, an additional rule is implemented:

- If a refrigerant fault is diagnosed, then air-side fault diagnosis is skipped.
- If a refrigerant fault is not filtered, the result for the air-side fault is displayed.

The n-class evaluation matrix of diagnosis classification results is shown in Figure 78. Diagnosis for condenser fouling (85% and 70% of the original airflow) has the highest accuracy with 100%, followed by undercharge (80% and 60% of the original charge) with an accuracy of 96%. The lowest diagnosis accuracy (58%) exists in the evaporator fouling case (85% and 70% of the original airflow). This fault is easily misdiagnosed as fault free. The reason behind this lower diagnosis accuracy is that feature temperatures in the evaporator fouling fault scenario sometimes overlap with temperature readings of the normal scenario under the same outdoor temperature (see Figure 79). This overlapping of temperatures makes it more challenging to

accurately diagnose the fault. Overall, the diagnosis accuracy is 90.18%, counting all cases (including fault-free ones). It should be noted that even though the accuracy of evaporator fouling diagnosis is not high, in practice, the malfunction alarm will be correct with the highest probability from the accumulative diagnosis results during a period.

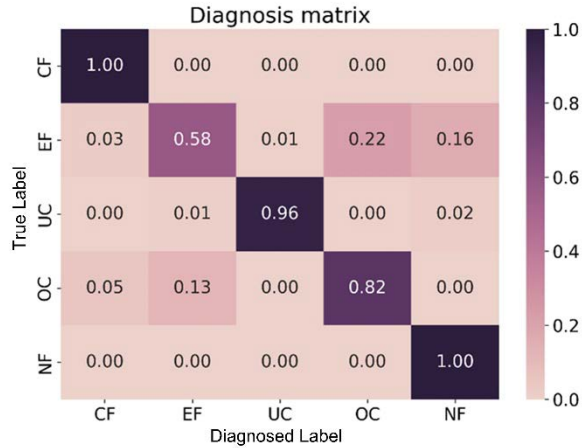


Figure 79. Diagnosis matrix for the FDD-VCC

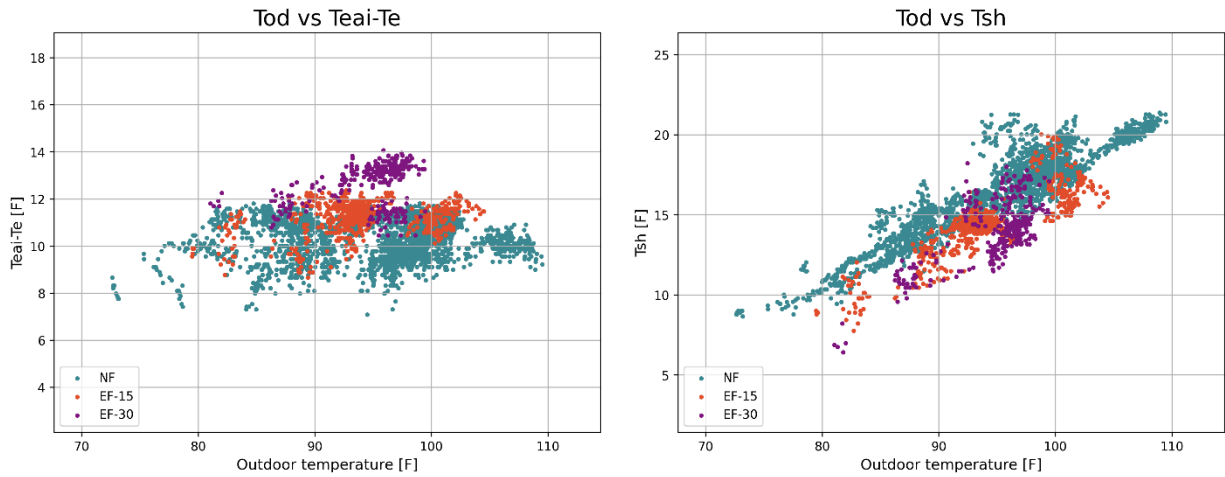


Figure 80. Temperature plot for evaporator inlet air temperature ($T_{\text{eai}}-T_e$) and suction line superheat (T_{sh})

T_{od} = outdoor dry-bulb temperature; NF = no fault; EF = evaporator fault

Besides, according to the confusion matrix for fault detection shown in Figure 78, the calculated values are listed in Table 32. It shows all metrics are higher than 90%. Especially, the detection accuracy that the developed hybrid FDD method obtains is 96.4%.

Table 32. Confusion Matrix for Fault Detection

Metric	Value
Sensitivity	93.5%
Specificity	100.0%
Precision	100.0%
Negative Predictive Value	92.6%
Accuracy	96.4%
F1-score	96.6%

7.2.3 MPC-Informed Rule-Based Control

7.2.3.1 Adaptive to the Occupancy

Figure 80 presents an energy comparison of heat pumps installed in Lab Home A and Lab Home B under occupancy adaption scenario 1. Lab Home A is the test home, while Lab Home B is the baseline home. It shows that due to a setback control strategy that adapts to the occupancy schedule, more than 14% energy saving was achieved, which meets the requirement that HVAC energy savings should be greater than 10%.

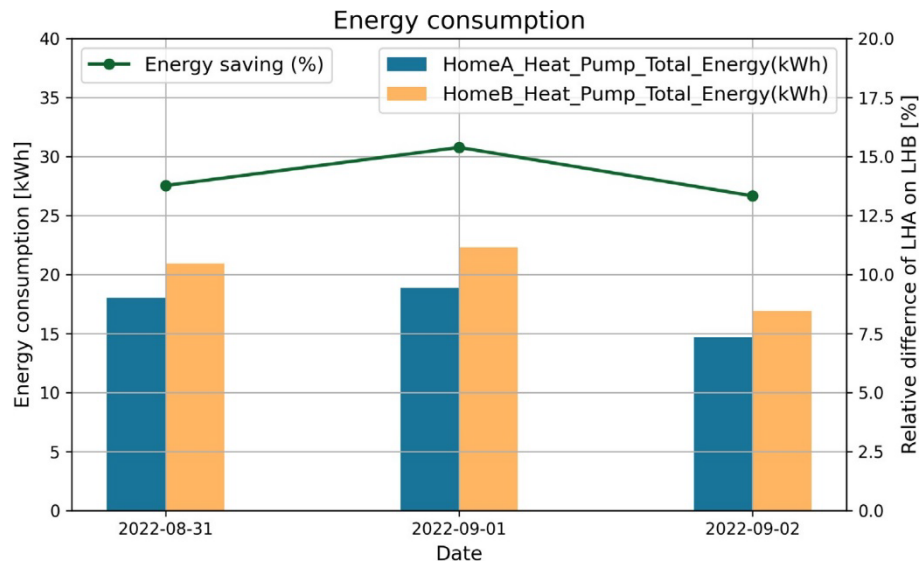


Figure 81. Energy consumption in Lab Home A and Lab Home B under occupancy adaption scenario 1

7.2.3.2 Adaptive to the Fault

Figure 81 shows an example day (Sept. 18, 2022) of the unmet hours comparison between Lab Home A and Lab Home B. In Lab Home B (baseline), the thermostat setpoint is constant at 76°F, while the precooling control strategy is implemented in Lab Home A (test home) with MPC-informed rules. It can be seen that with the adaptive control strategy in Lab Home A, all unmet hours (0.58°F-hr) are eliminated, compared to the baseline of Lab Home B. Figure 82 presents

unmet hours comparison of Lab Home A and B during the whole testing period. With precooling strategy, unmet hours could be decreased from 2.05°F-hr (Lab Home B) to 0.22°F-hr (Lab Home A). This benefit (difference between the control with/without precooling) can increase with the rise of outdoor temperature.

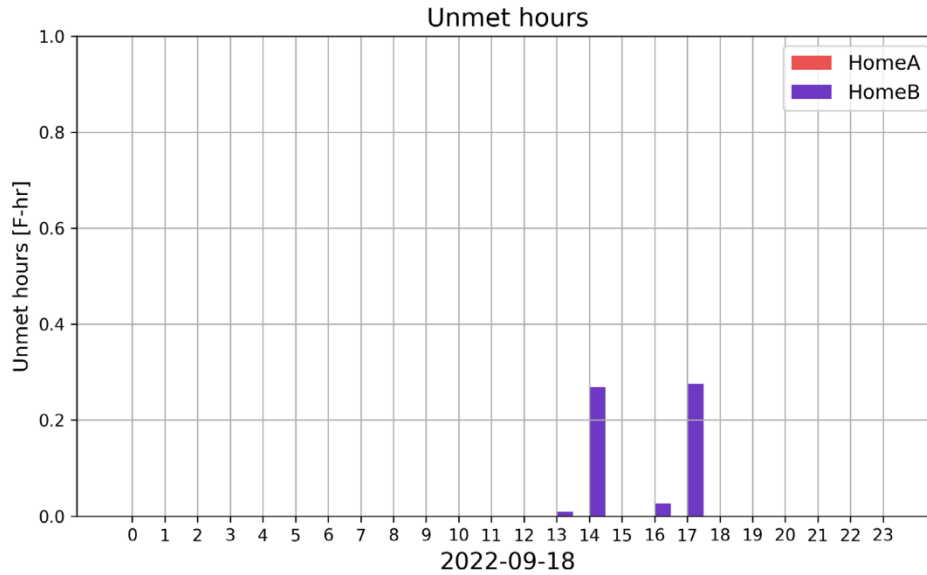


Figure 82. Unmet hours comparison between Lab Home A and Lab Home B

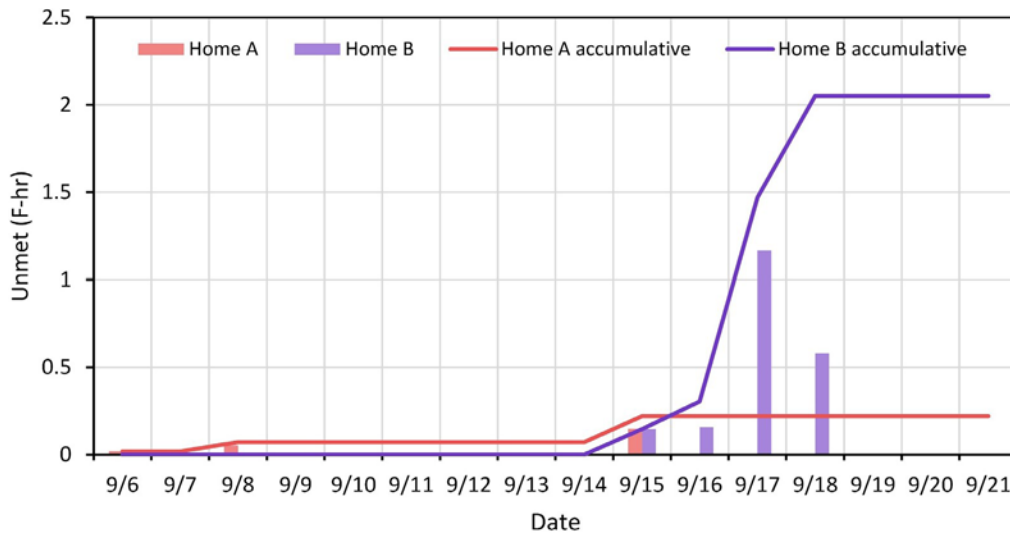


Figure 83. Unmet hours comparison of Lab Home A and B during the whole testing period

7.2.4 Data Predictive Control

The online DPC framework was executed from Aug. 23 at 8 a.m. local time (at the PNNL facility) until Aug. 29 at 8 a.m. local time. Figure 83 shows a timeline of the testing period with points of interest denoted.

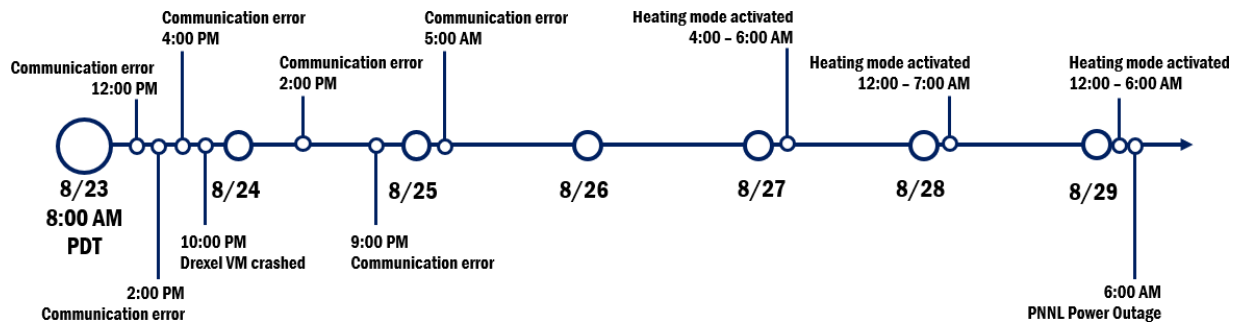


Figure 84. Online DPC testing timeline

For the first 48 hours of the testing, there were several communication errors (DU virtual machine crash, time zone mismatch, etc.) that resulted in the control framework quitting unexpectedly. The data during the communication errors was discarded from analysis. After August 25th at 6:00 AM, the DPC control framework was executed uninterrupted until August 29th at 6:00 AM, when the PNNL facility experienced a power outage.

At three points during the last three days of the testing period, the HVAC system accidentally entered heating mode due to an error present in the DPC control framework. The data from these periods were also discarded from analysis.

The DPC framework controlled the ecobee thermostat cooling setpoint remotely from the Drexel University campus. Figure 84 shows a plot of the setpoints for both Lab Home B (baseline, for reference), and Lab Home A (controlled by DPC). The plot also shows the HVAC energy for each Lab Home and the occupancy for Lab Home A. The insights from this plot are summarized in Table 33. The DPC strategy resulted in a 21% reduction in HVAC system power usage. It is believed that this reduction would be greater had the communication errors and heating mode issues been avoided. However, as can be seen from the plot in Figure 84, there is a high zone temperature in the evening hours, immediately after the lab home becomes occupied. These temperatures break the comfort constraints and result in 24 out of the 57 occupied hours (some occupied hours were removed due to erroneous data) being unmet hours for occupant comfort. Thus only 58% of the occupied time was met the occupant comfort criteria. As discussed in detail below, there was a discrepancy between the ecobee thermostat measurement and the iComfort sensor thermostat measurement at the same location. The zone temperature forecasting model (discussed previously) used in the DPC strategy used the iComfort sensor zone temperature measurement in its predictions as part of the supervisory control. Due to the 2°F difference present in the ecobee thermostat measurement used for local control, the zone temperature was always higher than the DPC strategy's forecast. This resulted in loss of efficiency of the strategy and contributed to the unmet hours for occupant comfort.

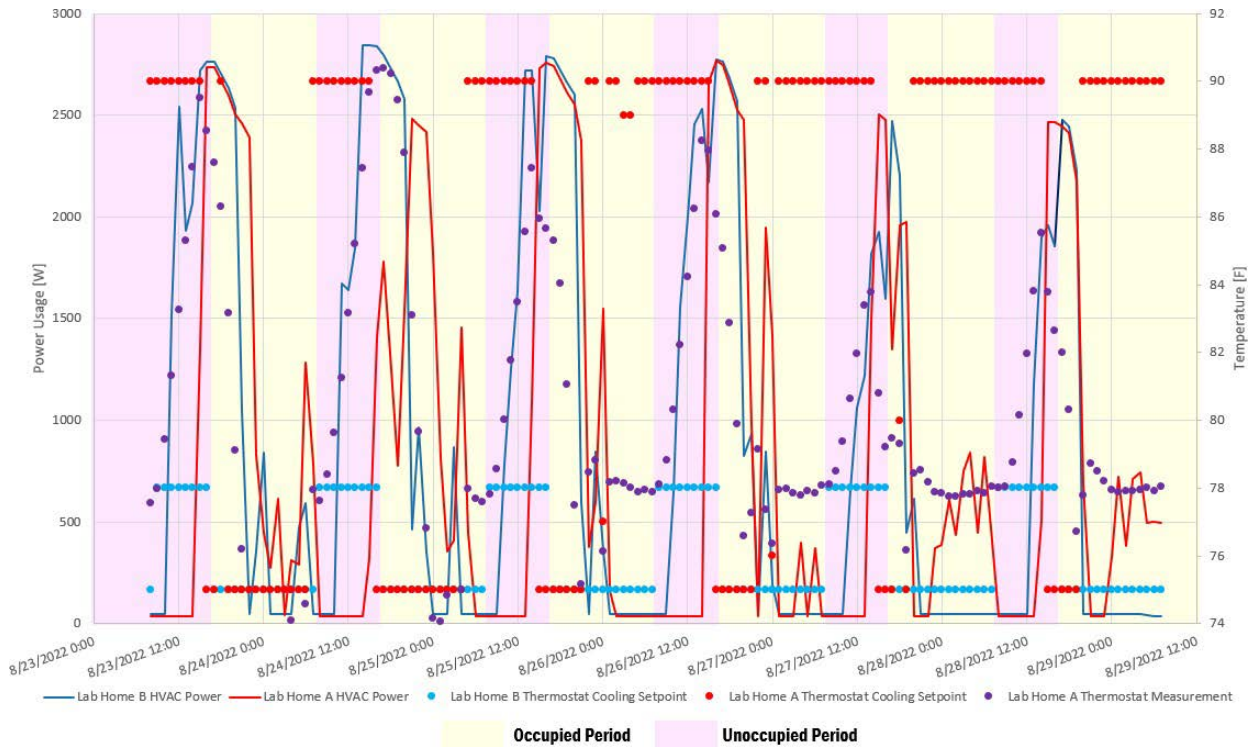


Figure 85. Drexel University online DPC testing period—thermostat setpoint and power

Table 33. Drexel University Online DPC Testing Period—Percentage Power Saved

Period	HVAC System Power Savings [%]
Whole period (8/23–8/29)	10
Whole period (communication errors removed)	21
8/23*	18
8/24*	41
8/25*	15
8/26*	13
8/27*	7
8/28*	7
8/29**	N/A

* With communication errors removed

** No data due to heating mode issue/facility power outage

7.3 Summary

This section demonstrates the stability of iComfort sensors and cloud server in an established lab testing bed, as well as the effectiveness and efficiency of developed FDD methods and adaptive control strategies. Two identical Lab Homes were used for the field testing. Among them, Lab Home A serves as the test home, while Lab Home B is the baseline home.

First, most of the sensors worked well during the experiment and streamed measurements to the cloud every minute. The 16 iComfort sensors collected and pushed 1,413,072 sets of temperature and humidity data (and airflow data from four of them). The cloud database's API served more than 5,198,000 query requests from the detection and control algorithms. The cloud database was working at 100% availability and was completely error-free during the experiment.

Secondly, for the FDD strategy demonstration, the accuracy of FDD for the heat pump system was 90.18%, counting all cases (including fault-free ones), with zero false alarms. The detection accuracy is 96.4%. Both of these two metrics met the required value of 80%.

Furthermore, for the energy saving from the home temperature setpoint control, 14% energy saving was obtained by occupancy-based setback strategies, or 10% was achieved by DPC. Both of them demonstrate $\geq 10\%$ energy saving required. In terms of thermal comfort improvement, unmet hours could be decreased from 2.05°F-hr (Lab Home B) to 0.22°F-hr (Lab Home A), which will help improve residents' thermal comfort under the malfunction of HVAC systems or in a heat wave.

The uncertainty analysis for the lab testing can be found in Appendix E.8.

8. Economic Analysis

8.1 Introduction

Commercial and residential buildings together comprise about 40% of primary energy consumption in the United States. While building automation systems intended to increase energy efficiency, lower operating costs, and improve indoor air quality have widely been adopted in the commercial sector, similar integrated systems are rarely seen in households. However, according to EIA's Residential Energy Consumption Survey (RECS), the residential sector accounts for 55% of the energy used in U.S. buildings (EIA 2018a). Further, 51% of household annual average energy consumption is restricted to space heating and cooling (EIA 2018b). This energy usage is often exacerbated due to undetected faults or inefficiently designed/installed HVAC systems. Previous studies have shown that households often consume 30% more energy annually than needed due to HVAC installation, commissioning, and performance issues (Metzger et al. 2017). In addition, most residential buildings do not have any indoor environment monitoring systems other than a single thermostat, making it difficult for occupants to operate their households with optimized comfort and energy usage (EERE).

As described, the primary goal of this project is to develop and demonstrate a scalable and low-cost IoT-based comfort control and automated fault diagnostics system for energy-efficient homes. The research integrates low-cost sensors, IoT-enabled devices, data analytics, and advanced controls to produce a novel residential occupant comfort and efficiency control system which can also automatically diagnose faults for HVAC systems. This project aims to fill the current market gap in the residential sector of products by providing integrated comfort control that considers the real-time performance of residential HVAC systems and occupants' thermal comfort.

The economic analysis in this section is intended to describe the value provided by the developed product and discuss current and future market opportunities, barriers, and applicable standards. The markets for sensors, AFDD systems, and smart home energy management systems are evaluated. In addition, some technical, economic, and other considerations are discussed in detail.

The primary audience for this section includes developers of the above-mentioned devices who could use this information to guide their innovations and marketing strategies. The secondary audience are homeowners who seek an overview of the residential sensors, AFDD products, and smart home management platforms currently available in the market. Research/consultancy firms, organizations working on building energy management, and professionals in the residential energy sector can also glean relevant insights.

8.2 Market Opportunity

The target market for this research is residential buildings with a focus on HVAC equipment and system and associated controls. The main objective of living environment conditioning for residents is to satisfy their well-being and work efficiency requirements, which became more

significantly essential when remote work became prevalent in 2020 (Mehta 2021). In the United States, 108.9 million out of 123.5 million housing units had installed air conditioning (AC) equipment as of 2020 (EIA 2020a). This number was 94 million of 113.6 million in 2009 (EIA 2009) and 82.9 million of 100.4 million in 2001 (EIA 2001). In addition, buildings consume around 40% of total energy (with residences accounting for 22% and commercial buildings consuming 18%) (EIA 2008) and are responsible for 35% of carbon emissions (EIA 2020b). Among them, almost half is consumed by HVAC (L. Wang and Hong 2013). In terms of home energy management systems, the smart thermostats global market is growing by 31% annually through 2024 (Yahoo Finance). The smart thermostat market is projected to reach \$6.2 billion by 2028 with a 17.5% market share (see Figure 85) (Prnewswire). Reducing building HVAC energy consumption, especially in the residential sector, has a significant potential to contribute to the 2030 U.S. greenhouse gas pollution reduction target (The White House 2021).

U.S. Smart Thermostat Market Size, 2017-2028 (USD Million)

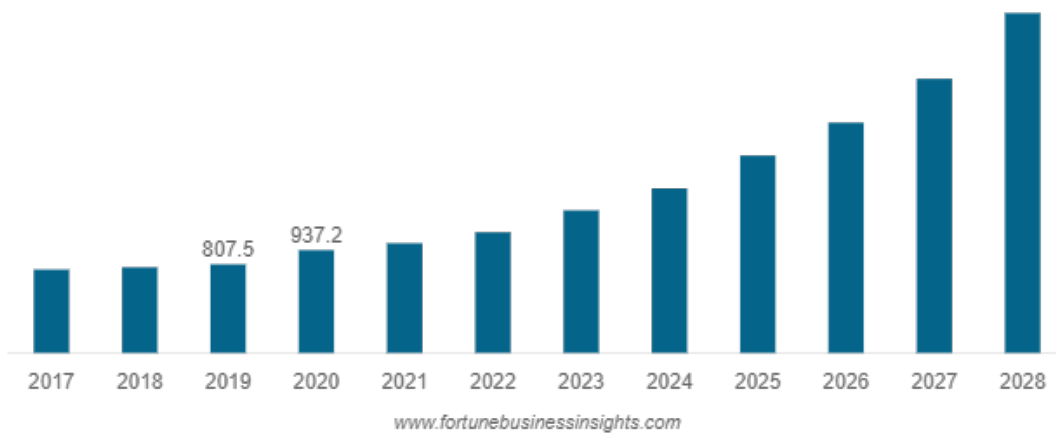


Figure 86. U.S. smart thermostat market size trend (Prnewswire)

Currently, the HVAC system sales for the residential market are a single distribution channel: from the manufacturers who design and build the HVAC equipment, to the distributors who sell it and the HVAC contractors, then to the homeowners who hire the HVAC contractors to install. HVAC controls (e.g., thermostats) are typically installed concurrently with the HVAC systems. The disconnection between the HVAC equipment and control manufacturers has left the market disjointed. Therefore, homeowners have alternatives for the optimized control system in their homes, other than the default systems that come with their HVAC units. Recent development and adoption of smart home technologies, such as IoT thermostats and IoT vents, demonstrate the strong desire for homeowners to adopt straightforward and cost-effective technologies to improve their comfort and life quality.

Building mechanical systems are inherently subject to gradual degradation and capacity decline over time. Typical operational faults may arise from improper installation, equipment degradation, sensor offset, or control logic problems (Yanfei Li and O'Neill 2018). Soft faults,

such as heat exchanger fouling, or a slow leakage through ductwork, are more difficult to detect and diagnose compared to hard failures (Breuker and Braun 1998a). Although some of these faults do not occur severely, they could lead to premature failure of the HVAC components, dissatisfied thermal comfort, or unnecessary energy cost. Based on a 2017 PNNL report (Metzger, Goyal, and Baechler 2017), if 60% of homes in the U.S. were wasting 30% of their HVAC energy on performance issues that could be fixed with better HVAC control, about 146 billion kWh, or 0.5 quads, could be saved. Therefore, FDD research applied to the air-cooled VCC system is attractive because this kind of system is widely used in most residential buildings and half of the commercial buildings in the U.S., such as rooftop units, heat pumps, etc. (Hu and Yuill 2021). There currently is no technology that is able to provide cost-effective AFDD and adaptive controls for maximized energy efficiency and occupant thermal comfort in residential homes.

On the other hand, frequent maintenance or replacement for building HVAC systems is not practical. Degradation easily results in difficulty in meeting the required thermal environment, especially amid a heat wave (Zuo et al. 2015). Overheating is harmful to human health and productivity, and can lead to heat-related illnesses, like heat stroke, heat cramps, or fainting (Howe and Boden 2007). This concern is further amplified by the impacts of climate change, which accelerates the frequency of extreme weather events and thus has been a hot topic in recent years (Simon Brown 2020).

To deal with severe heat wave conditions, several coordinated responses can be adopted:

- 1) Replace HVAC systems with new ones with a higher capacity
- 2) Retrofit the house (e.g., add envelope insulation or replace the windows)
- 3) Purchase thermal storage (e.g., an ice tank) to supplement the cooling ability of the original HVAC system to combat heat waves.

All these measures require additional initial investments, which are usually not feasible for ordinary families. An alternative method to the above steps is precooling, which is a control strategy that pre-cools the building preceding a given period to enhance the cooling effect by only utilizing the thermal mass of building envelopes and home furniture rather than extra equipment/devices. As long as the programmable thermostat or remote thermostat is installed in the house, precooling can be applied to alleviate the effect of a heat wave to some extent. This is what is required as a flexible supplementary measure for air conditioning amid a heat wave period.

Considering the limited computation ability and the requirement of higher control quality, the MPC-informed rule-based control strategy is cost-effective to be applied in residential thermostats in the form of “if-then.” It conducts the MPC offline in one hub, likely on a large scale, and then extracts several rules from its operation results (May-Ostendorp 2012).

Consequently, these rules can be easily applied in ordinary houses. The goal is to select a minimum set of inputs, feed them to the rule-based controls and maintain the same or close levels of thermal comfort and energy consumption with the MPC simultaneously. Compared to

merely expert knowledge-involved rules, MPC-informed rules are more optimal and automatic by deriving the merits of MPC operation. At the same time, it avoids the online execution of computationally expensive optimization, thus alleviating the computation load in building HVAC controllers.

8.2.1 Current Market

There is already a sizeable market for the smart home energy management system, including sensors, AFDD, and indoor climate control. In this subsection, the smart home energy management system market is introduced, while details regarding sensor market and AFDD market can be found in Appendix F.4 and F.5.

Smart Home Energy Management Systems

The United States is currently the leader in the deployment of home energy management systems (Y. Liu et al. 2016). Key technology companies in the smart home energy management market include Aclara, Nest Labs, General Electric Company, Logitech, Honeywell, Trilliant, and C3 Energy (Market Research Future).

Some of the open-source home energy management systems currently available include Building Energy Management Open-source Software (BEMOSS), WattDepot, Home Assistant, Honda's Smart Home, Neurio Home Energy Monitor, Freedomotic, and Power Matcher Suit (Zandi et al. 2018). While these tools are inexpensive due to their non-proprietary nature and can be used by different vendors, they can be difficult and time-intensive for non-technical users to deploy (Zandi et al. 2018). Google Home, Apple Homekit, Samsung Smartthings Hub, DreamWatts, and Siemen's Synco are some proprietary home energy management systems currently available in the market¹ (Zandi et al. 2018; Zafar et al. 2020). Proprietary home energy management systems are generally easy to deploy and have user-friendly interfaces. However, they can be expensive and require extensive installation by expert contractors (Zandi et al. 2018).

Advances in cloud computing, data analytics, and IoT-enabled devices will drive the growth of this market in the next few years. The communication technologies and software platforms of smart home energy management systems should be interoperable and compatible with appliances from different vendors (Y. Liu et al. 2016). The information collected by the smart home energy management system must be encrypted with proper cybersecurity measures to maintain customer privacy and protection (Zandi et al. 2018). Energy management in different homes in a community can be coordinated for increased demand response potential and to avoid rebound peaks.

¹ Note that throughout this report, we include several different company names. Building America, the Department of Energy, and the authors of this report do not endorse any specific company or product. These are included only as examples of currently available technology.

Very few people currently live in homes with smart energy controls, and most homeowners are unaware of the smart home energy management system products currently available on the market. While significant energy savings and cost reduction potential using smart home energy management systems have been demonstrated in some articles (Pang et al. 2021; Aliero et al. 2021; H. Zhang et al. 2020), these products should be marketed widely to the non-technical community and particularly to homeowners, who are the key stakeholders in this spectrum.

As more electric utilities start offering time-varying electricity prices like time-of-use rates or demand charges, homeowners might be motivated to invest in these technologies to save money without having to micromanage the operation and scheduling of multiple devices.

Several utility-led pilot studies and academic simulation-based literature have demonstrated that smart thermostats can yield significant HVAC energy savings in the residential sector (Pang et al. 2021). Smart thermostats had an approximate adoption rate of 7% in 2018 (Koupaei et al. 2020). Customer adoption of smart thermostats can further be increased by promoting awareness and utility offered rebates. Several utilities like Southern California Edison, Austin Energy, Pacific Gas & Electric, Georgia Power, and Baltimore Gas & Electric already offer rebates to customers investing in smart thermostats (some of these utilities require the customers to opt for time-varying pricing plans or request control of their thermostats during peak demand events to avail the rebates) (PGE ; Austin Energy). More utilities can follow in their footsteps to increase energy efficiency and cost savings in the residential sector.

Potential adopters of the developed IoT-based comfort control and fault diagnostics system are residential heat pump/air-conditioner manufacturers, residential service companies, smart home automation companies, and utility companies.

Table 34 describes prevailing smart thermostats on the market. Their features can be categorized into several groups:

- 1) Energy saving strategy: Provide temperature control during the time in need with multiple approaches, like a setback when residents are away, or turning off when the window/door is open.
- 2) Thermal comfort improvement: Precool/preheat the home before occupants arrive with the geofencing technique.
- 3) Alleviate occupant operation: Learn occupancy schedule/thermal preference automatically.
- 4) Integrated with demand response to the grid: Marginally adjust the indoor temperature around the community grid peak.
- 5) Carbon care: Help consumers conduct carbon trade.
- 6) Fault alert: Mostly report abnormal indoor temperature and remind filter replacement.
- 7) Energy report and saving advice: Help consumers understand the energy performance of the house, and provide advices on energy savings opportunities.

Table 34. Specification of Commercial Thermostats in the Market

Product Name	Brand	Price	Annual Energy Cost Saving	Saving Advice	Energy Report	Control From Anywhere	Away Setback	Geofencing	Door/Window Open	Schedule Learning
Amazon Smart Thermostat	Amazon	\$80	Average of \$50	N	N	Y	Y	N	N	N
AccuLink Platinum 850	American Standard	Not specify	Not specify	N	N	Y	N	N	N	N
Cor TP-WEM01 Smart Thermostat	Carrier	\$270	Not specify	N	N	Y	N	N	N	N
Infinity	Carrier	Not specify	~23%	N	N	Y	Y	N	N	Y
ecobee3 lite	ecobee	\$150	~23%	Y	Y	Y	Y	Y	Y	Y
ecobee Smart Thermostat Enhanced	ecobee	\$190	~26%	Y	Y	Y	Y	Y	Y	Y
ecobee Smart Thermostat With Voice Control	ecobee	\$220	~26%	Y	Y	Y	Y	Y	Y	Y
ecobee Smart Thermostat Premium	ecobee	\$250	~26%	Y	Y	Y	Y	Y	Y	Y
Sensi Smart Thermostat	Emerson	\$130	23%	N	Y	Y	N	Y	N	N
CYNC Smart Thermostat	GE	\$120	Not specify	N	Y	Y	Y	N	N	N
Google Nest Thermostat	Google Nest	\$130	Not specify	Y	N	Y	Y	N	N	N
Google Nest Learning Thermostat	Google Nest	\$249	Heating 10-12%, Cooling 15%	Y	Y	Y	Y	Y	N	Y
T9	Honeywell	\$180	Not specify	N	Y	Y	Y	Y	N	N
T10 PRO	Honeywell	\$230	Not specify	N	Y	Y	Y	Y	N	N
MoesGo Programmable WiFi Smart Thermostat	MoesGo	\$150	Over 23%	N	N	Y	N	N	Y	N
CT50 WiFi Smart Thermostat	Radio	\$65	Not specify	N	Y	Y	N	Y	N	N
Sensibo Sky	Sensibo	\$159	~40%	N	N	Y	Y	Y	N	N
Sensibo Air	Sensibo	\$199	~40%	N	N	Y	Y	Y	N	N
Sensibo Air PRO	Sensibo	\$279	~40%	N	N	Y	Y	Y	N	N
ComfortLink® II XL850 Thermostat	Trane	\$375	Not specify	N	N	Y	N	N	N	N
XL824 Thermostat	Trane	\$375	Not specify	N	N	Y	N	N	N	N
ComfortLink® II XL1050 Thermostat	Trane	\$675	Not specify	N	N	Y	N	N	N	N
Wyze Programmable Smart WiFi Thermostat	Wyze	\$74	Not specify	Y	Y	Y	Y	Y	N	N
Zen Thermostat	Zen	\$199	Not specify	N	N	Y	N	N	N	N

Product Name	Brand	Thermal preference learning	Specific room control	Humidity control	Community peak	TOU	Shift usage to cleaner grid time	Carbon trade	Fault alerts*
Amazon Smart Thermostat	Amazon	N	N	N	N	N	N	N	Y
AccuLink Platinum 850	American Standard	N	N	Y	N	N	N	N	Y (2)
Cor TP-WEM01 Smart Thermostat	Carrier	N	N	Y	N	N	N	N	N
Infinity	Carrier	N	Y	Y	N	N	N	N	Y (1, 2)
ecobee3 lite	ecobee	N	Y	Y	Y	Y	Y	N	N
ecobee Smart Thermostat Enhanced	ecobee	N	Y	Y	Y	Y	Y	N	N
ecobee Smart Thermostat With Voice Control	ecobee	N	Y	Y	Y	Y	Y	N	N
ecobee Smart Thermostat Premium	ecobee	N	Y	Y	Y	Y	Y	N	N
Sensi Smart Thermostat	Emerson	N	N	N	N	N	N	N	Y (2, 3, 4)
CYNC Smart Thermostat	GE	N	N	N	N	N	N	N	N
Google Nest Thermostat	Google Nest	N	Y	N	N	N	N	N	Y (1)
Google Nest Learning Thermostat	Google Nest	Y	Y	N	Y	Y	Y	Y	Y (1)
T9	Honeywell	N	Y	N	Y	N	N	N	Y (1, 4)
T10 PRO	Honeywell	N	Y	Y	Y	N	N	N	Y (1, 4)
MoesGo Programmable WiFi Smart Thermostat	MoesGo	N	Y	N	N	N	N	N	N
CT50 WiFi Smart Thermostat	Radio	N	N	N	N	N	N	N	Y (1, 4)
Sensibo Sky	Sensibo	N	N	N	N	N	N	N	Y (4)
Sensibo Air	Sensibo	N	N	N	N	N	N	N	Y (4)
Sensibo Air PRO	Sensibo	N	N	N	N	N	N	N	Y (4)
ComfortLink II XL850 Thermostat	Trane	N	N	N	N	N	N	N	Y
XL824 Thermostat	Trane	N	N	N	N	N	N	N	Y
ComfortLink II XL1050 Thermostat	Trane	N	N	N	N	N	N	N	Y
Wyze Programmable Smart WiFi Thermostat	Wyze	N	Y	N	N	N			N
Zen Thermostat	Zen	N	N	N	N	N	N	N	N

*Fault number: 1-abnormal indoor temperature; 2-system needs maintenance; 3-abnormal efficiency; 4-filter replacement

8.2.2 This Product and Service

Compared with currently existing commercial products, the outcome completed in this project can be more cost-effective and multiple-functional. The team developed an IoT-based comfort and efficiency control system that can provide AFDD for central air conditioning, heat pumps, and air ducts, and conducts fault-adaptive controls in the residential sector. The schematic of the developed system is depicted in Figure 86. The product has three main components that are unique from the existing commercial products:

- 1) An inexpensive wireless distributed sensor system (with low-cost temperature, airflow, and humidity sensors) and a Raspberry Pi-based local hub that interfaces with the cloud and other IoT-enabled devices (e.g., thermostats).
- 2) AFDD for HVAC systems that utilizes real-time information from the sensor system.
- 3) A smart home energy management system to optimize energy efficiency and occupant comfort in buildings using advanced controls. The smart home energy management system includes a whole-house energy forecasting model, an indoor thermal environment model, and an occupant thermal comfort forecasting model.

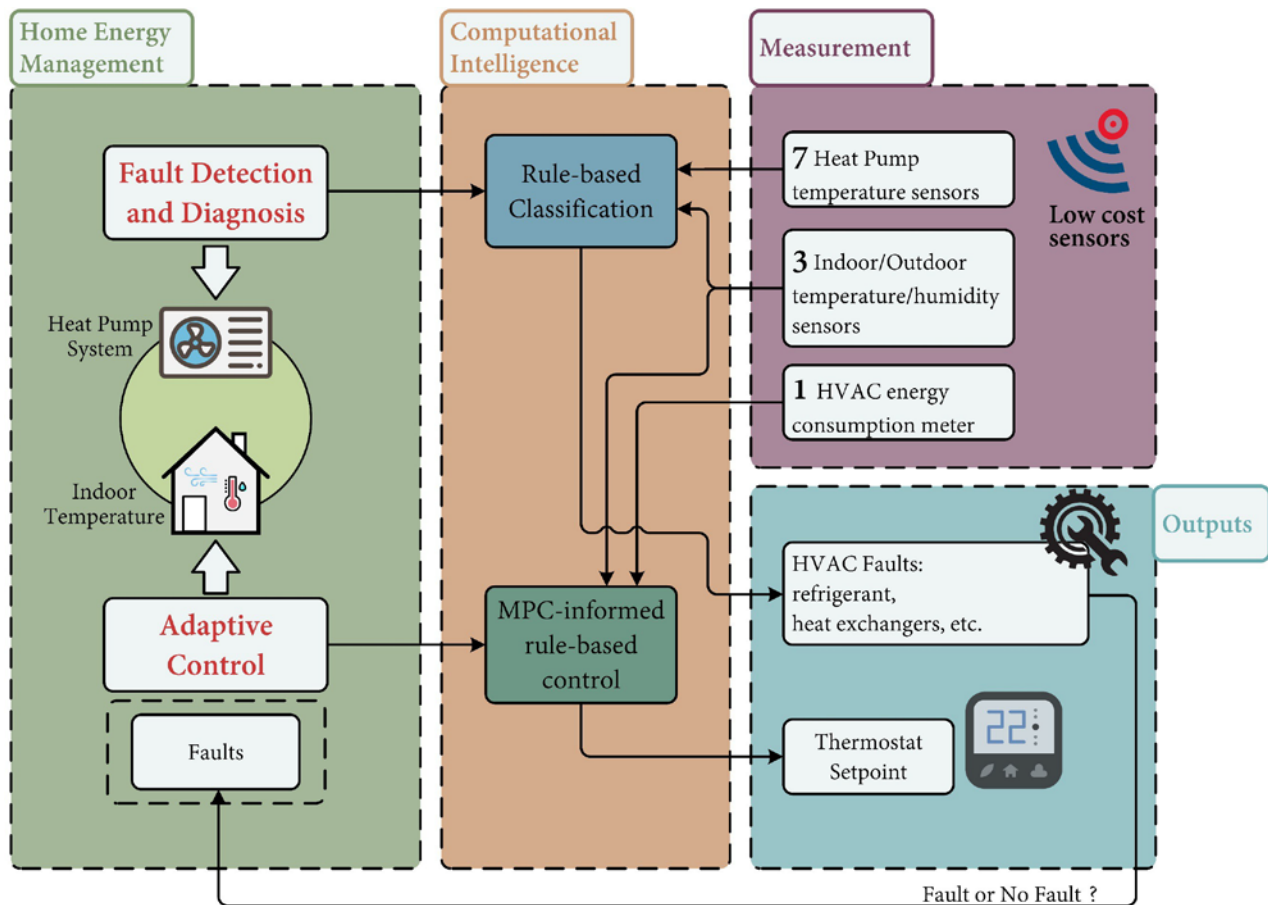


Figure 87. Structure of developed smart home energy management system

An interface demo for indoor climate monitoring in this home energy management systems is also developed. A screenshot example is shown in Figure 87, while the screenshot of all the interface is presented in Appendix F: Market analysis. This system can monitor real-time data from different locations in one house. The current indoor climate status and the historical data can be easily accessed.

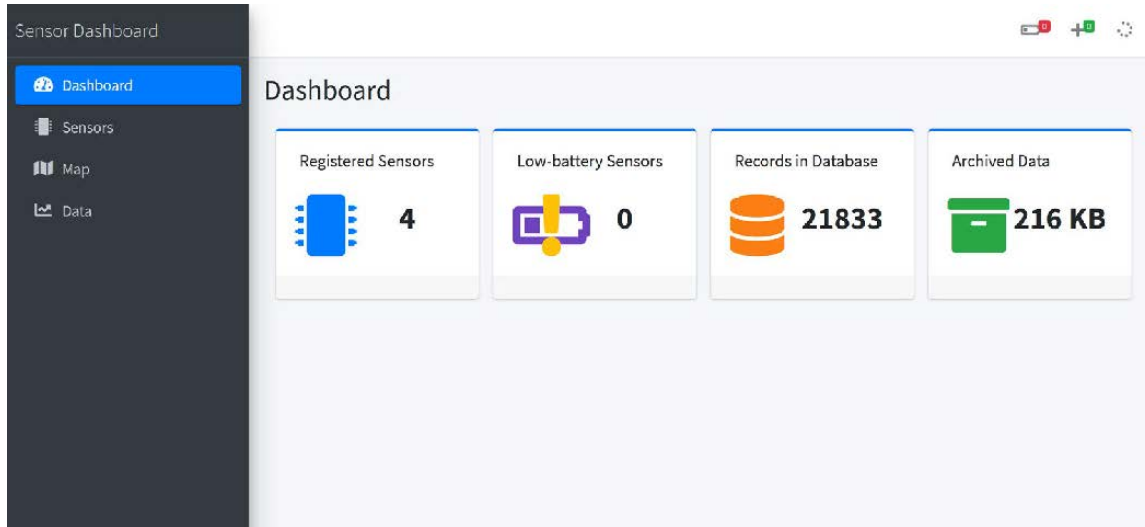


Figure 88. Interface demo for indoor climate monitoring in this home energy management systems

8.3 Life Cycle Cost Analysis

8.3.1 Unit Cost of Developed Devices and Services

The cost for the smart home energy management system completed in this project consists of three parts: the wireless sensors, the local hub, and the cloud service. Two sensors (temperature/humidity sensor and temperature/humidity/airflow sensor) are developed in this project. As listed in Table 35, the hardware cost for those two is \$14.10 and \$55.80, respectively. The assembly cost is approximately \$17 for one sensor, which was quoted in the quantity of 200. The local hub that communicates with the wireless sensors, collects the sensor data, and uploads the distributed measurement results to the cloud, is implemented using Raspberry Pi. The local hub costs \$76.25 on average. Amazon Web Service (AWS) serves as the Cloud system to collect, store, and analyze data submitted from hubs and to provide a user interface through a website. Its cost depends on the sensor numbers (i.e., the number of data streams) and the frequency of receiving and storing data. According to our application, the cost is \$0.13 per month for one wireless sensor with a data streaming timestep of 5 minutes.

Table 35. Unit Cost of the Hardware and Software for iComfort Smart Home Control System

Category	Product Name	Cost
Wireless Sensor	Temperature/Humidity Sensor	\$14.10
	Temperature/Humidity /Airflow Sensor	\$55.80
	Assembly fee	\$17.00
Local Hub	Raspberry Pi	\$76.25
Cloud	Amazon Web Services (monthly per sensor)	\$0.13

8.3.2 Cost-Effectiveness Analysis

This study conducts a cost-effectiveness analysis following the working procedures in NIST Handbook 135 (Kneifel and Webb 2020). A diagram is presented in Figure 88 to illustrate the structure. The cost-effectiveness analysis framework includes three major parts: definition of life cycle cost analysis (LCCA) parameters, definition of key performance indicators, and collection of supporting data.

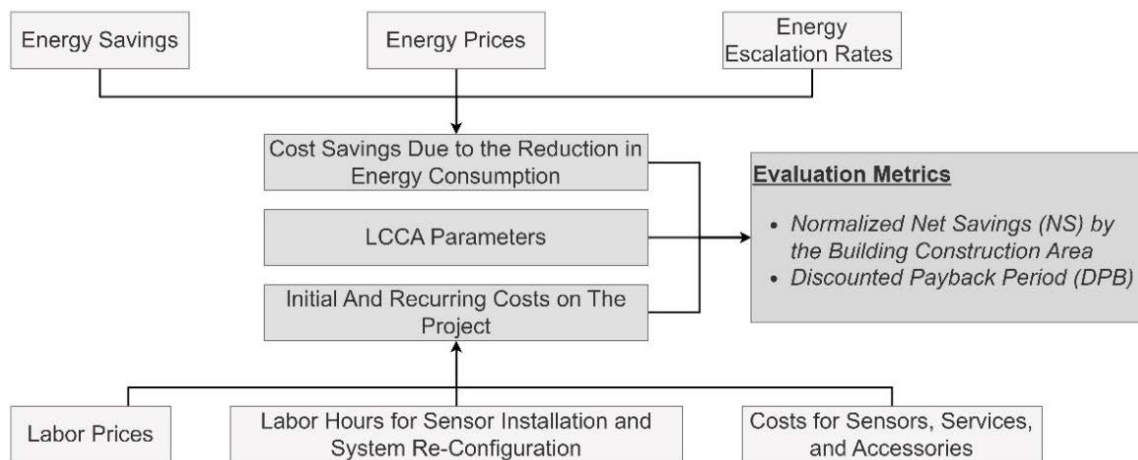


Figure 89. Structure of the cost-effectiveness analysis (Pang 2022)

8.3.3 Nationwide Energy Simulation Suite

The representative cities in the DOE residential prototype building models and top 30 population cities result in 41 cities, which are denoted in Figure 89. The climate zone that has the highest number of selected cities is 4A. It includes Baltimore (MD), Charlotte (NC), Cincinnati (OH), New York City (NY), Philadelphia (PA), St. Louis (MO), Washington DC (DC).

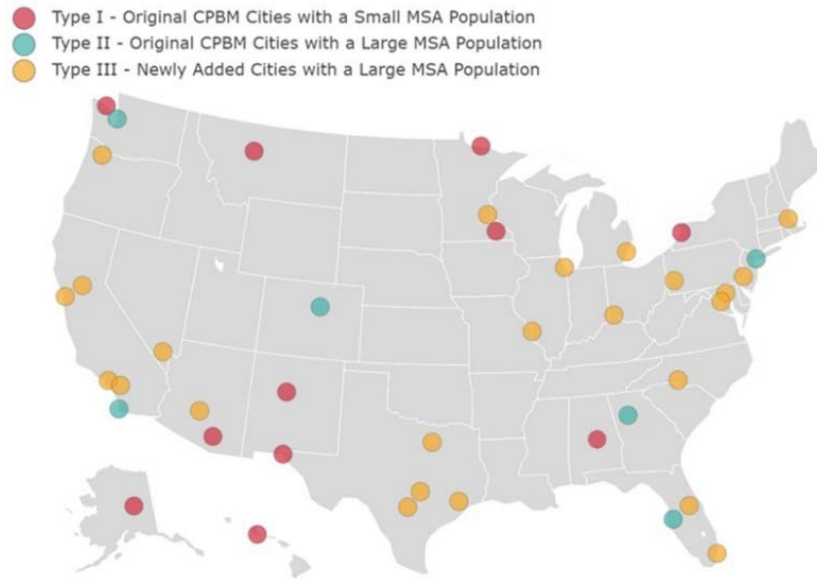


Figure 90. Geographical distribution of 41 selected cities in the US
MSA stands for metropolitan statistical area

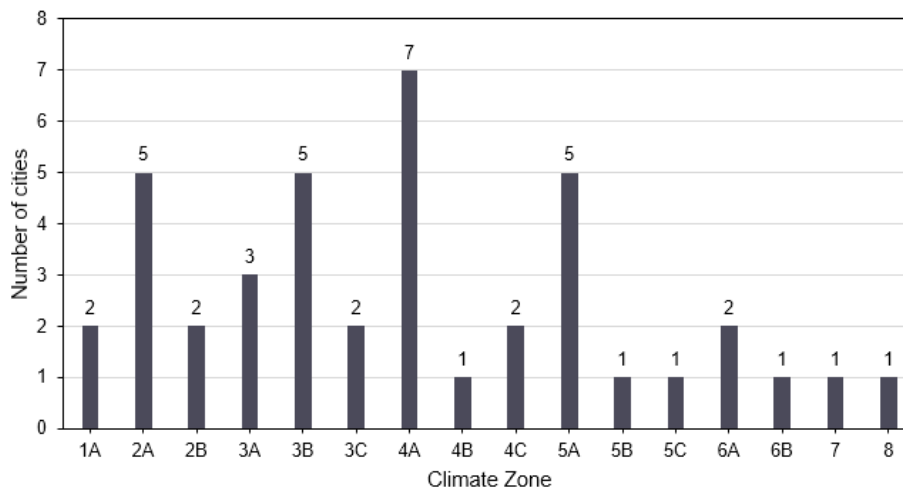


Figure 91. Number of selected cities in each climate zone

8.3.4 Definition of LCCA Parameters

The present investigation employs the LCCA plan outlined in a report by Hart and Liu (2015), which encapsulates the methodology employed by PNNL to appraise the cost-effectiveness of modifications in building energy codes. The selected plan primarily draws upon Scenario 2 (pertaining to private or business ownership) displayed in the report, albeit with necessary adjustments to account for the scope of this study. For example, the analysis period is truncated from 30 years to 10 years, given the lifespan of sensors, and tax deductions are excluded. The LCCA plan adopted in this study is presented in Table 36.

Table 36. LCCA plan

Parameter	Symbol	Value
Period of Analysis	L	10 years
Energy Price	/	Varies from city to city based on the BLS data
Energy Escalation Rate	/	Based on the NIST Energy Escalation Rate Calculator
Loan Term	M_L	10 years ($L = M_L$)
Loan Interest Rate	I	6.00%
Nominal Discount Rate	D_n	6.00% (same as I)
Real Discount Rate	D_r	4.06%
Inflation Rate	R	1.87% annual
Property Tax Rate	/	Not considered
Federal/State Income Tax Rate	/	Not considered

All supporting data that include electricity price, data for computing base-year energy cost savings, future energy cost savings, material costs and labor costs are all described in Appendix F: Market analysis.

8.3.5 Key Performance Indicators

8.3.5.1 Net Savings

In this study, the net savings (NS) metric is utilized to evaluate the cost savings of HVAC controls over the long term, relative to a base case. NS is computed by taking the difference between the operational savings derived from an energy efficiency measure and the corresponding additional investment, as expressed in Equation (19). To account for the effects of discounts over time, the LCCA method is employed, which aggregates all relevant project costs over a specified study period. Consequently, all costs and savings are discounted to present values (PV) for analysis. PV represents the current value, as of the base date, of a future cash payment or receipt, and its calculation is presented in Equation (20), where A_0 is the base-date price, D_n is the nominal discount rate, and t is the number of periods from the base date. The nominal discount rate D_n is typically defined as the interest rate that makes an investment indifferent between cash amounts received or paid at different points (Fuller et al. 2001).

$$NS = PV_{operational\ savings} - PV_{additional\ investment} \quad (19)$$

$$PV = A_0 * \frac{1}{(1 + D_n)^t} \quad (20)$$

Figure 91 shows energy saving on a yearly basis. Energy savings calculations are derived from baselines, utilizing the DOE prototype residential building EnergyPlus models from 41 selected cities across the United States. An average of 15% energy saving rate was used for each city in this study. Figure 92 shows the net saving under different escalation scenarios. It shows that Fairbanks has the highest net saving potential. Different escalation scenarios do not make a significant difference.

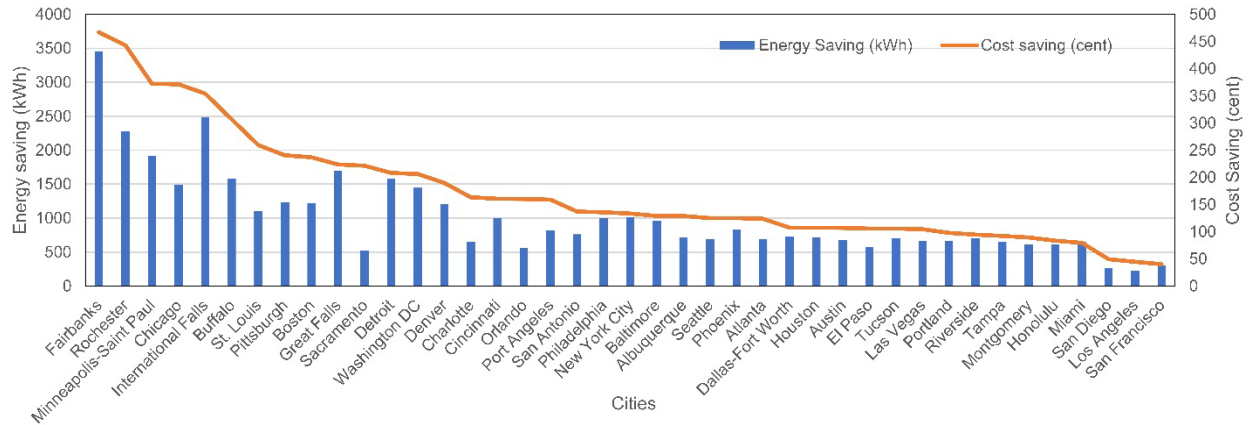


Figure 92. Energy saving and cost saving

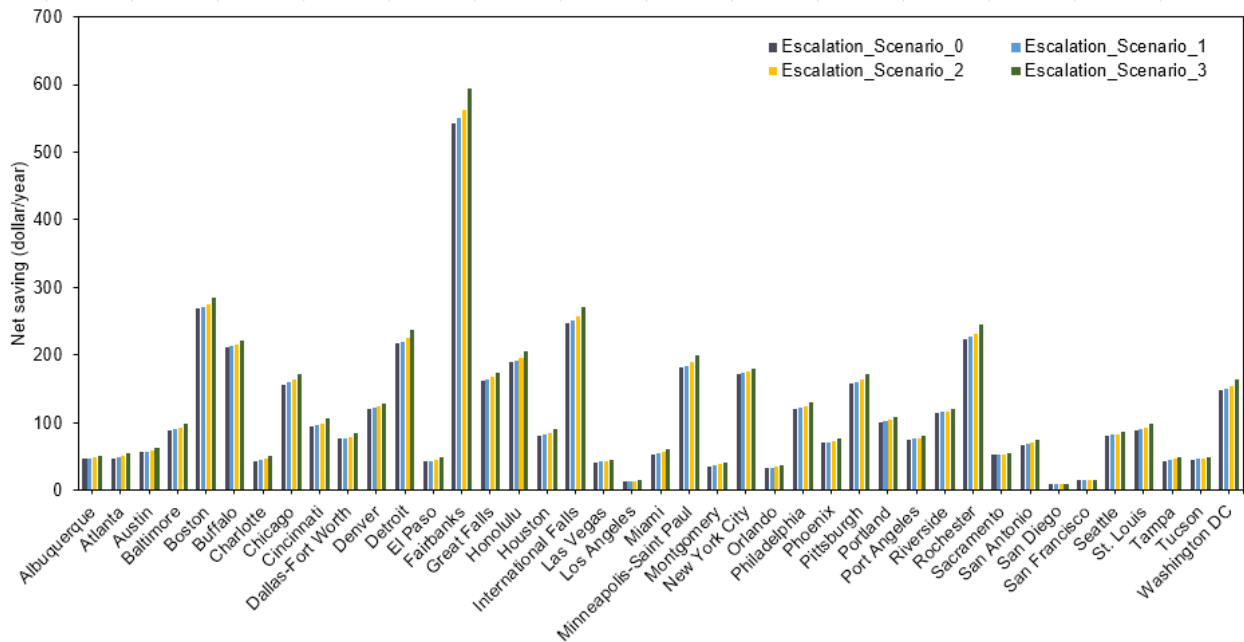


Figure 93. Year-based net saving

8.3.5.2 Payback Period

Discounted payback period is another metric that is frequently utilized in LCCA. The payback period is a measure of the duration required for the cumulative savings from a project to recuperate the investment cost and any associated expenses. Typically, two common payback period methods are employed in building energy analysis to determine the economic viability of a single project. The first method is the simple payback period, which does not factor in the time value of money and is generally deemed less precise. The second method is the discounted payback period, which takes into account the time value of money by incorporating discounted cash flows. In this study, the discounted payback period method is utilized due to its greater accuracy.

Figure 94 shows the discount payback period for 41 cities (only including escalation scenario 0, as there is not much different between different scenarios). Corresponding to net savings result, the cities that have a high net saving have a shorter payback period. Most cities can get full payback in four years. Eight cities can achieve full payback in one year. Three cities (Los Angeles, San Diego, and San Francisco) need more than five years to achieve full payback.

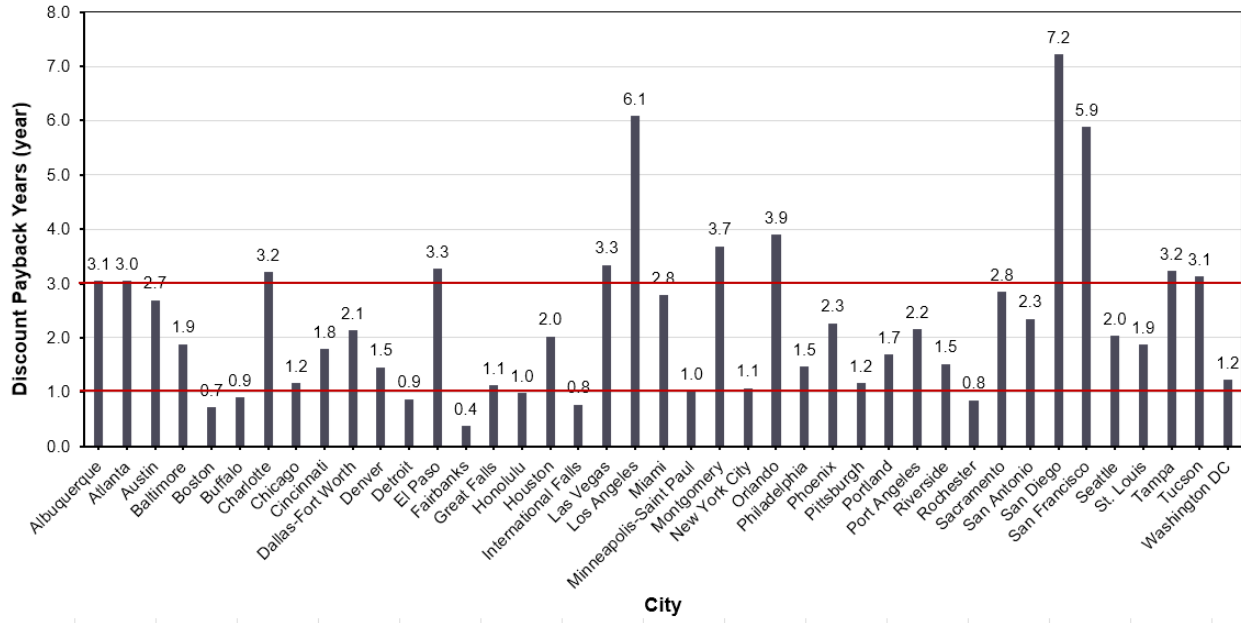


Figure 94. Discount payback period

8.3.6 Parametric Analysis

As investments are made in the development of available sensors, it is anticipated that the cost of these sensors will decline over time. For instance, the Funding Opportunity Announcement of the ARPA-E SENSOR program (ARPA-E 2018) has established a target price of \$0.08 per square foot of construction area for an occupant counting sensor as a benchmark for achieving acceptable monetary savings.

This study recognizes the considerable uncertainty associated with sensor network pricing and thus conducts a parametric analysis to examine the impact of sensor prices on the discounted payback period of an MPC-informed rule-based control project. Specifically, the cost of a sensor unit is varied across a range to assess the sensitivity of the discounted payback period to the price fluctuations and to determine at what price level a project can attain an acceptable discounted payback period.

The outcomes of this analysis are presented in Figure 95, where the x- and y-axes correspond to the representative city and the ratio of the sensor price to its original value, respectively. The cities are arranged in ascending order of cost-effectiveness, from left to right. Furthermore, the color of each cell corresponds to the discounted payback period duration. For Fairbanks, it is feasible to recover the initial investment within one year, regardless of whether the sensor network price is 10% or 200% of the prototype price. In the majority of other cities, it is possible

to recoup the costs within five years, even with a higher price compared to the prototype ones. A longer payback period is typically associated with warmer climates, such as Los Angeles, San Diego, and San Francisco. This correlation primarily arises because baseline energy consumption in these locations is lower, a factor that is largely attributed to the predominance of cooling. In severely cold locations, such as Boston and New York City, where heating is predominant, higher baseline energy consumption is typically observed. However, this relationship does not hold true universally. For instance, despite being a warmer climate, Honolulu still yields a shorter payback period since the energy price is higher in Honolulu.

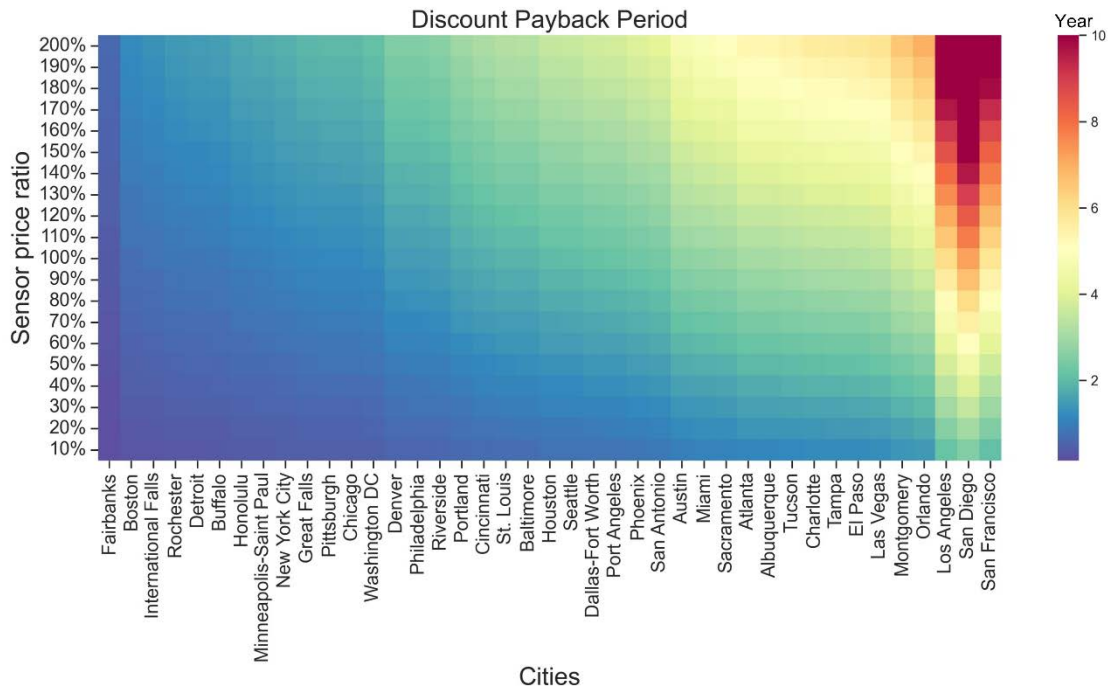


Figure 95. Discount payback periods for different sensor prices

9. Conclusions

This report presents a cost-effective and straightforward smart home system that delivers an improved occupant-comfort-oriented thermal environment compared to the baseline control.

We first created a low-cost and distributed wireless sensor system for energy and comfort-oriented control. To achieve the diagnosis and control goal, scalable algorithms for active learning-based models, AFDD, and adaptive controls were developed. Real-time house performance monitoring and automated diagnostics leads to fewer faults and avoidance of equipment damage. Improved occupant comfort through an adaptive control considers both HVAC health status and occupant’s thermal comfort. Improved energy efficiency avoids unnecessary energy use and operation cost for homeowners. At the end, all developed algorithms were demonstrated in PNNL’s lab testing, followed by an economic analysis. The technology details are summarized in Figure 96.

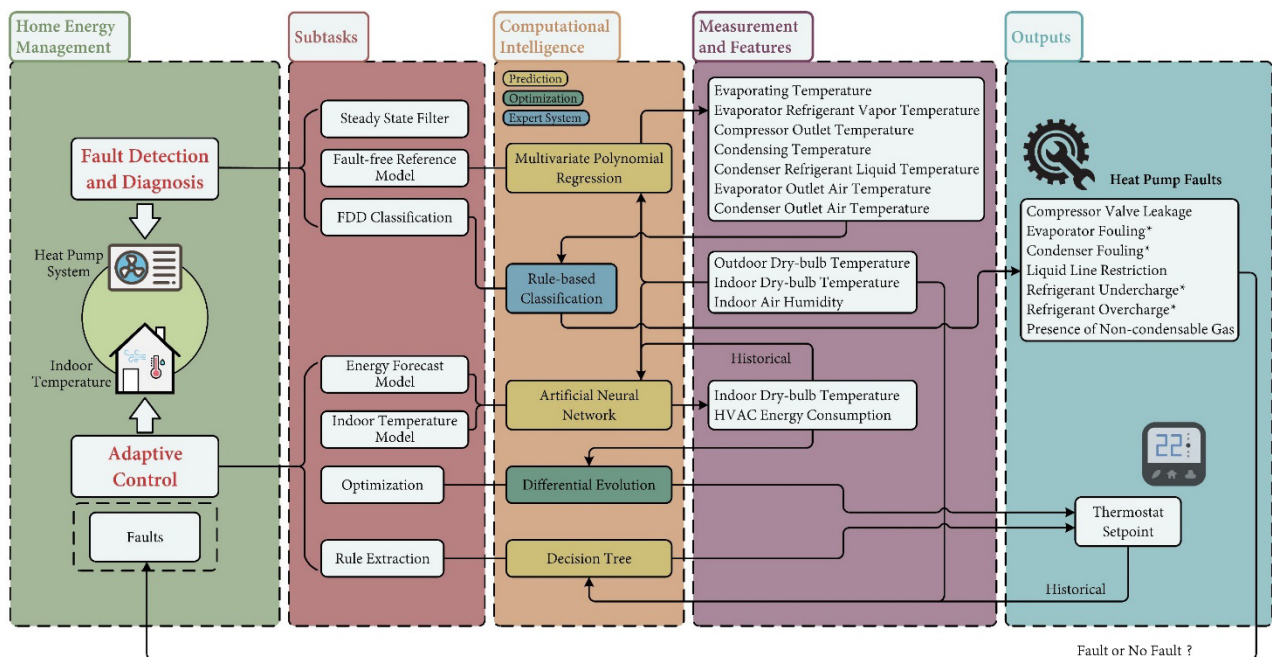


Figure 96. Smart Home Energy Management coupled with FDD for VCC systems and MPC/rule-based adaptive control

For the sensing platform, the wireless sensor modules have high resolution and are capable of measuring temperature and relative humidity with a resolution of 0.1°C and 0.1%, respectively. The local hub can communicate with the wireless sensors successfully, as well as collect data, and upload the measurement results to the cloud. The cloud service is provided by Amazon Web Services, and the data handling functions are developed within the AWS, which enables real-time data processing, storage, downloading, and display. The Temperature-Humidity Sensing Platform (THSP) was able to send readings to a hub within at least 100 meters in an open space and was able to penetrate at least three walls in an indoor test. Long-term testing showed that the system continuously worked for 60 days without human intervention, overcoming at least two

power outages and several network disconnections while successfully restoring its normal functions.

For the fault modeling of the residential HVAC system, an expandable fault library was created first, which consists of fault taxonomy that defines each fault and its systematic structure, as well as fault modeling elements such as fault attributes (direction types, bounds, and prevalence) and the corresponding objects and parameters in EnergyPlus. Fault modeling was implemented using EnergyPlus to generate 3,000 faulty models, representing 3000 fault scenarios with limited faults. These models can be used to simulate operational faults in residential HVAC systems and conduct a fault-relative investigation, including understanding the impact of faults, guiding and testing AFDD strategies, and assisting with adaptive controls.

For the learning models, a framework was developed for creating learning-based models to forecast HVAC energy consumption, zone temperature, and occupant thermal comfort. The framework was tested on a virtual testbed and then applied to real data from the PNNL lab test homes. The models were developed using machine learning techniques such as MARS and kSVM, and a systematic feature selection process was used to select the most relevant features for the models. The evaluation results showed that the developed models performed accurately according to desired performance metrics. Specifically, the HVAC energy consumption and zone temperature forecasting models achieved a normalized mean absolute error of <15%, while the occupant thermal comfort forecasting model achieved less than 10% misjudgment.

For the fault detection and diagnosis in the residential HVAC system, two cases are investigated: duct leakage and vapor compression cycle (VCC) system. The duct leakage case uses a robust multivariate temporal (RMT) based variate selection method to identify relevant variables for forecasting the target variable, and a convolution neural network (CNN)-based model to forecast the target variable during faulty periods. The VCC case investigates three existing rule-based AFDD methods and proposes a hybrid approach that integrates two of these methods to achieve higher diagnosis accuracy for different types of faults. The evaluation of the developed strategy for duct leakage detection showed that the fault can be flagged accurately at 100% at the beginning and end period of duct leakages when using the attic mean zone temperature as the target variate. The hybrid FDD approach achieved an overall diagnosis accuracy of 83.02% when counting only fault cases and 90.18% when counting all cases, including fault-free ones. The two-class confusion matrix for detection showed that all metrics were higher than 90%, with a detection accuracy of 96.4%.

For the comfort-oriented adaptive control, it is designed mainly for the condition where the degradation of residential HVAC systems is developed. To leverage the benefits of optimized control strategies from MPC and at the same time ensure their practical application in ordinary households, MPC-informed rule extraction is employed. This technique conducts the MPC offline in one hub, probably on a large scale, and then extracts several rules from its operation results. Consequently, these rules can be applied easily in ordinary houses. This framework is

implemented in the prototype building and generates several control rules in the form of a decision tree. It demonstrates that thermal comfort can be improved with MPC-informed rules generated by the simulation results: During the same run period of testing and training, unmet hours decrease from 10°C-hr to 5.1°C-hr during July 14 to Aug. 2, and from 0.6°C-hr to 0 during Aug. 13 to 22; when applied to a different period, the MPC-informed rule control generated from one period can mitigate the unmet hours from 9.2°C-hr to 5.2°C-hr, with a more than 60% decrease rate. Furthermore, the online computation time for MPC-informed RBC is significantly faster than the original MPC. On average, MPC consumes 870 minutes for a 10-day running period, while MPC-informed RBC finishes in 0.2 minutes on average with the same computer configuration, which is 4,350 times faster. This indicates that the developed approach is not only effective in improving thermal comfort but also efficient in terms of computational time.

For the field testing in the PNNL Lab Homes, the sensors were found to work stably and streamed measurements to the cloud every minute. The cloud database had 100% availability and was error-free during the experiment. The project also demonstrated FDD methods for the heat pump system, achieving an accuracy of 90.18% and a detection accuracy of 96.4%, both meeting the required value of 80%. The project also showed that occupancy-based setback strategies and DPC can save 14% and 10% of energy, respectively, both demonstrating $\geq 10\%$ energy savings required. In terms of thermal comfort improvement, unmet hours could be decreased from 2.05°F-hr to 0.22°F-hr, which can improve residents' thermal comfort under the malfunction of HVAC systems or in the heat wave period.

Future work includes:

- 1) For the faulty models, the fault prevalence is assumed to follow some statistical distribution, rather than the real survey results. This is because the survey work is the lack of existing research data. Once well-organized survey distribution of residential HVAC faults is generated, it is easy to replace the assumed distribution with more professional ones.
- 2) The impact analysis and fault detection based on the fault library is not conducted as comprehensive work. The focus of this study is to develop a fault library for residential HVAC systems and to develop the workflow for fault simulation model generation. A more comprehensive analysis of residential HVAC faults will be explored in the future.
- 3) A hybrid FDD approach for VCC system is only limited to the single faults. So future work will involve investigation of multiple faults. The corresponding data are in preparation.
- 4) For the duct leakage FDD, the detection accuracy needs to be improved. In order to learn the adaptive threshold to classify the instantaneous predictive error output from the forecasting model, a 1D SVM classifier is being tested. Since the output data from the forecasting model is imbalanced and contains a greater number of fault-free samples than faulty samples, the fault classifier model is found to be biased. Hence, a data augmentation technique referred to as Synthetic Minority Oversampling Technique (SMOTE) can be used to address this issue.

The output samples from SMOTE can then be used to train the 1D SVM fault classifier. We plan to integrate the fault classifier model into our developed framework in the future.

Alternatively, a statistical difference approach could also be implemented to differentiate the fault-free and faulty period.

- 5) MPC-informed rules can be enhanced by deploying MPC and extracting rules in a wider range of climate zones. It will help improve thermal comfort in different locations. Benefits from precooling only using building thermal mass are limited. Other types of active thermal storage systems could be explored in the future.
- 6) The control design and testing were only conducted in the cooling season. It would be valuable to explore the performance in the heating season and shoulder season.

10. Publications

The following publication is also affiliated with this award:

Yang, Tao, Arkasama Bandyopadhyay, Zheng O'Neill, Jin Wen, and Bing Dong. 2021. "From occupants to occupants: A review of the occupant information understanding for building HVAC occupant-centric control." *Building Simulation*. 15: 913-932.
<https://doi.org/10.1007/s12273-021-0861-0>.

11. References

6:20-cv-00075 - *Ecofactor Inc v. Google LLC*.

Afram, Abdul, Farrokh Janabi-Sharifi, Alan S. Fung, and Kaamran Raahemifar. 2017. Artificial neural network (ANN) based model predictive control (MPC) and optimization of HVAC systems: A state of the art review and case study of a residential HVAC system. *Energy and Buildings* 141: 96-113.

Ahmed, Jerine. 2013. "Measuring Residential HVAC Faults and Their Effects".

Aliero, Muhammad Saidu, Kashif Naseer Qureshi, Muhammad Fermi Pasha, and Gwanggil Jeon. 2021. Smart Home Energy Management Systems in Internet of Things Networks for Green Cities Demands and Services. *Environmental Technology & Innovation* 22: 101443.

Alladi, Tejasvi, Vinay Chamola, Biplab Sikdar, and Kim-Kwang Raymond Choo. 2020. Consumer IoT: Security vulnerability case studies and solutions. *IEEE Consumer Electronics Magazine* 9 (2): 17-25.

Alzghoul, Ahmad, Björn Backe, Magnus Löfstrand, Arne Byström, and Bengt Liljedahl. 2014. Comparing a knowledge-based and a data-driven method in querying data streams for system fault detection: A hydraulic drive system application. *Computers in Industry* 65 (8): 1126-1135.

Andersson, Christian, Johan Åkesson, and Claus Führer. 2016. Pyfimi: A python package for simulation of coupled dynamic models with the functional mock-up interface.

ARPA-E. 2018. "Saving Energy Nationwide in Structures with Occupancy Recognition."
<https://arpa-e.energy.gov/technologies/programs/sensor>.

ASHRAE. 2017. *ANSI/ASHRAE Standard 55-2017: Thermal Environmental Conditions for Human Occupancy*.

ASHRAE. 2018a. *ANSI/ASHRAE/IES Standard 90.2-2018: Energy-Efficient Design of Low-Rise Residential Buildings*.

ASHRAE. 2018b. *ANSI/ASHRAE/IES Standard 100-2018: Energy Efficiency in Existing Buildings*.

ASHRAE. 2019. *ANSI/ASHRAE Standard 62.2-2019: Ventilation and Acceptable Indoor Air Quality in Residential Buildings*.

Assaf, Roy, Ioana Giurgiu, Frank Bagehorn, and Anika Schumann. 2019. "MTEX-CNN: Multivariate time series explanations for predictions with convolutional neural networks." 2019 IEEE International Conference on Data Mining (ICDM).

Au-Yong, Cheong Peng, Azlan Shah Ali, and Faizah Ahmad. 2014. Improving occupants' satisfaction with effective maintenance management of HVAC system in office buildings. *Automation in Construction* 43: 31-37.

Austin Energy. "Power Partner Thermostats."

- <https://savings.austinenergy.com/rebates/residential/offerings/cooling-and-heating/pp-thermostat/https://savings.austinenergy.com/rebates/residential/offerings/cooling-and-heating/pp-thermostat/>.
- Bailey, Margaret B., and Jan F. Kreider. 2003. Creating an automated chiller fault detection and diagnostics tool using a data fault library. *ISA Transactions* 42 (3): 485-495.
- Basarkar, Mangesh, Xiufeng Pang, Liping Wang, Philip Haves, and Tianzhen Hong. 2011. Modeling and simulation of HVAC faults in EnergyPlus.
- Bellanco, I., E. Fuentes, M. Vallès, and J. Salom. 2021. A review of the fault behavior of heat pumps and measurements, detection and diagnosis methods including virtual sensors. *Journal of Building Engineering* 39.
- Bode, Gerrit, Simon Thul, Marc Baranski, and Dirk Müller. 2020. Real-world application of machine-learning-based fault detection trained with experimental data. *Energy* 198.
- Bourguignon, Marcelo, Rodrigo B Silva, and Gauss M Cordeiro. 2014. The Weibull-G family of probability distributions. *Journal of Data Science* 12 (1): 53-68.
- Braun, James E. 2003. Automated Fault Detection and Diagnostics for Vapor Compression Cooling Equipment. *Journal of Solar Energy Engineering* 125 (3): 266-274.
- Breuker, Mark. 1997. "Evaluation of a statistical, rule-based fault detection and diagnostics method for vapor compression air conditioners." Thesis (MSME)--Purdue University, ME, Dec., 1997.
- Breuker, Mark, and James Braun. 1997. "Demonstration of a statistical, rule-based fault detection and diagnostic method on a rooftop air conditioning unit." CLIMA 2000 Conference Proceedings.
- Breuker, Mark, and James Braun. 1998a. Common Faults and Their Impacts for Rooftop Air Conditioners. *HVAC&R Research* 4 (3): 303-318.
- Breuker, Mark, and James Braun. 1998b. Evaluating the Performance of a Fault Detection and Diagnostic System for Vapor Compression Equipment. *HVAC&R Research* 4 (4): 401-425.
- Brown, Scott, Brian Thornton, and Sarah Widder. 2013. *Review of Residential Low-Load HVAC Systems*. Pacific Northwest National Lab (PNNL), Richland, WA (United States).
- Brown, Simon. 2020. Future changes in heatwave severity, duration and frequency due to climate change for the most populous cities. *Weather and Climate Extremes* 30: 100278.
- Brumbaugh, James E. 2012. *Audel HVAC Fundamentals, Volume 1: Heating Systems, Furnaces and Boilers*. Vol. 1. John Wiley & Sons.
- BTO (Building Technologies Office). 2016. *Multi-Year Program Plan Fiscal Years 2016-2020*. <https://www.energy.gov/eere/buildings/articles/multi-year-program-plan#:~:text=The%20Department%20of%20Energy's%20Building,BTO's%20strategies%20and%20goals%20for>
- Bursill, Jayson, Liam O'Brien, and Ian Beausoleil-Morrison. 2020. Multi-zone field study of rule extraction control to simplify implementation of predictive control to reduce building energy use. *Energy and Buildings* 222: 110056.
- Bursill, Jayson, William O'Brien, and Ian Beausoleil-Morrison. 2019. Experimental application of classification learning to generate simplified model predictive controls for a shared office heating system. *Science and Technology for the Built Environment* 25 (5): 615-628.
- Butzbaugh, Joshua B, Abraham SD Tidwell, and Chrissi A Antonopoulos. 2020. *Automatic Fault Detection & Diagnostics: Residential Market Analysis*. Pacific Northwest National Lab (PNNL), Richland, WA (United States).

- Cetin, Kristen S., Mohammad Hassan Fathollahzadeh, Niraj Kunwar, Huyen Do, and Paulo Cesar Tabares-Velasco. 2019. Development and validation of an HVAC on/off controller in EnergyPlus for energy simulation of residential and small commercial buildings. *Energy and Buildings* 183: 467-483.
- Chen, Bin. 2000. "Evaluating the potential of on-line fault detection and diagnosis for rooftop air conditioners." Master's Thesis, School of Mechanical Engineering, Purdue University.
- Chen, Bin, and James E Braun. 2000. "Simple fault detection and diagnosis methods for packaged air conditioners." International Refrigeration and Air Conditioning Conference at Purdue.
- Chen, Bin, and James E Braun. 2001. Simple rule-based methods for fault detection and diagnostics applied to packaged air conditioners. *ASHRAE Transactions* 107: 847.
- Chen, Jianli, Liang Zhang, Yanfei Li, Yifu Shi, Xinghua Gao, and Yuqing Hu. 2022. A review of computing-based automated fault detection and diagnosis of heating, ventilation and air conditioning systems. *Renewable and Sustainable Energy Reviews* 161: 112395.
- Chen, Yimin, Eliot Crowe, Guanqing Lin, and Jessica Granderson. 2020. What's in a Name? Developing a Standardized Taxonomy for HVAC System Faults.
- Chen, Zhe, Peng Xu, Fan Feng, Yifan Qiao, and Wei Luo. 2021. Data mining algorithm and framework for identifying HVAC control strategies in large commercial buildings. *Building Simulation* 14 (1): 63-74.
- Chen, Zhelun, Zheng O'Neill, Jin Wen, Ojas Pradhan, Tao Yang, Xing Lu, Guanqing Lin, et al. 2023. A review of data-driven fault detection and diagnostics for building HVAC systems. *Applied Energy* 339: 121030.
- Cheung, Howard, and James E Braun. 2015. *Development of Fault Models for Hybrid Fault Detection and Diagnostics Algorithm*. National Renewable Energy Lab (NREL), Golden, CO (United States).
- Cheung, Howard, and James E. Braun. 2013a. Simulation of fault impacts for vapor compression systems by inverse modeling. Part I: Component modeling and validation. *HVAC&R Research* 19 (7): 892-906.
- Cheung, Howard, and James E. Braun. 2013b. Simulation of fault impacts for vapor compression systems by inverse modeling. Part II: System modeling and validation. *HVAC&R Research* 19 (7): 907-921.
- Cheung, Howard, and James E. Braun. 2016. Empirical modeling of the impacts of faults on water-cooled chiller power consumption for use in building simulation programs. *Applied Thermal Engineering* 99: 756-764.
- Chintala, Rohit, Jon Winkler, and Xin Jin. 2021. Automated fault detection of residential air-conditioning systems using thermostat drive cycles. *Energy and Buildings* 236: 110691.
- Christensen, Ken, Pedro Reviriego, Bruce Nordman, Michael Bennett, Mehrgan Mostowfi, and Juan Antonio Maestro. 2010. IEEE 802.3 az: the road to energy efficient ethernet. *IEEE Communications Magazine* 48 (11): 50-56.
- Cigler, Jiri, Jan Siroky, Milan Korda, and Colin Jones. 2013. "On the selection of the most appropriate MPC problem formulation for buildings." 11th REHVA World Congress CLIMA 2013.
- Coffey, Brian. 2011a. "Using building simulation and optimisation to calculate control lookup tables offline." 12th Conference of International Building Performance Simulation Association.
- Coffey, Brian. 2011b. "Using building simulation and optimization to calculate lookup tables for

- control." University of California, Berkeley.
- Coffey, Brian. 2013. Approximating model predictive control with existing building simulation tools and offline optimization. *Journal of Building Performance Simulation* 6 (3): 220-235.
- Crawley, Drury B, Linda K Lawrie, Frederick C Winkelmann, Walter F Buhl, Y Joe Huang, Curtis O Pedersen, Richard K Strand, et al. 2001. EnergyPlus: creating a new-generation building energy simulation program. 33 (4): 319-331.
- Danova, T. 2014. "The Connected Home Report: Forecasts and Growth Trends for the Leading 'Internet of Things' Market. Business Insider Intelligence."
<http://www.businessinsider.com/connected-home-forecasts-and-growth-2014-9>.
- de Wilde, Pieter. 2014. The gap between predicted and measured energy performance of buildings: A framework for investigation. *Automation in Construction* 41: 40-49.
- Density. 2022. "Density™ Occupancy Sensors - Actionable Workplace Insights."
- DEVOPS. Decision Tree Classification Algorithm.
- Documentation, EnergyPlus. 2019. Engineering reference-EnergyPlus 8.5. *The Reference to EnergyPlus Calculation*.
- DOE. 2018. Residential HVAC Installation Practices: A Review of Research Findings.
- DOE. 2021. *Residential Prototype Building Models*.
- Domahidi, Alexander, Fabian Ullmann, Manfred Morari, and Colin N Jones. 2012. "Learning near-optimal decision rules for energy efficient building control." 2012 IEEE 51st IEEE Conference on Decision and Control (CDC).
- Domahidi, Alexander, Fabian Ullmann, Manfred Morari, and Colin N. Jones. 2014. Learning decision rules for energy efficient building control. *Journal of Process Control* 24 (6): 763-772.
- Downey, Tom, and John Proctor. 2002. "What can 13,000 air conditioners tell us." the Proceedings of the 2002 ACEEE Summer Study on Energy Efficiency in Buildings.
- Drgoňa, Ján, Damien Picard, Michal Kvasnica, and Lieve Helsen. 2018. Approximate model predictive building control via machine learning. *Applied Energy* 218: 199-216.
- Ecobee. Ecobee API documentation.
- EERE. "IoT Based Comfort Control and Fault Diagnostics System for Energy Efficient Homes."
<https://www.energy.gov/eere/buildings/iot-based-comfort-control-and-fault-diagnostics-system-energy-efficient-homes>.
- EIA. 2001. *Residential energy consumption survey (RECS)*.
- EIA. 2008. *U.S. energy information administration*. International Energy Outlook 11: 1-3.
- EIA. 2009. *Residential energy consumption survey (RECS)*.
- EIA. 2018a. *Use of energy explained*.
- EIA. 2018b. *What's New in How We Use Energy at Home*.
- EIA. 2020a. *Residential energy consumption survey (RECS)*.
- EIA. 2020b. *US Energy-Related Carbon Dioxide Emissions 2020*.
- EIA. 2022a. Annual Electric Power Industry Report, Form EIA-861 detailed data files.
- EIA. 2022b. "Electric Sales, Revenue, and Average Price."
- EIA. 2022c. "Natural Gas."
- EIA. 2022d. US Energy Information Administration.
- Ejenakevwe, Kevwe A., and Li Song. 2021. "Review of Fault Detection and Diagnosis Studies on Residential HVAC Systems." ASME 2021 International Mechanical Engineering Congress and Exposition.

- Florida, University of Central. "Investigation of the Prevalence and Energy Impacts of Residential Comfort System Faults – Hot-Humid and Hot-Dry Climates." <https://www.energy.gov/eere/buildings/field-study-characterize-fault-prevalence-residential-comfort-systems>.
- Frank, Stephen, Xin Jin, Daniel Studer, and Amanda Farthing. 2018. Assessing barriers and research challenges for automated fault detection and diagnosis technology for small commercial buildings in the United States. *Renewable and Sustainable Energy Reviews* 98: 489-499.
- Fuller, Sieglinde K., Amy S. Rushing, and Gene M. Meyer. 2001. *NISTIR 6806 Project-Oriented Life-Cycle Costing Workshop for Energy Conservation in Buildings*. National Institute of Standards and Technology.
- Ginestet, S., D. Marchio, and O. Morisot. 2008. Evaluation of faults impacts on energy consumption and indoor air quality on an air handling unit. *Energy and Buildings* 40 (1): 51-57.
- Granderson, Jessica, Rupam Singla, Ebony Mayhorn, Paul Ehrlich, Draguna Vrabie, and Stephen Frank. 2017. Characterization and survey of automated fault detection and diagnostic tools. *Report Number LBNL-2001075*.
- Gunay, Burak. 2016. "Improving energy efficiency in office buildings through adaptive control of the indoor climate." Carleton University.
- Gunay, Burak, Mohamed Ouf, William O'Brien, and Guy Newsham. 2019. "Building Performance Optimization for Operational Rule Extraction."
- Han, H., B. Gu, T. Wang, and Z. R. Li. 2011. Important sensors for chiller fault detection and diagnosis (FDD) from the perspective of feature selection and machine learning. *International Journal of Refrigeration* 34 (2): 586-599.
- Hart, Philip R, and Bing Liu. 2015. *Methodology for Evaluating Cost-effectiveness of Commercial Energy Code Changes*. Pacific Northwest National Lab (PNNL), Richland, WA (United States).
- Heo, Jaehyeok, W. Vance Payne, and Piotr A. Domanski. 2012. *FDD CX: A Fault Detection and Diagnostic Commissioning Tool for Residential Air Conditioners and Heat Pumps*.
- Heo, Jaehyeok, William V Payne, Piotr A Domanski, and Zhimin Du. 2015. *Self-Training of a Fault-Free Model for Residential Air Conditioner Fault Detection and Diagnostics*.
- Home Advisor. "Thermostat Costs." <https://www.homeadvisor.com/cost/heating-and-cooling/install-a-thermostat/>.
- Homod, Raad Z. 2014. *Modeling and fault-tolerant control developed for HVAC systems*.
- Hosseini, Arash, and Mazdak Nik-Bakht. 2021. Knowledge Discovery by Analyzing the State of the Art of Data-Driven Fault Detection and Diagnostics of Building HVAC. *CivilEng* 2 (4): 986-1008.
- Howe, Allyson S, and Barry P Boden. 2007. Heat-related illness in athletes. *The American Journal of Sports Medicine* 35 (8): 1384-1395.
- Hu, Yifeng, and David P. Yuill. 2021. Effects of multiple simultaneous faults on characteristic fault detection features of a heat pump in cooling mode. *Energy and Buildings* 251: 111355.
- ICC. 2018. *International Code Council International Energy Conservation Code 2018*.
- IEEE. 2020. *IEEE 802.15.4-2020 Standard*. 15.
- Interagency Working Group on Social Cost of Greenhouse Gases, United States Government. 2021. *Technical Support Document: Social Cost of Carbon, Methane, and Nitrous Oxide*

- *Interim Estimates under Executive Order 13990*

- Joe, Jaewan. 2022. Investigation on pre-cooling potential of UFAD via model-based predictive control. *Energy and Buildings* 259: 111898.
- Katipamula, Srinivas, and Michael Brambley. 2005a. Review Article: Methods for Fault Detection, Diagnostics, and Prognostics for Building Systems—A Review, Part I. *HVAC&R Research* 11 (1): 3-25.
- Katipamula, Srinivas, and Michael Brambley. 2005b. Review Article: Methods for Fault Detection, Diagnostics, and Prognostics for Building Systems—A Review, Part II. *HVAC&R Research* 11 (2): 169-187.
- Katipamula, Srinivas, Woohyun Kim, Robert G Lutes, and Ronald M Underhill. 2015. *Rooftop unit embedded diagnostics: Automated fault detection and diagnostics (AFDD) development, field testing and validation*. Pacific Northwest National Lab (PNNL), Richland, WA (United States).
- Khire, Ritesh, and Marija Trcka. 2013. "Model based failure mode effect analysis on whole building energy performance." 13th Conference of International Building Performance Simulation Association, Chambery, France, August 26-28.
- Kim, Janghyun, Stephen Frank, James E. Braun, and David Goldwasser. 2019. Representing Small Commercial Building Faults in EnergyPlus, Part I: Model Development. *Buildings* 9 (11).
- Kim, Janghyun, Stephen Frank, Piljae Im, James E. Braun, David Goldwasser, and Matt Leach. 2019. Representing Small Commercial Building Faults in EnergyPlus, Part II: Model Validation. *Buildings* 9 (12).
- Kim, Minsung, W Vance Payne, Piotr A Domanski, Seok Ho Yoon, and Christian JL Hermes. 2009. Performance of a residential heat pump operating in the cooling mode with single faults imposed. *Applied Thermal Engineering* 29 (4): 770-778.
- Kim, Minsung, William V Payne, Piotr A Domanski, and Christian Hermes. 2006. *Performance of a Residential Heat Pump Operating in the Cooling Mode with Single Faults Imposed (NISTIR 7350)*.
- Kim, Minsung, Seok Ho Yoon, W Vance Payne, and Piotr A Domanski. 2008. *Cooling mode fault detection and diagnosis method for a residential heat pump*.
- Kneifel, Joshua D., and David H. Webb. 2020. *NIST Handbook 135 2020 Edition - Life Cycle Cost Manual for the Federal Energy Management Program*. National Institute of Standards and Technology
- Kong, Meng, Bing Dong, Rongpeng Zhang, and Zheng O'Neill. 2022. HVAC energy savings, thermal comfort and air quality for occupant-centric control through a side-by-side experimental study. *Applied Energy* 306: 117987.
- Koupaei, Diba Malekpour, Taikgun Song, Kristen S Cetin, and Jongho Im. 2020. An assessment of opinions and perceptions of smart thermostats using aspect-based sentiment analysis of online reviews. *Building and Environment* 170: 106603.
- Le, Khang, Romain Bourdais, and Hervé Guéguen. 2014. From hybrid model predictive control to logical control for shading system: A support vector machine approach. *Energy and Buildings* 84: 352-359.
- Lees, F. P. 1979. Fault Detection and Diagnosis in Chemical and Petrochemical Processes. *AIChE Journal* 25 (5): 907-907.
- Li, D., Y. Zhou, G. Hu, and C. J. Spanos. 2017. Optimal Sensor Configuration and Feature Selection for AHU Fault Detection and Diagnosis. *IEEE Transactions on Industrial*

- Informatics* 13 (3): 1369-1380.
- Li, Guannan, Huanxin Chen, Yunpeng Hu, Jiangyu Wang, Yabin Guo, Jiangyan Liu, Haorong Li, et al. 2018. An improved decision tree-based fault diagnosis method for practical variable refrigerant flow system using virtual sensor-based fault indicators. *Applied Thermal Engineering* 129: 1292-1303.
- Li, Yanfei. 2018. "An innovative fault analysis framework to enhance building operations." Mechanical Engineering, University of Alabama.
- Li, Yanfei, and Zheng O'Neill. 2016. "An EnergyPlus/OpenStudio based Fault Simulator for Buildings." ASHRAE Winter Meeting, Orlando, FL.
- Li, Yanfei, and Zheng O'Neill. 2019. An innovative fault impact analysis framework for enhancing building operations. *Energy and Buildings* 199: 311-331.
- Li, Yanfei, and Zheng O'Neill. 2018. A critical review of fault modeling of HVAC systems in buildings. *Building Simulation* 11 (5): 953-975.
- Li, Yunhua, Mingsheng Liu, Josephine Lau, and Bei Zhang. 2014. Experimental study on electrical signatures of common faults for packaged DX rooftop units. *Energy and Buildings* 77: 401-415.
- Liu, Sicong, Silvestro Roberto Poccia, K Selcuk Candan, Maria Luisa Sapino, and Xiaolan Wang. 2018. Robust multi-variate temporal features of multi-variate time series. *ACM Transactions on Multimedia Computing, Communications, and Applications (TOMM)* 14 (1): 1-24.
- Liu, Yuanyuan, Bo Qiu, Xiaodong Fan, Haijing Zhu, and Bochong Han. 2016. Review of smart home energy management systems. *Energy Procedia* 104: 504-508.
- Lu, Xing, Yangyang Fu, Zheng O'Neill, and Jin Wen. 2021. A holistic fault impact analysis of the high-performance sequences of operation for HVAC systems: Modelica-based case study in a medium-office building. *Energy and Buildings* 252: 111448.
- Lyu, Yan, Yiqun Pan, Tao Yang, Yuming Li, Zhizhong Huang, and Risto Kosonen. 2021. An automated process to calibrate building energy model based on schedule tuning and signed directed graph method. *Journal of Building Engineering* 35: 102058.
- Market Research Future. "Market Synopsis of Smart Home Energy Management Device Market." <https://www.marketresearchfuture.com/reports/smart-home-energy-management-device-market-1194>.
- Matulka, Rebecca. 2013. *Energy Saver 101*. DOE.
- May-Ostendorp, Peter. 2012. "Offline model predictive control of mixed mode buildings for near-optimal supervisory control strategy development." University of Colorado at Boulder.
- May-Ostendorp, Peter, Gregor Henze, Charles Corbin, Balaji Rajagopalan, and Clemens Felsmann. 2011. Model-predictive control of mixed-mode buildings with rule extraction. *Building and Environment* 46 (2): 428-437.
- May-Ostendorp, Peter, Gregor Henze, Balaji Rajagopalan, and Charles Corbin. 2013. Extraction of supervisory building control rules from model predictive control of windows in a mixed mode building. *Journal of Building Performance Simulation* 6 (3): 199-219.
- May-Ostendorp, Peter, Gregor Henze, Balaji Rajagopalan, and Doreen Kalz. 2013. Experimental investigation of model predictive control-based rules for a radiantly cooled office. *HVAC&R Research* 19 (5): 602-615.
- Mehta, Prashant. 2021. Work from home—Work engagement amid COVID-19 lockdown and employee happiness. *Journal of Public Affairs* 21 (4): e2709.

- Metzger, Cheryn, Siddharth Goyal, and Michael C Baechler. 2017. *Review of Residential Comfort Control Products and Opportunities*. Pacific Northwest National Lab (PNNL), Richland, WA (United States).
- Meyers, Robert J, Eric D Williams, and H Scott Matthews. 2010. Scoping the potential of monitoring and control technologies to reduce energy use in homes. *Energy and buildings* 42 (5): 563-569.
- Mirnaghi, Maryam Sadat, and Fariborz Haghighat. 2020. Fault detection and diagnosis of large-scale HVAC systems in buildings using data-driven methods: A comprehensive review. *Energy and Buildings* 229.
- Mowris, Robert, Ean Jones, and Robert Eshom. 2012. Laboratory measurements of residential HVAC installation and maintenance faults. *ASHRAE Transactions* 118 (2): 165-173.
- Nelson, William, and Charles Culp. 2022. Machine Learning Methods for Automated Fault Detection and Diagnostics in Building Systems: A Review. *Energies* 15 (15): 5534.
- NIST. Energy Escalation Rate Calculator.
- NIST. 2022. *Energy Escalation Rate Calculator (EERC) User Guide*.
- Noble, William S. 2006. What is a support vector machine? *Nature Biotechnology* 24 (12): 1565-1567.
- Otto, Kevin, Bryan Eisenhower, Zheng O'Neill, Shui Yuan, Igor Mezic, and Satish Narayanan. 2012. "Prioritizing building system energy failure modes using whole building energy simulation." Proceedings of SimBuild.
- Pang, Zhihong. 2022. "Development, Quantification, and Demonstration of the Occupancy-based Controls for Smart and Healthy Buildings." Texas A&M University.
- Pang, Zhihong, Yan Chen, Jian Zhang, Zheng O'Neill, Hwakong Cheng, and Bing Dong. 2021. How much HVAC energy could be saved from the occupant-centric smart home thermostat: A nationwide simulation study. *Applied Energy* 283: 116251.
- Payne, William V. 2020. *Residential Air-Conditioner and Heat Pump System, Cooling Mode, Rule-Based Chart Fault Detection and Diagnosis Software User's Guide*.
- Pearce, David. 2003. The social cost of carbon and its policy implications. *Oxford review of economic policy* 19 (3): 362-384.
- Pedregosa, Fabian, Gaël Varoquaux, Alexandre Gramfort, Vincent Michel, Bertrand Thirion, Olivier Grisel, Mathieu Blondel, et al. 2011. Scikit-learn: Machine Learning in Python. *Journal of Machine Learning Research* 12: 2825-2830.
- PGE. "Smart Thermostat." https://www.pge.com/en_US/residential/save-energy-money/savings-solutions-and-rebates/rebates-by-product/smart-thermostats/smart-thermostats.page.
- Pignatiello, Joseph. 1988. An overview of the strategy and tactics of Taguchi. *IIE transactions* 20 (3): 247-254.
- Piscitelli, Marco Savino, Silvio Brandi, Giovanni Gennaro, Alfonso Capozzoli, Fabio Favoino, and Valentina Serra. 2019. "Advanced Control Strategies for the Modulation of Solar Radiation in Buildings: MPC-Enhanced Rule-Based Control." Proceedings of Building Simulation 2019: 16th Conference of IBPSA.
- Prnewswire. "Smart Thermostat Market is Projected to Reach USD 6207.13 Million by 2028." <https://www.prnewswire.com/news-releases/smart-thermostat-market-is-projected-to-reach-usd-6207-13-million-by-2028--says-brandessence-market-research-301635362.html>.
- Qiu, Shunian, Fan Feng, Zhengwei Li, Guang Yang, Peng Xu, and Zhenhai Li. 2019. Data mining based framework to identify rule based operation strategies for buildings with

- power metering system. *Building Simulation* 12 (2): 195-205.
- Rahman, Aowabin, Amanda D. Smith, Yulong Xie, Jermy Thomas, and Casey D. Burleyson. 2022. Methodology and analytical approach to investigate the impact of building temperature setpoint schedules. *Journal of Building Performance Simulation* 15 (1): 128-147.
- Robillart, M, P Schalbart, and B Peuportier. 2014. "Extraction of heating control rules from the dynamic programming method for load shifting in energy-efficient building." 9th International Conference on System Simulation in Buildings.
- Robillart, M., P. Schalbart, and B. Peuportier. 2017. Derivation of simplified control rules from an optimal strategy for electric heating in a residential building. *Journal of Building Performance Simulation* 11 (3): 294-308.
- Rogers, Austin, Fangzhou Guo, and Bryan Rasmussen. 2019a. A review of fault detection and diagnosis methods for residential air conditioning systems. *Building and Environment* 161.
- Rogers, Austin, Fangzhou Guo, and Bryan Rasmussen. 2019b. Uncertainty analysis and field implementation of a fault detection method for residential HVAC systems. *Science and Technology for the Built Environment* 26 (3): 320-333.
- Rojas-Domínguez, Alfonso, Luis Carlos Padierna, Juan Martín Carpio Valadez, Hector J Puga-Soberanes, and Héctor J Fraire. 2017. Optimal hyper-parameter tuning of SVM classifiers with application to medical diagnosis. *IEEE Access* 6: 7164-7176.
- Rossi, Todd. 1995. "Detection, diagnosis, and evaluation of faults in vapor compression equipment." Purdue University.
- Rossi, Todd, and James Braun. 1997. A Statistical, Rule-Based Fault Detection and Diagnostic Method for Vapor Compression Air Conditioners. *HVAC&R Research* 3 (1): 19-37.
- Rotondo, Julia, Robert Johnson, Nancy Gonzales, Alexandra Waranowski, Chris Badger, Nack Lange, Ethan Goldman, et al. 2016. *Overview of existing and future residential use cases for connected thermostats*. Energetics Inc., Washington, DC (United States); Vermont Energy Investment.
- Salsbury, TI, and RC Diamond. 2001. Fault detection in HVAC systems using model-based feedforward control. *Energy and Buildings* 33 (4): 403-415.
- Shahnazari, Hadi. 2018. "Fault Diagnosis and Fault Tolerant Control of Complex Process Systems."
- Shi, Zixiao, and William O'Brien. 2019. Development and implementation of automated fault detection and diagnostics for building systems: A review. *Automation in Construction* 104: 215-229.
- Shih, Huang-Chia. 2014. A robust occupancy detection and tracking algorithm for the automatic monitoring and commissioning of a building. *Energy and Buildings* 77: 270-280.
- Singh, Vijay, Jyotirmay Mathur, and Aviruch Bhatia. 2022. A Comprehensive Review: Fault Detection, Diagnostics, Prognostics, and Fault Modelling in HVAC Systems. *International Journal of Refrigeration*.
- Sofos, Marina, Jared T Langevin, Michael Deru, Erika Gupta, Kyle S Benne, David Blum, Ted Bohn, et al. 2020. *Innovations in sensors and controls for building energy management: Research and development opportunities report for emerging technologies*. National Renewable Energy Lab (NREL), Golden, CO (United States).
- Statistics, U.S. Bureau of Labor. 2023. Average energy prices for the United States, regions, census divisions, and selected metropolitan areas.

- Szegedy, Christian, Wei Liu, Yangqing Jia, Pierre Sermanet, Scott Reed, Dragomir Anguelov, Dumitru Erhan, et al. 2015. "Going deeper with convolutions." Proceedings of the IEEE conference on computer vision and pattern recognition.
- Taal, Arie, Laure Itard, and Wim Zeiler. 2018. A reference architecture for the integration of automated energy performance fault diagnosis into HVAC systems. *Energy and Buildings* 179: 144-155.
- Taguchi, Genichi. 1987. *System of experimental design; engineering methods to optimize quality and minimize costs*.
- Tanner, Ryan Adams. 2014. "Stochastic optimization of building control systems for mixed-mode buildings." University of Colorado at Boulder.
- The White House. 2021. 2030 Greenhouse Gas Pollution Reduction Target.
- Tiwaskar, Manoj, Yash Garg, Xinsheng Li, K Selçuk Candan, and Maria Luisa Sapino. 2021. Selego: robust variate selection for accurate time series forecasting. *Data Mining and Knowledge Discovery* 35: 2141-2167.
- Touran, Ali. 2003. Calculation of contingency in construction projects. *IEEE transactions on engineering management* 50 (2): 135-140.
- Trafsys. 2022. "Trafsys - People Counting Systems."
- Turner, W. J. N., I. S. Walker, and J. Roux. 2015. Peak load reductions: Electric load shifting with mechanical pre-cooling of residential buildings with low thermal mass. *Energy* 82: 1057-1067.
- U.S. Census Bureau. 2022. "Explore Census Data."
- University of Nebraska–Lincoln. "A Field Study to Characterize Fault Prevalence in Residential Comfort Systems." <https://www.energy.gov/eere/buildings/investigation-prevalence-and-energy-impacts-residential-comfort-system-faults-hot>.
- Van Rossum, Guido. 2007. "Python Programming Language." USENIX annual technical conference.
- Vaughan-Nichols, Steven J. 2010. Gigabit Wi-Fi is on its way. *Computer* 43 (11): 11-14.
- Venkatasubramanian, Venkat, Raghunathan Rengaswamy, and Surya N. Kavuri. 2003. A review of process fault detection and diagnosis Part II: Qualitative models and search strategies. *Computers & Chemical Engineering* 27 (3): 313-326.
- Venkatasubramanian, Venkat, Raghunathan Rengaswamy, Surya N. Kavuri, and Kewen Yin. 2003. A review of process fault detection and diagnosis Part III: Process history based methods. *Computers & Chemical Engineering* 27 (3): 327-346.
- Venkatasubramanian, Venkat, Raghunathan Rengaswamy, Kewen Yin, and Surya N. Kavuri. 2003. A review of process fault detection and diagnosis Part I: Quantitative model-based methods. *Computers & Chemical Engineering* 27 (3): 293-311.
- Wang, Chenli, Kaleb Pattawi, and Hohyun Lee. 2020. Energy saving impact of occupancy-driven thermostat for residential buildings. *Energy and Buildings* 211.
- Wang, Liping, Steve Greenberg, John Fiegel, Alma Rubalcava, Shankar Earni, Xiufeng Pang, Rongxin Yin, et al. 2013. Monitoring-based HVAC commissioning of an existing office building for energy efficiency. *Applied Energy* 102: 1382-1390.
- Wang, Liping, and Tianzhen Hong. 2013. *Modeling and simulation of HVAC faulty operations and performance degradation due to maintenance issues*. Lawrence Berkeley National Lab (LBNL), Berkeley, CA (United States).
- Wei, Chih-Chiang, and Nien-Sheng Hsu. 2009. Optimal tree-based release rules for real-time flood control operations on a multipurpose multireservoir system. *Journal of Hydrology*

- 365 (3-4): 213-224.
- Wheeler, Grant, Michael Deru, Adam Hirsch, and Thien-Kim L Trenbath. 2020. *Provider and User Perspectives on Automated Fault Detection and Diagnostic Products for Packaged Rooftop Units*. National Renewable Energy Lab (NREL), Golden, CO (United States).
- Widén, Johan. 2015. Evaluation of Smart Home API with a developed application to a heating system.
- Wilson, Eric, Cheryn Engebrecht-Metzger, Scott Horowitz, and Robert Hendron. 2014. *2014 Building America House Simulation Protocols*. National Renewable Energy Lab (NREL), Golden, CO (United States).
- Winkler, Jon, Saptarshi Das, Lieko Earle, Lena Burkett, Joseph Robertson, David Roberts, and Charles Booten. 2020. Impact of installation faults in air conditioners and heat pumps in single-family homes on U.S. energy usage. *Applied Energy* 278.
- Xu, Shichao, Yangyang Fu, Yixuan Wang, Zheng O'Neill, and Qi Zhu. 2021. "Learning-based framework for sensor fault-tolerant building HVAC control with model-assisted learning." Proceedings of the 8th ACM International Conference on Systems for Energy-Efficient Buildings, Cities, and Transportation, Coimbra, Portugal.
<https://doi.org/10.1145/3486611.3486644>.
- Yahoo Finance. "Smart Thermostats Global Market to Grow by 31% Annually Through 2024." <https://finance.yahoo.com/news/smart-thermostats-global-market-grow-131300415.html>.
- Yan, Ke, Lulu Ma, Yuting Dai, Wen Shen, Zhiwei Ji, and Dongqing Xie. 2018. Cost-sensitive and sequential feature selection for chiller fault detection and diagnosis. *International Journal of Refrigeration* 86: 401-409.
- Yoshimura, M., and N. Ito. 1989. "Effective diagnosis methods for air-conditioning equipment in telecommunications buildings." Conference Proceedings., Eleventh International Telecommunications Energy Conference, 15-18 Oct. 1989.
- Yu, Min Gyung, and Gregory S. Pavlak. 2022. Extracting interpretable building control rules from multi-objective model predictive control data sets. *Energy* 240: 122691.
- Yuill, David P. 2014. "Development of methodologies for evaluating performance of fault detection and diagnostics protocols applied to unitary air-conditioning equipment."
- Yuill, David P, Howard Cheung, and James E Braun. 2014. "Evaluation of fault detection and diagnostics tools by simulation results of multiple vapor compression systems." Proceedings of 15th International Refrigeration and Air Conditioning Conference.
- Yuill, David P., and James E. Braun. 2013. Evaluating the performance of fault detection and diagnostics protocols applied to air-cooled unitary air-conditioning equipment. *HVAC&R Research* 19 (7): 882-891.
- Yuill, David P., and James E. Braun. 2016. Effect of the distribution of faults and operating conditions on AFDD performance evaluations. *Applied Thermal Engineering* 106: 1329-1336.
- Zafar, Usman, Sertac Bayhan, and Antonio Sanfilippo. 2020. Home energy management system concepts, configurations, and technologies for the smart grid. *IEEE access* 8: 119271-119286.
- Zandi, Helia, Teja Kuruganti, Edward Allan Vineyard, and David Fugate. 2018. Home Energy Management Systems: An Overview.
- Zeng, Zhaoyun, Wannu Zhang, Kaiyu Sun, Max Wei, and Tianzhen Hong. 2022. Investigation of pre-cooling as a recommended measure to improve residential buildings' thermal resilience during heat waves. *Building and Environment* 210: 108694.

- Zhang, Huiliang, Di Wu, and Benoit Boulet. 2020. "A Review of Recent Advances on Reinforcement Learning for Smart Home Energy Management." 2020 IEEE Electric Power and Energy Conference (EPEC).
- Zhang, Liang. 2018. "Data-driven Whole Building Energy Forecasting Model for Data Predictive Control."
- Zhang, Liang, and Jin Wen. 2018. Apply Active Learning in Short-term Data-driven Building Energy Modeling.
- Zhang, Liang, and Jin Wen. 2019. A systematic feature selection procedure for short-term data-driven building energy forecasting model development. *Energy and Buildings* 183: 428-442.
- Zhang, Liang, and Jin Wen. 2021. Active learning strategy for high fidelity short-term data-driven building energy forecasting. *Energy and Buildings* 244: 111026.
- Zhang, Liang, Jin Wen, Can Cui, Xiwang Li, and Teresa Wu. 2016. Experiment Design and Training Data Quality of Inverse Model for Short-term Building Energy Forecasting.
- Zhang, Rongpeng, and Tianzhen Hong. 2017. Modeling of HVAC operational faults in building performance simulation. *Applied Energy* 202: 178-188.
- Zhao, Yang, Tingting Li, Xuejun Zhang, and Chaobo Zhang. 2019. Artificial intelligence-based fault detection and diagnosis methods for building energy systems: Advantages, challenges and the future. *Renewable and Sustainable Energy Reviews* 109: 85-101.
- Zhao, Yang, Fu Xiao, Jin Wen, Yuehong Lu, and Shengwei Wang. 2014. A robust pattern recognition-based fault detection and diagnosis (FDD) method for chillers. *HVAC&R Research* 20 (7): 798-809.
- Zuo, Jian, Stephen Pullen, Jasmine Palmer, Helen Bennetts, Nicholas Chileshe, and Tony Ma. 2015. Impacts of heat waves and corresponding measures: a review. *Journal of Cleaner Production* 92: 1-12.

Appendix A: IoT-Based Sensor Network

A.1 Example Data for the Sensor Network

```

{
  "record-id-start": "00140999",
  "record-latest": {
    "record-id": "00183520",
    "value": {
      "temperature": 24.46326446533203,
      "humidity": 55.1461067199707,
      "battery": 3025,
      "airflow": 0
    },
    "sensor-id": "HAABQAAUKA3DATJZGUQA0000",
    "timestamp": 1628181001
  },
  "sensor-id": "HAABQAAUKA3DATJZGUQA0000",
  "sensor-type": "TH Sensor",
  "unit": {
    "temperature": "degC",
    "battery": "mV",
    "humidity": "%RH"
  },
  "record-id-latest": "00183520",
  "report-interval": 60,
  "sensor-name": "Bedroom"
}

```

Figure 97. Example data in the sensor information table

```

{
  "record-id": "00183520",
  "value": {
    "temperature": 24.46326446533203,
    "humidity": 55.1461067199707,
    "battery": 3025,
    "airflow": 0
  },
  "sensor-id": "HAABQAAUKA3DATJZGUQA0000",
  "timestamp": 1628181001
}

```

Figure 98. Example data in the sensor data table

	Record id	Time	Temperature(°C) / Humidity(%RH)
170	000000ab	2020-12-10 20:34:22	"26.88/50.7"
171	000000ac	2020-12-10 20:34:26	"26.88/50.6"
172	000000ad	2020-12-10 20:34:32	"26.89/50.4"
173	000000ae	2020-12-10 20:34:36	"26.90/50.3"
174	000000af	2020-12-10 20:34:46	"26.96/50.0"
175	000000b0	2020-12-10 20:34:51	"27.02/49.8"
176	000000b1	2020-12-10 20:34:57	"29.92/49.9"
177	000000b2	2020-12-10 20:35:01	"49.86/29.6"
178	000000b3	2020-12-10 20:35:07	"59.95/11.2"
179	000000b4	2020-12-10 20:35:11	"64.51/9.7"
180	000000b5	2020-12-10 20:35:16	"61.97/9.6"

Figure 99. Sample data from the cloud database

```

Sensor Hub System v3.3
Status      Running  Processed: 3651
Current Time 2021-02-28 00:12:42

Sensors      Sensor      Next Submission  Last Reading
Bedroom      Waiting     02-28 00:12:14  24.76°C 57.7% 2.936V
Living Roo   0:00:02    02-28 00:12:34  24.50°C 53.5% 2.969V
Study        0:00:16    02-28 00:12:34  27.32°C 49.6% 2.956V
    
```

Figure 100. Sensor measurements received by the hub

```

Sensor Hub System v3.4
Status      Running  Processed: 27
Current Time 2022-04-29 19:09:17

Sensors      Sensor      Next Submission  Last Reading
NewS-FUADY   0:00:05     04-29 19:09:06  25.48°C 45.0% 3.003V 0.00m/s
NewS-FMABA   0:00:13     04-29 19:08:56  25.46°C 45.9% 3.007V 0.00m/s
NewS-FUAEY   0:00:15     04-29 19:09:16  25.92°C 48.9% 2.965V 0.73m/s
NewS-JMACE   0:00:19     04-29 19:09:03  25.42°C 45.6% 3.016V 0.00m/s
NewS-FMACS   0:00:20     04-29 19:09:05  25.46°C 45.0% 3.000V 0.00m/s
    
```

Figure 101. The airflow reading on the hub display

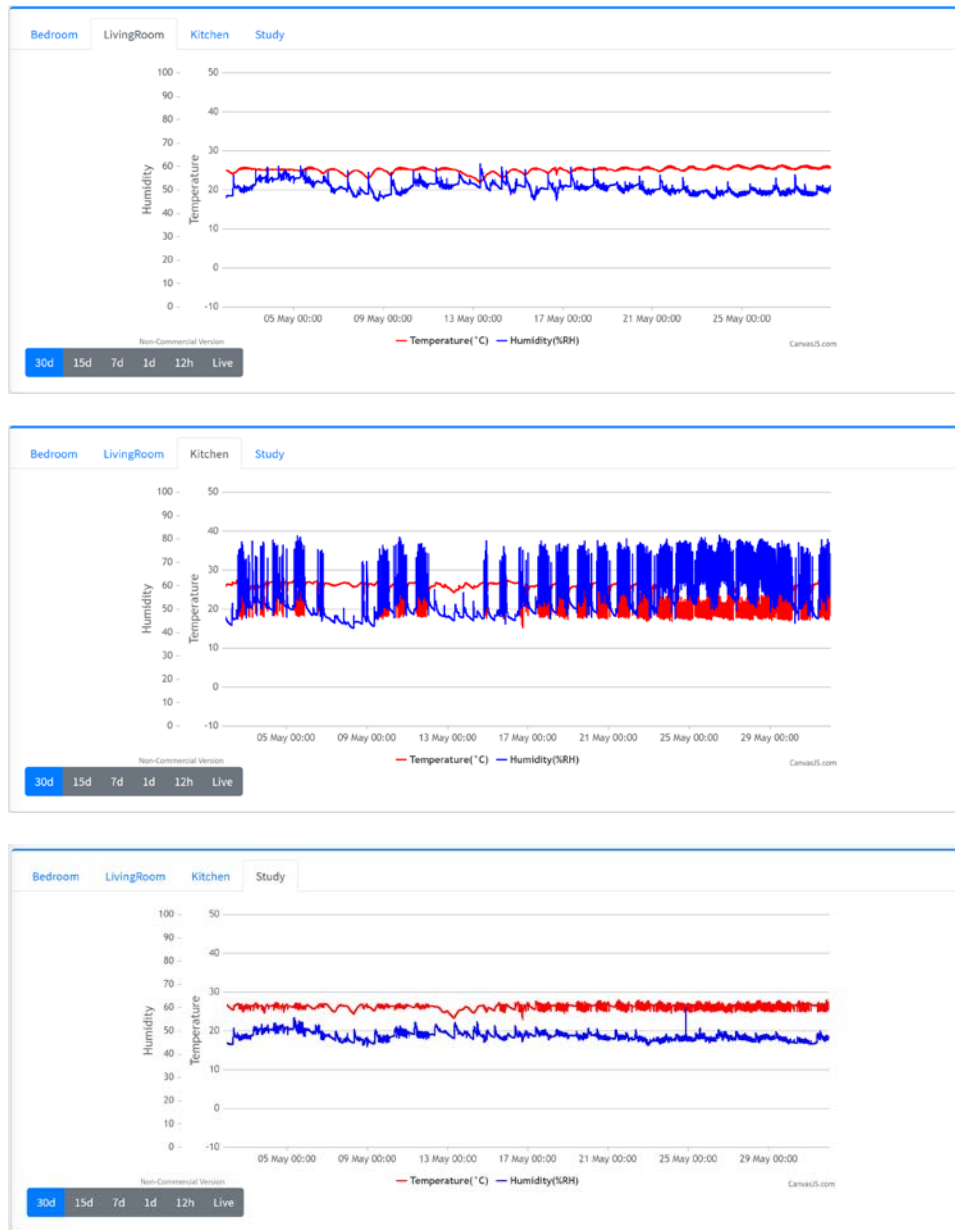


Figure 102. Temperature and humidity charts of 30 days' readings for living room, kitchen, and study room

A.2 Processing and Communication Module

The processing and communication module includes a LoRa transceiver (SX1262) and a microcontroller (MCU, STM32L412C8U6) to provide the basic LoRa communication functions and essential data acquisition and processing capability. The module measures 30mm × 22mm × 2mm and has 19 half-hole soldering pads (8 on the left side and 11 on the right side) for adding functional modules such as the temperature and humidity sensing module and the antenna.

Figure 103 shows a fully assembled processing and communication module. It is as small as about the size of a U.S. quarter coin. If necessary, the size can be further reduced.

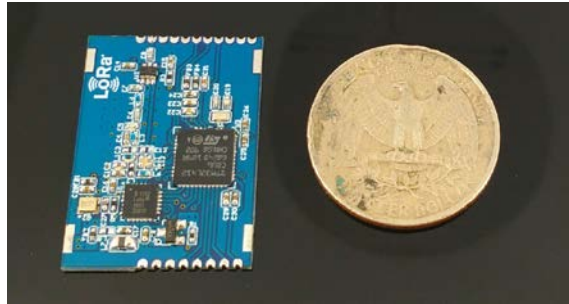


Figure 103. Processing and communication module

The SX1261 LoRa transceiver is connected to the STM32 MCU by the SPI bus. The module provides multiple interfaces for inter-chip communications, including GPIO, SPI, IIC, and UART. Figure 104 shows the internal connection and available interfaces of a processing and communication module.

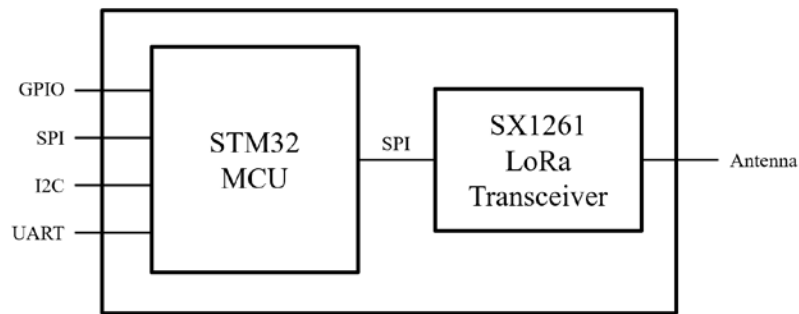


Figure 104. Components and interfaces in the processing and communication module

The SX1261 LoRa transceiver is a low-power, long-range sub-GHz radio transceiver for long-range wireless applications. The transceiver is designed for a long battery life that consumes down to 4.2 mA current in an active receive mode. The chip also integrates a DC-DC converter and low-dropout regulator that allows the chip to be powered by a wide range of input voltage (1.8V ~ 3.7V). With the integrated power amplifier, the SX1261 can transmit up to +15 dBm.

Appendix B: Basics for Residential Building Systems

B.1 Basics for Residential Building Systems

Residential buildings are classified physically by the types of foundation. There are three typical types: slab-on-grade, basement, and crawl space. A rough drawing compares these three types, as shown in Figure 105.

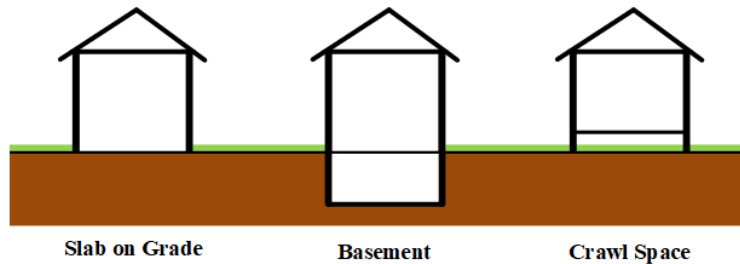


Figure 105. Three types of residential building foundations

Compared to the HVAC system in commercial buildings, a residential HVAC unit's operation is subjected to a similar law of physics, but it is simpler because it only needs to cool or heat a much smaller space (Scott Brown et al. 2013). Figure 106 summarizes all components in the residential HVAC system and displays the energy flow from the energy source to the end user, through heating/cooling units and medium (Matulka 2013; Brumbaugh 2012). Red lines and red boxes represent the heating process, and the blue represents the cooling process.

Table 37 and Table 38 show the relationships between energy source, heating/cooling source, and medium commonly used by residential buildings. In most residential buildings, heating is done by a gas furnace or a boiler. The HVAC system in residential buildings also includes a pipe system for the fluid transferring the heat for the hydronic system or the ductwork for the forced air system. Cooling (i.e., air conditioning, or AC) is the reverse of heating. Currently, most residential air conditioners and heat pumps provide heating and/or cooling through a vapor-compression cycle. Ventilation in residential buildings can either be forced or natural. Forced ventilation systems are most often used to improve indoor air quality and occupant thermal comfort. The application of natural ventilation is limited, especially in humid and warm months.

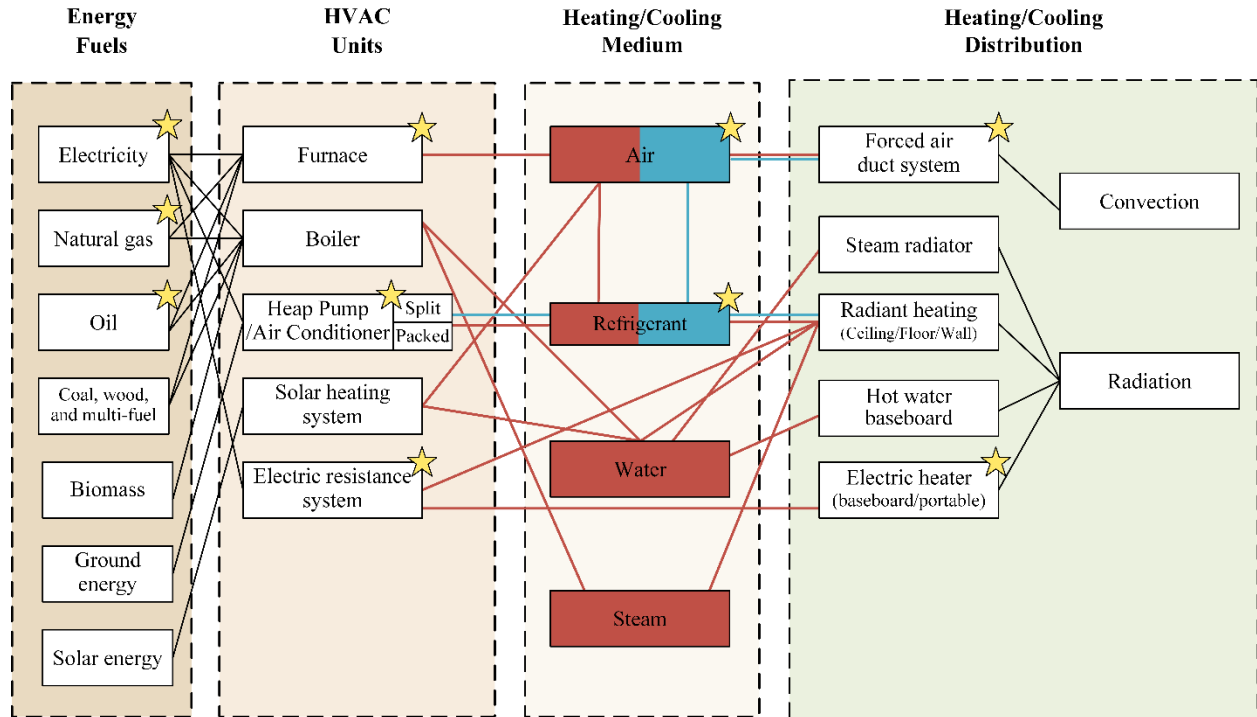


Figure 106. Energy flow mechanism of residential heating/cooling systems

Stars mark the most prevailing combination of HVAC components in the United States (DOE); Red lines and red boxes represent the heating process, while the blue ones show the cooling process.

- 1) **Energy fuels:** Only electricity and ground energy can be used for both cooling and heating system in general. The rest are usually utilized only for heating the room, as they release the heat by burning.
- 2) **HVAC units:** In most residential buildings, heating is done by a gas furnace or a boiler, while cooling is completed through a vapor-compression cycle.
- 3) **Heating/cooling medium:** Air/refrigerant is the primary medium for heating and cooling. Water and steam sometimes serve as the heat transfer medium by radiation.
- 4) **Heating/cooling distribution:** Forced ventilation systems are most often used to improve indoor air quality and comfort, as the application of natural ventilation is limited, especially in humid and warm months.

Table 37. Energy source used in residential HVAC systems

System	Medium	Energy Source						
		Natural Gas	Propane	Heating Oil	Electricity	Biomass	Ground	Solar
Furnace	Air	√	√	√	√			
Boiler	Water/steam	√	√	√	√	√		
Air conditioner	Refrigerant				√			
Heat pump	Refrigerant				√		√	
Active solar heating	Water/air							√
Electric heating					√			

Table 38. Distribution and medium used in residential HVAC systems

System	Medium	HVAC Equipment				
		Furnace	Heat Pump	Active Solar Heating	Boiler	Electric Baseboard
Forced air system	Air	√				
Steam radiant	Steam				√	
Radiant heating	Refrigerant, water, steam, electricity		√	√	√	√
Hot water baseboard (Hydronic heat)	Water			√	√	
Electric heating	Electricity					√

In this project of fault modeling, we focus our research on two selected groups of HVAC systems: heat pumps and vapor-compression air conditioners with furnaces in the slab-on-grade residential building, since currently these two combinations are most common and have more complicated possible faults in the residential sector (DOE).

B.2 Air Loop and Water Loop in the EnergyPlus Model of Residential Prototype Building Model

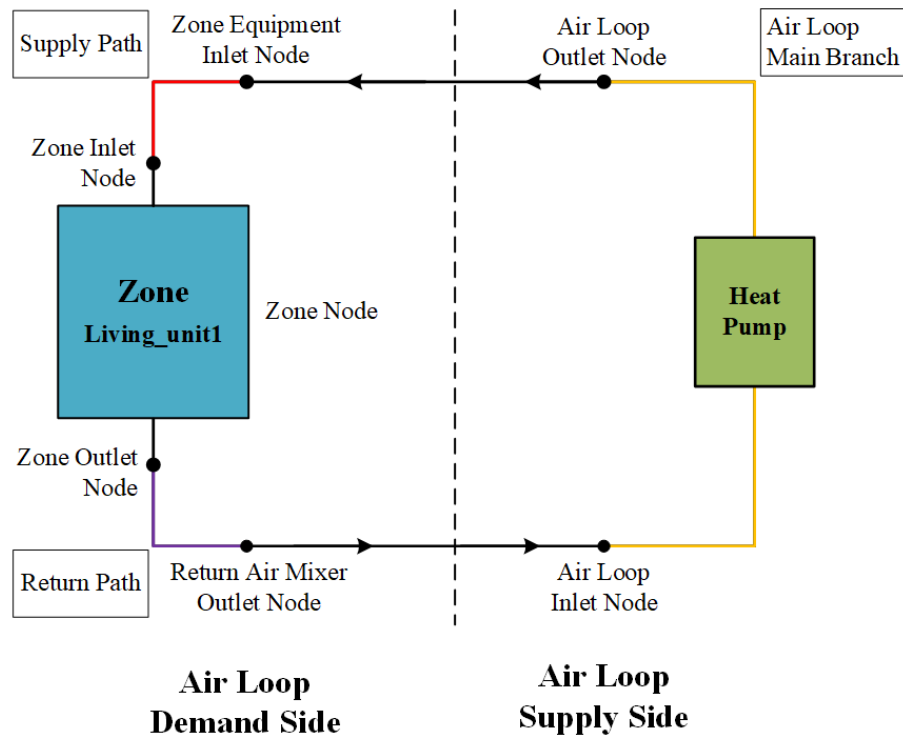


Figure 107. Air loop in the EnergyPlus model of the prototype residential building

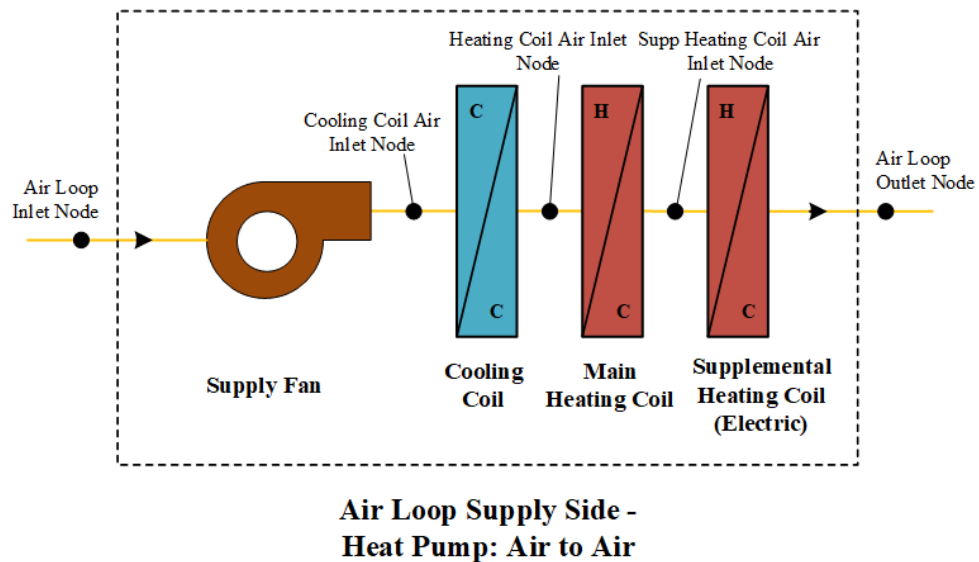


Figure 108. Heat pump module in the EnergyPlus model of the prototype residential building

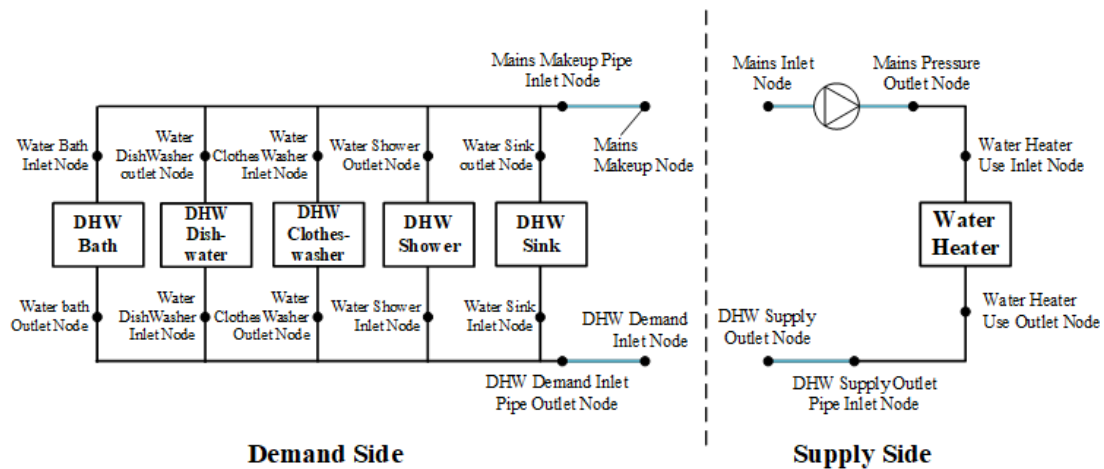


Figure 109. Water loop in the EnergyPlus model of the prototype residential building

B.3 Energy Consumption Analysis for a Typical Operation

Because the heating system is the heat pump, supplemented by the electric resistance, only electricity consumption for the heating is reported. The resistive heating coil is a standby component to provide additional warmth when the primary heating system falls short of the heating demand. When activated, the supplemental resistive heating coil imparts extra heat to the air circulated within the building, compensating for the main system's heating capacity deficit. The activation of this supplemental heating coil is generally regulated by the thermostat setpoint. If the heat demand exceeds the main system's supply capacity, the thermostat's control logic triggers the supplemental heating coil. This control logic is based on the difference between the thermostat setpoint and the current indoor temperature, as well as the outdoor temperature.

Figure 110 shows the monthly energy consumption of heating and cooling in this prototype residential building in Houston weather conditions. This is a typical energy consumption pattern. The peak consumption of cooling is higher than heating because the outdoor temperature deviation from the expected limits for indoor temperature based comfort is higher in summer in Houston.

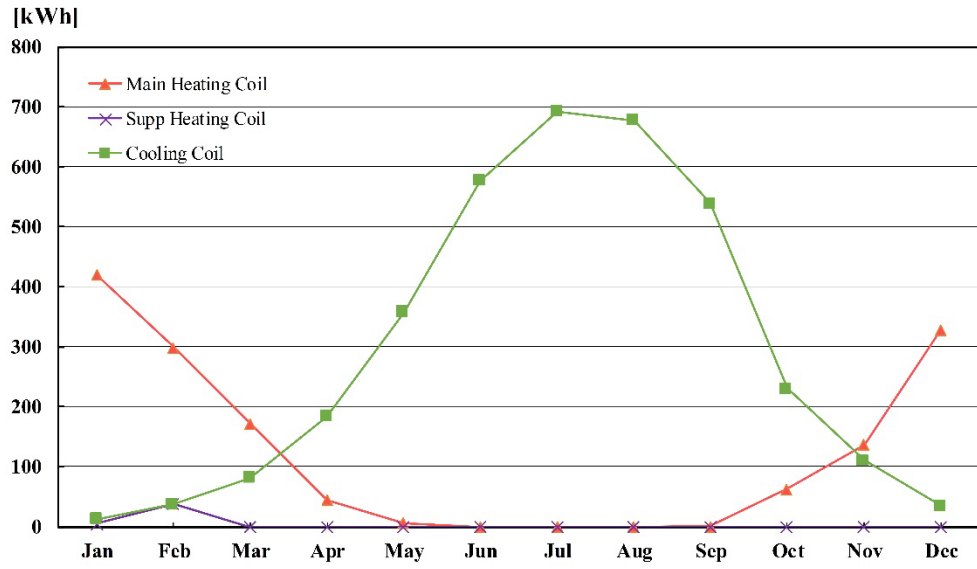


Figure 110. Heating and cooling energy consumption

Appendix C: Fault Modeling for Residential HVAC Systems

C.1 Examples of the PDF Distribution for Different Fault Types

The prevalence distribution is calculated based on the relative fault bias of the fault behavior, as defined in Equation (21).

$$z = \frac{x - x_0}{x_0} \quad (21)$$

where z is the relative bias, x_0 is the nominal value (fault-free) of the model parameter, and x is the fault model parameter.

Fault-by-Lacking

This type of fault leads to fault-related parameters decreasing with the increased severity. Condenser fouling is a typical example. When it occurs, air conditioning or heat pump COP will perform less than the COP with the fault-free case. Its occurrence distribution follows the Weibull model (Bourguignon, Silva, and Cordeiro 2014). The equation of fault-by-lacking is defined in Equations (22) - (25):

$$\text{pdf} = -3e^{z^3} z^2 \quad (22)$$

$$\text{cdf} = 1 - e^{z^3} \quad (23)$$

$$z = [\ln(1 - \text{cdf})]^{1/3} \quad (24)$$

$$z \in [-1, 0] \quad (25)$$

where the probability distribution function (pdf) shows the fault occurrence rate distribution corresponding to the specified cumulative distribution function (cdf).

Fault-by-Excess

The second type is the fault that results in fault-related parameters increasing compared with the fault-free ones. Typical faults include the fan pressure increase due to a dirty air filter. The equation of fault-by-excess is defined in Equations (26) - (29):

$$\text{pdf} = 8e^{-\left(\frac{z+0.2}{0.5}\right)^2} \left(\frac{z+0.2}{0.5}\right) \quad (26)$$

$$\text{cdf} = 1 - e^{-\left(\frac{z+0.2}{0.5}\right)^2} \quad (27)$$

$$z = 0.5[-\ln(1 - \text{cdf})]^{1/2} - 0.2 \quad (28)$$

$$z \in [-1, 0] \quad (29)$$

Fault-by-Deviating

The third fault type is the case that the fault-associated parameters can be both increasing and decreasing compared with the fault-free models. Typical faults are the sensor/thermostat offsets. The equation of fault-by-excess is defined in Equation (30):

$$\text{pdf} = \frac{1}{\sqrt{2\pi\sigma^2}} e^{-\frac{z^2}{2\sigma^2}} \quad (30)$$

Fault-by-Uniform

The fourth type of fault with a uniform PDF curve is relatively rare. One typical example is the schedule fault. The equation of fault-by-excess is defined in Equation (31):

$$\text{pdf} = \frac{1}{b - a} \quad (31)$$

An example of the PDF distribution for fault-by-lacking is shown in Figure 111.

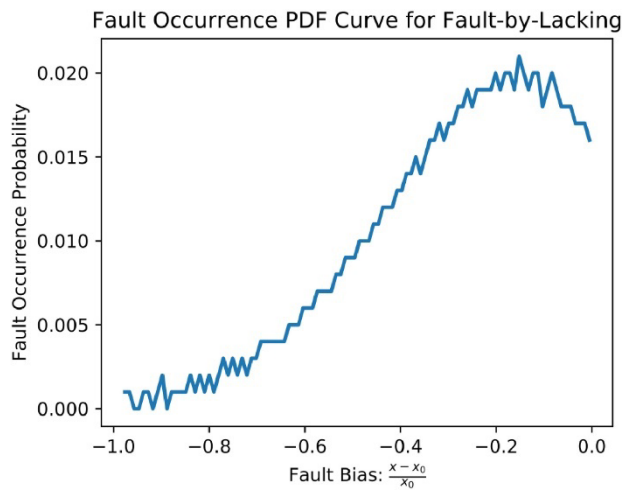


Figure 111. An example of fault-by-lacking PDF curve
(Yanfei Li and O'Neill 2019)

An example of the PDF distribution for fault-by-excess is shown in Figure 112.

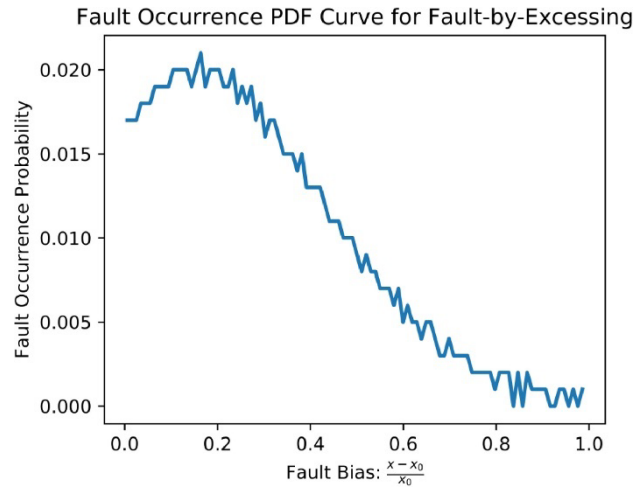


Figure 112. An example of fault-by-excess PDF curve
(Yanfei Li and O'Neill 2019)

An example of the pdf distribution for fault-by-deviating is shown in Figure 113.

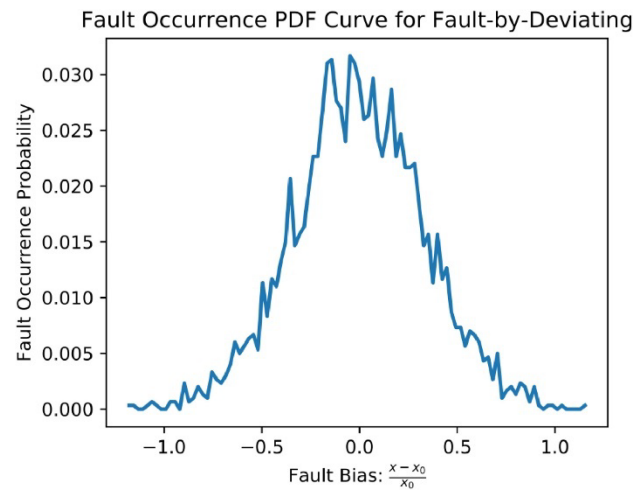


Figure 113. An example of fault-by-deviating PDF curve
(Yanfei Li and O'Neill 2019)

An example of the pdf distribution for fault-by-uniform is shown in Figure 114.

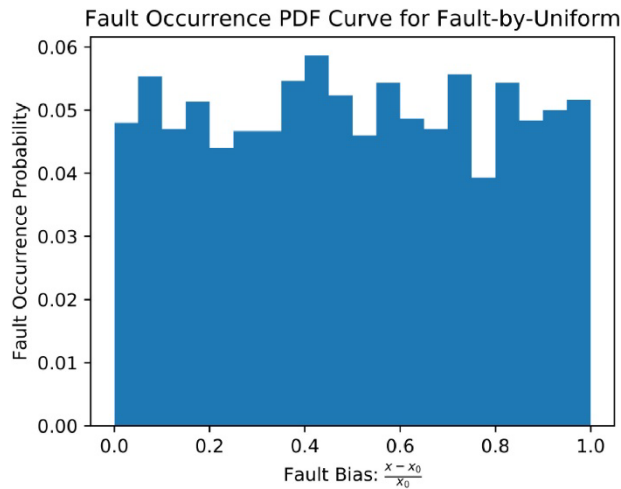


Figure 114. An example of fault-by-uniform PDF curve
(Yanfei Li and O'Neill 2019)

C.2 Fault Impact Analysis

Based on the developed fault library for residential HVAC systems, fault impact analysis is conducted with the prototype building model in Houston. Analysis criteria include:

- 1) Single faults are injected into the baseline models.
- 2) A selected double-faults case is simulated to compare the combination impact and individual impact.
- 3) All faults are injected into the residential building model simultaneously.

C.2.1.1 Matrix for Fault Impact Analysis

Table 39 describes the fault level information for 12 faults in four faulty systems (i.e., heat pump, air handler, air loop, thermostat) and includes the fault-free normal condition. Some heat pump-related faults, like heat transfer fouling, liquid line restriction, and the presence of non-condensable gas, are integrated and represented in the symptoms of the heat pump (COP and capacity), as they are difficult to be simulated in EnergyPlus.

Table 39. Fault Factors and Levels for Residential HVAC Modeling

IDF ID	Fault Name	Faulty Object in IDF	Faulty Parameter in IDF	Normal Value	Fault Mode Unit	Faulty Levels
CC-COP	Cooling COP Degradation	Coil:Cooling:DX:SingleSpeed	Gross Rated Cooling COP	4.07	1	90%,80%,60%
CC-Cap	Cooling Capacity Degradation		Gross Rated Total Cooling Capacity		W	90%,80%,60%
HC-COP	Heating Efficiency Degradation	Coil:Heating:DX:SingleSpeed	Gross Rated Heating COP	3.69	1	90%,80%,60%
HC-Cap	Heating Capacity Degradation		Gross Rated Heating Capacity		W	90%,80%,60%
HCE-Eff	Electric Heating Efficiency Degradation	Coil:Heating:Electric	Efficiency	1.00	1	90%,80%,60%
HCE-Cap	Electric Heating Capacity Degradation		Nominal Capacity		W	90%,80%,60%
Fan-TEff	Blade Dirty	Fan:OnOff	Fan Total Efficiency	0.50	1	90%,80%,60%
Fan-Meff	Motor Worn-Out		Motor Efficiency	0.86	1	90%,80%,60%
Fan-PR	Air Filter Dirty		Pressure Rise	400.00	Pa	90%,80%,60%
ADL-ELR	Air Duct Leakage	AirflowNetwork:Distribution:Component:LeakageRatio	Effective Leakage Ratio	0.10	1	90%,80%,60%
Inf-ELA	Envelope Infiltration	ZoneInfiltration:EffectiveLeakageArea	Schedule	56.669 (long wall)/42.502 (short wall)	cm ²	90%,80%,60%
Therm-OSP	Thermostat Offset	FaultModel:ThermostatOffset	Reference Thermostat Offset	0.00	Delta C	-1, -0.5, 0.5, 1

C.2.1.2 Single Fault

We designed the experiment for single fault analysis using orthogonal arrays of Taguchi methods (Pignatiello 1988). Orthogonal design of experiment can avoid the exponential growth of factors number resulting from full factorial design, and at the same time, maintain the ability of interaction analysis. The 12 factors and four levels (including normal and faulty ones) follow the design in Table 39. The orthogonal table of $L_{64}(4^{12})$ is shown in Table 40, which is adapted from Taguchi L_{64} (type B) Orthogonal Design (Taguchi 1987). Eventually, 65 cases are simulated in total, much less than 4^{12} of full factorial design.

Table 40. Orthogonal Design of Experiment Table $L_{64}(4^{12})$

No. of cases	Factors											
	A	B	C	D	E	F	G	H	I	J	K	L
1	A1	B1	C1	D1	E1	F1	G1	H1	I1	J1	K1	L1
2	A1	B1	C1	D1	E1	F2	G2	H2	I2	J2	K2	L2
3	A1	B1	C1	D1	E1	F3	G3	H3	I3	J3	K3	L3
4	A1	B1	C1	D1	E1	F4	G4	H4	I4	J4	K4	L4
5	A1	B2	C2	D2	E2	F1	G1	H1	I1	J2	K2	L2
6	A1	B2	C2	D2	E2	F2	G2	H2	I2	J1	K1	L1
7	A1	B2	C2	D2	E2	F3	G3	H3	I3	J4	K4	L4
8	A1	B2	C2	D2	E2	F4	G4	H4	I4	J3	K3	L3
9	A1	B3	C3	D3	E3	F1	G1	H1	I1	J3	K3	L3
10	A1	B3	C3	D3	E3	F2	G2	H2	I2	J4	K4	L4
11	A1	B3	C3	D3	E3	F3	G3	H3	I3	J1	K1	L1
12	A1	B3	C3	D3	E3	F4	G4	H4	I4	J2	K2	L2
13	A1	B4	C4	D4	E4	F1	G1	H1	I1	J4	K4	L4
14	A1	B4	C4	D4	E4	F2	G2	H2	I2	J3	K3	L3
15	A1	B4	C4	D4	E4	F3	G3	H3	I3	J2	K2	L2
16	A1	B4	C4	D4	E4	F4	G4	H4	I4	J1	K1	L1
17	A2	B1	C2	D3	E4	F1	G2	H3	I4	J1	K2	L3
18	A2	B1	C2	D3	E4	F2	G1	H4	I3	J2	K1	L4
19	A2	B1	C2	D3	E4	F3	G4	H1	I2	J3	K4	L1
20	A2	B1	C2	D3	E4	F4	G3	H2	I1	J4	K3	L2
21	A2	B2	C1	D4	E3	F1	G2	H3	I4	J2	K1	L4
22	A2	B2	C1	D4	E3	F2	G1	H4	I3	J1	K2	L3
23	A2	B2	C1	D4	E3	F3	G4	H1	I2	J4	K3	L2

No. of cases	Factors											
	A	B	C	D	E	F	G	H	I	J	K	L
24	A2	B2	C1	D4	E3	F4	G3	H2	I1	J3	K4	L1
25	A2	B3	C4	D1	E2	F1	G2	H3	I4	J3	K4	L1
26	A2	B3	C4	D1	E2	F2	G1	H4	I3	J4	K3	L2
27	A2	B3	C4	D1	E2	F3	G4	H1	I2	J1	K2	L3
28	A2	B3	C4	D1	E2	F4	G3	H2	I1	J2	K1	L4
29	A2	B4	C3	D2	E1	F1	G2	H3	I4	J4	K3	L2
30	A2	B4	C3	D2	E1	F2	G1	H4	I3	J3	K4	L1
31	A2	B4	C3	D2	E1	F3	G4	H1	I2	J2	K1	L4
32	A2	B4	C3	D2	E1	F4	G3	H2	I1	J1	K2	L3
33	A3	B1	C3	D4	E2	F1	G3	H4	I2	J1	K3	L4
34	A3	B1	C3	D4	E2	F2	G4	H3	I1	J2	K4	L3
35	A3	B1	C3	D4	E2	F3	G1	H2	I4	J3	K1	L2
36	A3	B1	C3	D4	E2	F4	G2	H1	I3	J4	K2	L1
37	A3	B2	C4	D3	E1	F1	G3	H4	I2	J2	K4	L3
38	A3	B2	C4	D3	E1	F2	G4	H3	I1	J1	K3	L4
39	A3	B2	C4	D3	E1	F3	G1	H2	I4	J4	K1	L1
40	A3	B2	C4	D3	E1	F4	G2	H1	I3	J3	K2	L2
41	A3	B3	C1	D2	E4	F1	G3	H4	I2	J3	K1	L2
42	A3	B3	C1	D2	E4	F2	G4	H3	I1	J4	K2	L1
43	A3	B3	C1	D2	E4	F3	G1	H2	I4	J1	K3	L4
44	A3	B3	C1	D2	E4	F4	G2	H1	I3	J2	K4	L3
45	A3	B4	C2	D1	E3	F1	G3	H4	I2	J4	K2	L1
46	A3	B4	C2	D1	E3	F2	G4	H3	I1	J3	K1	L2
47	A3	B4	C2	D1	E3	F3	G1	H2	I4	J2	K4	L3
48	A3	B4	C2	D1	E3	F4	G2	H1	I3	J1	K3	L4
49	A4	B1	C4	D2	E3	F1	G4	H2	I3	J1	K4	L2
50	A4	B1	C4	D2	E3	F2	G3	H1	I4	J2	K3	L1
51	A4	B1	C4	D2	E3	F3	G2	H4	I1	J3	K2	L4
52	A4	B1	C4	D2	E3	F4	G1	H3	I2	J4	K1	L3
53	A4	B2	C3	D1	E4	F1	G4	H2	I3	J2	K3	L1

No. of cases	Factors											
	A	B	C	D	E	F	G	H	I	J	K	L
54	A4	B2	C3	D1	E4	F2	G3	H1	I4	J1	K4	L2
55	A4	B2	C3	D1	E4	F3	G2	H4	I1	J4	K1	L3
56	A4	B2	C3	D1	E4	F4	G1	H3	I2	J3	K2	L4
57	A4	B3	C2	D4	E1	F1	G4	H2	I3	J3	K2	L4
58	A4	B3	C2	D4	E1	F2	G3	H1	I4	J4	K1	L3
59	A4	B3	C2	D4	E1	F3	G2	H4	I1	J1	K4	L2
60	A4	B3	C2	D4	E1	F4	G1	H3	I2	J2	K3	L1
61	A4	B4	C1	D3	E2	F1	G4	H2	I3	J4	K1	L3
62	A4	B4	C1	D3	E2	F2	G3	H1	I4	J3	K2	L4
63	A4	B4	C1	D3	E2	F3	G2	H4	I1	J2	K3	L1
64	A4	B4	C1	D3	E2	F4	G1	H3	I2	J1	K4	L2

The effect index of each fault is computed by Equation (32). The quantity is like a sensitivity analysis to analyze what factors have a higher effect on the output, i.e., energy consumption.

$$\text{var}(f(x) | x_i) \approx \frac{1}{3} \sum_{j=1}^3 (\mu - \mu_{x_i, L_j})^2 \quad (32)$$

where,

x_i is the variable for one factor,

$f(x)$ is the output of the model, i.e., energy consumption,

μ is the overall mean of output,

μ_{x_i, L_j} is the means for each variable level.

Figure 115 and Figure 116 show the impact of a single fault on the heating and the cooling separately, and the overall HVAC energy consumption, throughout a year. Figure 117 illustrates monthly effects from the aspect of each fault, where the deeper color represents a higher impact. Consistent with our knowledge, heating-related faults are found to have the largest impact in winter, while cooling-related faults dominate during summer. Additionally, fan-related faults have a high influence coefficient only in the cooling and shoulder seasons. Leakage, including duct leakage and envelope infiltration, have a higher impact on energy consumption when it is the heating season. Thermostat offset in $\pm 1^\circ\text{C}$ range has less effect, compared to other faults.

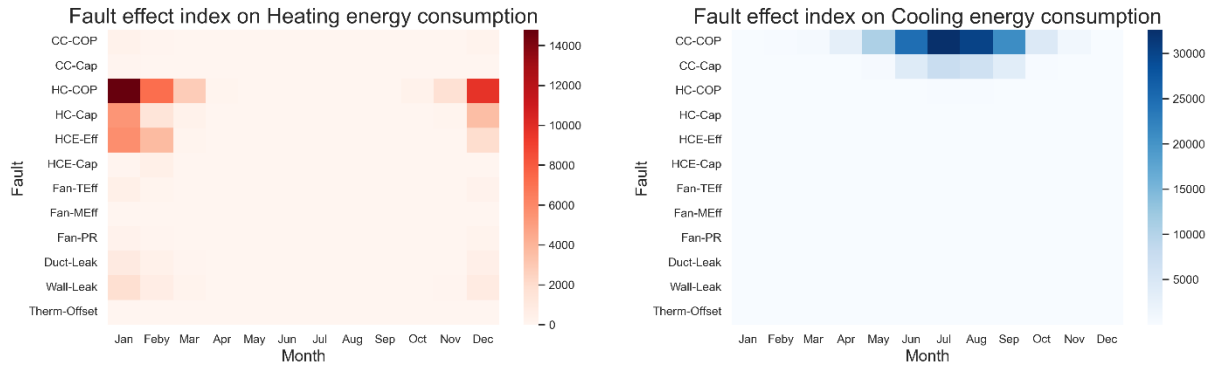


Figure 115. Monthly fault effect on the heating and cooling energy consumption

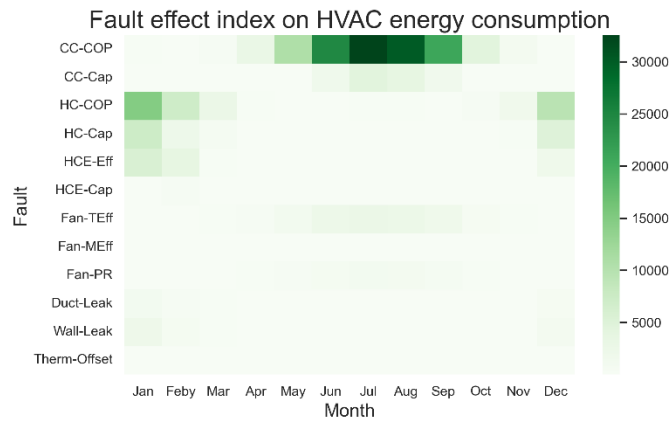


Figure 116. Monthly fault effect on the overall HVAC energy consumption

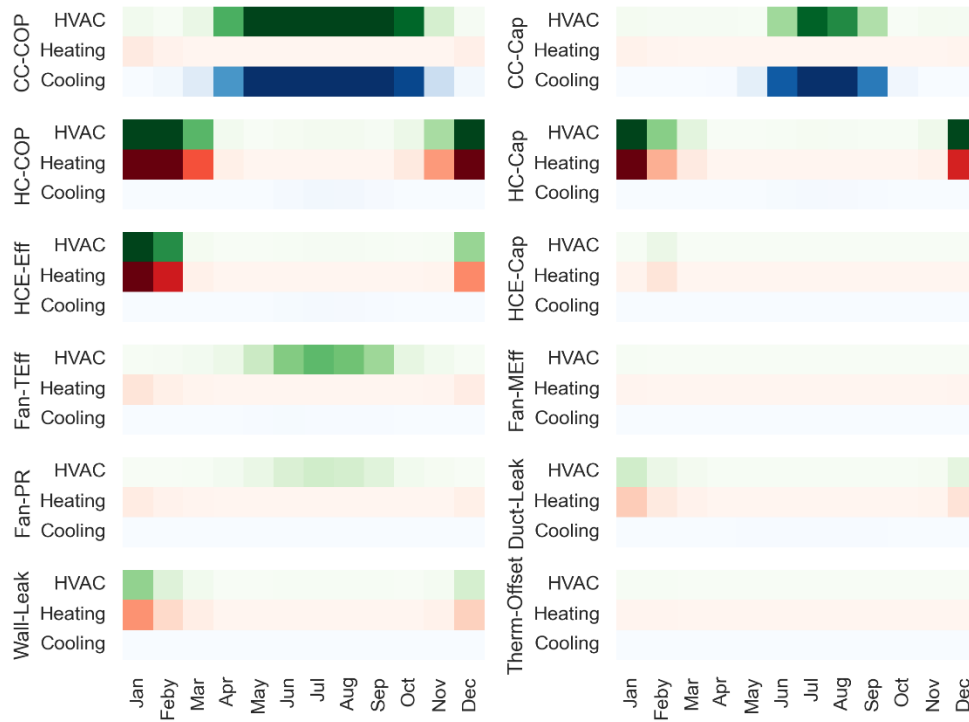


Figure 117. Monthly effect on the energy consumption for each fault

C.1.3 Double Faults

Double faults are simulated separately and are integrated to investigate the different impacts between the individual and the integrated.

The fault impact of a single fault is described by Equations (33) - (34).

$$F(A) = E(\text{fault } A) - E(\text{Baseline}) \quad (33)$$

$$F(B) = E(\text{fault } B) - E(\text{Baseline}) \quad (34)$$

Where F is the fault impact metrics, while E is energy consumption.

Double fault impact is defined as the additional change, compared to the sum of two individual fault impacts (Khire and Trcka 2013). It can be calculated by Equation (35).

$$F(AB) = [E(\text{faults } A \& B) - E(\text{Baseline})] - [F(A) + F(B)] \quad (35)$$

Figure 118 depicts an example of the impact comparison of individual and coupled faults. Additional fault combination impact can be positive or negative. It shows an example of a comparison of two individual faults (cooling coil COP decrease and fan total efficiency decrease) and their coupled fault. The first gray bar is the HVAC energy consumption of the baseline model. The second bar represents the cooling coil capacity degradation result, where the cyan segment is the additional energy consumption compared to the baseline. Similarly, the yellow segment in the third bar represents the extra consumption due to the fan total efficiency

decrease. In the fourth bar group, the impact of the former is higher than the latter, which means the combination of cooling coil COP decrease and fan total efficiency decrease has a negative effect on the HVAC energy consumption.

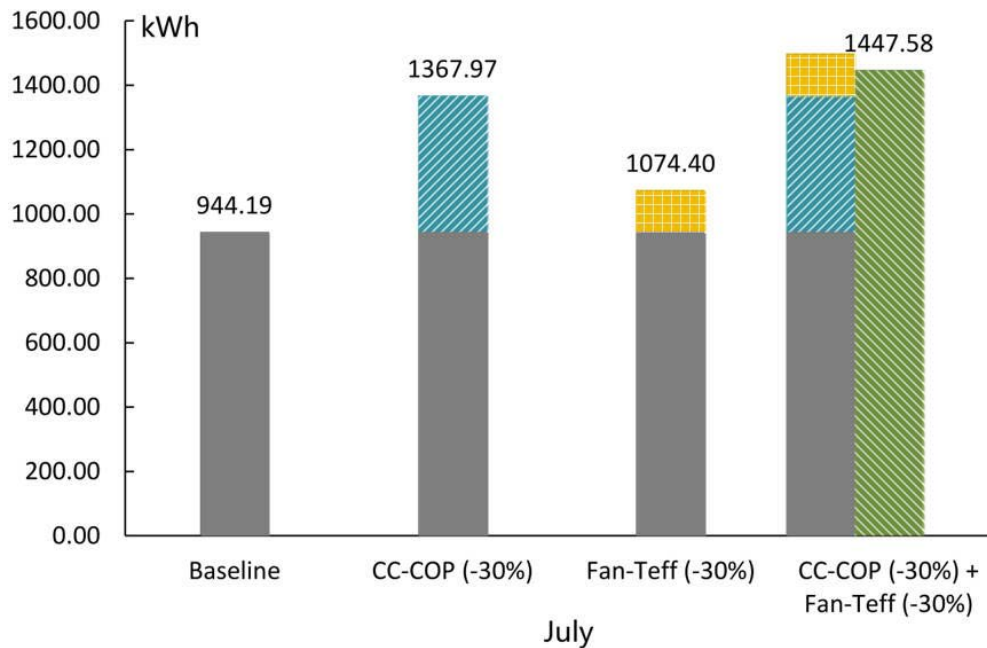


Figure 118. Performance comparison between individual and coupled faults during the month of July (residential building in Houston)

C.1.4 Multiple Faults

Three thousand fault EnergyPlus models are generated as described in Section 4.2. Figure 119 illustrates the fault sampling distribution of cooling coil COP. The COP decrease results from eight lacking faults: condenser fouling, evaporator fouling, liquid line restriction, non-condensable gas in the refrigerant, charge fault, compressor degradation, expansion valve restriction, and four-way reverse valve leakage. Those eight faults follow the lacking distribution, shown in Figure 31(a). Due to the random feature of sampling, the combination of these multiple lacking-type faults shows a normal-like distribution.

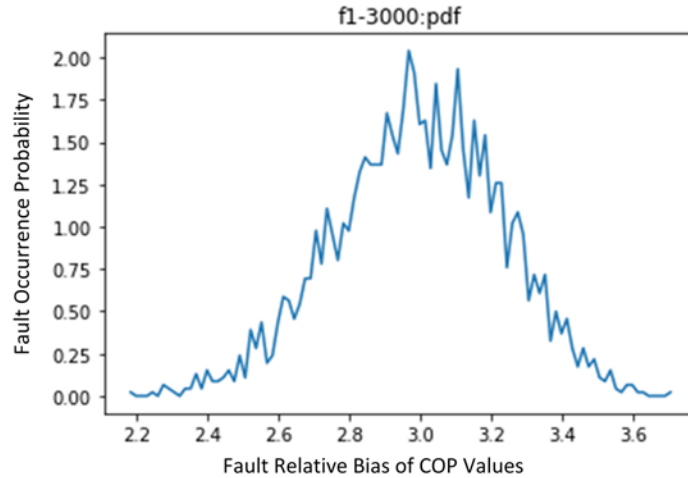


Figure 119. Fault sampling distribution of cooling coil COP values in 3,000 fault models

Figure 120 shows the HVAC energy consumption distribution from these 3,000 simulations. In this case, we can see that energy consumption from the faulty EnergyPlus models increases as compared to the normal case. This is because a majority of faults developed in this project contribute to an increase in energy consumption. Even though thermostat control schedule fault may contribute to energy savings, Figure 115–Figure 117 demonstrate that thermostat offset has less impact on the HVAC energy consumption compared to other faults.

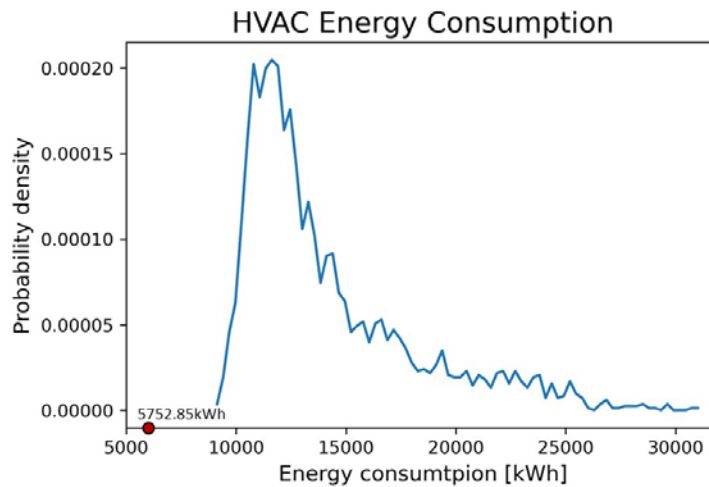


Figure 120. Probability distribution of HVAC energy consumption from 3000 fault simulations

The X-axis is the total energy consumption, Y-axis is the probability of each consumption, and the red dot displays the output from the normal case without any fault.

C.3 Fault Library for the Residential HVAC System

Table 41. Fault Library for Residential HVAC Systems

Fault Taxonomy			Fault Impact	Fault Modeling					
Faulty System	Faulty Component	Fault Name	Faulty Symptom	Modeling Approach ¹	Faulty Object in IDF	Faulty Parameter in IDF	Value Type	Fault Direction	Fault Bound (Yunhua Li et al. 2014; Ahmed 2013; Mowris et al. 2012; M. Kim et al. 2009; B. Chen and Braun 2000; Breuker and Braun 1998a)
Heat Pump	Condenser	1) Condenser fouling*	Heating/cooling efficiency and capacity	D	Coil:Cooling:DX:SingleSpeed, Coil:Heating:DX:SingleSpeed	Gross Rated Cooling COP Gross Rated Total Cooling Capacity Gross Rated Heating COP Gross Rated Heating Capacity	Continuous	Lacking	-19%~-30%; -10%~-21%
	Evaporator	2) Evaporator fouling*		D			Continuous	Lacking	-3%~-17%; -9%~-20%
	Compressor	3) Compressor degradation*		D			Continuous	Lacking	Null/-8%~-24%
	Valve	4) Expansion valve restriction		D			Continuous	Lacking	
		5) Reverse valve leakage		D			Continuous	Lacking	-11%~-23%; -10.9%
		6) Liquid line restriction		D			Continuous	Lacking	-8.7%~-55%; -7.5~-34%
	Refrigerant	7) Presence of non-condensable gas		D			Continuous	Lacking	-1%~-21%; -2%~-33%
		8) Refrigerant undercharge/line leakage*		D			Continuous	Lacking	-2%~-67%; -3%~-39%
		9) Refrigerant overcharge		D			Continuous	Lacking	-1%~-17%; 1%~4.5%
Furnace	Heat Exchanger	10) Heat exchanger fouling	Burner efficiency and capacity	D	Coil:Heating:Fuel	Burner Efficiency Nominal Capacity	Continuous	Lacking	No source
	Gas Valve	11) Valve block		D			Continuous	Lacking	No source
	Ignitor	12) Ignite malfunction		D			Discrete	Lacking	No source
	Draft Inducer	13) Motor problem		D			Discrete	Lacking	No source
		14) Draft inducer damper stuck close		D			Discrete	Lacking	No source
Air Handler	Electric Resistance ²	15) Electric coil fouling	Heating/cooling efficiency and capacity	D	Coil:Heating:Electric	Efficiency Nominal Capacity	Continuous	Lacking	No source
	Blower	16) Blade dirty	Pressure rise; fan energy; airflow	D	Fan:OnOff	Fan Total Efficiency	Continuous	Lacking	No source
		17) Motor worn-out	Pressure rise; fan energy; airflow	D		Motor Efficiency	Continuous	Lacking	No source
	Air Filter	18) Air filter dirty	Pressure rise; fan energy; airflow	D		Pressure Rise	Continuous	Excessing	No source
Air Loop	Air Duct	19) Air duct leakage*	Pressure rise; fan energy; airflow; heating/cooling energy	D	AirflowNetwork:Distribution:Component:LeakageRatio	Effective Leakage Ratio	Continuous	Excessing	6%~30%

Fault Taxonomy			Fault Impact	Fault Modeling					
	Envelope	20) Envelope infiltration	Pressure rise; fan energy; airflow; heating/cooling energy	D	a)ZoneInfiltration: EffectiveLeakageArea b)AirflowNetwork:MultiZone: Surface:EffectiveLeakageArea	a) Schedule b) Effective Leakage Area	Continuous	Uniform	No source
	Register	21) Register stuck/diffuser blocked	Pressure rise; fan energy; airflow; heating/cooling energy				Continuous	Excessing	No source
Thermostat	Mode	22) Incorrect HVAC on/off mode	Heating/cooling energy; thermal comfort	D	ThermostatSetpoint: DualSetpoint	Heating/Cooling Setpoint Temperature Schedule	Discrete	Uniform	No source
	Schedule	23) Inappropriate setpoints for thermostats	Heating/cooling energy; thermal comfort	D		Heating/Cooling Setpoint Temperature Schedule	Discrete	Uniform	No source
	Bias	24) Thermostat offset	Heating/cooling energy; thermal comfort	N	FaultModel:ThermostatOffset	Reference Thermostat Offset	Discrete	Normal	No source

* The most common fault in the residential HVAC

¹ D = Direct modeling: heating/cooling efficiency and capacity; N = Native fault objective: thermostat offset

² Heat Pump Heating Supplementary

Appendix D: Fault Detection and Diagnosis for Residential HVAC Systems

D.1 Evaluation Metrics

Evaluation metrics are essential to evaluate and compare the effectiveness of selected FDD classification methods. Evaluating an FDD method can be conducted from various perspectives, including cost, generality and transferability, capability, modeling efforts, interpretability, automation level, etc. (J. Chen et al. 2022; Shi and O'Brien 2019). The capability, which represents the accuracy of detecting and diagnosing the existing faults, is the most effective and prevailing metrics to assess FDD methods. For the detection, four typical metrics were provided in (Bode et al. 2020):

- True positive, where the sample is true, and the prediction is true
- True negative, where the sample is false, and the prediction is false
- False positive, where the sample is false, and the prediction is true
- False negative, where the sample is true, and the prediction is false.

Similarly, four evaluation metrics are specified for detection and diagnosis (Yuill and Braun 2016; Bode et al. 2020):

- Accuracy (also known as correctness rate, i.e., the sum of true positive and true negative): detected or diagnosed result is the same as the actual failure
- False alarm (i.e., false positive): the degradation level does not exceed a given threshold, but the abnormal operation is reported
- Misdiagnosis: the AFDD detects a fault correctly as its presence, but the fault diagnosed is different from the actual one
- Missed detection (i.e., false negative): a fault is present, but the AFDD does not detect it.

The most common metric is the accuracy rate and false alarm. They show the correction rate in the total diagnosis cases and the misdetection rate of fault-free cases as faulty.

The confusion matrix, as shown in Figure 120, is often used to evaluate the performance of a classification task in a comprehensive way on a two-class and n-class basis (Han et al. 2011). A two-class case, which consists of normal condition and fault condition, is more often picked for fault detection tasks. It includes sensitivity (i.e., recall), specificity, precision, negative predictive value, accuracy, and F1 score with equations marked in Figure 120(a). Fault diagnosis is a multiclass classification problem (Zhao et al. 2014; D. Li et al. 2017). Its task is to determine which fault class the data belong. Thus, the n-class type, shown in Figure 120(b), is considered with multiple fault conditions. The classification accuracy of the n^{th} fault class is displayed for

each fault and no-fault condition. It equals the ratio between class n samples that are correctly classified and the total class n data samples (G. Li et al. 2018).

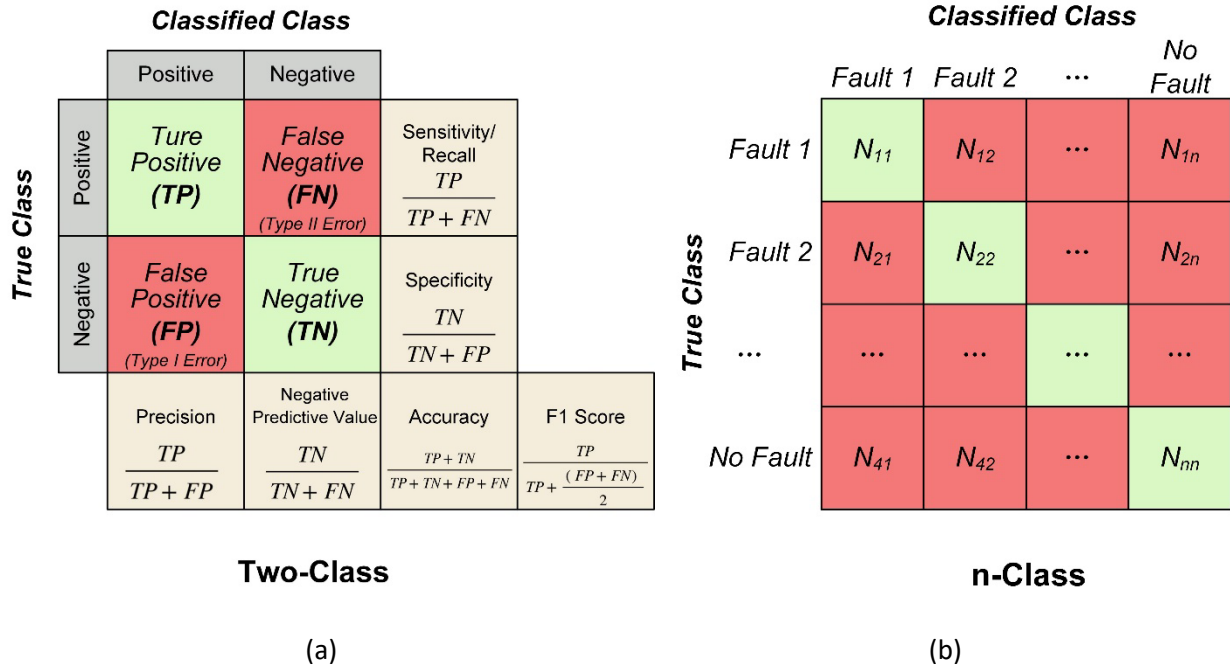


Figure 121. Confusion matrix for fault detection

D.2 Forecasting Results and Absolute Difference Error for Duct Leakage Case

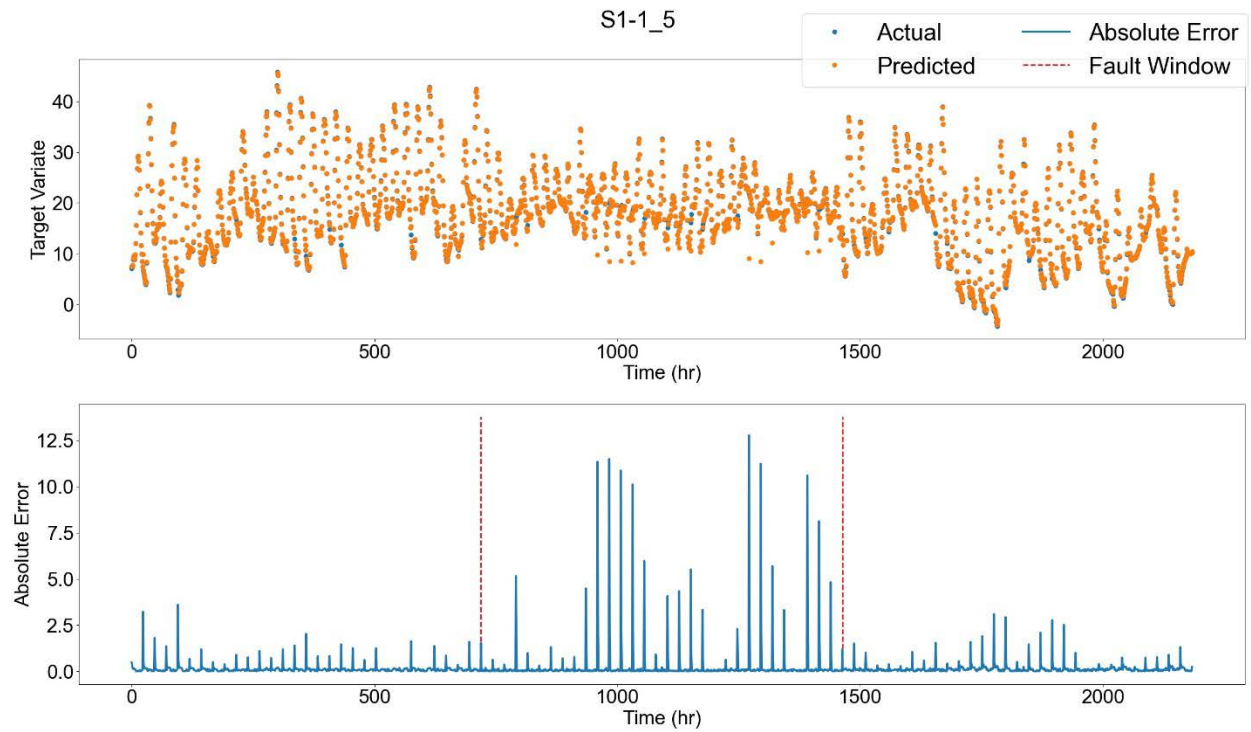


Figure 122. Forecasting results and absolute difference error for Scenario 1-1 (50% leakage)

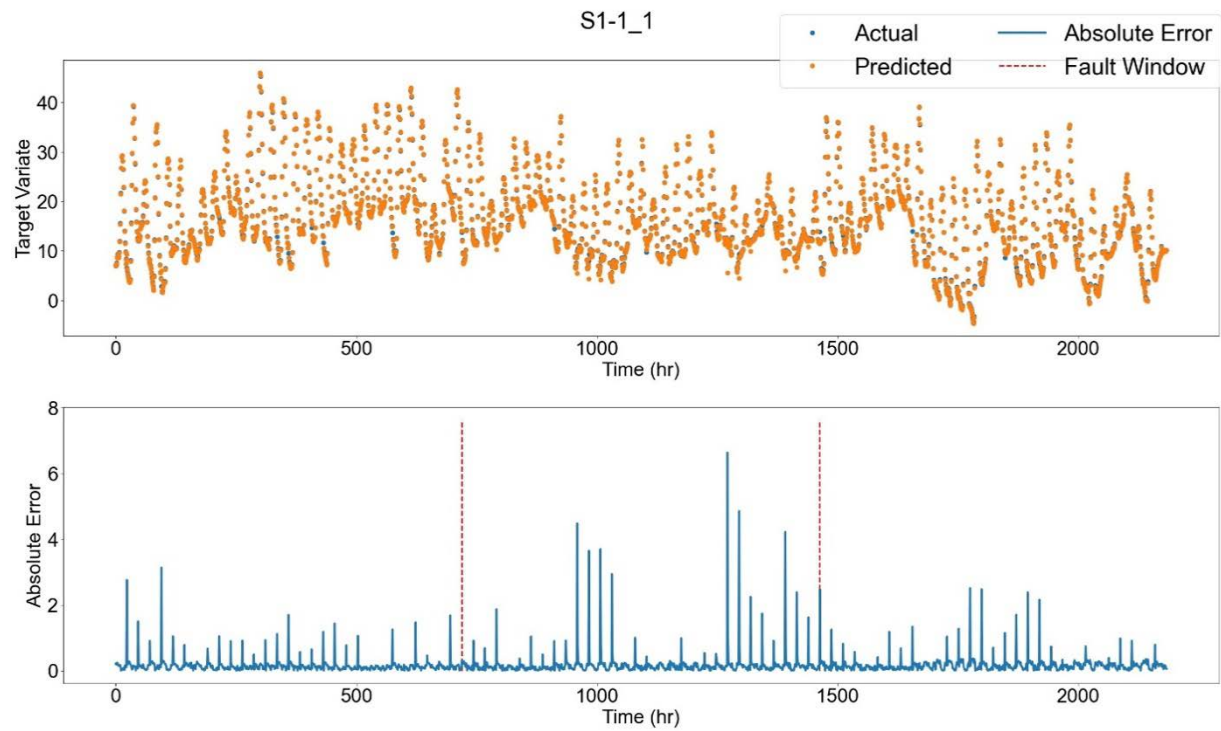


Figure 123. Forecasting results and absolute difference error for Scenario 1-1 (10% leakage)

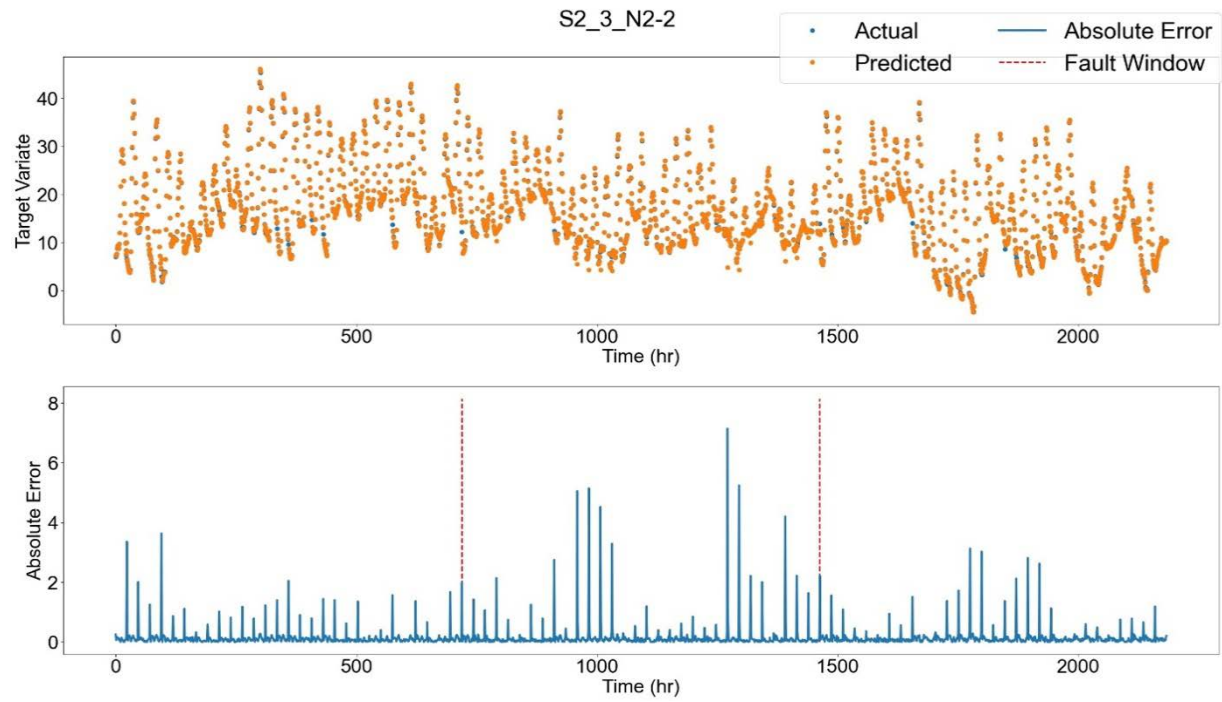


Figure 124. Forecasting results and absolute difference error for Scenario 2 (N2-2)

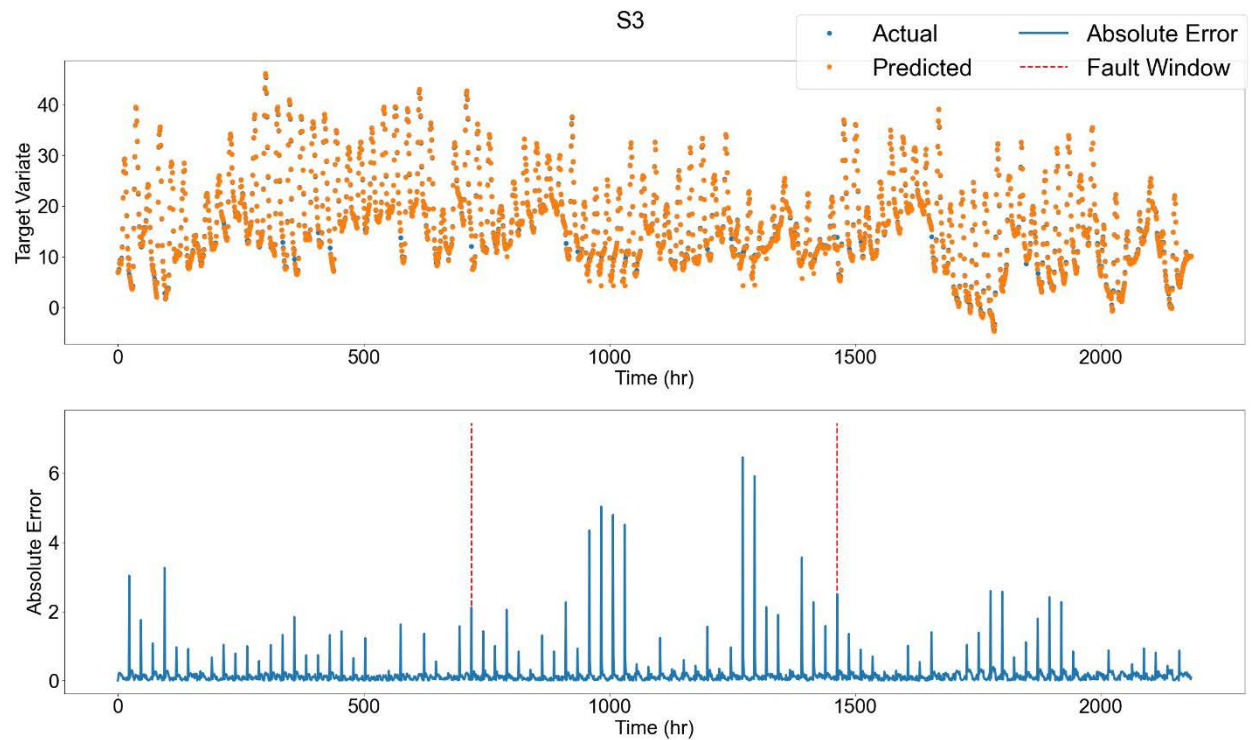
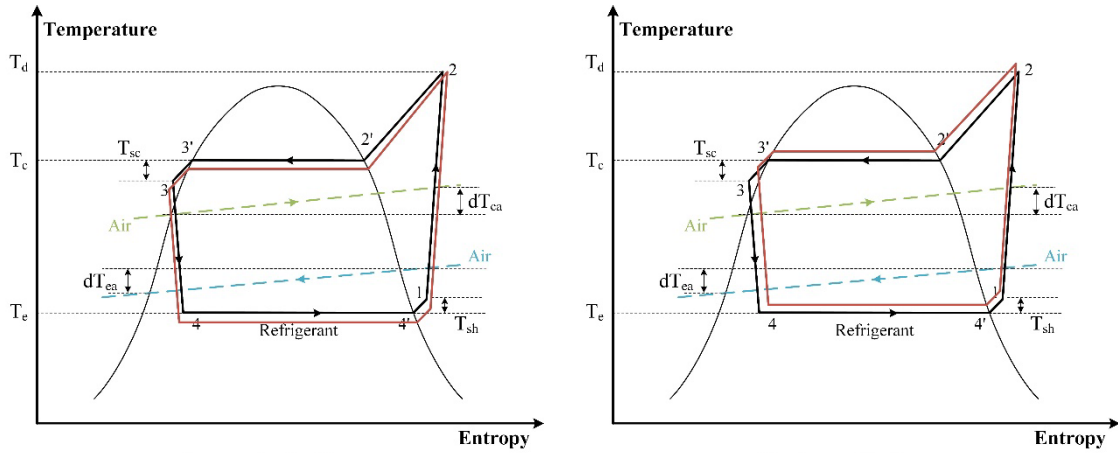


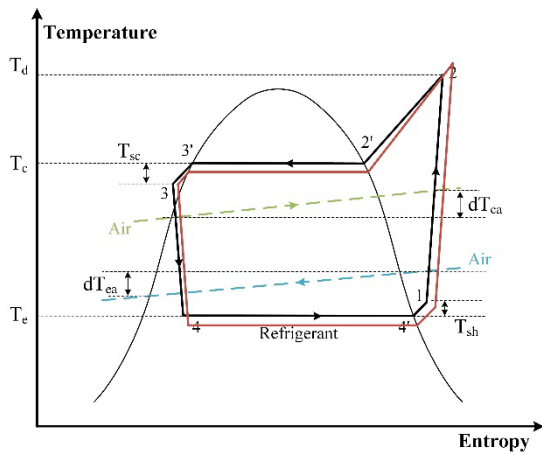
Figure 125. Forecasting results and absolute difference error for Scenario 3

D.3 Temperature-Entropy in Normal and Faulty Conditions of a VCC System

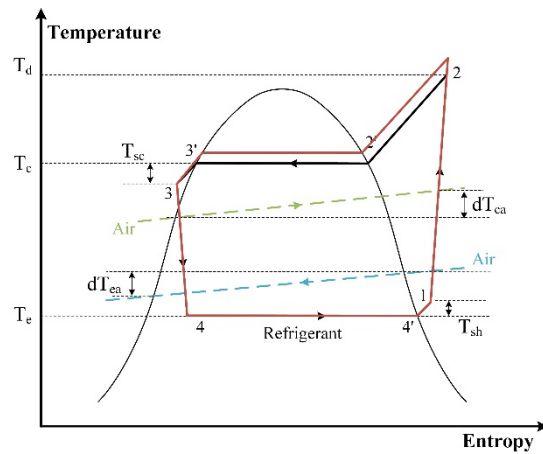


Evaporator Fouling

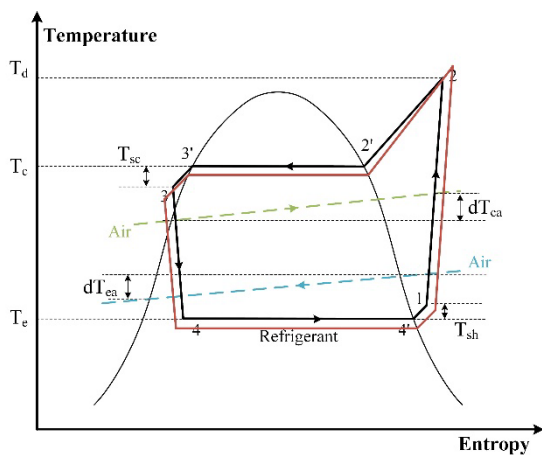
Condenser Fouling



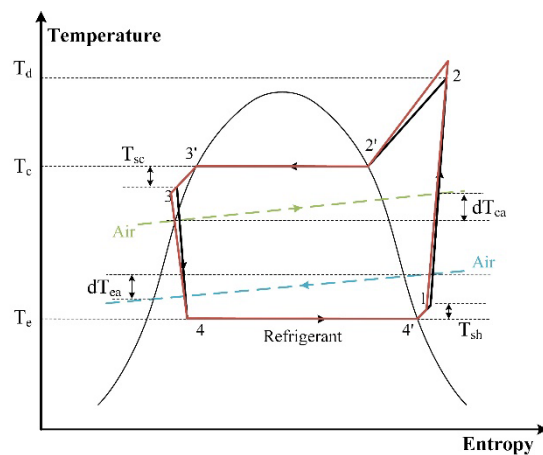
Refrigerant Undercharge



Refrigerant Overcharge



Liquid Line Restriction



Non-condensable Gas

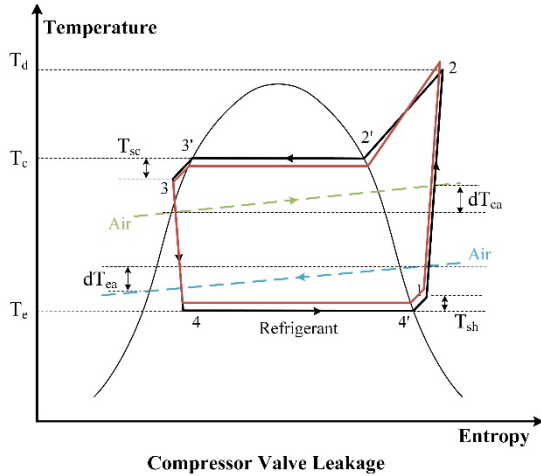


Figure 126. Comparison of temperature-entropy in normal (black line) and faulty (red line) condition of a VCC system

Note: Fault impact on the air side is not illustrated.

D.4 FDD Classification Methods for the VCC System

Three existing AFDD methods for the residential VCC system are investigated: statistical rule-based chart, sensitivity ratio method, and simple rule-based method.

D.4.1 Statistical Rule-Based Chart

The statistical rule-based chart is characterized by considering probabilities in three uncertainty sources: measurement noise uncertainty, steady-state uncertainty, and fault-free model uncertainty. It identifies faults with change direction patterns (i.e., increase \uparrow , decrease \downarrow , or remain unchanged \rightarrow) for a set of features (shown in Table 42) corresponding to a given fault, and calculates statistical probabilities to classify the current operation state. Change directions are determined by a predefined threshold for each feature. The basic calculation workflow consists of:

- 1) Calculating the probabilities of three directions for each feature (i): $P(C\uparrow|X_i)$, $P(C\downarrow|X_i)$, $P(C\rightarrow|X_i)$
- 2) Calculating the individual probability of corresponding feature directions for each fault (j): $P(C_{ij})$
- 3) Calculating the overall probability for each fault(j): P_j

Table 42. Rule-Based Chart of Seven Features for VCC FDD

(M. Kim et al. 2008)

	Zone*	T _e	T _{sh}	T _d	T _c	T _{sc}	dT _{ca}	dT _{ea}
Compressor valve leakage (CV)	A	↑	→	↑	↓	↓	↓	↓
Improper outdoor airflow (CF)	A	↑	→	↑	↑	↓	→	↓
	B	↓	↑	↑	↑	↓	↓	↓
Improper indoor airflow (EF)	A	↓	→	→	↓	→	↓	↑
Liquid-line restriction (LL)	A	→	→	→	→	→	→	→
	B	↓	↑	↑	↓	↑	↓	↓
Refrigerant undercharge (UC)	A	→	→	→	↓	↓	↓	↓
	B	↓	↑	↑	↓	↓	↓	↓
Refrigerant overcharge (OC)	A	→	→	↑	↑	↑	→	→
No fault (NF)	-	→	→	→	→	→	→	→

 *Zone A: T_{sh} < 9°C; Zone B: T_{sh} > 9°C

Fault probability is a key calculation for fault diagnosis. Its inputs include:

- 1) FDD neutral threshold ε_i
- 2) Predicted mean of features $\bar{x}_{i,NF}$
- 3) Measured mean of features \bar{x}_i
- 4) Amplification factor s (assumed as 1 at first; will be adjusted in the field test).

Equations for probabilities of three directions for each feature (i) are provided as Equation (36) - (38) (M. Kim et al. 2008). The summation equals 1 as Equation (39).

$$P(C_{\downarrow}|X_i) = P(x_i \geq \mu_i + \varepsilon_i) = \frac{1}{2} \left[1 - \operatorname{erf} \left(\frac{r_i + \varepsilon_i}{\sqrt{2}\sigma_{i,NF}} \right) \right] \quad (36)$$

$$P(C_{\uparrow}|X_i) = P(x_i \leq \mu_i - \varepsilon_i) = \frac{1}{2} \left[1 + \operatorname{erf} \left(\frac{r_i - \varepsilon_i}{\sqrt{2}\sigma_{i,NF}} \right) \right] \quad (37)$$

$$P(C_{-}|X_i) = P(\mu_i - \varepsilon_i < x_i < \mu_i + \varepsilon_i) = \frac{1}{2} \left[\operatorname{erf} \left(\frac{r_i + \varepsilon_i}{\sqrt{2}\sigma_{i,NF}} \right) - \operatorname{erf} \left(\frac{r_i - \varepsilon_i}{\sqrt{2}\sigma_{i,NF}} \right) \right] \quad (38)$$

$$P(C_{\downarrow}|X_i) + P(C_{\uparrow}|X_i) + P(C_{-}|X_i) = 1 \quad (39)$$

The diagnosed fault will be the one with the highest probability after calculation. More explanation of equations for probabilities of three directions for each feature (i) and fault identification table can be found in the work of Kim et al. (2008).

D.4.2 Sensitivity Ratio Method

The core concept of the sensitivity ratio method is to use a unique pair of measurements for each fault type, where one measurement is sensitive to the fault and the other is not (B. Chen and Braun 2000). The sensitivity ratio of one fault is represented as Equation (40).

$$R_i = \frac{|r_{insens,i}|}{|r_{sens,i}|} \quad (40)$$

where, R_i is the fault sensitivity ratio; $r_{insens,i}$ and $r_{sens,i}$ are the residuals for the insensitive and sensitive measurements, respectively.

The residual of a given temperature measurement T is defined as Equation (41):

$$r_T = T_{actual} - T_{pred} \quad (41)$$

where, T_{actual} is the measurement and T_{pred} is the model prediction for normal operation.

In order to identify a fault, at least one of the fault sensitivity ratios must be less than 1, as shown in Figure 126 (B. Chen and Braun 2000). All the sensitive and insensitive measurement residuals are expected to be below the noise threshold (determined by specific users) in normal conditions. In the work of Chen et al. (2000), the residuals are set to 0.1°F , and the computed sensitivity ratios are 1. As a fault occurs, at least one of the fault-sensitive residuals should increase to exceed the noise threshold, and the corresponding sensitivity ratio should decrease. A fault type, i , is reported if $R_i < 1$. A more detailed description of workflow can be found in the work of Chen et al. (2000).

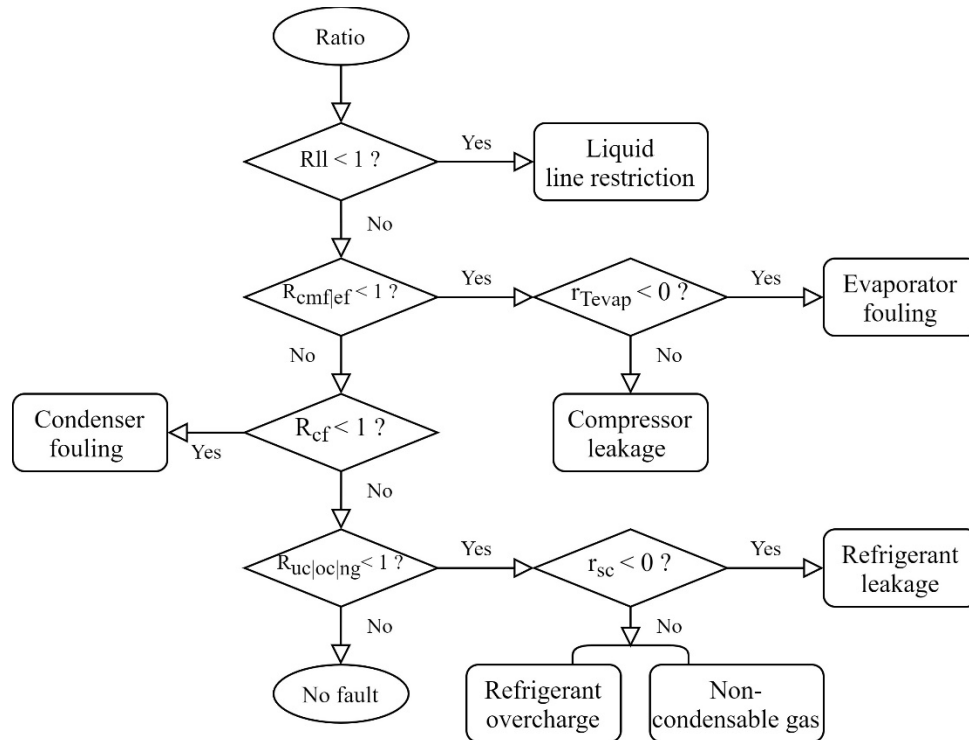


Figure 127. Sensitivity ratio method

D.4.3 Simple Rule-Based Method

The simple rule-based method conducts FDD by comparing performance indices of raw data with preset thresholds (B. Chen and Braun 2000) (see Table 43). It is crucial to find indicators that are sensitive to faults but insensitive to operating conditions. Generally, air-side features are more sensitive to air-side faults. It is also applied to the refrigerant side. In addition, for each type of fault, there should be a particular pattern of changes in the performance indices. The no-fault/fault ranges in Table 43 are predefined by Chen et al. (2000). Those ranges require additional adjustments for specific cases, which are usually derived from the quantile or confidence interval of feature values distribution in the normal condition.

Table 43. Simple Rule-Based Method

(B. Chen and Braun 2000)

Fault Type	Performance Indices	Sensors and Locations	No-Fault Range*	Fault Range*
Evaporator fouling	$(T_{eai}-T_e)$ is abnormally high	T_e, T_{ra}	32–33°F	>34°F
Condenser fouling	(T_c-T_{od}) is abnormally high	T_c, T_{od}	19–20°F	>21°F
Liquid line restriction	dT_{ll} is abnormally high	$T_{ll,in}, T_{ll,out}$	1–2°F	>3°F
Refrigerant leakage	T_{sc} is abnormally low	T_c, T_{cl}	13–14°F	<12°F
Refrigerant overcharge	T_{sc} is abnormally high			>15°F
Non-condensable gas	T_{sc} is abnormally high			>15°F
Compressor leakage	$(T_{eai}-T_e)$ is abnormally low	T_e, T_{ra}	32–33°F	<31°F

*These values are examples extracted from the work of Chen et al. (2000), which should be adjusted specifically in the practical cases.

11.1.1 D.4.4 Comparison of Measured and Predicted Temperature

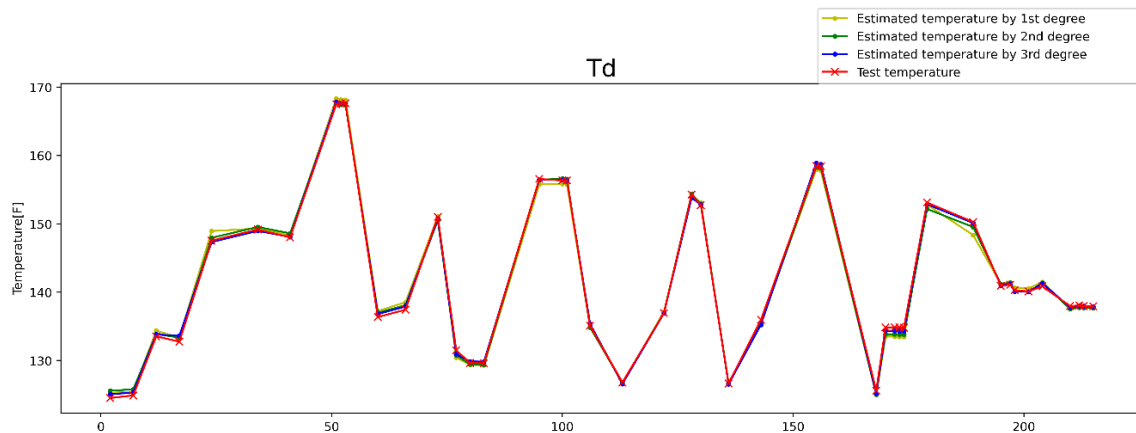


Figure 128. Comparison of measured and predicted discharge temperature

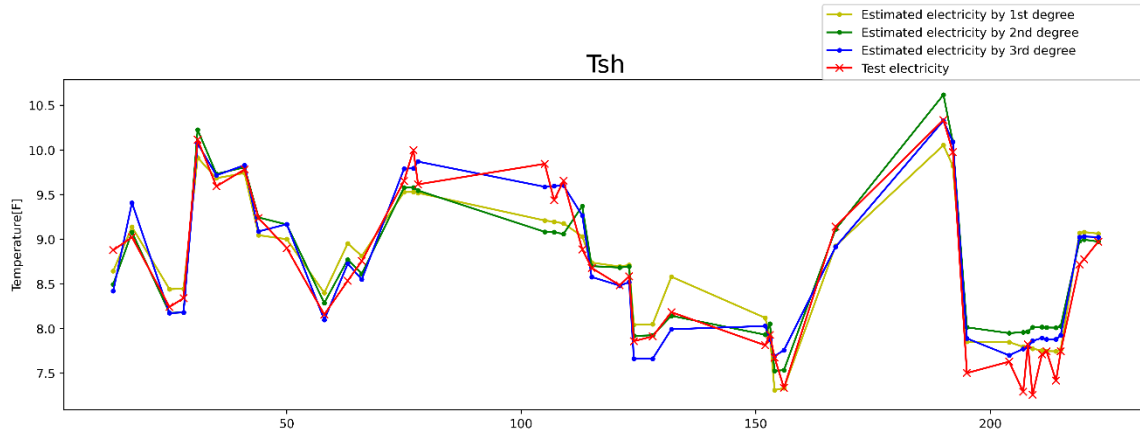


Figure 129. Comparison of measured and predicted superheating temperature

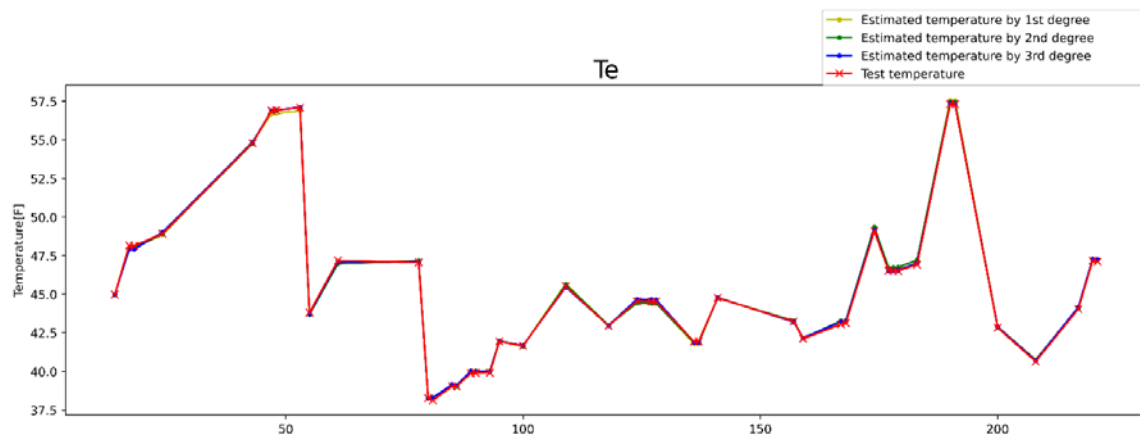


Figure 130. Comparison of measured and predicted evaporator temperature

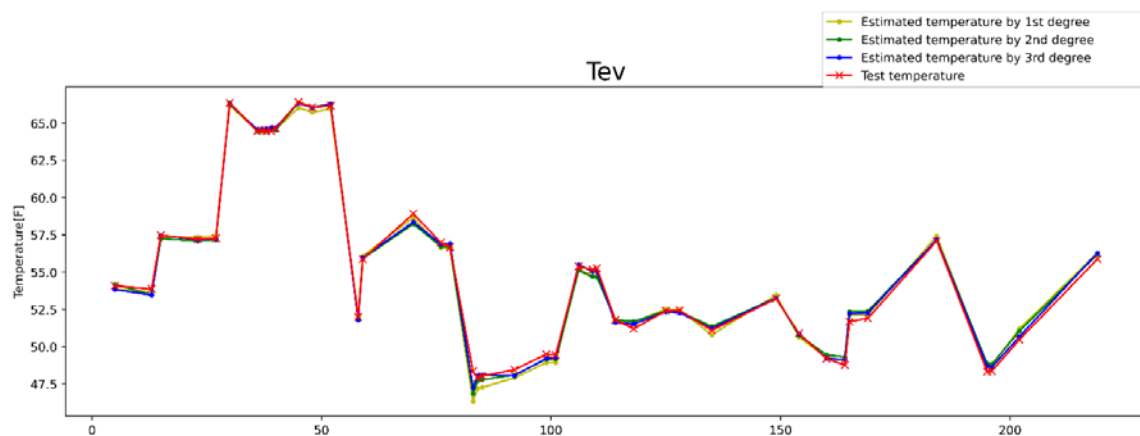


Figure 131. Comparison of measured and predicted evaporator exit refrigerant vapor temperature

D.4.5 Parameter Adjustment for Statistical Rule-Based Chart

Statistical rule-based chart is well-developed because it considers probabilities in three uncertainty sources (measurement noise uncertainty, steady-state uncertainty, and fault-free model uncertainty). In the FDD classification, the threshold standard deviation multiplier s and

the confidence interval of uncertainties k vary with specific datasets and are usually determined using professional experience. This is the biggest challenge for the application of this FDD method. As the diagnosis accuracy of the statistical rule-based chart is highly sensitive to s and k , a pre-investigation of optimum values is conducted around the default values ($k = 2$; $s = 1$) with training data. The accuracy results from multiple scenarios with different combinations of k and s are shown in Figure 132 for six fault cases (using the grid search). We can see that there is no single set of k and s values that can achieve optimum accuracy for all faulty cases. Moreover, even after the adjustment, the high accuracy rates only can be obtained for no fault, liquid line restriction, and undercharge cases, while it is difficult to obtain a satisfactory diagnosis accuracy rate for condenser fouling cases. This observation certainly implies that only one FDD method (statistical rule-based chart) is not sufficient to achieve desirable high detection and diagnosis accuracy.

The optimum sets of k and s are selected and listed in Table 44. The corresponding accuracy rates for each fault case are also included.

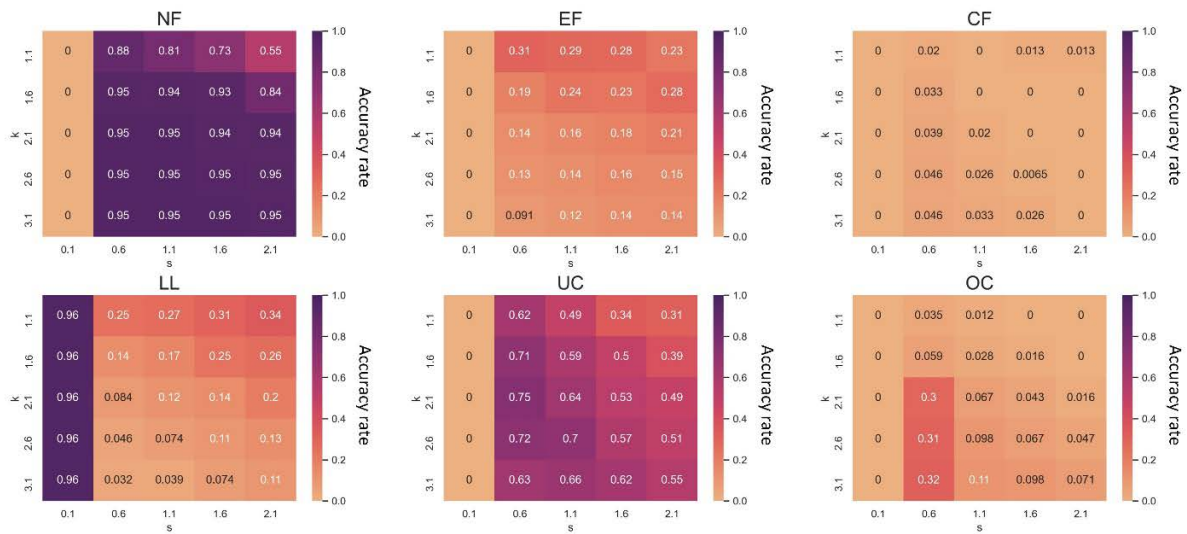


Figure 132. Accuracy rate results from statistical rule-based chart method with different combinations of k and s values

Table 44. Selected Optimum Set of k and s for Different Faults

k	s	Fault	Accuracy Rate
2.5	0.5	CF	4.60%
1	0.5	EF	63.11%
2	0.1	LL	100.00%
2	0.5	UC	69.49%
3	0.5	OC	32.10%
2	0.5	NF	100.00%

Appendix E: Lab Testing

E.1 Testing Timeline

Table 45 lists a timeline for the lab testing, which includes fault implementation, control strategies, and occupancy schedules for each day in both Lab Homes during the full testing period.

Table 45. Timeline for the Lab Testing

Week	Lab Home A – Test Home			Lab Home B – Baseline Home		Occupancy Schedule	Note
	Date	Fault	Control	Fault	Control		
Week 01	Aug. 08	40% overcharge	Constant of 24°C (76°F)	NA	NA	Schedule 2	
	Aug. 09	20% overcharge	Constant of 24°C (76°F)	NA	NA	Schedule 2	
	Aug. 10	15% evaporator fouling	Constant of 24°C (76°F)	NA	NA	Schedule 2	
	Aug. 11	30% evaporator fouling	Constant of 24°C (76°F)	NA	NA	Schedule 2	
	Aug. 12-14	Fault free	Constant of 24°C (76°F)	NA	NA	Schedule 2	Data missing due to communication issue
Week 02	Aug. 15	30% evaporator fouling	Constant of 24°C (76°F)	NA	NA	Schedule 2	
	Aug. 16	20% Undercharge	Constant of 24°C (76°F)	NA	NA	Schedule 2	
	Aug. 17	40% Undercharge	Constant of 24°C (76°F)	NA	NA	Schedule 2	
	Aug. 18-21	Fault free	Constant of 24°C (76°F)	NA	NA	Schedule 2	
Week 03	Aug. 22-29	No fault	Remote from DU	No fault	Controlled through DPC framework	Schedule 1	
Week 04	Aug. 30	NA	NA	NA	NA	NA	Communication test
	Aug. 31-Sep. 02	No fault	Remote from TAMU	No fault	Constant of 24°C (76°F)	Schedule 1	For adaptive to occupancy

		Lab Home A – Test Home		Lab Home B – Baseline Home		Occupancy	Note
Week	Date	Fault	Control	Fault	Control	Schedule	
	Sep. 03-05	No fault	Remote from TAMU	No fault	8:00-18:00 28°C (82°F) 18:00-8:00 24°C (76°F)	Schedule 1	For adaptive to occupancy
Week 05	Sep. 06	Evaporator fouling fault: 85% original airflow	Remote from TAMU	Evaporator fouling fault: 85% original airflow	Constant of 24°C (76°F)	Schedule 2	
	Sep. 07-08	Evaporator fouling fault: 85% original airflow Undercharge faults: 80% original charge	Remote from TAMU	Evaporator fouling fault: 85% original airflow Undercharge faults: 80% original charge	Constant of 24°C (76°F)	Schedule 2	
	Sep. 09-11	Evaporator fouling fault: 85% original airflow Undercharge faults: 60% original charge	Remote from TAMU	Evaporator fouling fault: 85% original airflow Undercharge faults: 60% original charge	Constant of 24°C (76°F)	Schedule 2	Keep the fault through the weekend
Week 06	Sep. 12-13	Evaporator fouling fault: 85% original airflow Overcharge faults: 115% original charge	Remote from TAMU	Evaporator fouling fault: 85% original airflow Overcharge faults: 115% original charge	Constant of 24°C (76°F)	Schedule 2	
	Sep. 14	Evaporator fouling fault: 85% original airflow Overcharge faults: 130% original charge	Remote from TAMU	Evaporator fouling fault: 85% original airflow Overcharge faults: 130% original charge	Constant of 24°C (76°F)	Schedule 2	
	Sep. 15-16	Evaporator fouling fault: 70% original airflow	Remote from TAMU	Evaporator fouling fault: 70% original airflow	Constant of 24°C (76°F)	Schedule 2	transfer to the next fault in the late afternoon of Sep. 16 (Fri.)

	Lab Home A – Test Home			Lab Home B – Baseline Home		Occupancy	Note
Week	Date	Fault	Control	Fault	Control	Schedule	
		Undercharge faults: 80% original charge		Undercharge faults: 80% original charge			
	Sep. 17-18	Condenser fouling fault: 70% original airflow	Remote from TAMU	Condenser fouling fault: 70% original airflow	Constant of 24°C (76°F)	Schedule 2	Keep the fault through the weekend
		Undercharge faults: 80% original charge		Undercharge faults: 80% original charge			
Week 07	Sep. 19	30% Condenser fouling fault: 70% original airflow	Remote from TAMU	30% Condenser fouling fault: 70% original airflow	Constant of 24°C (76°F)	Schedule 2	
		20% Undercharge faults: 80% original charge		20% Undercharge faults: 80% original charge			
	Sep. 20-21	15% Condenser fouling fault: 85% original airflow	Remote from TAMU	15% Condenser fouling fault: 85% original airflow	Constant of 24°C (76°F)	Schedule 2	
		20% Undercharge faults: 80% original charge		20% Undercharge faults: 80% original charge			
	Sep. 22-23	15% condenser fouling fault: 85% original airflow	Remote from TAMU	15% Condenser fouling fault: 85% original airflow	Constant of 24°C (76°F)	Schedule 2	transfer to the next fault in the late afternoon of Sep. 23 (Fri.)
	Sep. 23-25	30% Condenser fouling fault: 70% original airflow	Remote from TAMU	30% Condenser fouling fault: 70% original airflow	Constant of 24°C (76°F)	Schedule 2	Keep the fault through the weekend

E.2 Occupancy Simulation

The Lab Homes were unoccupied during the testing period, so to characterize the performance of the IOT-based comfort control, occupant behavior and occupant-driven loads must be simulated. First, occupancy sensor values were simulated to determine how the control responds to occupant behavior. In addition to the simulated occupancy sensors, an electric heater was scheduled to reflect the heat gain from kitchen appliances.

E.2.1 Occupancy Sensor Schedules

The low-cost iComfort sensors included physical occupancy sensors in six rooms. Rather than use the actual measurements from these sensors, the control relied on simulated occupancy

sensor measurements. Figure 133 outlines two schedules for the occupancy sensors. Schedule 1 simulates an unoccupied home between 9:00 a.m. and 6:00 p.m., and Schedule 2 simulates an occupied home between 9:00 a.m. and 6:00 p.m. All separate schedules are combined as one integrated schedule for the whole building occupancy.

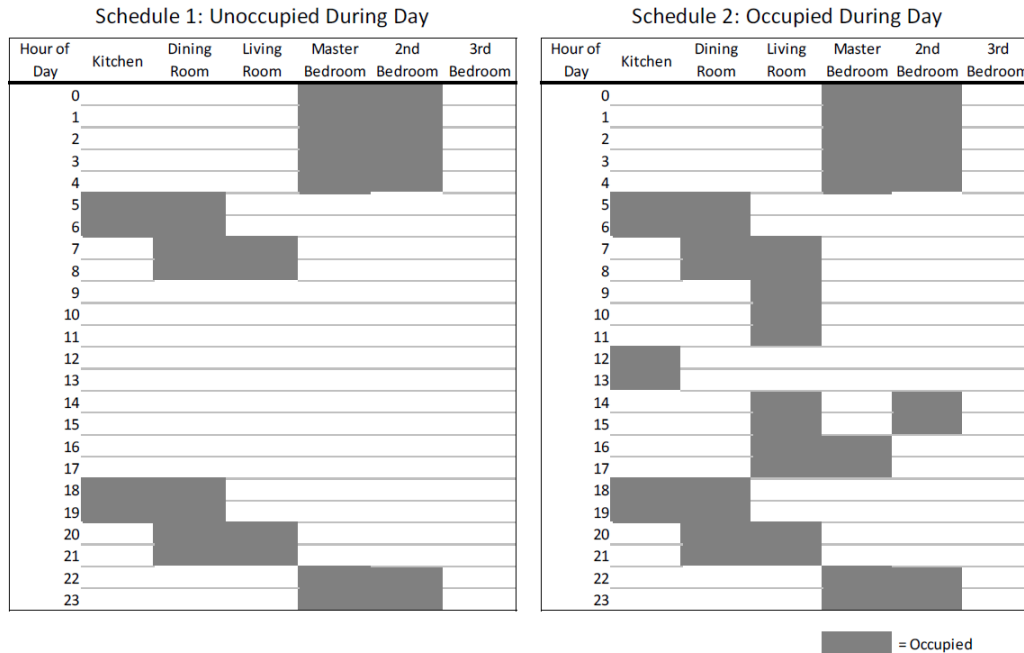


Figure 133. Two simulated occupancy schedules that are used to test and characterize the performance of the IOT-based comfort control

E.2.2 Appliance Load Schedule

The heat gain from larger appliances (e.g., range, oven, dishwasher, clothes washer and dryer) was simulated using a 500 W electric resistance space heater located in the kitchen and dining area of the homes. Both homes used this schedule to match the loads in the baseline home and controlled home. As shown in Figure 134, the space heater operated for three 30-minute periods during the day: starting at 5:30 a.m., 6:30 p.m., and 8:30 p.m.

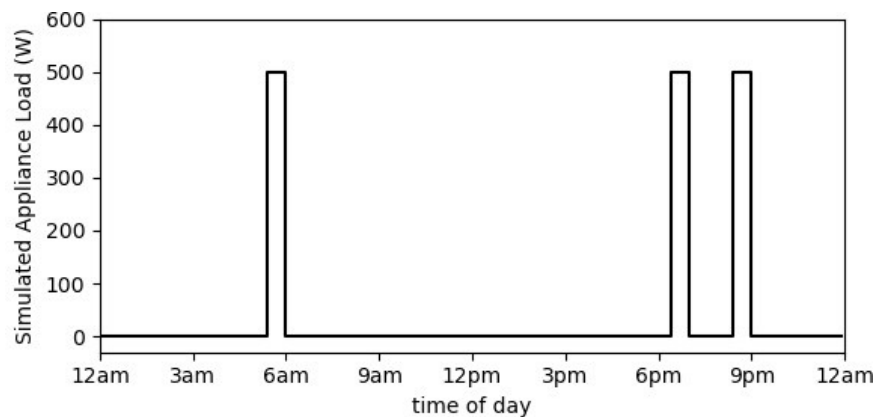


Figure 134. Simulated appliance load schedule that is implemented using an electric resistance space heater

While Lab Homes can simulate other occupant-driven loads, changing from one schedule to another is time-consuming. The developed appliance schedule accounts for the largest heat gains and was used for both schedules outlined in Figure 133, eliminating the need for any changeover.

E.3 Sensor Installation

The Lab Homes are outfitted with a comprehensive set of sensors to measure building performance. Table 46 summarizes the list of sensors available in each of the homes. These sensors provide detailed data on building operation to evaluate the impact of various energy conservation measures on building energy performance and occupant comfort.

The homes have power meters on every breaker in the electrical panel for detailed electrical end-use data. There are temperature sensors in every living space, the crawl space under the home, multiple supply registers, and the exterior of the homes. There are a few relative humidity sensors found inside and outside of the homes. The Lab Homes also have a weather station to record the outdoor temperature, relative humidity, wind speed, wind direction, solar irradiance, and barometric pressure. These meters and sensors serve as supplementary and backup for the iComfort sensors.

Table 46. Sensor Overview in Lab Homes

Measurement Type	Quantity	Notes
Power	48	Meter on every breaker (includes all appliances)
Temperature	39	Located in living spaces, supply air registers, outside, and on water lines
Relative Humidity	4	Two inside the home, two on the exterior
Other	9	Includes solar irradiance, wind speed, wind direction, air pressure, and water flow

While the Lab Homes contain a wide variety of sensors, there are specialized research needs that require the installation of additional sensors. To create a suitable test bed for the control algorithms, additional sensors were installed in the Lab Homes to create a suitable test bed. There are three different sets of sensors that were installed in the Lab Homes:

- 1) iComfort sensors that were developed for this project
- 2) Temperature sensors that were installed on the HVAC unit for FDD testing
- 3) Various temperature/relative humidity data loggers.

iComfort Sensors

The iComfort sensors, developed for this project, were deployed into Lab Home A (the test home) along with a hub that shows sensor status for each sensor. In total, 16 iComfort sensors

were deployed in the test Lab Home, and they are shown in Figure 135. The sensors measure a combination of airflow, temperature, relative humidity, and occupancy.

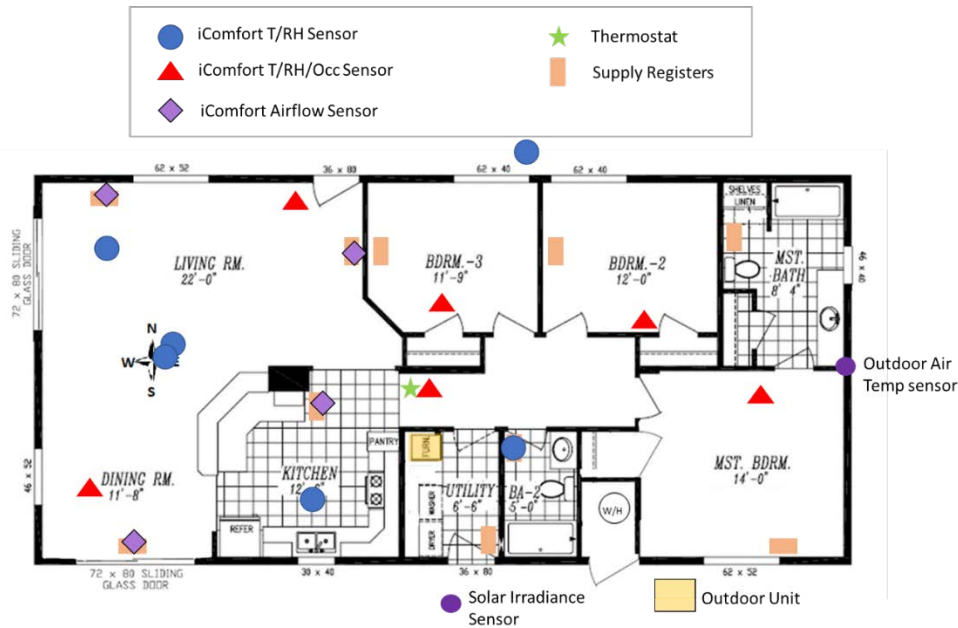


Figure 135. Installation map of iComfort sensors

HVAC FDD Sensors and Data Loggers

To evaluate the HVAC Fault Detection and Diagnostic (FDD) tests, eight additional temperature sensors were installed and used a DS18B20 chip to measure temperature. These sensors are connected to a Raspberry Pi using a single GPIO, and use “One Wire” to communicate with the Raspberry Pi. The added sensors for this project are described below in Table 47, and their locations are plotted in Figure 135.

Table 47. Installed Sensors for HVAC FDD Testing

Measurement	Sensor Location
Evaporator coil temperature	Indoor unit, return bend on evaporator
Suction line temperature	Outdoor unit, on compressor suction line
Discharge line temperature	Outdoor unit, on compressor discharge line
Condensing temperature	Outdoor unit, return bend on condenser
Liquid line temperature	Outdoor unit, at condenser outlet
Condenser outlet air temperature	Outdoor unit, above fan
Evaporator inlet air temperature	Thermocouple by indoor air inlet
Supply air temperature	Supply duct inside the home

Active Learning-Based Performance Model Sensors

For the Active Learning-Based Performance Model, there are three types of sensors that were installed in the Lab Homes. The first two are the custom sensors built specifically for this project. The first of these measures the occupancy state, the temperature, and the relative humidity of the space. Four of these sensors were installed within the homes at various locations. The second type of custom sensor measures the air speed, temperature, and relative humidity within the space. Four of these were located within the main gathering area of the homes. Two additional relative humidity sensors were installed for verification purposes in the main gathering area of the home. Table 48 details these sensors, and Figure 135 shows the installation locations for the custom iComfort sensors.

Table 48. Required Sensors for the Active Learning Based Performance Model

Sensor Origin	Quantity	Measurements	Sensor Location(s)
PNNL	2	Heat pump and furnace power	Breaker box
PNNL	1	Total building power	Breaker box
PNNL	1	Outdoor air temperature	East side of Lab Home B
PNNL	1	Outdoor relative humidity	East side of Lab Home B
PNNL	1	Outdoor wind speed	Roof of Lab Home B
PNNL	1	Outdoor wind direction	Roof of Lab Home B
PNNL	1	Barometric pressure	East side of Lab Home B
PNNL	1	Solar irradiance	South side of Lab Home B
iComfort	8	Occupancy, temperature, relative humidity	See map on Figure 5
iComfort	8	Air speed, temperature, relative humidity	See map on Figure 5
PNNL	2	Relative humidity (for verification)	Living Room, Dining Area

In addition to the location of the new sensors, Figure 135 displays other key equipment and sensors for reference. The supply registers, which are on the floor, are shown for each space. The heat pump outdoor unit and indoor unit (labeled ‘FURN.’; located in the utility room) are also highlighted. The thermostat is in the hallway. The solar irradiance sensor is located on the south wall, and the outdoor air temperature sensor is in a shaded alcove on the eastern side of the house.

E.4 Metrics and Targets

E.4.1 Metrics and Targets for Sensors and Measurements

Table 49 displays the metrics and targets specifically related to sensing within the Lab Homes. The metrics apply to the sensors identified in Table 47 and Table 48. For the required sensors, there is a minimum data acquisition rate of two minutes per sample. Additionally, all sensor

measurements that are required for control decisions are available in the iComfort database within 30 seconds. Finally, the sensors are available and transmitting for at least 95% of the testing period.

Table 49. Metrics and Targets for Sensing During Testing

Metric	Description	Target
Sensors and Data Acquisition (Highest Priority Sensors)		
Data Acquisition Rate	The sampling period for measured values.	< 2 min.
Reliability of Measured Values	The portion of sampling periods during which no sensor measurements are received.	< 5%
Time Delay of Measured Values	The average amount of time between when the sensor measurement occurs and when the measurement is available in the cloud.	< 30 sec.

E.4.2 Metrics and Targets for Control Signal Capability

The control decision generated by the comfort control is the thermostat setpoint. The setpoint is implemented remotely using the Ecobee API (Ecobee).

Changing the setpoint when desired is a critical capability for testing the control algorithm. The success with which the control signal may be changed is quantified using two metrics: the reliability of the control signal and the time delay of the control signal. These metrics are defined and targets are specified for each metric below.

Reliability of Control Signal: The portion of setpoint API commands that are not received and implemented on the physical thermostat device within 5 minutes. **Target: Less than 5%.**

Time Delay of Control Signal: The average amount of time between the setpoint API command being sent and the setpoint on the physical thermostat device being received. **Target: Less than 2 minutes.**

E.5 Weather Conditions

The Lab Homes are based at Richland, Washington, which is located at approximately 46.3°N, 119.3°W. The front door of the house faces north. Richland, which is located in Energy Information Administration (EIA) climate zone 2, is characterized by a semi-arid climate with warm summers and cool winters. The average wintertime lows are in the mid-20s°F, and the average summertime highs are in the low 100s°F. The average precipitation is 7 to 8 inches per year.

The lab testing was conducted in August and September of 2022. During that period, the highest outdoor temperature was 105°F on Aug. 18 and the lowest temperature was 42°F on Sep. 17. To be specific, during the MPC-informed rule-based control period, the highest and lowest temperatures were 93°F on Sep. 7 and 42°F on Sep. 17.

E.6 Fault Implementation

The rule-based FDD methods can diagnose some of the most common process faults in the air duct and vapor compression-based cooling systems: duct leakage, evaporator and condenser fouling, high and low refrigerant charge, refrigerant flow restriction in the liquid line, and degradation of the compressor or three-way reversing valve (reversing valve applies to heat pumps only), etc. Implementing some faults, such as placing paper over the evaporator filter to simulate evaporator fouling, does not require major changes to the system and are therefore considered to be non-invasive (Kim et al. 2008; Rossi and Braun 1997).

Implementing other faults, such as using a hot gas bypass line to simulate compressor leakage, require significant changes to the system and are highly invasive. Highly invasive implementation methods such as those for liquid line restriction and compressor/valve leakage can be implemented on laboratory systems but not on field systems. The PNNL Lab Homes are designed and intended to operate identically to one another and to reflect field operation.

Making significant changes to the refrigerant lines may degrade the design of the Lab Homes; at the conclusion of the FDD study, they may not operate identically to one another and may be less reflective of field systems.

Therefore, the FDD testing is limited to implementation methods that can easily and reliably revert to the original condition after testing. The faults that were tested include condenser fouling, evaporator fouling, low refrigerant charge, and high refrigerant charge.

E.6.1 Implementing Condenser and Evaporator Fouling Faults

Condenser and evaporator fouling can occur on both the air side and the refrigerant side of the heat exchangers. Air-side fouling is the most common and is easier to simulate. Therefore, this study is limited to testing air-side fouling. Condenser air-side fouling occurs as debris such as dirt, leaves, or grass clippings cover the heat exchanger coils. Evaporator air-side fouling more commonly occurs as the air filter accumulates dust and other particles. Previous studies (Katipamula et al. 2015; Rogers et al. 2019b) have implemented fouling by preventing airflow through parts of the heat exchanger or air filter using strips of paper (see Figure 136).

To improve the simulation of heat exchanger fouling, a mesh screen is placed over the heat exchanger. The mesh screen restricts airflow more uniformly over the heat exchanger area. However, in order to achieve the desired level of airflow restriction, strips of tape are added to the mesh screen. They are applied perpendicular to the flow of refrigerant. This method is used to achieve fault severity levels of 15% and 30% airflow reduction for both the evaporator and condenser. Figure 137 shows an example of fouling fault simulation.

Adjusting the mesh screen and tape in order to achieve the desired airflow reduction requires an airflow measurement. An air velocity measurement is taken at several points across the flow section using a hot wire anemometer probe. While this method is unlikely to produce an accurate airflow measurement, it provides an indication of how much airflow has been reduced relative to the initial baseline (i.e., the percent reduction).



Figure 136. Condenser fouling implemented using paper

Archived photos from PNNL, not directly from this specific testing



Figure 137. Photo of evaporator fouling simulation

E.6.2 Implementing Low and High Refrigerant Charge Faults

To implement refrigerant charge faults, the existing baseline charge is first measured. Then the refrigerant is adjusted to different levels relative to the baseline. Low refrigerant charge faults are tested at 60% and 80% of the baseline; high refrigerant charge faults are tested at 115% and 130% of the baseline. Figure 138 shows how the refrigerant charge was conducted.

All details related to the implementation of different faults and their severity levels are presented in Table 50.

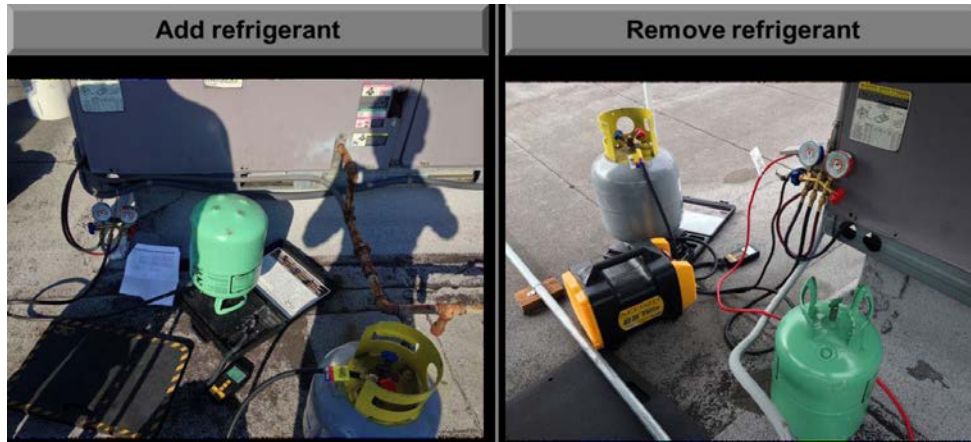


Figure 138. Refrigerant overcharge and undercharge simulation
 Archived photos from PNNL, not directly from this specific testing

Table 50. Details of Fault Scenarios

Scenarios	Charge Test	Fouling Test	Adj. (oz)	Charge (oz)	Sheets LHA	CFM-Evap	CFM-Cond
1	No faults	n/a	0	132	0	1140	1440
2	40% overcharge	n/a	56	188	0	1130	No measured
3	20% overcharge	n/a	28	160	0	1137	No measured
4	20% undercharge	n/a	-26	106	0	1150	No measured
5	40% undercharge	n/a	-52	80	0	No measured	No measured
6	n/a	15% evaporator fouling	0	132	3	935	n/a
7	n/a	30% evaporator fouling	0	132	9	775	n/a
8	n/a	15% condenser fouling	0	132	3	No measured	1240
9	n/a	30% condenser fouling	0	132	9	No measured	1005

E.7 Operation Schedules

The homes are unoccupied, but equipment has been installed within the homes to simulate occupant loads. Specifically, incandescent lighting is placed in different rooms of the homes that can be controlled remotely to simulate heat gains. Additionally, water and electrical appliance loads can be simulated by remotely scheduling electric resistance heaters. While heat gains and water use can be simulated, there is currently no way to add the humidity gain from occupants in

the homes. The main factors that affect indoor humidity are outdoor air infiltration and heat pump operation in the cooling mode.

The current occupancy simulation schedule was designed to reflect the Building America House Simulation Protocols (Wilson 2014). Figure 139 shows the measured power over a day for the devices used to simulate occupant and plug load impacts. The lights in various rooms are turned on and off throughout the day to reflect occupants moving from one room to the next. For example, the bedroom lights are on in the evening, and the kitchen lights are on in the afternoon and evening. An electric resistance heater is used in the dining/kitchen area to reflect the higher power usage of the oven, range, and smaller kitchen appliances.

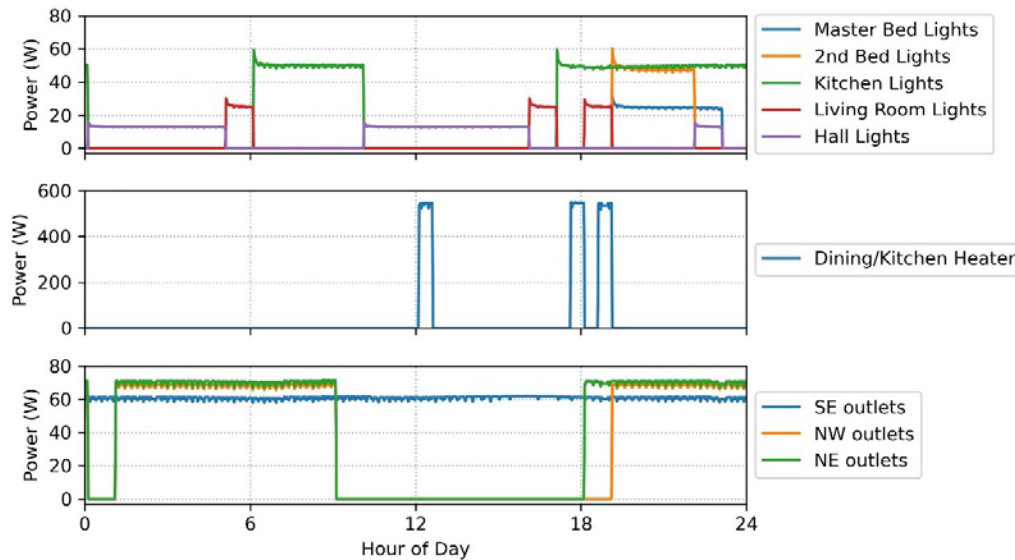


Figure 139. Typical occupant load simulation for the PNNL Lab Homes including heat gains from lighting, occupants, and appliances

To modify the equipment schedule, an operator must manually adjust the schedule for each individual power breaker. The process is cumbersome and prone to error. The difficulty in adjusting the schedule limits the flexibility in providing heat gain schedules with realistic uncertainty regarding start time, duration, and magnitude of energy usage. Of note, the maximum period for any schedule is one day, so reprogramming is required for different days.

E.8 Uncertainty Analysis

The uncertainty for indoor temperature control mainly derives from the sensor measurement and the future weather forecast.

The indoor temperature fed into the control algorithm is from the iComfort sensor. A near-optimal setpoint is generated and then sent to the Ecobee thermostat. Figure 140 illustrates the comparison of temperature readings from the iComfort sensor (blue curve) and Ecobee thermostat (red curve) at the same location. The solid green line represents the setpoint. It can be seen that there is around a 2°F difference between the iComfort sensor and the Ecobee

thermostat. One possible reason is that the indoor air going through the thermostat is warmed by the heat that is generated by the microprocessor operation. The temperature from the Ecobee thermostat is used for the local control while the temperature from iComfort is used for the supervisory control. This discrepancy impacts the accuracy of indoor temperature control.

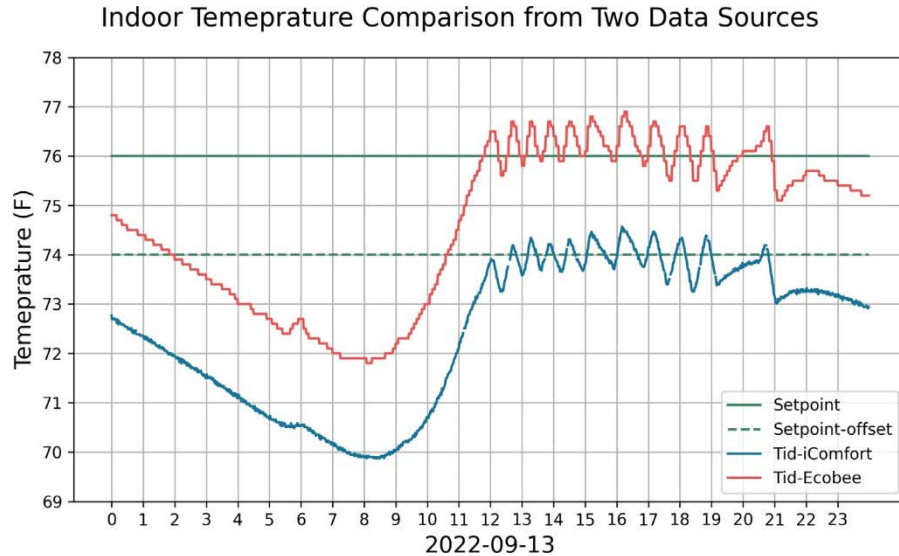


Figure 140. Indoor temperature comparison from iComfort and Ecobee

Another sensor uncertainty exists in the heat pump-related temperature measurement during FDD testing. An obvious issue can be found in the subcooling temperature. In this project, subcooling is defined as the difference between condensing temperature and condenser liquid temperature, which is positive. But Figure 140 shows that the subcooling temperature is sometimes below zero (marked with red dots). This is mainly due to the small value for subcooling temperature, which is easily measured as abnormal ones with drifting of sensors. Therefore, in the FDD analysis, those periods of data with abnormal values are removed in the data preprocessing stage.

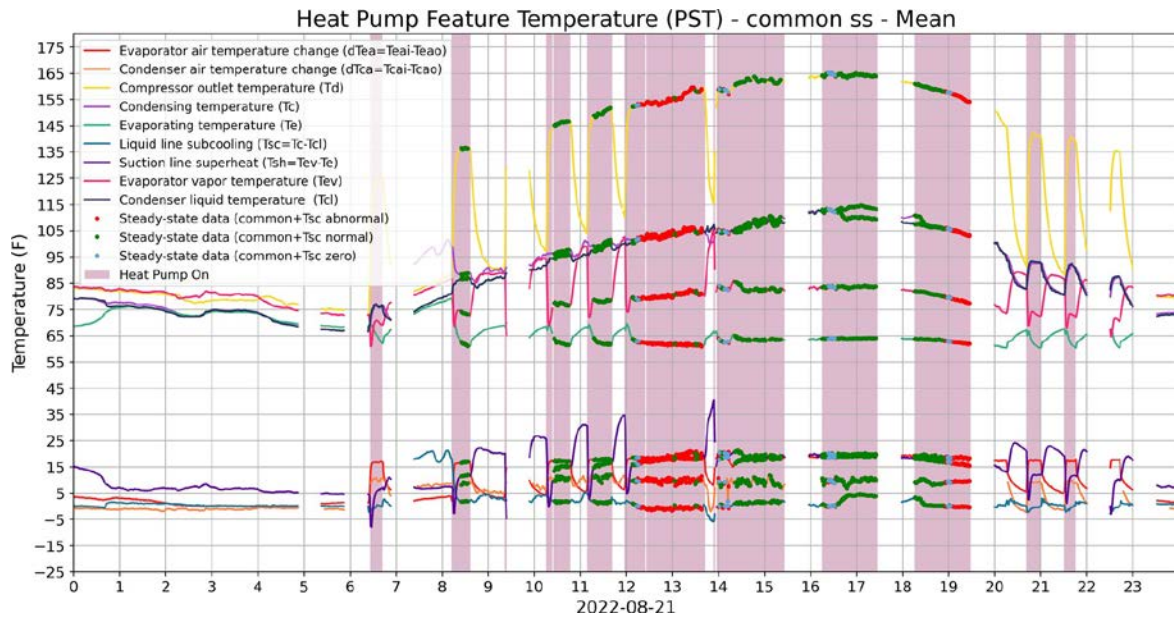


Figure 141. Heat pump feature temperature

Another uncertainty comes from the discrepancy between predicted weather and real weather. Future outdoor dry-bulb temperature is used for the supervisory control. These values are directly extracted from the National Oceanic and Atmospheric Administration (NOAA) data server. Figure 141 shows the comparison of forecast outdoor dry-bulb temperatures from NOAA and the real ones from local sensors. Temperature from NOAA is on an hourly basis, while the local sensor measures data every minute. It can be seen that the change trends of the two curves are similar, but there is some discrepancy at every clock. At night, the forecast temperature tends to be higher than real values, with a maximum of around 6°F. During the day, the condition is inverse. This inaccuracy of outdoor dry-bulb temperature prediction also results in uncertainty in the supervisory control.

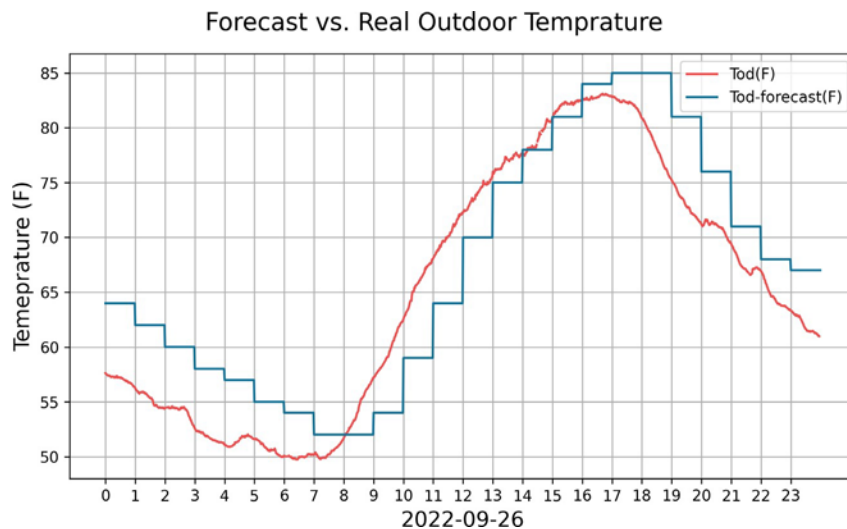


Figure 142. Comparison of forecast and real outdoor dry-bulb temperature

Appendix F: Market Analysis

F.1 Codes and Standards

The following standards and guidelines apply to our product as well as the market products surveyed in the following subsections:

ANSI/ASHRAE Standard 55-2017: Thermal Environmental Conditions for Human Occupancy:

This standard specifies the combination of indoor thermal environmental conditions (temperature, thermal radiation, humidity, and airspeed) and personal factors (activity and clothing) that produces acceptable indoor thermal environmental conditions to the majority of healthy adult occupants within a particular space at up to 3,000 m of altitude (ASHRAE 2017). This standard was first published in 1966 and is applicable for spaces occupied for at least 15 minutes by people not sleeping/reclining, not wearing highly impermeable clothing, and not having extremely high metabolic rates (ASHRAE 2017).

ANSI/ASHRAE Standard 62.2-2019: Ventilation and Acceptable Indoor Air Quality in Residential Buildings: This standard specifies the minimum requirements for mechanical and natural ventilation systems and building envelopes in residential buildings with non-transient occupants (ASHRAE 2019). Acceptability is defined as a majority of occupants in the space not expressing dissatisfaction regarding smells or other irritations, and the space having contaminants below any health risk levels occupants (ASHRAE 2019). This standard does not consider thermal comfort requirements or biological, chemical, and physical contaminant occupants (ASHRAE 2019).

ANSI/ASHRAE Standard 100-2018: Energy Efficiency in Existing Buildings: Retrofitting existing infrastructure can be more cost-effective and environmentally friendly than constructing new sustainable energy-efficient buildings (ASHRAE 2018b). This ASHRAE standard provides guidelines for improving energy efficiency and thermal performance of existing (residential and non-residential) buildings or building portions that result in a decrease in energy consumption (ASHRAE 2018b). It establishes an energy management plan, energy targets, audit requirements, as well as implementation and verification requirements (ASHRAE 2018b).

ANSI/ASHRAE/IES Standard 90.2-2018: Energy-Efficient Design of Low-Rise Residential Buildings: This standard specifies minimum design, construction, and verification criteria for energy efficient new non-transient residential buildings (and new portions of existing residential buildings) (ASHRAE 2018a). It provides requirements regarding the building envelope, HVAC and mechanical systems, service hot-water systems, other major appliances, lighting systems, snow and ice melt systems, as well as pools and spas (ASHRAE 2018a). The recent revision to Standard 90.2 in 2018 also acknowledges the significant role of renewable energy and other on-site power systems in improving the energy efficiency of the whole building (ASHRAE 2018a).

International Code Council International Energy Conservation Code (IECC) 2018: The IECC reduces energy consumption and the environmental footprint of new and renovated (residential

and commercial) buildings by specifying minimum criteria for energy features and thermal performance (ICC 2018). Some of the stipulations include setting requirements for different components of the building envelope (like fenestration, ceiling, walls, etc.), providing guidelines to prevent air leakage, and specifying the efficiency of lighting equipment (ICC 2018).

IEEE 802.15.4 standard: This standard was first introduced in 2003 and specifies the operation of low-cost, low-speed wireless personal area networks (IEEE 2020). IEEE 802.15.4 provides the physical layer and media access control and is the basis for various applications like Zigbee and Z-wave, which are used in smart home energy management systems (IEEE 2020).

IEEE 802.11 standard: Many smart home appliances and smart home energy management systems are connected using WiFi. The IEEE 802.11 standard specifies the physical layer and media access control for WiFi communication in various frequencies, and was first created in 1997 (Vaughan-Nichols 2010).

IEEE 802.3 standard: IEEE 802.3 is one of the leading communication standards used for wired ethernet networks in smart home energy management systems (Christensen et al. 2010). It provides the physical layer and media access control, and was first introduced in 1983 (Christensen et al. 2010). Since then, the standard has periodically been updated to keep up with technical advancements (Christensen et al. 2010).

There is a lack of standards in the residential AFDD product market about testing approaches, fault types that need to be consistently reported, fault codes, and what information to report to stakeholders (Butzbaugh et al. 2020).

F.2 Barriers and Limitations

There are a number of technical, market, and other barriers that affect the adoption of occupant thermal comfort, home energy management, and automated fault diagnostic products in the residential sector.

F.2.1 Cost

Previous studies have shown that cost is the primary obstacle preventing the widespread adoption of smart HVAC devices in homes (Danova 2014). For example, the price of commonly available smart thermostats ranges from \$65 in addition to professional installation costs of \$675, with the price of \$100~\$300 for the most prevailing ones. Thus, the total expenditure can be more than 10 times the cost of a manual thermostat (Home Advisor). Many electric utilities offer rebates on these products but, in return, request control of those devices during peak demand events (which many customers might not be comfortable with). Further, most of the AFDD devices available today are meant for large commercial buildings where the financial returns are substantial (Granderson et al. 2017). It is not financially feasible to scale these down to small residential buildings without building automation systems (Granderson et al. 2017). Currently, only high-end, variable-speed HVAC systems have embedded AFDD software with monitoring capability (Butzbaugh, Tidwell, and Antonopoulos 2020). Finally, the integration of advanced controls and home energy automation systems might not always guarantee energy and cost

savings. For example, if a household has one member who works from home, the setpoint temperature might not be able to be lowered at any time of the day while maintaining occupant comfort levels. Thus, adopters might be hesitant to invest in these technologies without guaranteed returns.

F.2.2 Lack of Customer Awareness

Customers often have difficulty figuring out the terms and symbols of smart thermostat display panels as well as the complexity of the software (Meyers et al. 2010). To mitigate this issue, all future smart controls must have user-friendly interfaces. Additionally, building owners are often unsure that wireless sensors will operate as reliably as their wired counterparts, and technicians often do not have enough training to properly install and commission wireless sensors (Sofos et al. 2020).

Further, while AFDD products can improve energy efficiency and occupant comfort level in buildings by minimizing equipment downtime, most homeowners are unaware of the products currently available and their potential benefits (Butzbaugh, Tidwell, and Antonopoulos 2020). HVAC contractors also require additional training regarding how to use smart diagnostic tools or utilize diagnostic data (Butzbaugh, Tidwell, and Antonopoulos 2020).

Although the global smart home energy management market has developed rapidly over the past few years, most residential customers are uninformed about the devices available and choose to rely on old technology (Market Research Future). Further, homeowners are often only interested in installing smart energy efficiency controls at the time of home construction or a preplanned renovation or replacement of failed equipment (Frank et al. 2018).

F.2.3 Communication Barriers

The communication technologies should be interoperable across the various smart appliances as well as future and legacy systems. Interferences from other communication sources and signal crosstalk could be a potential barrier to optimized performance of smart home energy management systems, and these should be eliminated (Sofos et al. 2020).

F.2.4 Increased Reliance on Technology and Connectivity

The proper functioning of connected sensors, smart home energy management systems, and AFDD devices all depend on having a strong internet connection and their ability to maintain occupant comfort, maximize energy efficiency, and detect faults accurately might be hampered if the WiFi is down or the home is situated in a rural area without fast and reliable internet access.

F.2.5 Lack of Standards

There is a lack of standards in the residential AFDD product market about testing approaches, fault types that need to be consistently reported, and what information to report to stakeholders. Further, since standardized communication software does not exist, the indoor unit, outdoor unit, and connected thermostat need to be part of a set produced by the same manufacturer (Butzbaugh, Tidwell, and Antonopoulos 2020). Industry-set protocols for fault codes also do not

exist, and contractors have to keep themselves updated on fault code sets used by different manufacturers (Butzbaugh, Tidwell, and Antonopoulos 2020).

F.2.6 Privacy and Network Security Issues

The issue of cybersecurity and privacy also exists since any IoT-enabled device can be hacked if smart password practices are not followed. There have been alarming news in the past about cybercriminals gaining control of smart thermostats and increasing the room setpoint to 90°F (Alladi et al. 2020). As a result of the absence of building energy managers like in the large commercial sector, homeowners have the onus of installing security updates on their IoT-connected devices or regularly hiring contractors to do so. Further, the data collected by smart devices must be protected using high-quality encryption or other cybersecurity measures, and any identifiable information should be removed before sharing with third-party companies or research organizations (Rotondo et al. 2016). For example, if a smart device has information about the time of day when homeowners leave for work, that data could be used for security breaches.

F.2.7 Unavailability of Data

Advanced AFDD or optimized home energy management requires empirical disaggregated energy consumption and appliance-level data from the residential sector. This data is very rare, and when available, the quality might not be adequate for the control algorithm or machine learning algorithm to learn from and detect faults accurately. Further, the data collected might not be made widely available to preserve customer privacy, security rights, and satisfaction (Rotondo et al. 2016). Finally, whole-house energy management systems must have interoperable datasets available from all IoT-enabled smart appliances so that these devices can securely exchange operative information (Rotondo et al. 2016).

F.2.8 Lack of Mandatory Residential Dynamic Electricity Prices

While more electric utilities in the United States are offering residential dynamic rates like time-of-use rates or critical peak pricing to encourage load-shifting behavior, these options are often voluntary. Mandating these pricing schemes, in addition to embedding smart HVAC devices to receive real-time price signals, could increase customer energy savings and motivate more homeowners to invest in these technologies (Granderson et al. 2017).

F.3 Intellectual Property

There are an extensive number of patents for smart home energy management systems. Table 52 collects several active patents from ecobee and Google Nest, as the quantity of smart home energy management system-related patents is large, and these two companies are prominent in this field. Those patents reflect the product features in Table 34. Intellectual property is complicated in this field currently. For example, EcoFactor sued Google in 2020, claiming that its Nest thermostats infringed on its patents related to “early on” and won the lawsuit with \$20 million compensation (*6:20-cv-00075 - Ecofactor Inc v. Google LLC*), even though Google is reportedly planning to appeal the verdict. EcoFactor has also accused ecobee and Amazon.

Table 52. Selected Patents for Smart Home Energy Management Systems

Patent Number	Patent Name	Assignee	Application Granted
US6508407B1	Apparatus for remote temperature control	ecobee Inc.	01/21/2003
US20130238140A1	HVAC controller with a device scheduling program	ecobee Inc.	02/24/2015
US20130018513A1	HVAC controller with predictive set-point control	ecobee Inc.	04/28/2015
US9016593B2	System and method for web-enabled enterprise environment control and energy management	ecobee Inc.	04/28/2015
US20140039691A1	Multidimensional heating and cooling system	ecobee Inc.	10/06/2015
US9377791B2	Monitoring user position to determine a time for providing a specified state at a user premises	ecobee Inc.	06/28/2016
US9696052B2	HVAC controller with predictive setpoint control	ecobee Inc.	07/04/2017
US20170074540A1	Intelligent thermostat control system	ecobee Inc.	09/26/2017
US9978290B2	Identifying a change in a home environment	ecobee Inc.	05/22/2018
US20210302052A1	Thermostat device with improved energy optimization	ecobee Inc.	In progress
US11143429B2	Control device for HVAC fan coil units	ecobee Inc.	In progress
US8510255B2	Occupancy pattern detection, estimation and prediction	Google LLC., Nest Labs Inc.	08/13/2013
US8554376B1	Intelligent controller for an environmental control system	Google LLC., Nest Labs Inc.	10/08/2013
US8606374B2	Thermodynamic modeling for enclosures	Google LLC., Nest Labs Inc.	12/10/2013
US8630741B1	Automated presence detection and presence-related control within an intelligent controller	Google LLC., Nest Labs Inc.	01/14/2014
US8630742B1	Preconditioning controls and methods for an environmental control system	Google LLC., Nest Labs Inc.	01/14/2014

Patent Number	Patent Name	Assignee	Application Granted
US8965587B2	Radiant heating controls and methods for an environmental control system	Google LLC., Nest Labs Inc.	02/24/2015
US9298197B2	Automated adjustment of an HVAC schedule for resource conservation	Google LLC., Nest Labs Inc.	03/29/2016
US9459018B2	Systems and methods for energy-efficient control of an energy-consuming system	Google LLC., Nest Labs Inc.	10/04/2016
US9714772B2	HVAC controller configurations that compensate for heating caused by direct sunlight	Google LLC., Nest Labs Inc.	07/25/2017
US9810442B2	Controlling an HVAC system in association with a demand-response event with an intelligent network-connected thermostat	Google LLC., Nest Labs Inc.	11/07/2017
US9890970B2	Processing and reporting usage information for an HVAC system controlled by a network-connected thermostat	Google LLC., Nest Labs Inc.	02/13/2018

However, the outcome of this project avoids patent violations entirely after reviewing the existing patent literature. No blocking patents have been found to prevent the freedom to operate under any new intellectual property discovered or created under this project. The FDD methods are developed based on the published FDD approaches, which were proposed by Chen et al. (2000), Breuker et al. (1997), and the NIST (M. Kim et al. 2008). Control strategies, derived from the MPC and rule extraction process, are unique and completed by the team independently. The intent of this project, including engaging an industrial partner and potentially interested companies, is to make the intellectual property widely available, which will provide the largest market impact possible. The experimental data generated from this project will be public data. This project involves both hardware and software prototypes and development.

F.4 Sensors in the Market

Temperature, humidity, and airflow are key parameters to ensure occupant health and comfort as well as to maintain energy-efficient homes. Temperature and humidity control inside a home is important for occupant comfort and mold prevention. If humidity levels within a home are not maintained within certain limits, occupants can be susceptible to health risks in addition to indoor mold and mildew problems and issues with wood finishes. Insufficient airflow in a home can cause stagnant contaminants inside the building, build up odors, cause chronic allergies, and wear down the HVAC system.

Table 53. Specification of Commercial Sensors in the Market

Product Name	Brand	Price	Compatible with a smart thermostat?	Function	Notes
Smart Sensor	ecobee	\$50.00	Y	Temperature/humidity and occupancy	
Smart Sensor for Doors and Windows	ecobee	\$40.00	Y	Doors and windows	
Temperature Sensor	Nest	\$39.00	Y	Temperature/humidity	
Smart Room Sensor	Honeywell	\$41.99	Y	Temperature/humidity	
Thermostat Smart Room Sensors	Wyze	\$29.98	Y	Temperature/humidity and occupancy	
Smart ZigBee PIR Motion Sensor	MoesGo	\$19.99	Y	Occupancy	Required MoesGo ZigBee Hub (\$27.99)
Smart ZigBee Door and Window Sensor	MoesGo	\$19.99	Y	Doors and windows	Required MoesGo ZigBee Hub (\$27.99)
Smart IR Remote Sensor	MoesGo	\$29.99	Y	Temperature/humidity	
FILTERSCAN Home Air Filter Monitor	Clean Alert	\$129.00	N	Air filter monitor	

Nest, ecobee, Honeywell, etc., offer a range of smart sensor products from approximately \$19.99 to \$50.00, detailed in Table 53. In addition to measuring temperatures, these thermostats can also sense humidity. Some of these sensors also have occupancy sensing ability to assist in keeping particular rooms comfortable or save energy when the occupants are not at home (e.g., the ‘Home’ and ‘Away’ features in a Nest learning thermostat) (Pang et al. 2021). However, this data should be encrypted with appropriate cybersecurity measures to avoid security breaches. A smart airflow sensor is seldom in the current market. FILTERSCAN WiFi Home Air Filter Monitor (\$129) is an example that alerts homeowners once the filter is clogged and needs to be replaced.

Technological innovations and increased customer awareness/interest will drive the growth of sensors in the residential market over the next decade. The advanced sensor market is expected to grow to \$3.2 billion by 2025 (Sofos et al. 2020). For integrated success in this spectrum, the goals of technology developers (selling more sensors, developing inexpensive low-power sensors, etc.) and homeowners (buying fewer sensors, reducing electricity bills using data from sensors, etc.) need to be aligned (Sofos et al. 2020). A study on users' perception of commercially available smart thermostats found that users discuss more about cost, control, ease of use, installation, etc. (Koupaei et al. 2020). Thus, developments of new sensors must focus on these aspects of design and operation.

While the capital cost of wireless sensors can be considerably low, the installation and maintenance costs of the sensor networks should be reduced for successful widespread deployment (Sofos et al. 2020). Future cost-effective wireless sensors must also be easily mountable and interoperable with legacy and future control infrastructure (Sofos et al. 2020). Often, homeowners are hesitant that wireless sensors will function as reliably as their wired counterparts (Sofos et al. 2020). These notions should be eliminated with utility-led awareness drives and marketing strategies demonstrating real-world comparative analyses. Further, technicians should be provided with training for proper installations and knowledge of how integrated wireless sensors function (Sofos et al. 2020).

F.5 Automated Fault Detection and Diagnosis in the Market

Table 54. Current AFDD Technologies for Residential HVAC Systems

Excerpt from Butzbaugh, Tidwell, and Antonopoulos (2020)

Manufacturer – AFDD-Enabled Product	Integrated System?	Shares Maintenance Information with Service Provider?	Hardware Cost	Diagnostic Service Type/Cost?
American Standard – AccuComfort	Yes, with Nexia home automation system	Yes, a specified service provider will have access to the information	Depends on configuration	\$9.99/mo. for Nexia plus costs of service provider
Armstrong Air – Comfort Sync	Yes	Yes	Depends on configuration	Responsive to alerts/regularly scheduled maintenance; depends on service provider
Carrier – Infinity Bryant – Evolution	Yes	Yes, including remote software system updates	Depends on configuration	Responsive to alerts/regularly scheduled maintenance; depends on service provider
Coleman – Echelon and Charge View	Yes	No, only with homeowner	Depends on configuration	Regularly scheduled maintenance/emergency calls
Emerson – Sensi Predict	No, compatible with most HVAC	Yes, subscribed service from Emerson sends alerts to service provider and homeowner	~ \$280–450	Depends on service provider
Fraser-Johnston – multiple light system	Yes	No, homeowner or service provider must go to the physical unit and look at the light's color	Depends on configuration	Regularly scheduled maintenance/emergency calls
Goodman/Amana – ComfortBridge	Partially – does not require a Goodman/Amana thermostat	Yes, provided service provider has app	Depends on configuration, homeowner's thermostat choice	Depends on service provider
Lennox – iComfort	Yes	Yes, will share alerts with service provider and homeowner	Depends on configuration	Responsive to alerts/regularly scheduled maintenance; depends on service provider
Loxone – Smart HVAC Controls	Unknown	No, only with homeowner	Depends on configuration	Depends on service provider
Luxaire – Acclimate and Charge Smart	Yes	No, only with homeowner	Depends on configuration	Regularly scheduled maintenance/emergency calls
Maytag/Frigidaire/ Broan – iQ Drive	Yes	No, must go to the physical unit and read a two-digit code	Depends on configuration	Regularly scheduled maintenance/emergency calls
Rheem/Ruud – EcoNet	Yes	No, only with homeowner	Depends on configuration	Regularly scheduled maintenance/emergency calls
Trane – ComfortLink II	Yes	Yes, a specified service provider will have access to the information	Depends on configuration	\$9.99/mo for Nexia plus costs of service provider
York	Yes	Yes, user can determine what information service providers have access to	Depends on configuration	Responsive to alerts/regularly scheduled maintenance; depends on service provider

AFDD is currently common in large commercial buildings—some common “software-as-a-service” products include Clockworks by KGS buildings, Analytika by Cimetrics, and Building Analytics by Schneider Electric (Frank et al. 2018). Only high-end, variable-speed residential central air conditioning/air-source heat pump models currently have embedded AFDD (which has the added benefit of not increasing installation costs) in the residential sector. The root cause behind this low adoption is the high cost of the sensors of the embedded systems that connect the outdoor and indoor units (Butzbaugh, Tidwell, and Antonopoulos 2020). Additionally, some third-party AFDD products are available that could be attached to already-installed equipment and operated digitally (Butzbaugh, Tidwell, and Antonopoulos 2020). An overview of the major

residential AFDD products currently available is provided in Table 54 (Butzbaugh, Tidwell, and Antonopoulos 2020).

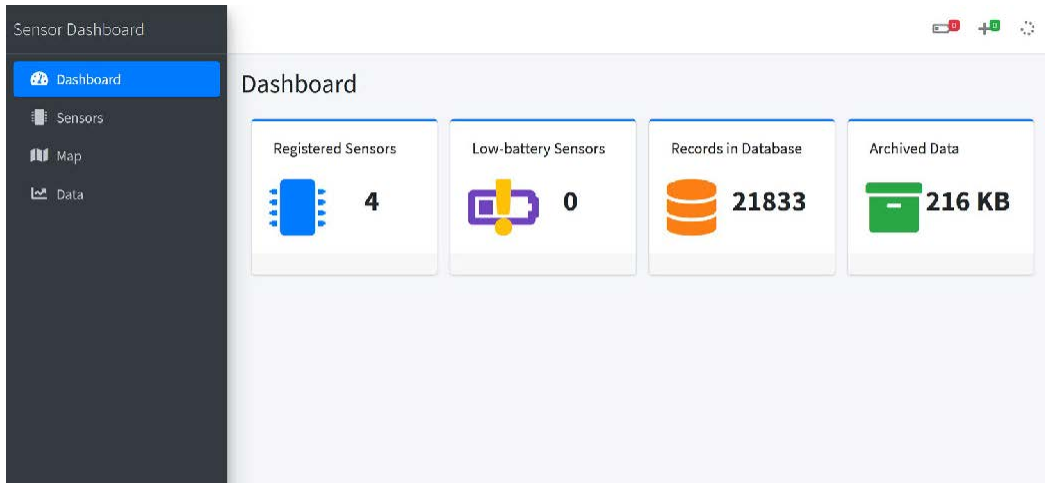
Research has shown that 10%–20% of HVAC systems will need replacement in the next five years. When a piece of equipment fails at the later stages of the lifetime, they are generally more expensive to repair, and this presents a great opportunity for the homeowner to invest in AFDD-embedded systems (Butzbaugh, Tidwell, and Antonopoulos 2020).

Data must be collected on the energy savings and reduction in customer expenditure before and after AFDD-embedded technologies are installed to clearly communicate the efficacy and value of these devices to homeowners (Wheeler et al. 2020). Pricing information must be widely made available and incentives like pay-for-performance service plans should be offered to encourage homeowners to invest in these technologies. Electric utilities in regions of the country that already provide incentives for ENERGY STAR[®] certified appliances or smart thermostats can utilize these partnerships to promote residential AFDD approaches (Butzbaugh, Tidwell, and Antonopoulos 2020).

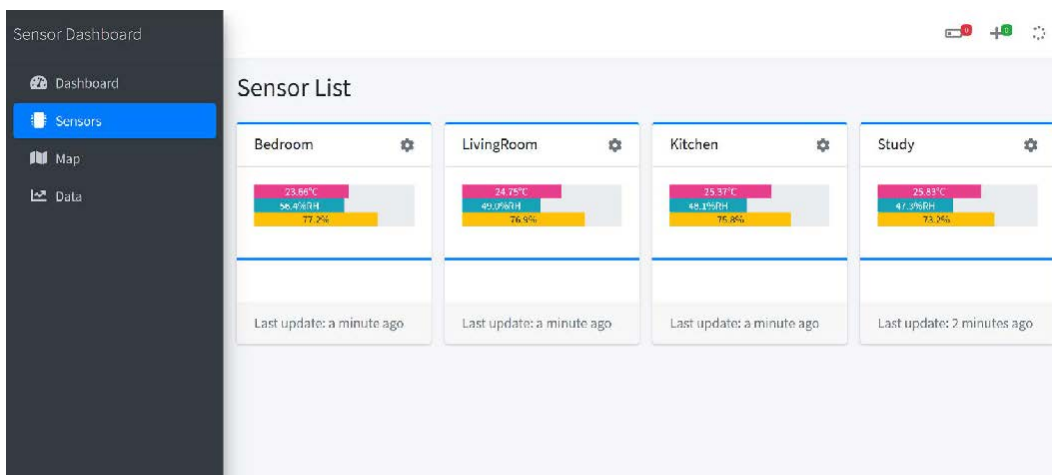
Additionally, future AFDD approaches must minimize the reliance of algorithms on historical data since such disaggregated temporal datasets from a wide variety of residences are very rare. FDD methods can be classified into quantitative analysis, qualitative analysis, and historical data analysis, which is commonly accepted by multiple researchers (Venkatasubramanian, Rengaswamy, and Kavuri 2003; Venkatasubramanian, Rengaswamy, Kavuri, et al. 2003; Venkatasubramanian, Rengaswamy, Yin, et al. 2003; Katipamula and Brambley 2005a, 2005b; Mirnaghi and Haghghat 2020; Singh, Mathur, and Bhatia 2022; Alzghoul et al. 2014). Historical data analysis, also known as data-driven methods in some research studies, is increasingly prevalent in the past two decades, largely due to the rapid development of communication technology. However, compared to the data-driven approaches, the knowledge-based reference still has irreplaceable advantages, such as being much simpler, having less computation load, less data required, easily interpretable, etc. Therefore, a rule-based approach is more likely to be deployed in currently ordinary homes, as it complies with unitary physics principles and does not necessarily depend on a mass of measured data for training (Rogers, Guo, and Rasmussen 2019a). This logic is behind the AFDD method proposed in this project.

Finally, an ideal AFDD system should be low cost, reliable, have low false diagnostic rates, be compatible with other AFDD tools, be automatically configurable, and use heuristic evidence (Shi and O'Brien 2019). Since residential AFDD products are still at a nascent stage, near-term AFDD technologies should focus on reporting high-priority faults that significantly affect energy efficiency (Butzbaugh, Tidwell, and Antonopoulos 2020). As research in this area continues, HVAC contractors can continue using inexpensive smart diagnostic tools to perform targeted measurements and detect faults.

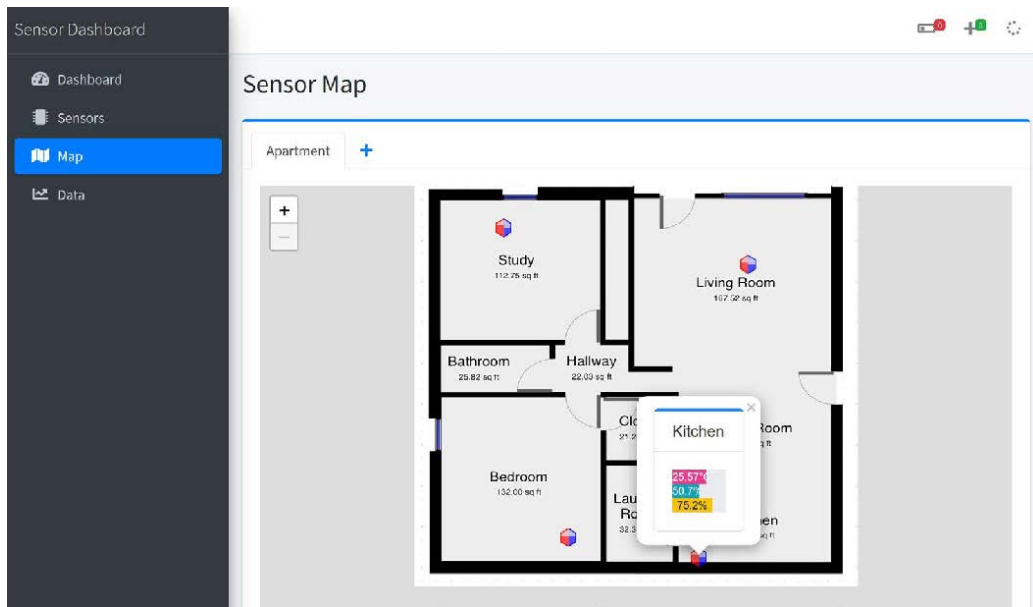
F.6 Interface Demo for Indoor Climate Monitoring in the Home Energy Management System We Created



Dashboard



Sensor list



Sensor map



Measurement data

Figure 143. Interface demo for indoor climate monitoring in this home energy management system

Appendix G: Economic Analysis

G.1 Electricity Price

The prices of electricity for residential buildings are obtained through the U.S. Bureau of Labor Statistics (Statistics 2023). 22 cities have data that is located exactly at the same locations. For the remaining cities, their price data is represented by the corresponding regions. For example, in the case where there is no direct data available for Austin, the data for West South Central is utilized to represent it.

All data are for the residential buildings in 2022, except Houston, Atlanta, Detroit, and Denver, which have some data missing. So for this case, the price escalation from 2021 in the corresponding area is used to estimate the electricity price in one given month of a city. For example, shown in Table 55, the 2022 price data in April and June is missing for Houston. As Houston is located in the West South Central region, the escalation rates of electricity price from 2021 in April and June in the West South Central region is used to estimate the price data on the basis of 2021. This is also applied to other cities that have missing data.

Table 55. Example of Data Processing for Missing Electricity Price

Region	Houston (dollar)		West South Central (dollar)		
Year	2021	2022	2021	2022	Escalation rate of 2021-2022
Jan	0.139	0.138	0.116	0.132	13.79%
Feb	0.143	0.148	0.117	0.134	14.53%
Mar	0.144	0.141	0.118	0.134	13.56%
Apr	0.141	0.165	0.119	0.139	16.81%
May	0.138	0.188	0.121	0.149	23.14%
Jun	0.138	0.177	0.126	0.162	28.57%
Jul	0.147	0.258	0.129	0.180	39.53%
Aug	0.152	0.257	0.133	0.182	36.84%
Sep	0.157	0.241	0.136	0.180	32.35%
Oct	NA	0.207	0.136	0.173	27.21%
Nov	0.156	0.182	0.134	0.163	21.64%
Dec	0.156	0.190	0.133	0.160	20.30%

The monthly electricity price data is plotted in Figure 144 and Figure 145, which shows that Honolulu has the highest electricity price. The electricity prices in Montgomery, Great Falls, and Internal Falls are relatively lower.

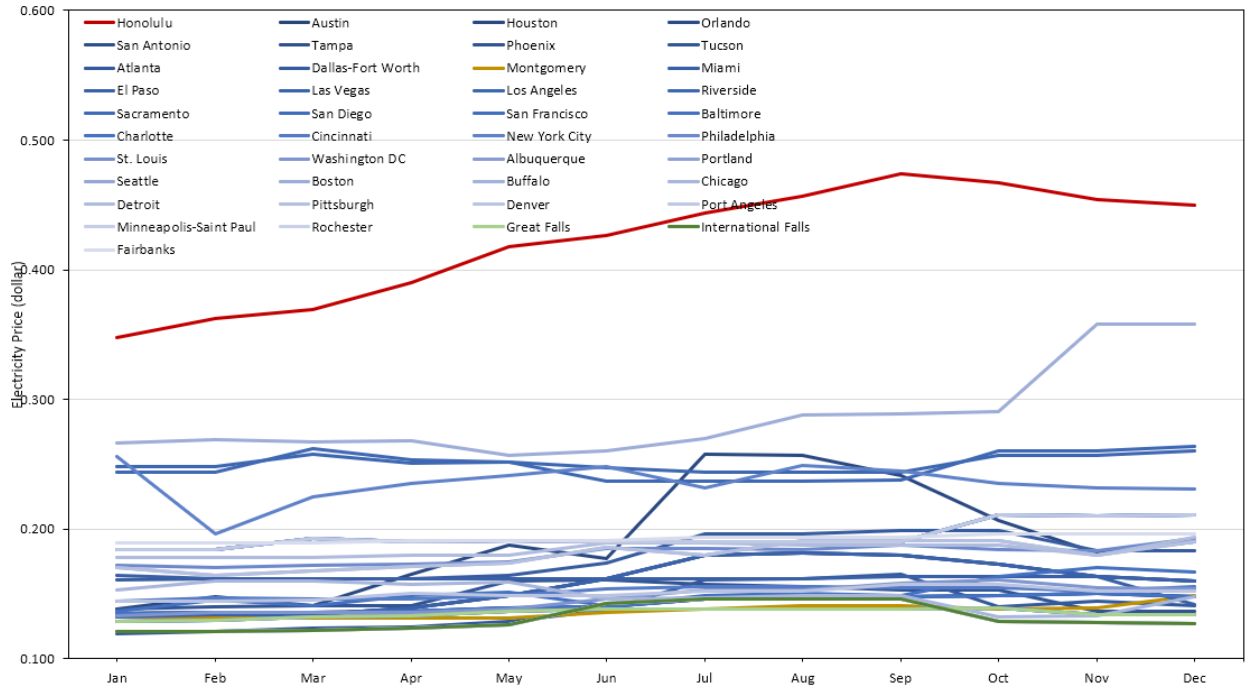


Figure 144. Monthly electricity price for 41 selected cities

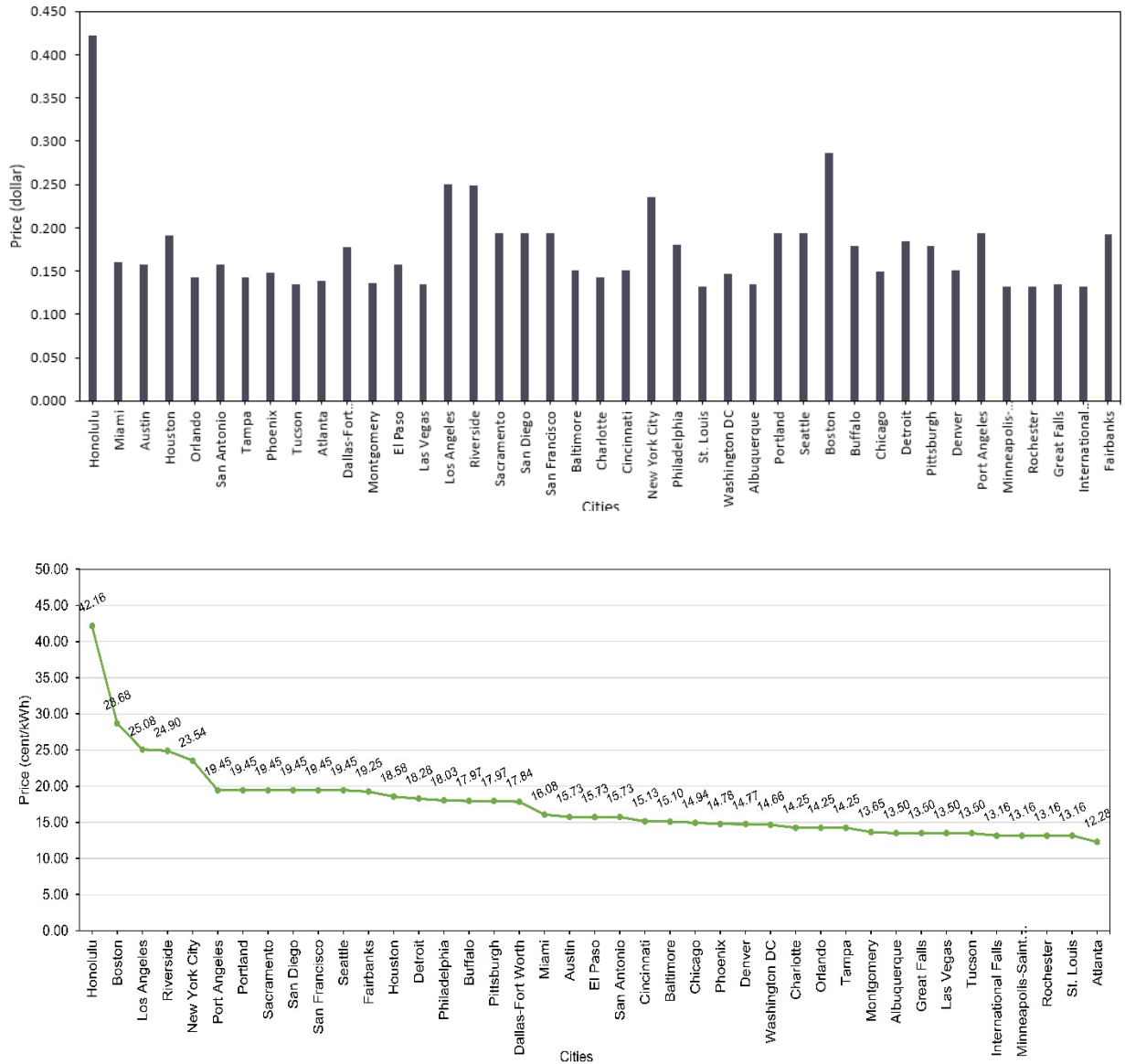


Figure 145. Annual electricity price on average for residential buildings in 41 selected U.S. cities (2022)

G.2 Data for Computing Base-Year Energy Cost Savings

The cost-effectiveness of an energy-efficiency project highly depends on two factors: the investment on the renovation, and the cost savings due to reductions in energy consumption. Relevant data are collected to calculate the savings and costs.

The inputs for computing energy cost savings include the reduction in energy consumption and price of electricity and natural gas. The equation to calculate the base-year energy cost savings is presented in Equation (42), where i is the type of fuel (i.e., electricity or natural gas), n is the number of fuel types in building operation, E_i is the reduction in fuel type i consumption, P_i is

the cost rate of the fuel type i in the base year, and C_i is the amount of monetary savings of the base year.

$$C_0 = \sum_{i=0}^n E_i * P_i \quad (42)$$

The results of energy savings for difference building types, cities, and energy code versions are obtained from the building energy simulation suite introduced in Section 8.3.3.

The commercial price of natural gas is obtained based on the database of the U.S. EIA (2022c), which provides an annual summary of the volumetric natural gas price and its average heating value (HV) in each state. The rate of natural gas per Btu is hence calculated using Equation (43). The gas price used in this study is based on the data of 2021, and is specific to each state.

$$P_g = P_{g,vol} / HV_g \quad (43)$$

The **commercial price of electricity is calculated based on the 2020 EIA-861 database** (EIA 2022b). Form EIA-861, also known as Annual Electric Power Industry Report, collects the operation data of electric power industry entities in the United States and its territories regarding the generation, transmission, distribution, and sale of electric energy (EIA 2022b). The EIA-861 database is considered a census of all U.S. electric utilities (EIA 2022a) due to its comprehensive coverage of the operational data of various distribution utilities and power marketers of electricity in this country. However, the local retail price of electric energy is not provided in the database because of many reasons, e.g., the dynamic tariff structure and intricate network of utility distribution—one county may be served by multiple power marketers and one power marketer can also serve multiple counties.

Given the knowledge gap, a workaround is taken to approximate the retail electricity price in the selected cities by making two homogenous assumptions. First, the price of electric energy delivered by one power marketer stays stable regardless of where and what the consumer is, the time of usage, and demand charge. This assumption can be represented by Equation (44), where $P_{e,j}$ is the retail electricity price of the power marketer j , while R_j and E_{e_j} are its total revenue (in dollars) and sold electricity (in kWh), respectively. Second, the electricity sold to a metropolitan statistical area (MSA) by various power marketers is proportional to their respective total electricity sale. The mathematical form of this assumption is presented in Equation (45), where j is the identifier of the power marketer, k is the identifier of the MSA, $E_{e_j,k}$ is the electricity sold by power marketer j to MSA k , E_{e_k} is the total electricity consumption of MSA k , and m is the number of power marketers that distribute electricity to MSA k .

$$P_{e,j} = R_j / E_{e_j} \quad (44)$$

$$E_{-e_{j,k}} = E_{-e_k} * \frac{E_{-e_j}}{\sum_{j=0}^m E_{-e_j}} \quad (45)$$

Hence, the retail electricity price of an MSA k (i.e., $P_{e,k}$) can be calculated following Equation (46). The identification of the geographical range of MSAs is based on the U.S. Census Bureau data (U.S. Census Bureau 2022). Albeit bearing lumped assumptions, the estimated retail electricity price plays an important role in the cost-effectiveness analysis by taking into consideration the impact of local energy price on the cost benefits of occupancy-based HVAC controls.

$$P_{e,k} = \frac{\sum_{j=0}^m R_j}{\sum_{j=0}^m E_{-e_j}} \quad (46)$$

G.3 Data for Computing Future Energy Cost Savings

The Energy Escalation Rate Calculator developed by NIST (NIST) is used to generate the energy escalation rate for the calculation of future energy costs over the performance period. The Energy Escalation Rate Calculator is developed on the basis of EIA's projections of the future energy price. The future energy cost savings can be calculated following Equation (47), where C_t is the energy cost savings in year t , and $EEER_i$ is the energy escalation rate of fuel type i . The energy escalation rate result is specific to different energy types and locations.

$$C_t = \sum_{i=0}^n E_i * P_i * (1 + EEER_i)^t \quad (47)$$

The Energy Escalation Rate Calculator generates four scenarios of energy escalation rate under different levels of estimated social cost of carbon (NIST). The social cost of carbon is originally defined as the monetary value of the damage done by emitting one more ton of carbon at some point of time (Pearce 2003). Considering social cost of carbon in a cost-benefit analysis reflects the societal value of reducing carbon emissions, and has been a regular practice of federal agencies in the decision-making of climate policies since 2008 (Interagency Working Group on Social Cost of Greenhouse Gases 2021). This study considers all four scenarios when calculating future cost savings to account for the benefits of carbon emissions reduction. These four scenarios are Baseline (with social cost of carbon not considered), Low, Medium, and High. Further details are available in the User Guide of the Energy Escalation Rate Calculator (NIST 2022). These values are directly exported from the Energy Escalation Rate Calculator tool.

G.4 Data for Computing Material Costs

The materials needed for implementing occupancy-based controls are primarily the occupancy sensors. The price of occupancy presence and occupant counting sensors designed for commercial building applications is determined based on a coherent consideration of the input from sensor developers during previous field testing (Kong et al. 2022) and a search of the prevailing products on the market (Density 2022; Traftsys 2022). In addition, the number of these two types of sensors are determined by the layout of buildings, i.e., the number and type of

zones. The input data for the computation of material costs are presented in Table 56. A contingency ratio of 10% is added on top of the total cost of sensors to account for any unexpected expenses during the installation progress (Touran 2003).

There are a lot of uncertainties with the price of occupancy sensors. Therefore, a parametric analysis is conducted to investigate how the change in sensor costs influences the payback of an occupancy-based control project.

Table 56. Input Data for the Computation of Material Costs

	Temperature/Humidity Sensor
Unit price of sensor	\$14.10
Number of sensors for air side	2
Number of sensors for refrigerant side	7
Local hub (e.g., Raspberry Pi)	\$76.25
Cloud (recurring) (e.g., Amazon Web Services, monthly per sensor)	\$0.13

G.5 Data for Computing Labor Costs

The developed sensor and service system in this project is straightforward to install, similar to other commercial smart home energy management systems, so generally the installation can be completed by the homeowner. This means no additional labor cost is required.

Appendix H: Literature Review

Table 57. Literature Review of Fault Modeling

Building type/ components	Modeling software	Fault description	Reference	Year
Office building	EnergyPlus	Four individual faults (plant pipe clog, economizer outdoor air damper leakage, fouled water heating coil, and room air temperature sensor offset)	Basarkar et al. (2011)	2011
Office building	Unspecified	Six individual HVAC faults (e.g., incorrect setpoint temperature, min outdoor air damper fails open)	Otto et al. (2012)	2012
Office building	TRNSYS	48 individual faults (e.g., O.A. damper stuck, Setpoint offset, Dirty coil)	Khire and Trcka (2013)	2013
Office building	EnergyPlus	16 individual faults (e.g., Supply air temperature sensor offset, Fouled cooling tower, Outdoor air damper leakage) and two combination scenarios	Wang and Hong (2013)	2013
Office building	EnergyPlus/ OpenStudio	Three individual faults (Outdoor air damper stuck, Fouled heating coil, and Supply fan stuck)	Li and O'Neill (2016)	2016
Office building	EnergyPlus	Four individual faults (Economizer sensor fault, Thermostat/Humidistat offset, Coil fouling, and Dirty air filter)	Zhang and Hong (2017)	2017
Office building	EnergyPlus/ OpenStudio	41 individual fault models (e.g., Outdoor air damper stuck, Supply fan degradation, Pump clog) and 129 combination scenarios	Li and O'Neill (2019)	2019
Office building	EnergyPlus/ Empirical equations/ Semi- empirical Models	17 individual faults (e.g., Economizer opening stuck, Non-standard refrigerant charging)	Kim et al. (J. Kim, Frank, Braun, et al. 2019; J. Kim, Frank, Im, et al. 2019)	2019
AHU	Simulink (SIMBAD library)	Three individual faults (Control of three-way valve, Mixing box damper, and Sensor inversion)	Ginestet et al. (2008)	2008

Air-cooled chiller and air-cooled unitary air conditioner	Empirical equations	Unspecified	Cheung and Braun (2013b, 2013a)	2013
Water-cooled chiller	Empirical equations	Four individual faults (overcharging, excess oil, non-condensable in refrigerant, and water-side condenser fouling)	Cheung and Braun (2016)	2016

Table 58. Comparison of Different FDD Methods for the VCC System

Authors	Year		Features										Fault-free reference model			Faults							FDD methods		
			Temperature										Pre.	Ele.				1	2	3	4	5		6	7
			Te	Tev	Tsh	Tc	Tcl	Tsc	Td	Toae	Tiac	dP	Power	Tia	Tidp	Toa	UC	OC	LL	CMF	CF	EF	NC		
Yoshimura	1989	Packaged air conditioner	√	√	√	√	√	√		√	√	√	√	No FFRM			√	√	√	√	√	√			Decision tree
Rossi	1995	RTU (fixed orifice)	√	√	√	√	√	√	√	√	√			√	√	√	√		√	√	√	√			Statistical rule-based chart
Breuker	1998	RTU	√	√	√	√	√	√	√	√	√			√	√	√	√		√	√	√	√			Statistical rule-based chart
Chen	2000	RTU (TXV)	√			√	√	√						√	√	√	√	√	√	√	√	√	√	√	Sensitivity ratio method
Chen	2000	RTU (TXV)						√		√	√			No FFRM			√	√	√	√	√	√	√	√	Simple rule-based method
Kim	2008	Split heat pump	√	√	√	√	√	√	√	√	√			√	√	√	√	√	√	√	√	√	√		Statistical rule based chart
Payne	2020	Split heat pump	√	√	√	√	√	√	√	√	√			√	√	√	√	√	√	√	√	√	√		Statistical rule based chart

Table 59. Literature Review of Rule Extraction Research

Author	Year	Rule extraction methods	Target system	Control variable	Data source	Open/closed loop testing	Control performance evaluation
Coffey (2011a, 2011b, 2013)	2011	Look-up table	External shading and natural ventilation	Shading percentage and natural ventilation percentage	Simulation (EnergyPlus and Modelica)	Closed loop	EC, TC (PPD)
Ostendorp (2011; 2012)	2011	Generalized linear model (GLM)	Natural ventilation with the window	Window on/off	Simulation: EnergyPlus	Open loop	EC
Domahidi (2012)	2012	Adaptive boosting (AdaBoost)	Six one-zone of different office buildings	Energy recovery load and unload, free cooling load and unload	Simulation (BACLab)	Open loop and closed loop	EC, TC (unmet hours)
Ostendorp (May-Ostendorp, Henze, Rajagopalan, and Corbin 2013)	2013	Classification and regression trees (CART), Generalized linear models (GLM), AdaBoost	Natural ventilation with the window	Window on/off	Simulation: EnergyPlus	Open loop and closed loop	TC
Ostendorp (May-Ostendorp, Henze, Rajagopalan, and Kalz 2013)	2013	CART	Thermo-active building systems cooling and natural ventilation	Window on/off, circulation pump pulse-width modulation (PWM) fractions	Field test	Closed loop	EC, TC, RMA
Domahidi (2014)	2014	Support vector machine (SVM), AdaBoost	Six one-zone of different office buildings	Energy recovery load and unload, free cooling load and unload	Simulation (BACLab)	Open loop and closed loop	EC, TC, (unmet hours)
Le (2014)	2014	SVM	Shading systems in residential building	Blind position (0,0.5,0.75,1)	Simulation (SIMBAD)	Open loop	TC (Tid violation), VC (Lum violation)
Tanner (2014)	2014	CART	Window controls in the simplified building model	Window state (closed, open)	Simulation (EnergyPlus)	Open loop and closed loop	EC, TC (PMV)

Author	Year	Rule extraction methods	Target system	Control variable	Data source	Open/closed loop testing	Control performance evaluation
Robillart (M Robillart et al. 2014)	2014	GLM	An experimental passive single-family house	Heating power	Simulation (COMFIE)	Open loop and closed loop	EC, TC, RMA, Cost, LS, CT
Drgoña (2018)	2018	Time Delay Deep Neural Network (TDNN)	One radiator per room fed by a central gas-boiler, in a six-zone building	Radiators heat flows	Simulation (Modelica)	Open loop and closed loop	EC, TC, CT
Robillart (M. Robillart, Schalbart, and Peuportier 2017)	2018	Beta Regression	Heating systems	Heating power	Simulation (COMFIE)	Closed loop	CT, RMA, EC, Cost, LS, TC (discomfort rates)
Qiu (2019)	2018	CART, Weighted association rule mining (WARM)	Lighting system chiller	On/off control sequencing control coordinated control	Field test	Open loop	RMA
Bursill (2019)	2019	Decision tree	Variable air volume system	The HVAC equipment is overridden or using reactive control	Field test	Open loop	EC
Gunay (2019)	2019	Decision tree	AHU system	AHU schedule, indoor temperature setpoint, outdoor air rate	Simulation (EnergyPlus)	Not test	NA
Piscitelli (2019)	2019	CART	Smart glazing	Discrete state of glazing	Simulation (EnergyPlus)	Open loop and closed loop	EC

IoT-Based Comfort Control and Fault Diagnostics System for Energy-Efficient Homes

Bursill (2020)	2020	Decision tree	Variable air volume system	Variable air volume damper position, variable air volume reheat coil valves, radiant heater valve position (only for heating)	Field test	Open loop	EC, TC
Chen (2021)	2021	Logistic regression	Chiller	On/off, chilled water temperature	Simulation (EnergyPlus)	Open loop	RMA

CART: Classification and regression trees

AdaBoost: Adaptive boosting

GLM: Generalized linear models

WARM: Weighted association rule mining

XGBoost: Extreme gradient boosting

PWM: Pulse-width modulation

VC: Visual comfort

EC: Energy consumption

TC: Thermal comfort

RMA: Rule model accuracy

CT: Computation time

LS: Load shifting



U.S. DEPARTMENT OF
ENERGY

Office of
**ENERGY EFFICIENCY &
RENEWABLE ENERGY**

For more information, visit: buildingamerica.gov

DOE/GO-102024-6120 · April 2024